

UNIVERSITY OF SOUTHAMPTON

**PIT INITIATION ON AUSTENITIC
STAINLESS STEELS**

by
John Stewart

TABLE OF CONTENTS

TABLE OF CONTENTS	i
ABSTRACT	vi
ACKNOWLEDGEMENTS	vii
LIST OF SYMBOLS	viii
LIST OF ABBREVIATIONS	xi
 CHAPTER 1 - INTRODUCTION	 1
1.1 THE CORROSION AND PASSIVITY OF STAINLESS STEELS	2
1.2 PITTING CORROSION OF STAINLESS STEELS	7
1.2.1 Pit Propagation	8
1.2.2 Pit Initiation	12
1.3 THE ORGANISATION AND OBJECTIVES OF THIS THESIS	18
 CHAPTER 2 - EXPERIMENTAL PROCEDURES	 21
2.1 SPECIMEN PREPARATION	22
2.2 ELECTROCHEMICAL METHODS	24
2.3 EXPERIMENTAL APPARATUS AND INSTRUMENTATION	27
2.3.1 Precautions Against Electrical Interference	29
2.4 PITTING EXPERIMENTS	30
2.4.1 Data Acquisition	30
2.5 DATA ANALYSIS	33
2.6 DISTRIBUTION OF PITTING BREAKDOWN POTENTIALS	41
 CHAPTER 3 - RESULTS AND DISCUSSION: SLOW ANODIC POTENTIAL SWEEP EXPERIMENTS	 42
3.1 INTRODUCTION	43
3.2 EXPERIMENTAL	44

TABLE OF CONTENTS

3.3 RESULTS	45
3.3.1 General Features of Slow Potentiodynamic Ramp Experiments	45
3.3.1.1 The Shapes of Current Transients	51
3.3.2 The Potential Ramp Rate	54
3.3.3 The Relationship Between Current Transients and Observed Pitting	54
3.3.4 Pit Sizes Represented by Current Transients	65
3.3.5 Current Densities in Unstable Pits	65
3.3.6 Characteristics of Pit Propagation	69
3.3.6.1 Current vs Time	69
3.3.6.2 The Physical Characteristics of Pits	75
3.4 DISCUSSION	80
3.4.1 General	80
3.4.2 Anodic Film Growth and Passive Current Density	84
3.4.3 Potential Dependence of Transients	85
3.4.4 Discussion of Pit Initiation and Propagation	88
3.4.4.1 Initiation	88
3.4.4.1.1 Effect of Potential Sweep Rate on Pit Nucleation Frequency and Feedback Model for Initiation	88
3.4.4.1.2 Alloy Microstructural Effects	89
3.4.4.2 Repassivation	90
3.4.4.2.1 Hypotheses on Repassivation Based on Potential Gradients and Changes in Resistance to Current Flow	90
3.4.4.2.2 Hypothesis on Repassivation Based on "Sulphur Exhaustion"	101
3.4.4.3 Propagation	101
3.5 SUMMARY	106
 CHAPTER 4 - THE EFFECTS OF SOLUTION FLOW ON THE INITIATION OF PITTING CORROSION ON STAINLESS STEELS	 108
 4.1 INTRODUCTION	 109
4.1.1 Laminar and Turbulent Flow in a Closed Conduit	110
4.2 EXPERIMENTAL	112
4.3 CALIBRATION	116

4.4 RESULTS	117
4.5 DISCUSSION	120
4.6 SUMMARY	125
CHAPTER 5 - THE IMPORTANCE OF SULPHIDE INCLUSIONS IN THE PITTING CORROSION OF STAINLESS STEELS	126
5.1 INTRODUCTION	127
5.1.1 The Origin and Types of Sulphide Inclusions in Stainless Steels	127
5.1.2 Experimental Observations of Pit Initiation at Sulphide Inclusions in Stainless Steels	130
5.1.3 Proposed Mechanisms of Pit Initiation at Sulphides	132
5.1.3.1 Physical Nature of Sulphide	132
5.1.3.2 Sulphide Dissolution	133
5.1.4 Methods of Improving Pitting Resistance	144
5.1.5 The Experimental Work Presented in this Chapter	146
5.2 EXPERIMENTAL	147
5.2.1 Model Alloy Production	147
5.2.2 Characterisation of Inclusions	147
5.2.2.1 Image Analysis	149
5.2.2.2 Chemical Composition of Inclusions	151
5.2.3 Pitting Experiments	152
5.3 RESULTS	153
5.3.1 Image Analysis	153
5.3.2 Chemical Composition of the Inclusions	161
5.3.2.1 EDS Analysis in the SEM	161
5.3.2.2 EDS and WDS Analysis in the EPMA	166
5.3.2.2.1 Corrections Applied to EPMA Data	166
5.3.3 Pitting Experiments	168
5.3.3.1 Nucleation Frequency of Unstable Pits	168
5.3.3.2 Pit Propagation	174
5.4 DISCUSSION	182
5.4.1 A Suggested Mechanism for the Nucleation of a Propagating Pit	185

TABLE OF CONTENTS

5.4.2 The Relationship Between Pit Lifetime and Inclusion Size Distribution	187
5.4.3 Some Comments on the Discrepancy Between the Total Number of Pits Observed and the Total Number of Sulphide Inclusions	188
5.5 SUMMARY	192
 CHAPTER 6 - THE IMPROVEMENT OF THE LOCALISED CORROSION RESISTANCE OF STAINLESS STEEL BY LASER SURFACE TREATMENT	 194
6.1 INTRODUCTION	195
6.2 THE IMPROVEMENT OF PITTING RESISTANCE USING LASER SURFACE MELTING	196
6.2.1 Experimental	196
6.2.2 Results	199
6.2.2.1 Pitting Experiments	199
6.2.2.2 Microstructural Characterisation	208
6.2.3 Discussion	214
6.2.3.1 Further Investigations of the Laser-Melted Zone	216
6.3 THE PREVENTION OF IGSCC USING LASER SURFACE MELTING	224
6.3.1 Experimental Procedure and Results	225
6.4 SUMMARY	231
 CHAPTER 7 - PIT NUCLEATION ON 316L	 233
7.1 INTRODUCTION	234
7.2 EXPERIMENTAL	238
7.3 RESULTS AND DISCUSSION	238
 CHAPTER 8 - CONCLUSIONS	 252

TABLE OF CONTENTS

APPENDICES	258
APPENDIX A - Metallurgical Aspects of Stainless Steels	259
APPENDIX B - Composition of Stainless Steels used in this Study	268
APPENDIX C - Relationship Between Constants (K_a and K_v)	269
APPENDIX D - Computer Program for the Solution of Equation 3.41	272
APPENDIX E - Calibration of the Flow Rig	273
APPENDIX F - Information on Inclusion Size and Shape Derived from Image Analysis	280
REFERENCES	281

UNIVERSITY OF SOUTHAMPTON

ABSTRACT

FACULTY OF SCIENCE

CHEMISTRY

Doctor of Philosophy

PIT INITIATION ON AUSTENITIC STAINLESS STEELS

by John Stewart

Mechanistic aspects of the initiation and early stages of growth of pitting corrosion on stainless steels in dilute chloride solution are described. Electrochemical techniques have been used to detect and follow the evolution of anodic current transients which occur at the nano-amp level prior to the onset of sustained pitting. These transients are shown to correlate with the occurrence of micropits on the specimen surface. Prior to repassivation, there was no difference in their current-time evolution to distinguish unstable micropits from pits which subsequently grew into stable macropits. The basic shapes of the experimentally-observed transients are shown to be consistent with a simple model of a developing pit.

Environmental and metallurgical factors which influence the nucleation and subsequent stability of micropits are identified and described. The imposition of solution flow does not affect the nucleation of pits but turbulent flow stops or inhibits their growth. Using two high purity 304L model alloys, one of which was doped with sulphur, in addition to a commercial purity 304L, it is shown conclusively that sulphur-rich inclusions dominate as pit nucleation sites. A hypothesis is introduced in which sulphur, derived from sulphide inclusions, helps to stabilise the growth of pits. It is proposed that the lifetime of unstable pits is related to inclusion size. These ideas are developed with the aid of experiments on laser treated specimens, in which surface melting was found to refine the inclusion population such that most were only visible in the transmission electron microscope. One consequence of this hypothesis is that below a certain size, sulphur-rich inclusions are too small to nucleate a damaging pit. A stochastic element of the early stages of pitting is suggested to be the availability of sulphur to catalyse the anodic dissolution process in the pit. Molybdenum has been found not to influence pit nucleation, but reduces the dissolution rate in an active pit. The requirement for molybdenum additions to stainless steels in the absence of harmful sulphur-rich inclusions is questioned. In a separate study involving laser processing, surface melting is shown to provide an effective way to prevent intergranular stress corrosion cracking in sensitised 304 stainless steel.

The work reported here is consistent with a general class of 'feedback' models. The implication of such theories is that the driving force for pit nucleation is the current in the passive state. In the present study it is shown that the passive current and the pitting activity vary with the volume fraction of sulphides in the steel, implying that local instabilities in the passive current occur at sulphide inclusions. Consistent with this, many small pits were associated with sulphide inclusions.

ACKNOWLEDGEMENTS

I would like to thank Dr. David Williams (Harwell) for his encouragement, guidance and contribution to this research. Professor Martin Fleischmann's insights and suggestions during the early stages of this work are also gratefully acknowledged. I would also like to thank Dr. Lawrence Peter (Southampton) in his role as guest supervisor towards the end of this work.

I am pleased to acknowledge the support of my colleagues in the Corrosion Technology Group at Harwell. In addition I enjoyed numerous discussions (on various topics) with Mr. Brett Wells, Dr. Roger Newman, and Dr. Brian Pickering.

My thanks are due to a number of people whose expertise and assistance is much appreciated: Mr. Dave Bolus (Image Analysis); Mr. Tony Bransden (laser processing); Dr. Colin Shepherd (transmission electron microscopy).

It is with the greatest of pleasure that I thank my wife Betty for her love and tolerance during the course of this work, and also for her substantial efforts in preparing the final manuscript.

John Stewart

January 1990

The work described in this thesis was undertaken as part of the Underlying Research Programme of the United Kingdom Atomic Energy Authority.

LIST OF SYMBOLS

ROMAN SYMBOLS

a	Specimen area
a	Pit mouth radius (Chapter 3)
A	Pit internal area
A, B	Parameters of high field growth law
b	Tafel slope
c_b	Bulk concentration of electro-active species
d	Hydraulic diameter (Chapter 4, Appendix E)
d	Minor axis of inclusion
D	Diffusivity (Chapter 4, Appendix E)
D	Major axis of inclusion
E	Potential
E_b	Pitting potential
\bar{E}	Electric field
E_n	Applied potential
E°	Equilibrium potential
E_o	Rest potential in pit solution
E_{rp}	Repassivation potential
F	Faraday constant
i	Current density
i_a	Current density of anodic process
i_c	Current density of cathodic process
i_{lim}	Limiting current density
i_o	Exchange current density
i_{plat}	Plateau current density
I	Current
k_a, k_R, k_v, k_l	Constants

LIST OF SYMBOLS

k_m	Mass transfer coefficient
m	Relative molecular mass
n	Number, as in number of specimens
N	Total number of specimens
p_c	Percolation threshold
$P(O)$	Survival probability
Q	Charge
r	Pit radius
R	Resistance to current flow at the pit mouth, (Chapter 3)
Re	Reynold's number
Sc	Schmidt number
Sh	Sherwood number
t	Time
T	Dimensionless time (Chapter 3)
T	Temperature (absolute)
u	Velocity
V	Volume
\dot{v}	Potential sweep rate
V_f	Volume fraction
V_m	molar volume
z	Number of electrons transferred in reaction

GREEK SYMBOLS

α	Transfer coefficient
α, β	Constants (Chapter 3)
β	Angle (Appendix C)
δ_d	Diffusion boundary layer thickness
δ_h	Viscous sub-layer (hydrodynamic boundary layer) thickness
ΔC	Concentration driving force
$\Delta \epsilon$	Dimensionless potential (Chapter 3)

LIST OF SYMBOLS

η	Overpotential
κ	Conductivity
λ	Wavelength of light (Chapter 5)
λ	Nucleation frequency of unstable pits
Λ	Nucleation frequency of stable (propagating) pits
μ	Probability of the death of an unstable pit
μ	Mean
ρ	Density
σ	Standard deviation
τ_c	Critical age for unstable pits
τ_s	Surface shear stress
ν	Kinematic viscosity

LIST OF ABBREVIATIONS

AES	Auger Electron Spectroscopy
AISI	American Iron and Steel Institute
AOD	Argon Oxygen Decarburisation
EDAX	Energy Dispersive Analysis by X-rays
EDS	Energy Dispersive Spectroscopy
EPMA	Electron Probe Microanalyser
ESCA	Electron Spectroscopy for Chemical Analysis
IGA	Intergranular Corrosion
IGSCC	Intergranular Stress Corrosion Cracking
m.l.i.	Mean Linear Intercept
REM	Rare Earth Metal
SCC	Stress Corrosion Cracking
SCE	Saturated Calomel Electrode
SEM	Scanning Electron Microscope
SOD	Steam Oxygen Decarburisation
TEM	Transmission Electron Microscope
VOD	Vacuum Oxygen Decarburisation
WDS	Wavelength Dispersive Spectroscopy
XPS	X-ray Photoelectron Spectroscopy
XRF	X-ray Fluorescence

CHAPTER 1

INTRODUCTION

CHAPTER 1 - INTRODUCTION

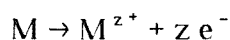
Undoubtedly the most important property of stainless steels is their corrosion resistance, without which they would find little commercial use, because their general level of formability and mechanical properties can be equalled or exceeded by other steels at a much lower cost. Therefore, stainless steels are used in applications requiring good corrosion resistance. These applications are numerous, ranging from, for example, kitchen utensils and cladding of buildings, to the containment of harmful chemicals and the construction of chemical plant.

Stainless steels do corrode however, and, unlike other (non-stainless) steels, where corrosion usually occurs in a predictable manner, their corrosion is often unexpected. Whilst the discovery of pitted cutlery is plainly irritating, it is usually tolerable. However, even this superficial damage would be unacceptable in, for example, some pharmaceutical applications, where the corrosion products would contaminate the process stream. When there is a risk of corrosion in critical applications, the corrosion performance of candidate materials must be assessed. Accelerated corrosion tests are commonly used in materials selection programmes or as part of plant failure investigations. For stainless steels, as indeed other alloy systems, the results of such studies account for a substantial proportion of the corrosion literature. Equally as important, in order to be able to specify and engineer more corrosion resistant materials it is necessary to determine the mechanisms and to identify the factors which contribute to the corrosion processes.

This study investigates mechanistic aspects of the initiation and early stages of growth of pits in a corrosion system of widespread technological importance: stainless steels in dilute chloride solutions.

1.1 THE CORROSION AND PASSIVITY OF STAINLESS STEELS

The successful use of stainless steels in corrosion engineering depends on the formation and maintenance of a thin chromium-rich passive surface layer with low ionic conductivity. The film reduces the current density of the anodic dissolution reaction:



The stability of the passive film depends on the pH of the solution and the electrode potential, and is also influenced by the composition of the environment and the underlying metal. Aggressive agents, such as the omnipresent chloride ion, can cause a loss of passivity, and corrosion damage ensues. The confinement of this damage to small areas, whilst the remainder of the alloy surface remains passive, explains the designation *localised* corrosion, a term which encompasses a number of different corrosion mechanisms. These mechanisms share the common characteristic that, once the corrosion has started, it remains localised and the effect on the alloy can be as devastating as it is unexpected.

The modes of localised corrosion other than pitting which may afflict stainless steels are **crevice corrosion**, which occurs in occluded regions, where a volume of stagnant solution separates two surfaces in close proximity. The surfaces may be metal/metal or metal/non-metal. Crevice corrosion is similar in many ways to pitting corrosion, and indeed on a microscopic scale a distinction between the two is often difficult to sustain (and probably unnecessary). For example, pit nucleation at inclusions is often referred to as a form of micro-crevicing, as pits have been observed to start at the inclusion/metal interface. On a larger scale crevice corrosion often occurs as a consequence of poor design or workmanship, particularly at joints. **Stress corrosion cracking** (SCC) and **corrosion fatigue** (CF), which in addition to a suitably corrosive environment, also require the presence of a tensile stress (or a cyclic stress in the case of corrosion fatigue). The role of the stress is to disrupt the passive film, enabling the underlying metal to corrode. The enormous body of literature which exists as a testament to the study of SCC and CF dictates that a prudent move at this point is to stop at this simplistic description. One point which is worth making though is that the vast bulk of these studies have been concerned with crack *propagation*. For example, many studies seek to define K_{ISCC} , the stress intensity factor below which SCC will not occur. Little attention has been given to issues of crack initiation, particularly from unnotched surfaces, where cracks are too small for a fracture mechanics approach to be applied. Consequently, design criteria which do not take account of crack initiation may be unduly pessimistic, and mechanistic descriptions which ignore crack initiation are necessarily lacking. The effect of microstructure on short stress corrosion cracks has only recently been considered^(1,2). A further category of localised corrosion is **intergranular corrosion**, which is usually associated with chemical heterogeneity at grain boundaries, leading to preferential dissolution in a suitably corrosive environment. Intergranular stress corrosion cracking (IGSCC) of sensitised stainless

steels is the specific case where chromium depletion at grain boundaries (from where the term "sensitised" arises), coupled with the presence of a tensile stress, may lead to intergranular fracture of components (in Chapter 6, a method to prevent the initiation of IGSCC, using laser surface treatment, is described).

Figure 1.1 shows a schematic polarisation curve for a stainless steel in a dilute hydrochloric acid solution, in which the parameters and terminology commonly used in studies of pitting corrosion are defined. Plots such as these may be generated using one of three electrochemical methods, all of which require the use of a potentiostat. The three variations are:

- (a) *potentiostatic*, in which the potential is held at a given potential until a constant current is established
- (b) *potentiodynamic*, where the potential is changed continuously at constant rate
- (c) *quasi-potentiostatic*, in which the potential is changed step-wise at the desired rate

It is usual to deaerate the test electrolyte, such that the current supplied for the corrosion reaction is provided only by the potentiostat, i.e. there is no contribution from the cathodic oxygen reduction reaction (for example) at the specimen surface.

For metal dissolution as the anodic reaction in a corroding system, the process can proceed in a number of ways. In the region of the curve marked A, the corrosion process proceeds under *activation* control, the kinetics of which are described by the Butler-Volmer and Tafel equations.

The net anodic (corrosion) current density, i , is given by the Butler-Volmer equation:

$$i = i_a - i_c = i_o \left[\exp \left(\frac{(1-\alpha) z F \eta}{RT} \right) - \exp \left(\frac{-\alpha z F \eta}{RT} \right) \right]$$

where:

i_a = current density of anodic process

i_c = current density of cathodic process

i_o = exchange current density

α = transfer coefficient, typically 0.5 for a simple electron transfer process

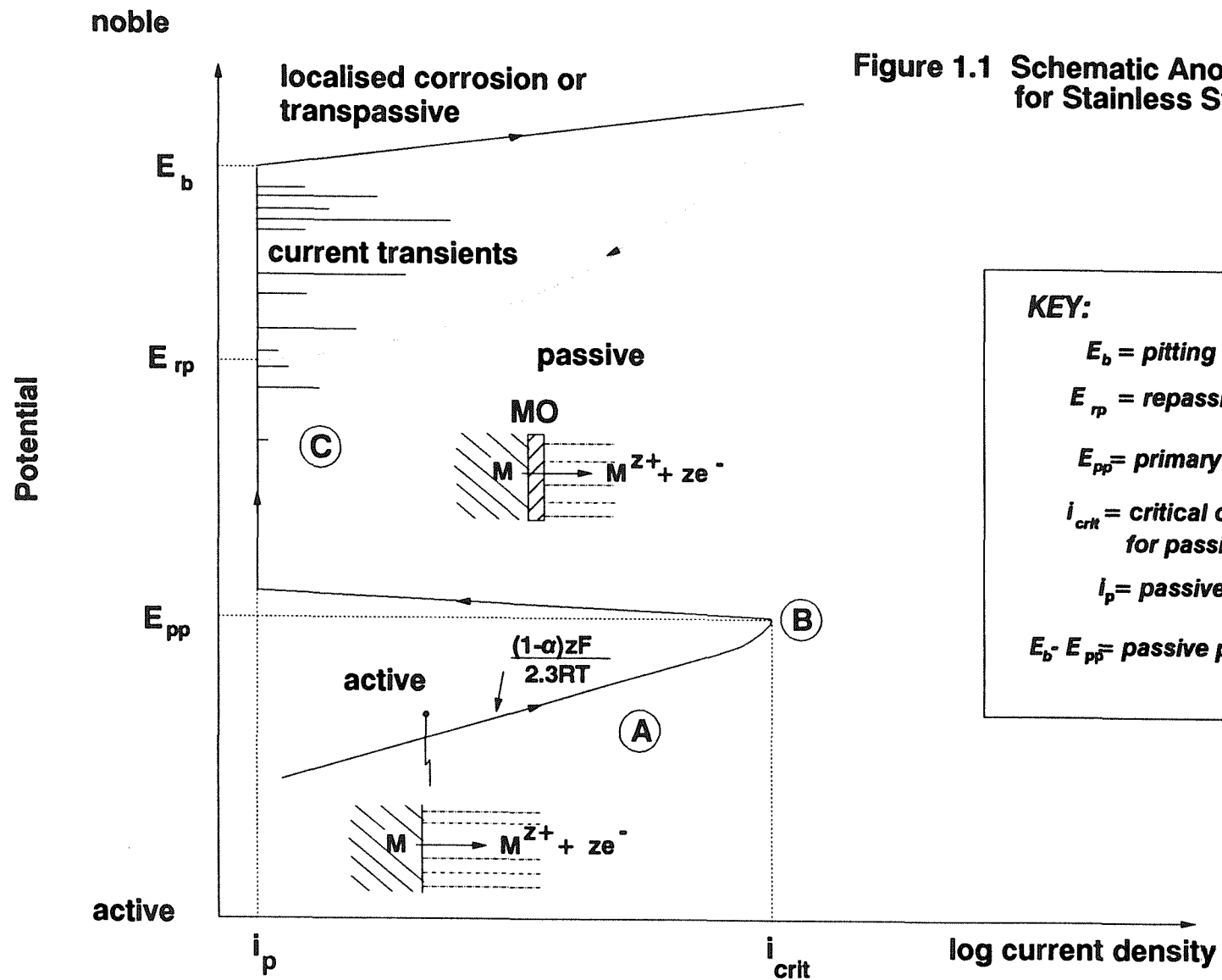


Figure 1.1 Schematic Anodic Polarisation Curve for Stainless Steel In Dilute HCl

KEY:

E_b = pitting potential

E_{rp} = repassivation potential

E_{pp} = primary passivation potential

i_{crit} = critical current density for passivation

i_p = passive current density

$E_b - E_{pp}$ = passive potential regime

η = over potential = $E - E^\circ$

E° = equilibrium potential

z, F, R, T , have their usual meanings

This equation is regarded as the fundamental equation of electrode kinetics, as it shows the way in which current density changes with exchange current density, overpotential, and the transfer coefficient. For most practical studies, it is more usual to use one of the limiting forms of the equation, at high anodic or high cathodic overpotentials. Thus at high positive overpotentials (associated with corrosion reactions), the anodic process dominates ($i_a \gg i_c$) and the second term may be ignored. The anodic current density is then given by:

$$i_a = i_o \left[\exp \left(\frac{(1 - \alpha) z F \eta}{RT} \right) \right]$$

and:

$$\log i_a = \log i_o + \frac{(1 - \alpha) z F \eta}{2.3 RT}$$

which is the well known Tafel equation.

For obvious reasons, stainless steels are not specified for use in environments where dissolution would proceed in a manner described by Tafel kinetics - as might occur in reducing acids for example. "Oxidising" environments are where the corrosion properties of stainless steels are of greatest benefit, as illustrated below.

Referring again to Figure 1.1, as the potential is increased in the positive direction and the metal continues to dissolve, the curve deviates from the linear $E - \log i$ behaviour expected from the Tafel equation. This deviation from activation control is associated with an increase in the concentration of corrosion products close to the dissolving bare metal surface. At some point the conditions for the formation of a solid oxide or hydroxide may be achieved (point B), leading to surface film formation, and a reduction in the current density to very low values. This process, which marks the onset of *passivity* for stainless steel, requires either a critical current density, i_{crit} , to be supplied, or a critical potential to be attained, the primary passivation potential

E_{pp} . The passive potential regime, region C in the diagram, may extend for many hundreds of millivolts.

Since the presence of oxide films on stainless steels was demonstrated by Evans and Stockwell⁽³⁾, a great deal of research effort has succeeded in providing some insight into the nature of the passive film. For example, the passive film on stainless steel is typically 1 to 5nm thick^(4,5), and is enriched in chromium⁽⁶⁻⁹⁾. With increasing chromium content in alloy, the film thickness and degree of crystallinity of the film decreases^(5,10,11). However, details of the elemental composition of the film and the compositional profile remain largely unresolved. To take just one example of this, it has been suggested by some workers⁽¹²⁾, using ellipsometry, that changes in the optical properties and thickness of the passive film were due to the incorporation of chloride. Contradictory arguments have been made on the basis of spectroscopic⁽¹³⁾ and electrochemical studies⁽¹⁴⁾.

As Figure 1.1 shows, continued anodic polarisation of the steel eventually leads to a further sustained increase in current density, marked E_b . For stainless steels this can be due to one of two dissolution mechanisms: localised corrosion or transpassive dissolution. The latter mechanism only occurs at high potentials (typically +1V or higher) in oxidising acid media, and results from oxidation of the chromium in the stainless steel to dichromate. Further increase in potential in the transpassive regime can lead to oxygen evolution. Localised corrosion, specifically pitting and crevice corrosion, occurs at much lower potentials in environments containing certain aggressive anions. This study addresses the issues governing pit initiation, and a further point to make with reference to the schematic anodic polarisation curve concerns this phenomenon. Prior to E_b , the passive current is seen to rise and fall in a series of anodic current pulses. These current pulses are central to this study, marking the nucleation, temporary propagation and repassivation of small "unstable" pits.

1.2 PITTING CORROSION OF STAINLESS STEELS

The phenomenon of pitting corrosion continues to attract a great deal of research effort, as it has done for the past 40 years or so. As a result, there is an enormous body of literature on the subject. There have been a number of useful review articles

published⁽¹⁵⁻²²⁾, and also a textbook⁽²³⁾. The intention here is to introduce the aspects of pitting which frame this study.

The mechanism by which pit propagation is sustained involves the coexistence of active and passive areas on the same surface, and is an important aspect of the pitting process. Equally important are the processes which occur before this stage is reached, that is, during the pit initiation stage when local passivity is lost and the mechanisms are activated which may ultimately lead to the formation of a propagating pit.

1.2.1 Pit Propagation

In contrast to pit initiation, which is introduced in the next section, there is a relatively broad consensus on the way in which pits propagate. The main features are illustrated by two schematic representations. Firstly, the schematic potential-pH diagram, Figure 1.2, derived from anodic polarisation curves such as that shown in Figure 1.1 shows domains of kinetic stability and instability. The second schematic, Figure 1.3, shows a pit cavity for a stainless steel pitting in neutral chloride solution. The anodic dissolution reaction at the pit base (point A, Figure 1.2) is balanced by the cathodic reaction on the adjacent passive surface (point B, Figure 1.2), or by the potentiostat in an electrochemical test. The increased concentration of metal ions within the pit results in the electro-migration of chloride ions (and other anions, if present), to maintain charge neutrality. The resulting metal chloro-complex (e.g. CrCl_6^{3-}) is hydrolysed by water. The consequent generation of acid lowers the pH to very low values, which prevents passivation, and promotes further dissolution of the metal. The effects of pH are demonstrated when stainless steel is polarised in increasingly concentrated hydrochloric acid solutions. Passivation occurs at a modest current in dilute concentrations (as depicted in the schematic, Figure 1.1), up to 1M, but is impossible in 4M HCl, Figure 1.4⁽²⁴⁾. The pH in an active pit on type 304L stainless steel was deduced from experimentation by Newman and Isaacs⁽²⁵⁾ to be about 0.5. Similar values have been measured in pit and crevice solutions⁽²⁶⁾. The driving force for the dissolution reaction is provided by the potential difference between the pit base and the passive metal surface (Figure 1.3), which may be a few hundred millivolts. A number of workers have recognised the need to understand the dissolution and passivation behaviour of stainless steel in solutions containing its own dissolution products (which must be the case in active pits), in order to understand the stability of pitting. Some studies have considered the polarisation behaviour of

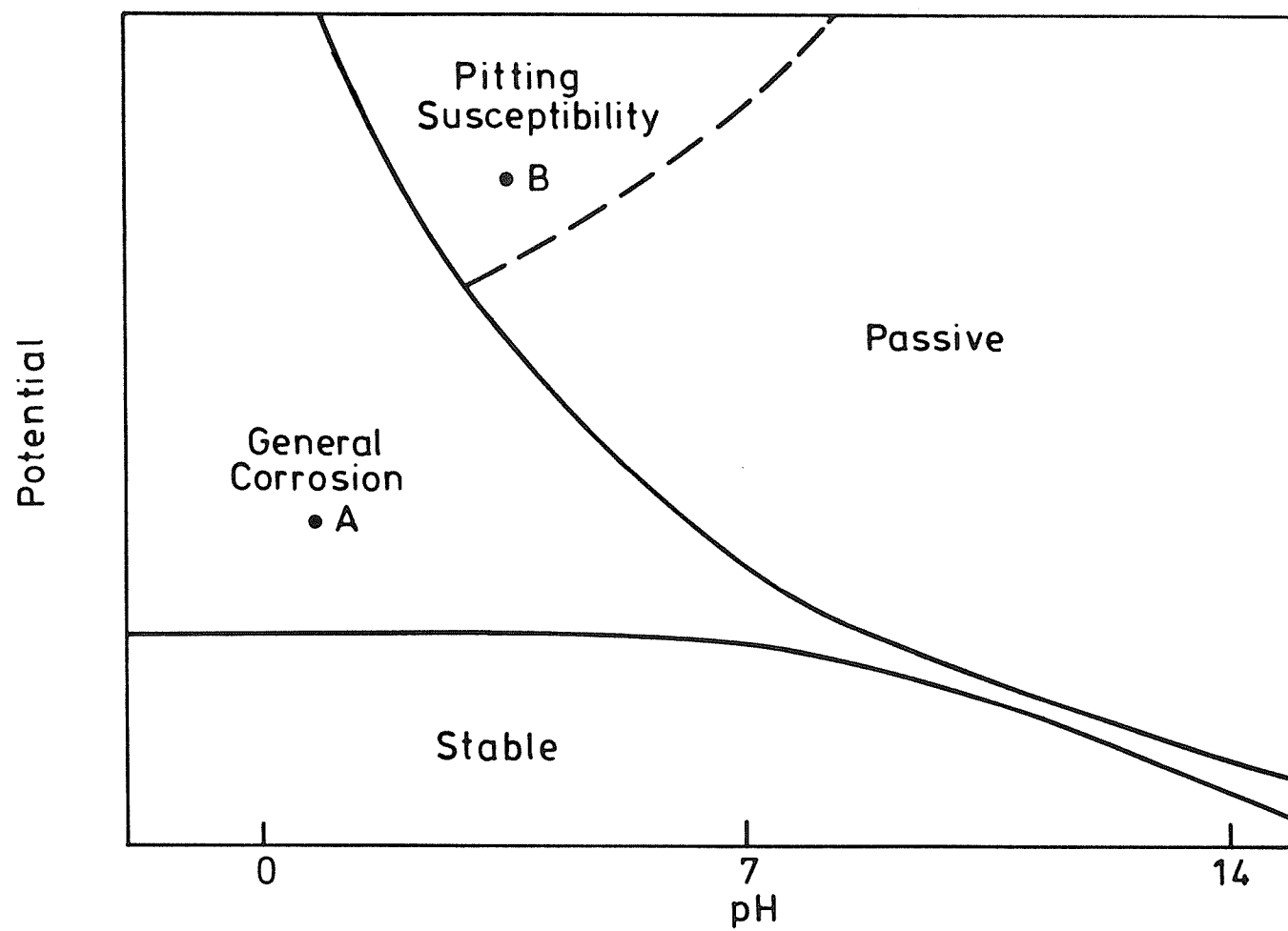
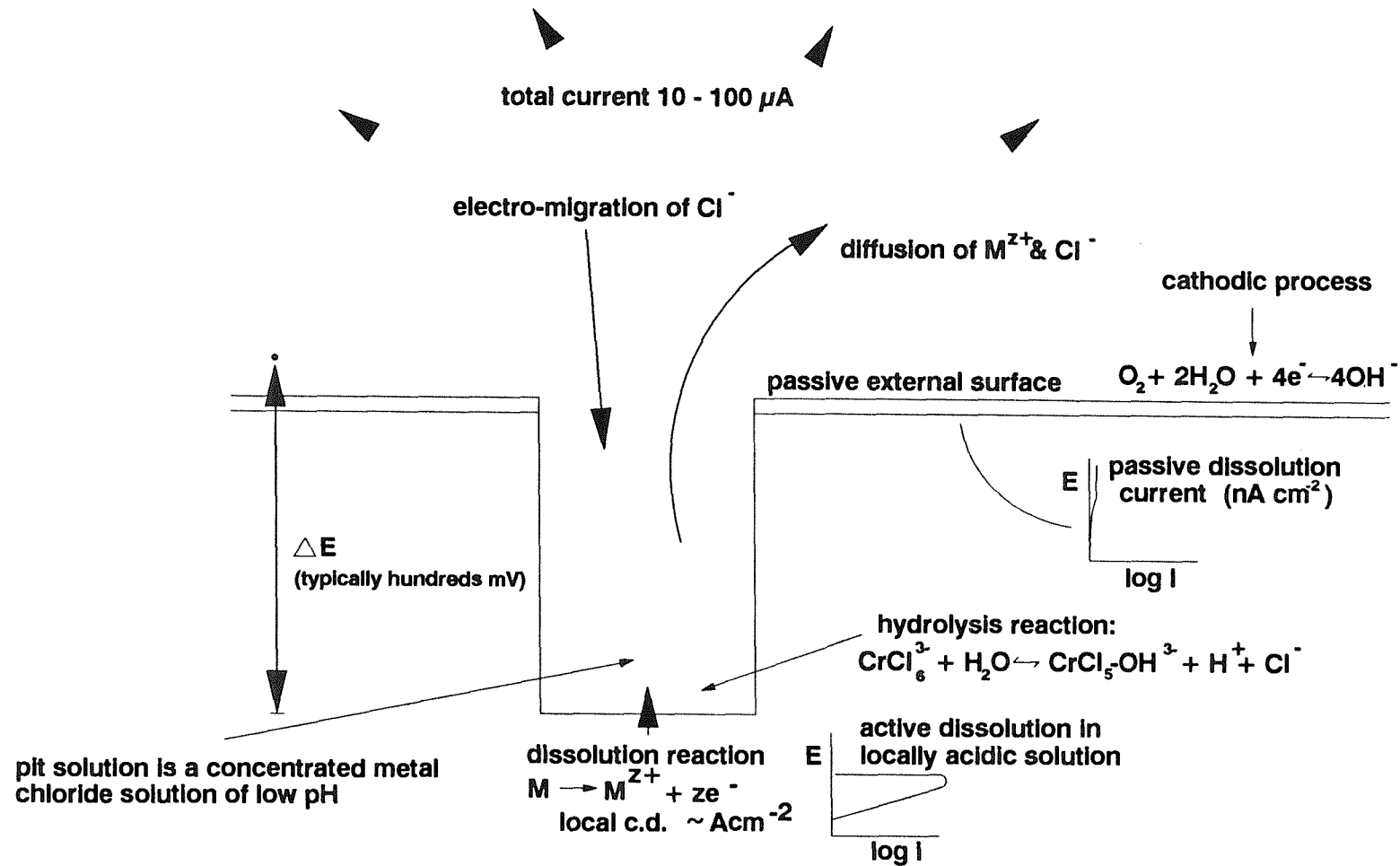


Figure 1.2 Schematic Potential-pH diagram for stainless steel in dilute chloride solutions.

Figure 1.3 Schematic Representation of Pit Propagation



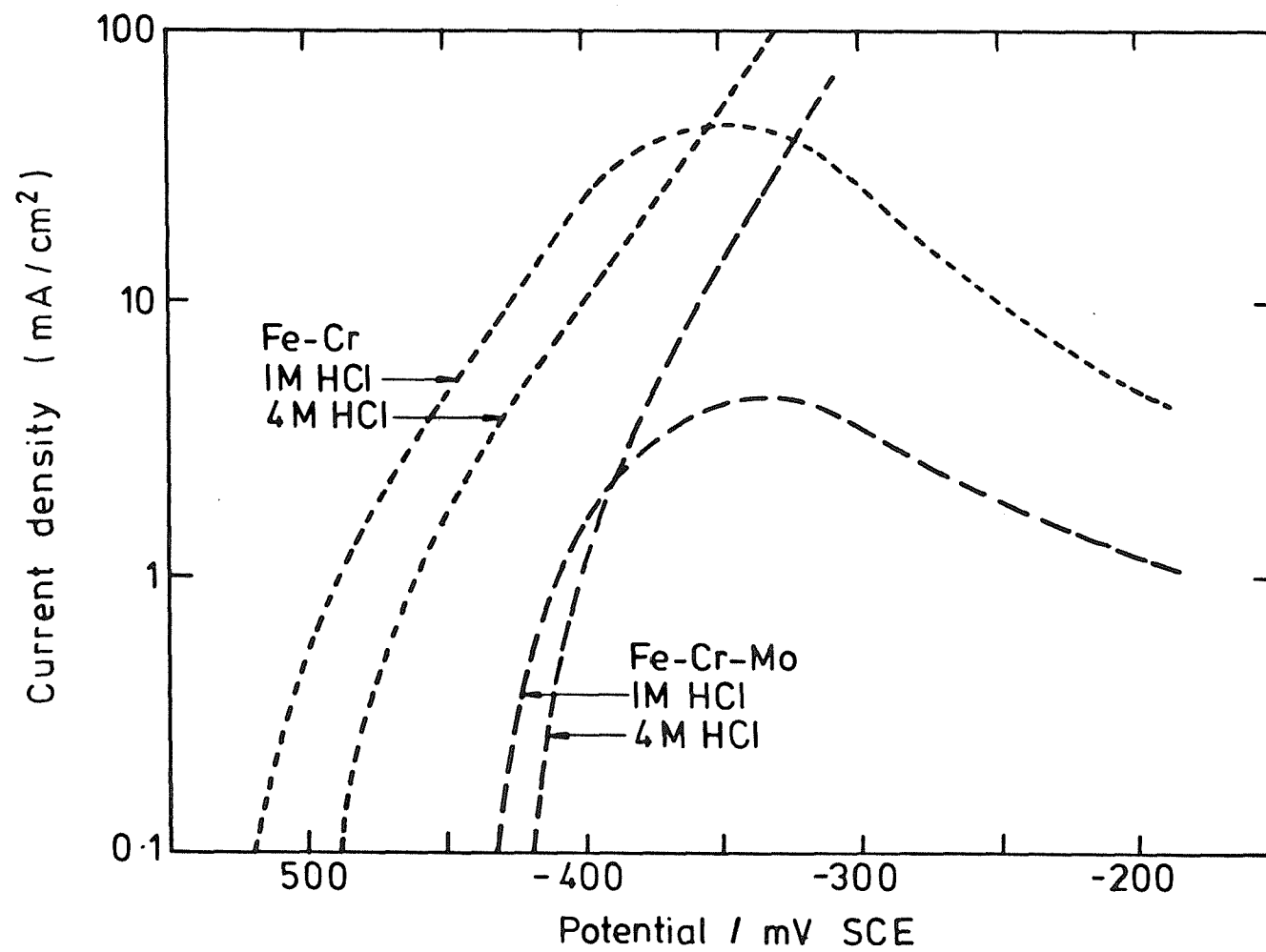


Figure 1.4 Anodic polarisation curves for stainless steel in HCl⁽²⁴⁾

stainless steel in solutions of chromium and iron chlorides⁽²⁷⁻³⁰⁾. Hakkarainen⁽³⁰⁾ concluded that pits repassivate when the degree of saturation of the solution falls below about 80%. A problem with this method is that the precipitation of a salt film makes it difficult to examine the anodic dissolution kinetics in concentrated solutions. Newman and co-workers^(25,31-33) overcame the problem of salt film precipitation by using an artificial pit method, which establishes a steep concentration gradient of metal ions, enabling dissolution rates to be measured up to the diffusion controlled limit (i.e. when a salt film precipitates). Supersaturation enabled the metal-ion concentrations to be raised to 1.5 times the equilibrium saturation value. This work showed that an active pit must contain a solution with greater than about 75%⁽³³⁾ of the saturation concentration of dissolved metal ions (c.f. Hakkarainen). This can arise because of the rapid fall in pH as the Cr^{3+} and Cl^- concentrations are increased in the pit⁽²⁷⁾ (due to the acidic hydrolysis constants of Cr^{3+} and the effects of high Cl^- concentration on the activity of H^+). The factors which contribute to pit stability, outlined above, are further illustrated by studies in which their individual contributions have been examined in isolation. So, for example, the addition of an inert anion, such as perchlorate^(34,35) or sulphate^(36,37) can prevent pitting by reducing the concentration of catalytic species in the pit (e.g. Cl^-) by electromigration. Acidification, to a pH where passivity cannot be attained, may be prevented by adding a sufficient concentration of pH buffer^(34,35). According to recent work⁽³⁴⁾ the removal of potential and concentration gradients may be achieved by intense stirring of the bulk solution. This final point will be addressed in Chapter 4, when pit stability under well characterised conditions of forced convection are studied.

1.2.2 Pit Initiation

For pits to initiate, there must be a local loss of passivity. Numerous mechanisms have been proposed by which this can occur⁽²³⁾. Most theories fall into one of the three main categories. In the **penetration mechanism**^(38,39), aggressive anions such as Cl^- are supposed to migrate through the oxide layer to the metal-oxide interface, providing a low resistance path through which rapid ionic transport can proceed. The **film breakdown** or **mechano-chemical mechanism**⁽⁴⁰⁻⁴³⁾, involves a mechanical breakdown of the passive film, providing direct access of aggressive anions to the underlying metal surface. The classical description of pit initiation is one of competitive **adsorption** between chloride ions and oxygen, leading to pit initiation at sites where chloride displaces oxygen^(15,44-47). Although this formative theory is no

longer considered appropriate, since it is now widely recognised that passive films are separate phases and not chemisorbed layers, more recent variations on this theme presume that passivation is a dynamic process, characterised by continual passivation and depassivation at local sites on the surface. It is postulated that Cl⁻ adsorption occurs at some of these sites, preventing repassivation and leading to pit nucleation⁽⁴⁸⁾.

In fact, all of these theories, which are discussed further in later chapters (notably Chapter 3), seek to account for the known potent effect of anions (principally of chloride and other halogen ions, but also for example of sulphur species) by postulating some specific effect on the passive film. Considered practically, the following observations can be made. First of all, when pits initiate, passivity is maintained over most of the surface, and few (sometimes only one) pits form: the difficulty with the above models is therefore to explain the stability of system, not the instability. Secondly, in all alloys of technological importance (and indeed in "pure" metals), microstructural features such as grain boundaries, precipitates and inclusions are likely to be present. These features are generally large in comparison to the thickness of the passive film, and it might therefore be anticipated that the properties of the passive film in these regions may be different (and usually less protective) from that on the parent metal. It would appear unnecessary to postulate a special passive film breakdown mechanism when defects such as these are already present. This point is taken up again in Chapter 5, when the role of inclusions in pit initiation is considered in detail.

Most theories of pitting corrosion are in general based on a consideration of two "characteristic" parameters: the *pitting potential* and *repassivation potential* (E_b and E_{rp} in Figure 1.1) are respectively defined as the potential below which no pits will initiate and the potential below which no pits will continue to propagate. Supposedly, between E_{rp} and E_b , pits which were nucleated above E_b may continue to propagate.

Whilst E_b and E_{rp} may provide *general* information, such as indicating a ranking order of pitting susceptibility for alloys in a given environment, where detailed information on the pitting process is required, their use is flawed: it is not possible to ascribe *unique* values to E_b and E_{rp} for a given material-environment combination; they, along with such parameters as the induction time for pit initiation, are highly

variable and depend, for example, on the way in which the experiments are performed^(23,49). An example of this is the dependence of E_b on the potential scan rate. According to some reports⁽⁵⁰⁻⁵²⁾ an increase in scan rate produces a noble shift in E_b , while others have found the opposite effect⁽⁵³⁾. More recently⁽⁵⁴⁾, using the apparatus and techniques developed for the experiments reported in this thesis (very slow anodic potential sweep experiments), it has been shown that the propensity to nucleate a pit is increased with increasing passive current density and that the passive current density varies as a function of the potential scan rate: the "pitting breakdown potential" (in this case a distribution of breakdown potentials for >30 specimens) was found to be independent of scan rate over three orders of magnitude. The predictive capability of methods which seek to define pitting susceptibility in terms of E_b or E_{rp} , often on the basis of a single experiment, must therefore be questionable. Practical experience supports this statement. For example, E_{rp} has been reported to be about +50mV SCE for type 304 stainless steel in dilute chloride solutions^(55,56), yet pits were found in type 304 tanks containing stagnant aerated solutions very dilute in Cl^- (as low as 100 ppm), where the rest potential was about -50 to 0 mV SCE⁽⁵⁷⁾. In this thesis (Chapter 3 and subsequently) it is shown that pits nucleate in very dilute chloride solutions at potentials as low as -190 mV SCE. Observations of pitting at similarly low potentials has recently been reported elsewhere⁽⁵⁸⁾.

Relationships of the form⁽²³⁾:

$$E_b = A - B \log [C] \quad (1.1)$$

are often given, where $[C]$ might be the concentration of an aggressive anion such as chloride, and B depends on various factors, such as the alloy, the supporting electrolyte and the measurement technique. The question may be raised, what use are they? It is shown in Chapters 3, 5 and 6 that the distribution of breakdown potentials for specimens tested under nominally identical conditions is approximately exponential, extending over a potential range of 100 to 300mV. Single measurements can be considered as estimates of the *most probable* value of the breakdown potential, although they are obviously not expected to be accurate. Equations such as (1.1), therefore indicate how this most probable value will change, although theories assuming their accuracy are probably of questionable value. An alternative approach to the problem of measuring and predicting pitting susceptibility has been to recognise that results of identical tests are not likely to be the same.

The analysis of the variability in corrosion data, rather than proposing mechanisms based on the dubious assumption of reproducible results is not new⁽⁵⁹⁾, although it is only more recently that probability theory has been applied to studies of pitting corrosion. Approached from this viewpoint, the irreproducible nature of the data can be taken account of in a theoretical treatment, and for this reason these methods of analysing pitting data are increasingly popular.

A statistical treatment of variable data requires that the results of groups of nominally identical experiments are analysed collectively, as an *ensemble*.

A number of models have been developed in which pitting is considered to occur as a *stochastic* (i.e. purely random) process^(35,60-62). These models vary in their level of sophistication. In one of the earliest attempts, Shibata and Takeyama⁽⁶¹⁾ evaluated the *survival probability* of stainless steel specimens as a function of potential, using apparatus in which 12 experiments were carried out simultaneously. The survival probability is a significant parameter in describing pitting, as it enables the probability of observing no pits on a surface at a given time to be determined. Shibata and Takeyama's formulation of the survival probability assumes the Markov property that the future probability of observing a pit is not influenced by the past history of the specimen. Thus the probability that an unpitted specimen at a time t will contain a pit in the next time interval dt is given by $\lambda(t) dt$, where $\lambda(t)$ is the pit generation probability per unit time at time t .

Defining the proportion of non-pitted specimens at time t as $P(O)$ the survival probability gives:

$$\frac{-dP(O)}{P(O)} = \lambda(t) dt$$

Rearranging, then integrating with $P(O) = 1$ at $t = 0$ and $\lambda(t) = \text{constant}$ gives:

$$P(O) = e^{(-\lambda t)}$$

Thus $\lambda(t)$ can be determined from a plot of $\ln(P(O))$ against time. In the method used by Shibata and Takeyama the time for each specimen to exhibit pitting under potentiostatic control was recorded. Pitting was defined to have initiated when the measured current exceeded $100 \mu A/cm^2$.

The survival probability $P(O)$ was defined as:

$$P(O) = 1 - \frac{n}{N + 1}$$

where:

n was the n th specimen in which pitting occurred at time t

N the total number of specimens

A logarithmic plot of survival probability was found to show three linear sections with increasing time, which were interpreted in terms of three different rate controlling features of the process. In fact, whilst this approach is perhaps useful for illustrating and taking account of the variability in the time to initiate a pit, it is of limited value when addressing the mechanistic aspects of pit initiation.

Many investigators have noted, when studying stainless steels in chloride solutions, the occurrence of current transients at potentials below E_b (35,36,51,54,58,60,63-69), which have generally been attributed to the breach and repair of the passive film and variously termed *pitting attempts*(68), *unstable pitting*(35,54,60,66) and *metastable pitting*(58). In this study, these non-propagating pits are called unstable pits. General or global models have been constructed which attempt to explain these observations. Mostly, a statistical approach has been adopted(35,60-62, 69,70), although a recent alternative approach has suggested that the phenomena are amenable to deterministic modelling.

In the stochastic model described by Williams and co-workers(35,60) the techniques of ensemble statistics, previously applied to nucleation and growth events in electrocrystallisation(71), were applied to the study of pit initiation. In this model, no distinction is made between unstable pits and stable (i.e. propagating) pits: all micropits have a finite probability of becoming a propagating macropit. Pits are nucleated randomly in time and space, with a frequency λ ($\text{cm}^{-2}\text{s}^{-1}$). Subsequently, each pit evolves by a deterministic growth process, during which time it has a probability μ (s^{-1}) of dying unless it survives beyond a critical age τ_c (s) when a regime of stable pit growth commences. According to this model, the nucleation frequency of stable pits, Λ ($\text{cm}^{-2}\text{s}^{-1}$) is:

$$\Lambda = a \lambda \cdot \exp(-\mu \tau_c)$$

where:

a = specimen area

The probability of the specimen surviving beyond a time t without corrosion, $P(O)$, is (at constant potential):

$$P(O) = \exp(-\Lambda t)$$

Therefore, this model takes the Shibata and Takeyama result and shows how it can be broken down into parameters describing more elementary steps in the overall process.

This model was consistent with the results of an experimental programme, which additionally noted strong effects of environmental conditions. These results were interpreted in terms of a simple model of local acidification for the initiation of pitting corrosion. Production of a gradient of acidity, on the scale of the surface roughness of the specimen, as a consequence of the small passive dissolution current of the metal, triggers off a local instability which is maintained by a local potential gradient. Fluctuations in these gradients, leading to the "birth" and "death" of events, arise because of fluctuations in the boundary layer at the metal surface: intense stirring of the solution was found to stop pitting. In this simple model, the requirement for pit initiation at "special sites", such as inclusions or cracks in the passive film (etc.) was eliminated. The strength of this approach is that the general model successfully describes a complex process using a small number of variables. It provides a framework within which to tackle experimentally the different aspects of the pit initiation process.

More recent studies have begun to challenge the assertion that pit initiation is a purely random process. Sharland's approach^(72,73) was to consider the pit initiation process as a dynamical system governed by a series of non-linear differential equations. She suggested that the highly oscillatory nature of the observed current transients may be related to the oscillatory or multiple steady state solution of these equations. In addressing the question of how random the seemingly random process of pit initiation is, her preliminary findings suggested that pit initiation is a deterministic process, and is governed by a minimum of four (unidentified) variables. In effect, this work is attempting to provide a general formulation of a "feedback" type model. The feedback coupling is that between the local composition and potential, and the

dissolution rate. A problem which arises is how to go about constructing a model in which the pitting frequency is very low.

1.3 THE ORGANISATION AND OBJECTIVES OF THIS THESIS

The role of global models such as those outlined above is to provide a formal, general description of pit initiation. Such general models have been useful for framing the research reported in this thesis. From the outset, the intention has been to address the "microscopic" processes which occur during pit nucleation, which ultimately lead to the formation of a damaging macropit.

A major theme of this work is the development of mechanistic arguments for pit initiation based on a physical interpretation of electrochemical noise data. In so doing, the important contributions of alloy microstructural features and pit morphology are recognised and highlighted. The outcome is a series of studies in which both electrochemical and metallurgical factors are shown to play important roles in the overall pitting process. An appreciation of the metallurgy of the stainless steels used in this study is useful in this context, and the relevant background is given in Appendix A.

A further aim of this study has been to indicate improved methods for the assessment of corrosion resistance. Although by its very nature, the accelerated corrosion test cannot exactly reproduce real corrosion situations, it is possible to extract useful information provided that the results are not wholly determined by the test method or overly aggressive environments. The experiments reported here have been designed to minimise as far as practicable the influence of the experimental technique on the outcome of the test.

The experimental apparatus and data analysis methods are given in Chapter 2. In order to examine electrochemically the early stages of pitting it was necessary to be able to measure reliably currents of a few tens of nA. This was achieved by using equipment with high resolution, and by excluding as far as possible extraneous noise signals. Very slow potential ramp experiments were used, starting from the region of the open circuit potential, in order to reduce as far as possible effects due to the imposed potential ramp. The experiments were designed to enable multiple

specimens to be polarised simultaneously: groups of experiments and large numbers of transients were analysed collectively to allow for the inherent variability in the data.

In Chapter 3, the high resolution afforded by the experimental technique is used to explore features of the pit initiation process. A one to one correlation between current transients and actual pits is established. One consequence of the high sensitivity of the apparatus was that unstable micropits were first observed at potentials as low as -190mV SCE. The results of the slow potential ramp experiments on commercial purity 304L are discussed in detail: film growth in the passive regime is shown to be consistent with high field ion migration; the basic shapes (i.e. current evolution with time) of the individual current transients is shown, with the aid of a simplified model of an evolving pit, to be consistent with two limiting conditions of surface area limited current ($i \propto t^2$) or solution resistance limited current ($i \propto t^{1/2}$) and the more commonly observed intermediate case of a balance between the two ($i \propto t$). Microscopy revealed that small pits were often associated with small sulphur-rich inclusions, and additionally that small pits were invariably covered with remnants of the surface metal. The discussion is framed around proposed mechanisms of pit initiation and repassivation.

In Chapter 4, a study of the effects of hydrodynamics on pit nucleation is described, following up on a suggestion from previous work⁽³⁴⁾ that pitting can be suppressed or prevented under conditions of forced convection, due to the destruction of local potential and concentration gradients. The results are consistent with the removal of developing concentration gradients *outside* the pit. Another speculative hypothesis is also advanced, based on the collapse or removal of the pit cover. The results indicate that flow does not affect the initiation of pits, but that turbulent flow prevents their growth unless they are well established.

Following on from the observations made in Chapter 3, a detailed study of the role of sulphur-rich inclusions on pit initiation is reported in Chapter 5. The combined use of electrochemical and microstructural techniques demonstrates conclusively that sulphur-rich inclusions dominate as pit nucleation sites. A hypothesis is introduced in which sulphur, derived from dissolving sulphide inclusions, has an important role in stabilising the growth of a pit. Strong evidence is provided for an assertion that the lifetime of unstable pits is related to inclusion volume. A stochastic element of this process is then the amount of sulphur available to catalyse the anodic dissolution

process in the pit: if the sulphur is exhausted at an early stage of growth, then the pit can repassivate. One consequence of this hypothesis is that below a certain size, sulphur rich inclusions are too small to nucleate pits.

In Chapter 6, support for this concept of a minimum sulphur-rich inclusion size is provided from experiments on laser surface melted specimens. The pitting resistance of laser treated specimens is markedly improved in comparison with the untreated steels, consistent with a removal or redistribution of large inclusions. Significantly, most of the sulphur was found to be retained in the melt zone, in the form of very small precipitates, which did not nucleate detectable pits. In a separate study, also reported in this chapter, it is demonstrated that laser surface melting is an effective method for preventing the initiation of intergranular stress corrosion cracking on sensitised stainless steel.

The improvement in pitting resistance conferred on 304L steel by reducing the size of the sulphides (or removing them altogether) was such as to result in pitting breakdown distributions comparable to type 316L stainless steel. This led to a questioning of the role of molybdenum - an alloying addition in 316L specifically to improve pitting resistance. A preliminary study is presented in Chapter 7. The nucleation frequency of unstable pits on 316L was found to be similar to 304L. The two alloys differed in the growth kinetics of the unstable pits. The results support a hypothesis that Mo additions effectively provide an antidote to the poisoning effect (on passivation) of sulphur, and hence that Mo additions may be unnecessary in the absence of harmful sulphur-rich inclusions.

The conclusions and future directions suggested by this study are presented in Chapter 8. Detailed reviews and discussion of relevant literature are given in each of the above chapters.

References are numbered sequentially within each chapter, and are collected at the end of the thesis by chapter number. Tables and Figures are positioned close to the relevant text in each chapter. Appendices are located just before the references, at the end of the thesis. Where an Appendix contains references, these are located at the end of that Appendix.

CHAPTER 2

EXPERIMENTAL PROCEDURES

CHAPTER 2 - EXPERIMENTAL PROCEDURES

This chapter gives experimental details and data analysis methodologies common to experiments performed in this study. Where specific variations were employed, these are detailed in the relevant chapters. The composition of the stainless steel used for the bulk of this study is given in Table 2.1. The steel was obtained as a 5mm thick plate of solution-annealed commercial purity AISI type 304L stainless steel. 25mm diameter disc specimens were milled from this stock material.

A number of alloy variants based on the AISI 304L specification were used for various parts of this study, and AISI type 316L was used in Chapter 7. The chemical analyses of these materials are given in the relevant chapters, and are collected together in Appendix B.

2.1 SPECIMEN PREPARATION

To study pitting corrosion it is obviously necessary to avoid crevice corrosion, which is a potential hazard because it tends to occur at lower electrode potentials than pitting. The following specimen preparation procedure was devised and practiced throughout this study:

- i) The disc specimens were shot-blasted on all surfaces except the 25mm diameter face to be used in the corrosion studies.
- ii) The specimens were immersed in acetone and given an ultrasonic cleaning treatment. Subsequently, the specimens were manipulated with tongs.
- iii) The specimens were given a priming treatment using a proprietary adhesive primer (Permabond "SIP"¹), and allowed to dry. They were then placed, face down, in individual 50mm diameter moulds.
- iv) Cold setting epoxy resin (Araldite MY753 resin and HY956 hardener in a 10:1 ratio) was degassed under vacuum and cast onto the specimens. The epoxy was cured under infra red lamps, which both accelerated the process and helped to ensure an even cure.

¹ Permabond "SIP" - is a trade name for a Union Carbide product (A-187): γ -Glycidioxypropyltrimethyloxysilane, a coupling agent which has an epoxy-compatible functional group. The silane end bonds to the metal surface. The primer consists of a mixture of methanol, water and silane in a ratio 18:2:1.

Table 2.1 Composition of Steel¹

STEEL TYPE	Weight % (Fe Balance)									
	Cr	Ni	Mn	Si	C	P	S	Mo	Cu	Ti
AISI 304L Spec. ²	18-20	8-12	1.50	1.00	0.030	0.045	0.030			
304L - CP	18.2	9.3	1.13	0.42	0.020	0.026	0.011	0.38	0.21	<0.02

NOTES

¹

- Analysis determined by X-ray fluorescence, except S and C (LECO)

²

- Single figures are maximum values

CP

= Commercial Purity

The effectiveness of this specimen preparation method is demonstrated in Figure 2.1, which shows the results of dye penetrant tests on specimens with and without the above priming procedure. The specimen prepared simply by casting epoxy onto the stainless steel disc is creviced, as highlighted by the red dye.

The method was not 100% successful, and occasionally crevice corrosion did occur at the epoxy/metal interface during pitting experiments. These rogue experiments were easily identified by their current/time characteristics, and confirmed by post-test examination (using dye penetrant where necessary). These results were discarded.

Electrical connection to the specimen was achieved by drilling a 6mm hole in the back of the specimen, using a flat-ended drill to produce a wide, shallow contact area. A self-tapping screw was used to facilitate the electrical connection. The screw was tipped with silver-loaded epoxy to ensure a reliable electrical connection to the specimen when the screw was tightened up.

The specimens were ground back approximately 0.5mm to expose fresh metal, and then prepared to the required finish for the pitting experiments - usually to grade 240 grit SiC - using irrigated grinding wheels. Finally the specimens were cleaned in an ultrasonic bath, rinsed in acetone and blown dry, and then incorporated into the electrochemical cell.

2.2 ELECTROCHEMICAL METHODS

Two electrochemical test cells were used in this work, one of which is described here. The second test cell was specific to the study of hydrodynamics, and is described in Chapter 4. Both employed a three electrode configuration, and were designed to enable multiple specimens to be tested during a single experiment.

Figure 2.2 shows the test cell used for most of the experiments described in this thesis. Specimens were fixed into the cell simply by clamping to a glass 25mm i.d. flat flange joint. A silicone rubber gasket, previously boiled in distilled water to remove any contaminants, was placed between the specimen and flange to ensure a water-tight fit. Seven specimens were used in each experiment, and were fixed into place around the perimeter of a round glass dish. The single saturated calomel electrode (SCE) and platinum counter electrode ($\approx 20\text{cm}^2$) were introduced centrally into the cell through

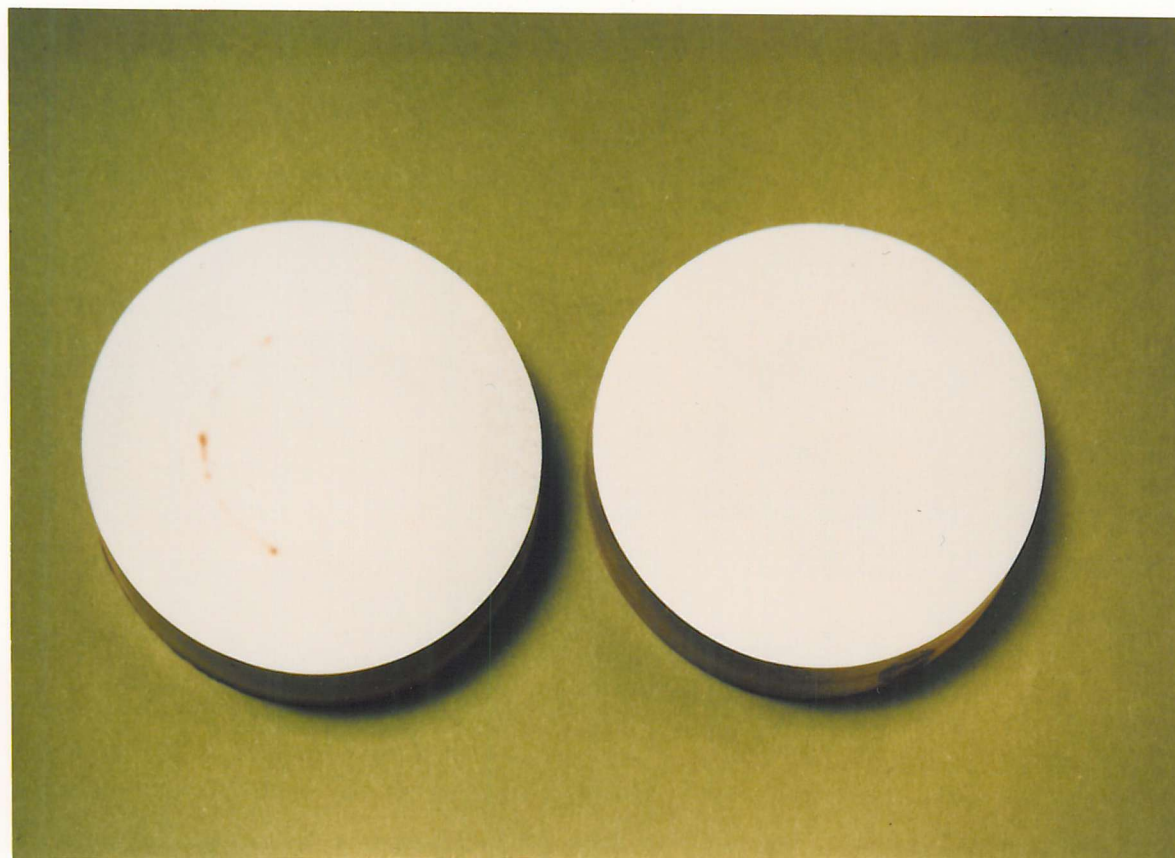


Figure 2.1 Results of dye penetrant tests on specimens which were (right) and were not (left) surface primed. The red dye indicates crevicing on the untreated specimen.

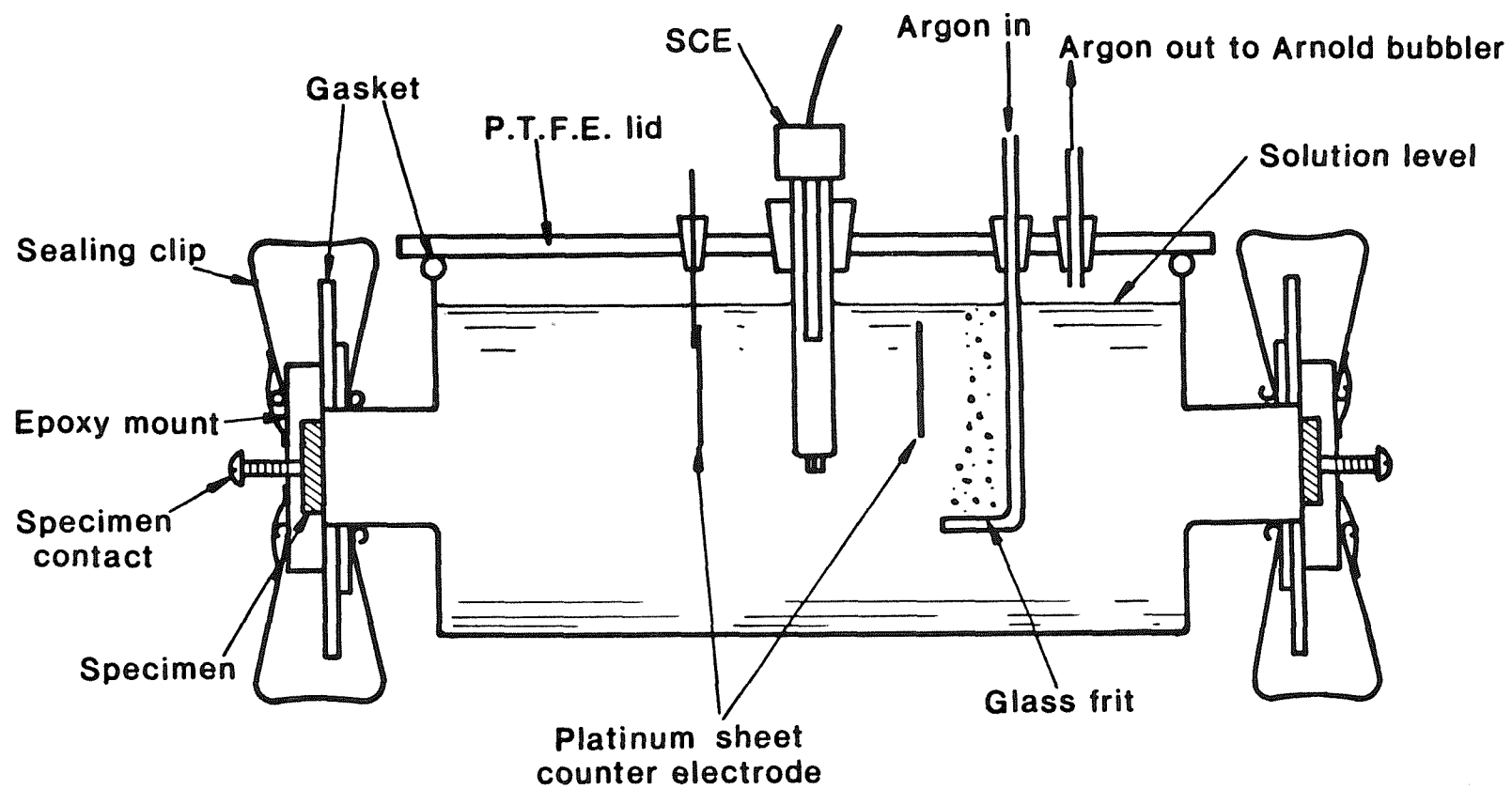


Figure 2.2 The Test Cell

the PTFE lid. Prior to each experiment, the test cell was deaerated using purified argon until stable rest potentials were measured on each of the specimens. A slow argon bleed was maintained throughout the experiment.

No temperature controls were applied during the experiments. The solution temperature was monitored at $19 \pm 2^\circ \text{C}$. The electrolyte used throughout this study was 1,000ppm (0.028M) chloride solution, prepared from analytical reagent grade sodium chloride and distilled water.

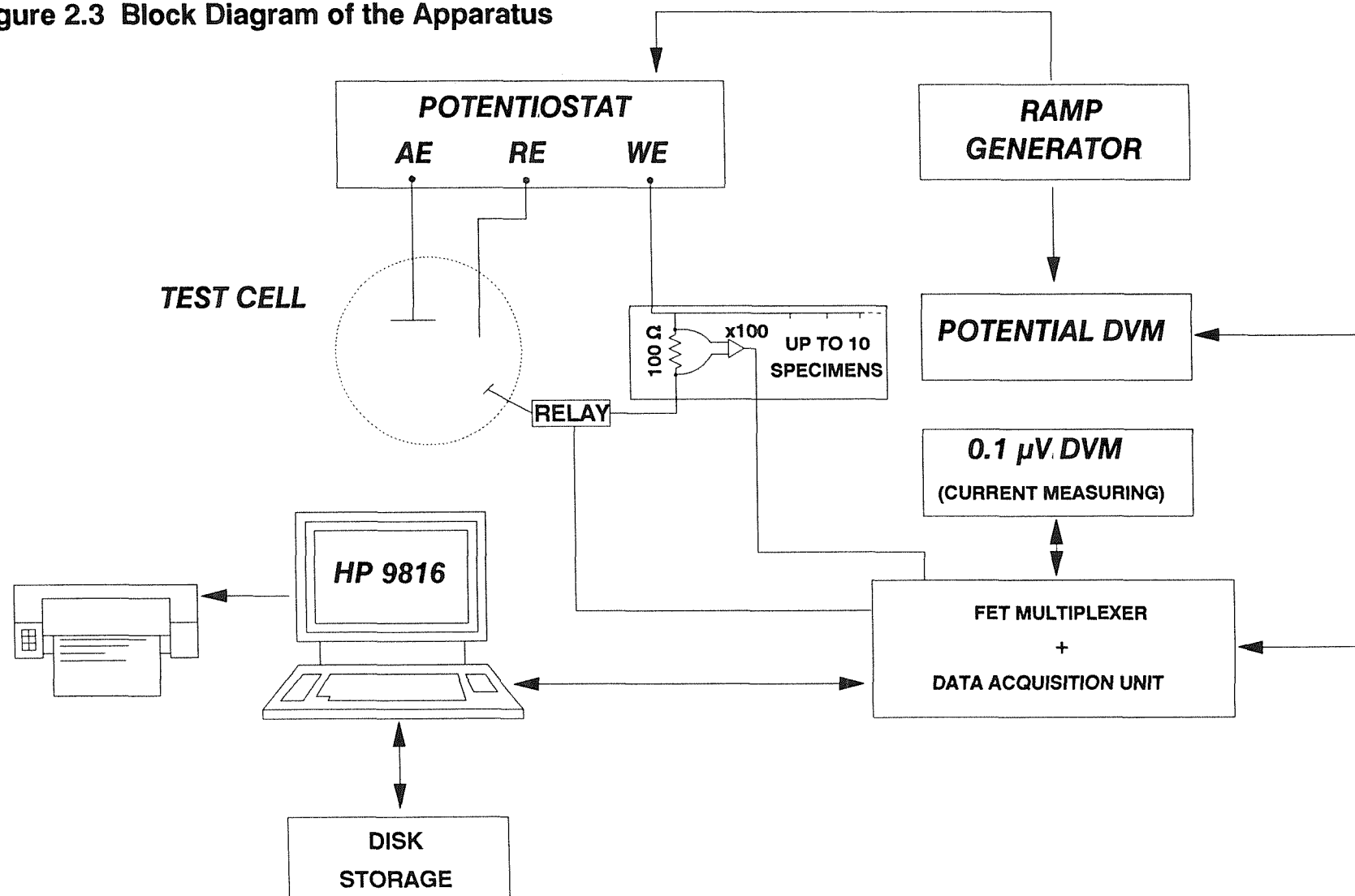
2.3 EXPERIMENTAL APPARATUS AND INSTRUMENTATION

This section describes the equipment used to acquire the data on pit initiation. In subsequent sections, the pitting experiments and data analysis methodologies are described.

The electrochemical apparatus, data acquisition instrumentation and computer programs were common to all experiments. A block diagram of the data acquisition apparatus is shown in Figure 2.3.

The cell current was measured as a voltage drop across a precision 100 ohm resistor inserted in series with each working electrode (specimen). A single low noise, low current (100mA) potentiostat, which was driven by a stable D.C. power supply, controlled all of the working electrodes; since the currents associated with unstable pits are very small (typically $< 1 \mu\text{A}$) the error ΔE in the working electrode potential was negligible - for example, $\Delta E = 0.1\text{mV}$ with a $1 \mu\text{A}$ current flowing. The voltage ramp was generated using a 16 bit digital ramp generator. The voltage across each working electrode resistor was magnified 100x using a low noise, low drift amplifier (H.B.Thompson) and sampled at 1Hz on each cell by a sensitive, high input impedance digital voltmeter ($6\frac{1}{2}$ digits, $0.1 \mu\text{V}$ resolution) and FET multiplexer. This arrangement, together with the precautions taken to minimise instrument noise and electrical interference outlined in the next section, achieved a very high resolution (typically 1pA at 1Hz). The data acquisition was controlled using a Hewlett-Packard 9816 microcomputer, and is described in Section 2.4.1.

Figure 2.3 Block Diagram of the Apparatus



2.3.1 Precautions Against Electrical Interference⁽¹⁾

Because the currents associated with unstable pitting transients are so small, precautions were taken to reduce the levels of external interference. Electrical interference, or **noise**, may simply be defined here as any A.C. Potential which appears at the potentiostat output but which is not part of the controlling signal at the input.

Noise, which basically impairs resolution, can be split up into a number of categories for analysis and treatment. These are briefly outlined below, together with the precautions taken to minimise their effects.

Mains frequency noise, or pick-up, can enter a system by four principal routes. These are ground loops, magnetic field induction, electric field induction, and electromagnetic radiation (radio).

In this work, the centre tap of the power supply - the system common - was earthed. This was the only earthing point in the system and was designed to minimise noise due to ground loops, which are a major cause of mains pick-up. The measuring circuitry was encased in thick steel sheet, the apparatus was placed on a thick steel plate and the mains leads were kept remote from measuring leads - all were precautions against magnetic field induction, which occurs when a current carrying mains lead passes sufficiently close to a sensitive conductor to induce a potential into it by transformer action. Another typical source is the transformer in mains operated instruments. The alternating field induces emf into any conductor which cuts its path. This is a common source of internal mains pick-up in instruments. The external field can be reduced to some extent by using metal enclosures. Whenever an alternating potential difference exists between two conductors, a capacitive current will flow between them. The two conductors are thus A.C. coupled, and if one of them happens to be a mains lead (not necessarily current carrying) and the other a sensitive, high impedance control lead, then the latter could suffer considerable mains pick-up by this electric field induction. Severity is proportional to the potential difference and to the effective surface area of the two conductors, and is inversely proportional to separation. The main precaution employed here was to keep mains leads remote from control leads. The measuring leads were screened and kept as short as practicable to reduce pick-up due to

electromagnetic radiation. All cable screens and metal enclosures were connected to the system common.

2.4 PITTING EXPERIMENTS

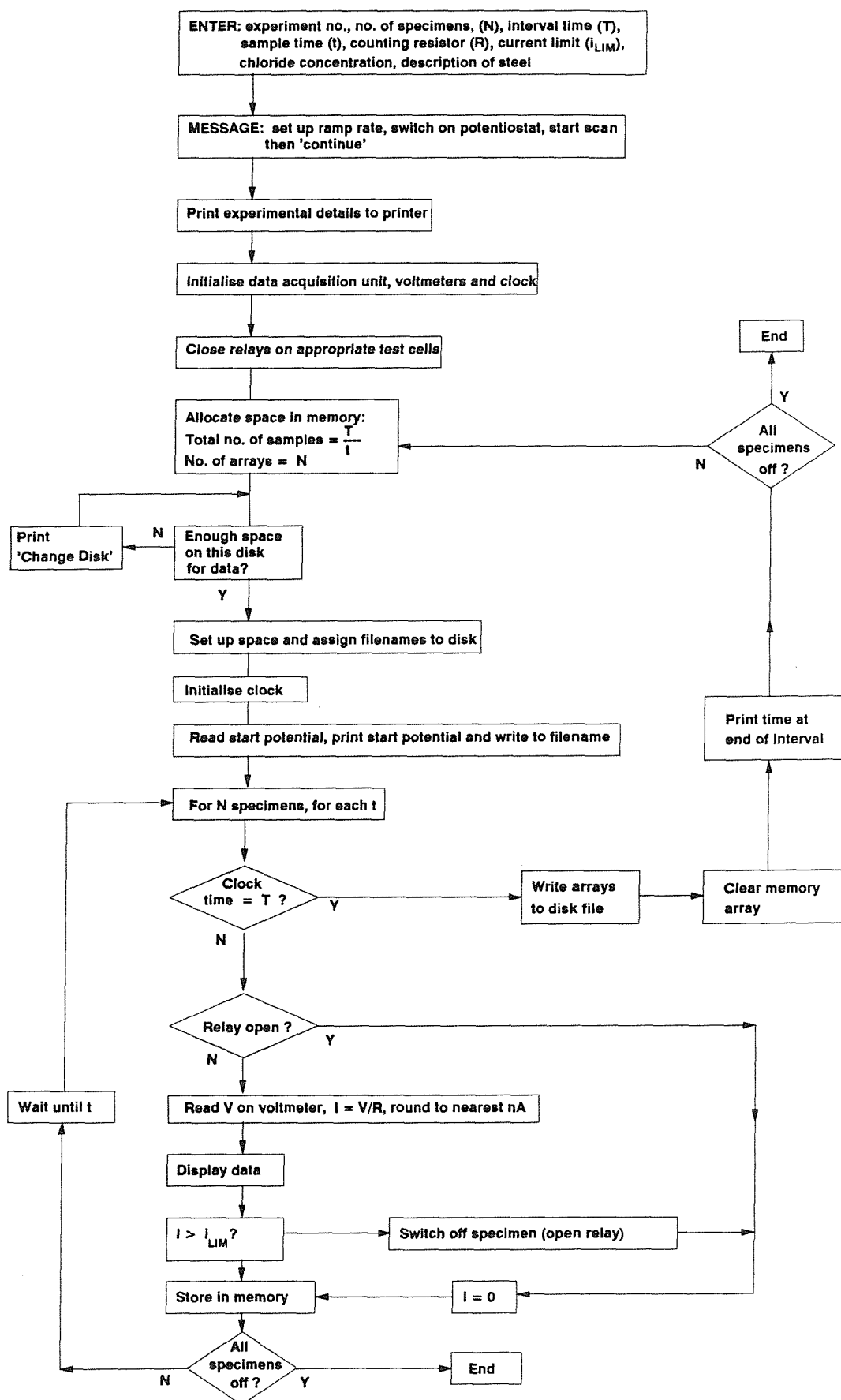
The experiments performed in this study largely comprised potentiodynamic polarisation (with some potentiostatic) experiments, of up to ten specimens, commencing from the open circuit potential (deaerated) and continuing until all specimens had nucleated a stable, propagating pit. Very slow potential ramp rates were employed with the aim of causing a minimum perturbation to the pitting process by the imposed ramp. A current level of $10\ \mu\text{A}$ was taken to mark the transition from unstable to stable pitting. This level was chosen by studying the results of previous pitting experiments⁽²⁾ on the same 304L stainless steel stock material, where much higher (typically $70\text{--}100\ \mu\text{A}$) switch-off current levels were used. It was observed that when growing pits attained a current level of $10\ \mu\text{A}$ or more, they did not subsequently repassivate. Therefore, in the experiments carried out in this study, as the individual specimens attained a current level of $10\ \mu\text{A}$, they were switched off. There are two advantages in being able to stop experiments at this low current level. Firstly the error in the potential applied to the other working electrodes remains negligible, and secondly the pits generated during these experiments are small and easily ground out, enabling the specimen to be re-used.

The data acquisition and data analysis tasks were to a large extent controlled by computer programs. A series of programs were written in BASIC on a Hewlett-Packard 9816 computer to facilitate data acquisition, data interrogation and reduction, and data analysis. In the following sections, the tasks implemented by the software are described. These programmable tasks were interspersed with others which were implemented by more laborious means.

2.4.1 Data Acquisition

The control of the experiment, data handling, storage and display were implemented using software written specifically for the task. Figure 2.4 shows a flow diagram of the data acquisition program. The main operations implemented by the software are given below:

Figure 2.4 Flow Diagram of Data Acquisition Program



For each time interval:

- (1) set up files on the storage device, according to the number of specimens and time interval chosen by the user, in advance of data acquisition to ensure storage space available. At this time the applied potential was read from the potential DVM and incorporated, along with the specimen number and time interval number, into the filename. A hard copy of the experimental details was printed, for subsequent incorporation into the lab. book;
- (2) read the current flowing on up to 10 cells at a sampling rate input by the user (usually 1Hz in this work), and store the data in arrays until the end of the time interval. This was facilitated by triggering the FET multiplexer which then stepped through the individual specimens enabling the fast-response, high resolution DVM to read the cell currents at each cycle;
- (3) download the data held in memory to the storage device, usually a 16Mb hard disk, at the end of each time interval (or experiment) for future analysis. The time interval used in this study was usually 10,000s, and a typical experiment consisted of 12 or more time intervals;
- (4) to display the status of the experiment on the computer screen, including the cell currents, interval number, potential, and time elapsed;
- (5) to switch off, by means of a relay switch, individual working electrodes as they exceeded a pre-set current limit (usually $10\ \mu\text{A}$).

An experiment would typically be carried out in the following sequence:

- (1) prepare specimens;
- (2) incorporate specimens into cell;
- (3) deaerate cell;
- (4) monitor open circuit potentials of specimens during deaeration until steady values approached (usually -300 to -400mV SCE within half an hour). Adjust ramp generator start point to the mean value of the open circuit potentials;
- (5) run data acquisition program and input experimental details;
- (6) pause program;

- (7) switch potentiostat to "run" and start ramp generator;
- (8) continue data acquisition program until all specimens switched off and all data stored.

When the experiment was finished, the cells were dismantled and the specimens examined for pits and crevices. Data obtained from creviced specimens were discarded.

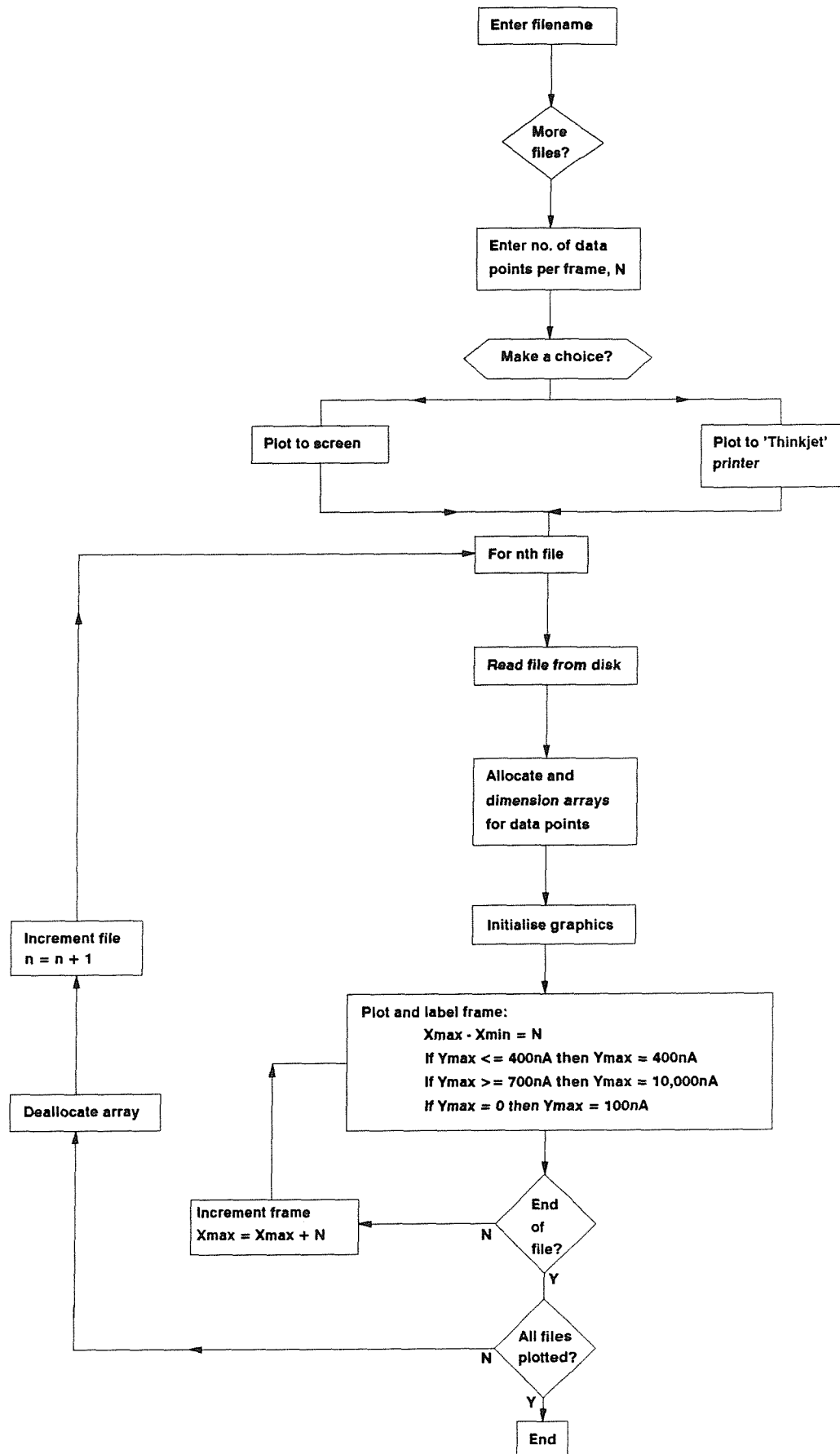
2.5 DATA ANALYSIS

The aim throughout this study was to address generic mechanistic issues fundamental to the understanding of pit initiation. Often, very simple data analysis procedures were the most informative.

Most experiments involved very slow potentiodynamic sweeps, and usually lasted in excess of 24 hours. With up to 10 experiments on each test (in the flow experiments), a large amount of data was inevitably accumulated. The first stage in the data analysis process was, therefore, to look at the quality of the data obtained, and to discard any poor data such as creviced specimens, or "noisy" current vs. time series which occasionally occurred during the course of an experiment due, for example, to a loose connection or a broken wire in the measuring circuitry. Also, due to the rarity of the pitting process, there were extended periods of time when no transients were observed (particularly at low potentials). Sequential screen plots were first obtained, to identify the files in which current transients had occurred. When these files had been identified, a hardcopy of the plots was obtained by dumping the data to a Hewlett-Packard "Thinkjet" printer. This sequence of operations was facilitated using a computer program which enabled files to be plotted out sequentially for each of the specimens. Since these hardcopies were subsequently used in the digitising procedure (see below), frame sizes were chosen to give sufficient resolution of the individual events: usually 1,000s intervals. A flow diagram of the program is given in Figure 2.5. The main features of the program were:

- (1) to enable the user to input the filename(s) of interest;
- (2) to enable the user to choose the number of data points to be plotted per frame - so that a file containing a 10,000s time interval could be plotted as, for example, 1 frame of 10,000s, or 10 frames of 1,000s etc.;

Figure 2.5 Flow Diagram of Data Inspection and Plotting Program I



- (3) to enable the user to choose a screen plot only, or to obtain a hard copy of the plots;
- (4) to plot out the files sequentially for all specimens, with axes scaled to fit the data.

Regions of interest in a given file could be examined in more detail using another program written in BASIC. The program, a flow diagram of which is given in Figure 2.6, enabled the following operations to be implemented:

- (1) call up a filename from the storage device;
- (2) display the minimum and maximum values of the file for both current and time as default options, whilst allowing the user to override these values;
- (3) plot the chosen current-time record on the computer screen, again with an option to change current and/or time scales;
- (4) provide an option to dump the screen plot to a plotter.

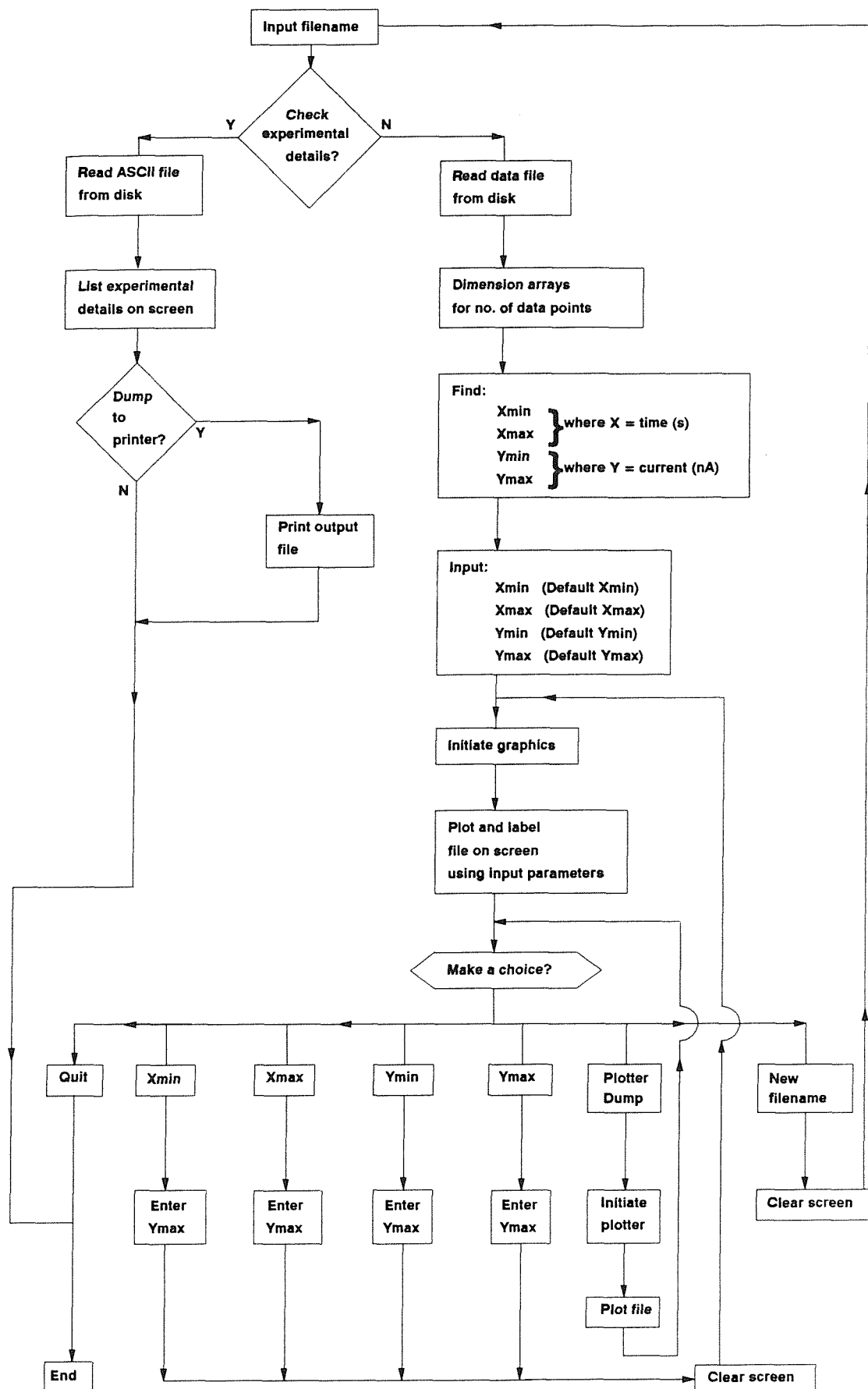
This program was particularly useful for calling up and examining specific regions of a data file, and for illustrating specific features of the current-time sequences. It was used to produce the figures of current vs. time sequences included in this thesis.

When the files containing current transients had been identified and plotted out, the next stage was to begin the process of characterising the transients. The nucleation frequency of unstable pits (λ) was obtained directly, simply by counting the current transients on all of the specimens for a given time interval:

$$\lambda = \frac{\text{total number of events}}{\text{total area of specimen(s)} \times \text{interval time}} \text{ (cm}^{-2}\text{s}^{-1}\text{)}$$

In order to analyse collectively information on the characteristics of the transients for a given set of experimental conditions (charge passed, current peak height, event lifetime etc.), each current transient was "captured" as four (x,y) points from a hardcopy of the file, using a digitising tablet, sequentially with respect to time. Four points were chosen because of the generally simple shape of the events - most were right-triangular - which meant that the digitised event provided a good approximation to the actual event. More points would obviously have produced a closer approximation to the actual event shape, but at a substantial time penalty in view of

Figure 2.6 Flow Diagram of Data Inspection and Plotting Program II



the number of events involved. The digitising was done in a consistent manner, such that:

- (a) the digitising sequence, points, 1-4, was always positive-going with respect to time;
- (b) points 1 and 4 were always the start and end of an event, respectively;
- (c) point 3 was always the peak current in the event.

Digitising was achieved with the aid of a computer program which was written to enable the following procedures to be implemented:

To prompt the user to:

- (1) input the time axis of the frame to be digitised;
- (2) locate the (x_{\min}, y_{\min}) and (x_{\max}, y_{\max}) points from the hardcopy plot on the digitising tablet using the digitising pen (i.e. define the boundaries of the frame to be digitised);
- (3) enter y_{\min} and y_{\max} (defining the minimum and maximum currents on the frame).

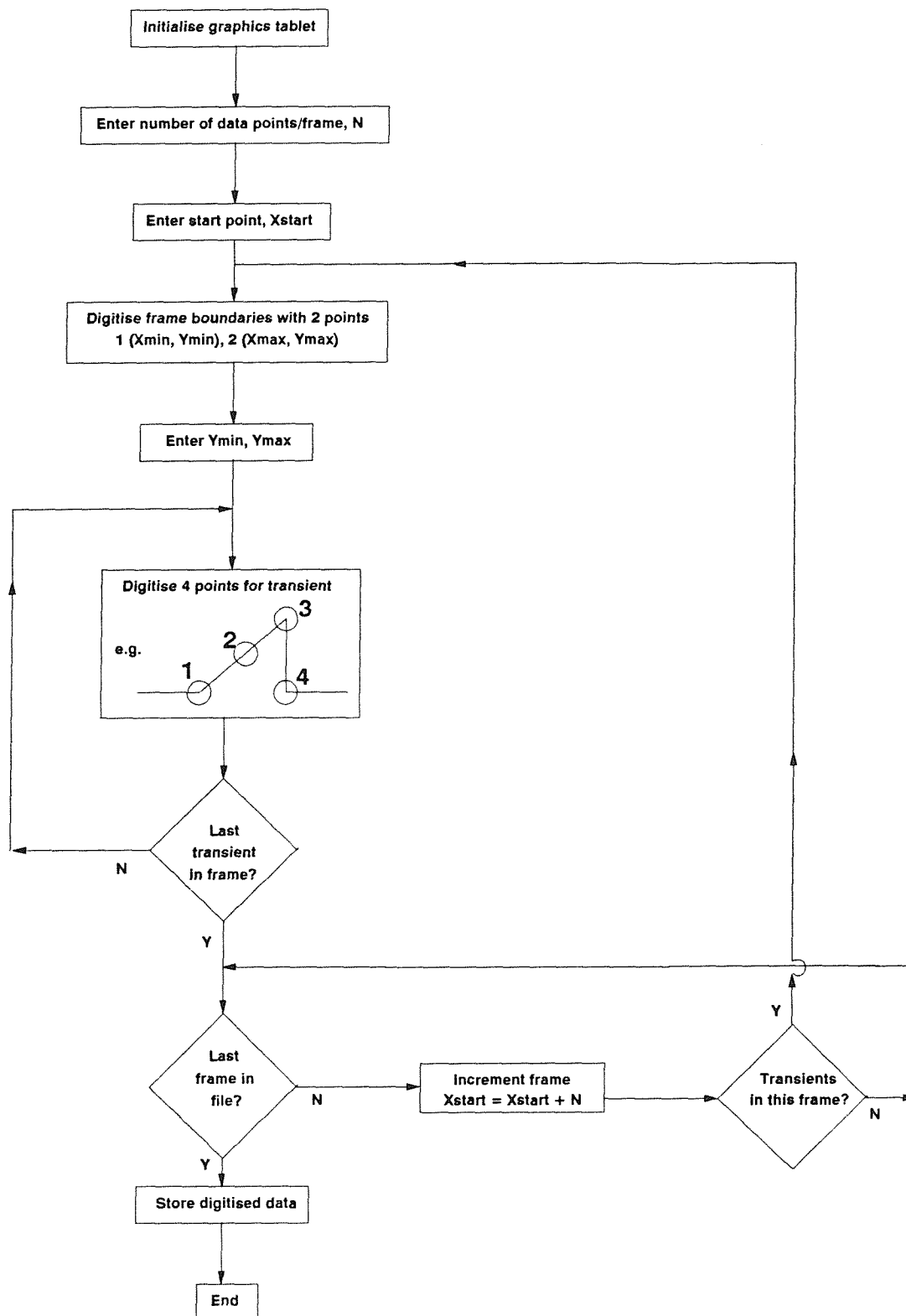
When these prompts were satisfied, the digitising routine was ready to accept data, which was invited with the prompt:

- (4) digitise 4 points.

This prompt was repeated after each event had been digitised. When all of the events in a frame had been digitised, the user could move on to the next frame, again working through prompts 1-4 above, or could elect to miss a frame (for example, if no transients were evident). When all of the frames on a given file had been digitised, the data could then be stored under a new filename for subsequent analysis. A flow diagram of these procedures is given in Figure 2.7.

Clearly, with four data points describing its shape, the "digital transient" did not capture all of the features of the actual transient. The errors in subsequent calculations (described below) were likely to have been greatest where the area under the current-time transient was required: pit radius and current density, for example. However, these errors were not significant in the subsequent analysis, and the method was sufficiently accurate to describe the trends involved for large numbers of

Figure 2.7 Flow Diagram of Digitising Tablet Program



transients (usually in excess of 300 and often in excess of 1,000 transients) for a given set of conditions. Errors in other parameters, such as peak heights, lifetimes and baseline currents were negligible because of the consistent manner in which the digitising was carried out (see above).

Once the individual current transients had been reduced to 4 (x,y) pairs of data points, it was then possible to look at the characteristics of large numbers of current transients as a function of electrode potential, alloy type and so on. This was achieved using simple analyses of many individual transients and facilitated by the program illustrated in the simplified flow diagram in Figure 2.8. The program was flexible, and was adapted and added to throughout the period of this work. The following are some of the procedures implemented:

1. call up files containing the digitised data;
2. add more data via the keyboard, which was useful for events which overlapped frame boundaries;
3. review the digitised data: this enabled rogue data to be edited out, which occasionally occurred due to an operator error during the digitising procedure;
4. analyse the digitised data. There were numerous ways to present the data on transients. The ones described below were found to best illustrate the data.

(i) Current Peak Height vs. Lifetime

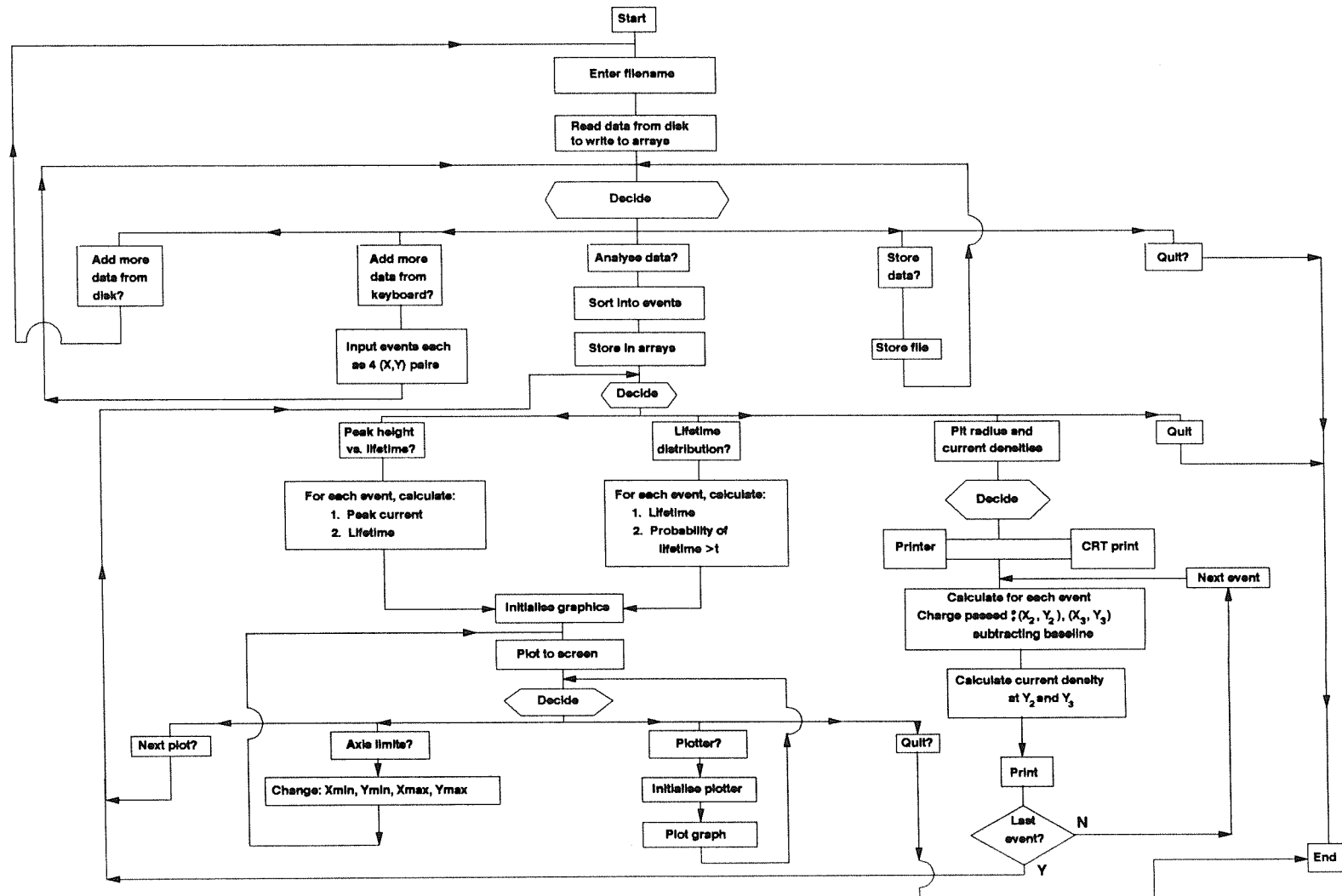
These diagrams were useful for rapidly assessing the trends in the data as a function of potential. The peak heights were calculated by subtracting the average baseline current $\left(\frac{(Y_1 + Y_4)}{2} \right)$ from the peak current in the event (Y_3)

for each transient in a given file. The lifetimes (t) were computed in seconds from $(X_4 - X_1)$.

(ii) Ln (Probability of Observing Lifetime > t) vs. t

The lifetime distribution of transients under a given set of conditions is useful for assessing whether there is more than one population of events. This plot was calculated by sorting the events into descending order of lifetime, and then calculating the probability for the j^{th} event from $\frac{\ln(j+1)}{\text{array size}+2}$

Figure 2.8 Flow Diagram of Data Analysis Program



Other simple calculations such as current density and pit radius, which were subsequently added, are described in relevant results chapters.

2.6 DISTRIBUTION OF PITTING BREAKDOWN POTENTIALS

As described earlier, experiments were stopped when the current exceeded the $10\ \mu\text{A}$ limit. For each set of conditions, with a large number of specimens (in excess of 30) this occurred over a range of potentials. Throughout this thesis, these results are presented as cumulative probability of breakdown distributions plotted against potential. These plots were calculated by arranging the breakdown potentials in descending order such that the most noble breakdown potential = 1, and the least noble potential = N, where N is the total number of specimens. The cumulative probability of breakdown for each event, n, was then calculated from $\frac{n}{N+1}$. Using this plot, it was possible to read of the potential at which, for example, 50% of the specimens tested under a given set of conditions had pitted, and it was also very useful for comparing breakdown distributions for different alloys, plotted on the same axes.

CHAPTER 3

RESULTS AND DISCUSSION: SLOW ANODIC POTENTIAL SWEEP EXPERIMENTS

CHAPTER 3 - RESULTS AND DISCUSSION: SLOW ANODIC POTENTIAL SWEEP EXPERIMENTS

3.1 INTRODUCTION

This chapter presents the results of very slow anodic potential ramp experiments (0.005mV/s) on the pitting characteristics of type 304L stainless steel in dilute chloride solutions. The experimental conditions were such that, in the period prior to the onset of sustained pitting, anodic current transients were detected above the background current. These transients are analysed, and this analysis is used as the foundation for the discussion of the mechanisms involved in the early stages of pitting.

First of all, the general features of the current transients observed during these experiments - their frequency, size and shape - are described as a function of electrode potential. Attention is then focussed on the effect of potential ramp rate on the unstable pitting characteristics, in order to examine how this may influence the outcome of experiments: the frequency and size of the transients, and the magnitude of the passive current. To facilitate this, the results from this study are compared with those reported by other workers, where faster ramp rates were used^(1,2). In a recent paper, Keddam and co-workers⁽¹⁾ considered the effect of ramp rate in the range 0.28 - 1mV/s on the magnitude and fluctuations of the passive current observed on type 304 stainless steel in dilute chloride solutions. These conditions were chosen to be representative of the ramp rates commonly used in studies of pitting corrosion. In an extension of the work reported in this thesis, Balkwill⁽²⁾ has conducted similar experiments, using the same experimental apparatus, at 5×10^{-5} V/s (0.05mV/s). It is shown that the slow potential ramp employed throughout this study more closely resembles real corrosion situations.

Experiments to test the correlation between current transients and pits are then described. Whilst a one to one relationship between unstable pits and transients is usually taken for granted, proof of this correlation, provided here, represents crucial information when using electrochemical noise techniques to study pitting corrosion.

The current transients are then examined in more detail. The current densities generated during the growth stage of unstable pits are interesting since they indicate the rate of the corrosion reaction, which in turn may help to identify the mechanisms involved. It is shown that both the current/time evolution and the current densities of unstable pits are no different from the early stages of stable (propagating) pitting.

The final results section in this chapter considers the morphology and physical characteristics of the pits formed during these experiments. Two features are of note. Firstly, small pits were often associated with sulphur-rich inclusions. Secondly, most pits were covered with remnants of the surface metal.

The discussion examines theories of pit initiation and repassivation in the light of these experimental results. Initiation is consistent with a description based on a "feedback" mechanism, in which the passive current density provides the driving force for pit initiation. The current evolution with time of the transients is examined in detail. Two limiting current/time relationships are derived in which at one extreme the current is limited by the surface area of the growing pit, and at the other by the solution resistance outside the pit. An equation is derived which, when solved numerically using appropriate input parameters, fully describes the current evolution with time between these limiting cases. The computer-generated current/time evolution is shown to be consistent with the shapes of experimentally observed transients. In the discussion of repassivation mechanisms, two suggestions are made on the basis of this study. The first, based on a collapse or removal of pit covers, has been alluded to previously by other workers. The second, based on repassivation when the supply of sulphur (from inclusions) runs out, is developed further in Chapters 5 and 6.

3.2 EXPERIMENTAL

The apparatus used for this work is described in detail in Chapter 2 (Sections 2.2 and 2.3). One change was made early in the experimental programme when it was realised that the ramp generator was causing electrical interference. This problem was solved by adding a simple filter to the output of the ramp generator (Section 3.3.1, Figure 3.2). Type 304L commercial purity stainless steel 5cm² disc specimens were used for all of the experiments reported in this chapter. Except where specified otherwise, the specimens were wet ground to a grade 240 grit surface finish. Experiments consisted

of a very slow anodic potential ramp, $5 \times 10^{-6} \text{V/s}$, starting from the average value of the rest potentials of the individual specimens, in 1,000ppm chloride solution. Seven individual experiments were carried out simultaneously. Subsequent analysis was based on data from at least fourteen experiments. The current was logged at 1Hz for the duration of the experiment, which typically lasted in excess of 24 hours. The specimens were individually switched off from the potential ramp by means of a relay switch as their measured current exceeded $10 \mu \text{A}$.

3.3 RESULTS

3.3.1 General Features of Slow Potentiodynamic Ramp Experiments

Figure 3.1 shows typical sections of current-time series recorded for individual specimens during these experiments. There are three observations of note. Firstly, current transients were detected at very low electrode potentials (see also Figures 3.3b and Figure 3.7). Secondly, the background currents were very low, typically $< 100 \text{nA}$ on the 5cm^2 specimens (Figures 3.1 and 3.3, for example). Thirdly, regular spikes were observed. The significance of the observations of current transients at such low (cathodic) potentials is discussed in Section 3.4. The low background currents were a direct consequence of the very slow potential scan rate used (see Section 3.3.2) and the procedures undertaken to reduce electrical interference (Chapter 2, Section 2.3.1). The regular spikes were found to be caused by the digital ramp generator: the potential ramp was generated as a series of steps, with a resolution of $153 \mu \text{V}$, and with a potential ramp rate of $5 \times 10^{-6} \text{V/s}$, a potential step could be anticipated approximately every 30s. This potential step corresponds with the current spikes observed in Figure 3.1. The spikes were removed by inserting a simple RC filter between the ramp generator output and the potentiostat, Figure 3.2. The time constant of the filter was chosen to be large (10s) such that the potential rise was smoothed.

Figure 3.3 shows sections of typical current-time series recorded for single specimens in the potential range -200mV to $+200 \text{mV}$ SCE with the ramp generator filter in place. At potentials between the rest potential (typically -400 to -300mV SCE) and -200mV SCE, a very low background current was measured, as in Figure 3.3a, with no evidence of current transients. As the specimens were further anodically polarised, current transients were generally evident at potentials in the region of -100mV SCE,

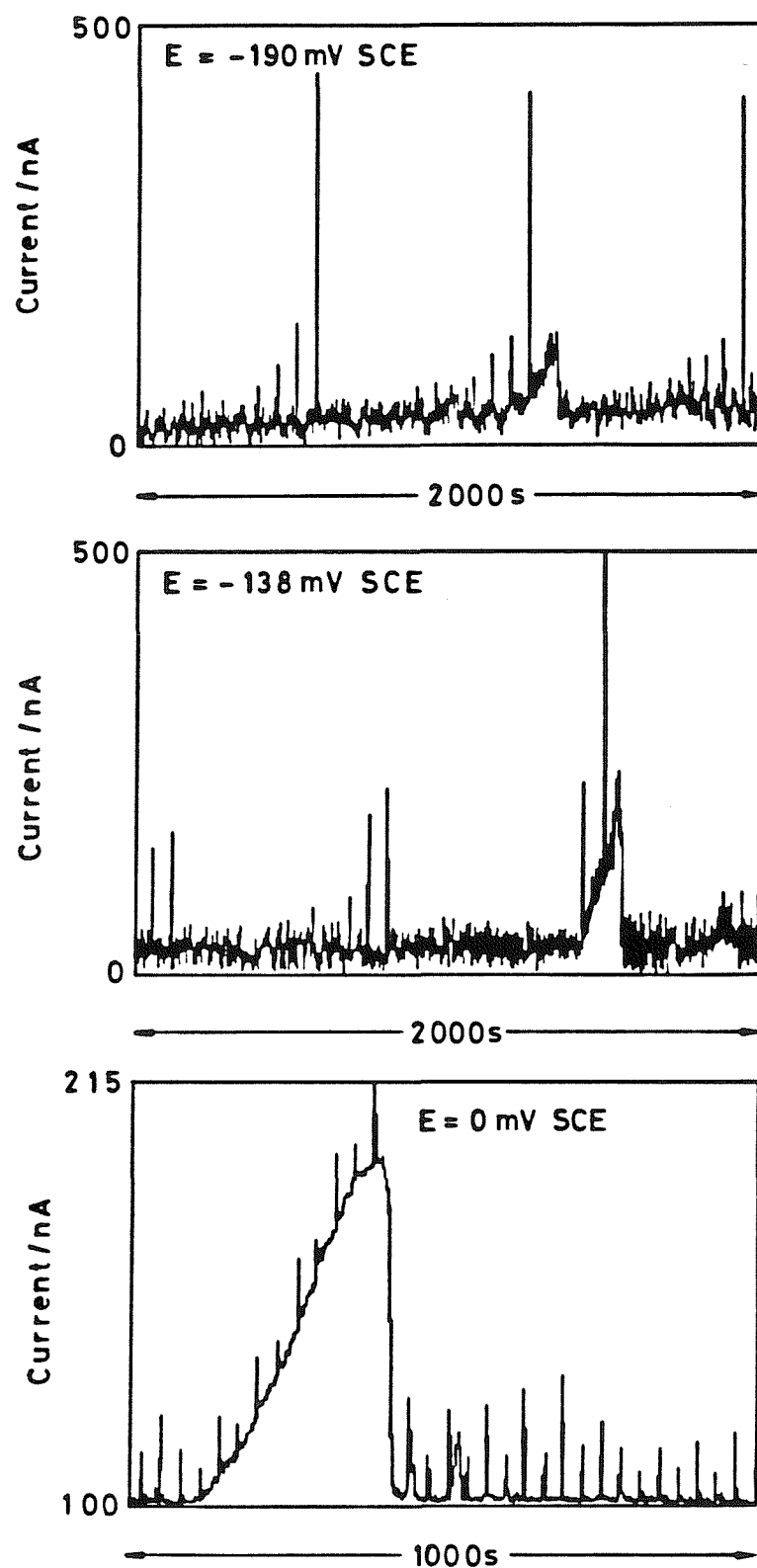
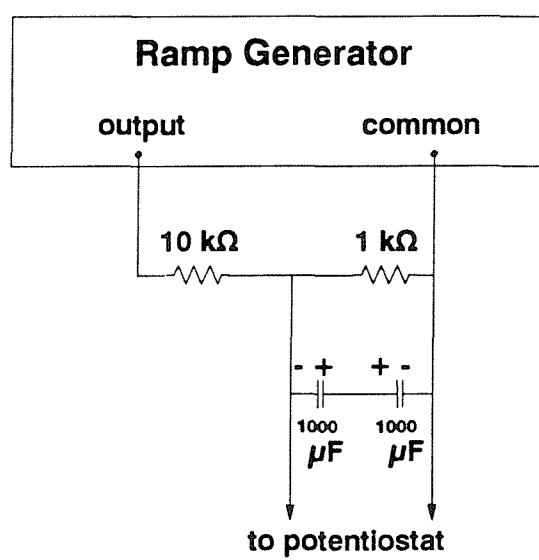


Figure 3.1 Current-time sequences showing anodic current transients (without ramp generator filter).

Figure 3.2 - Ramp Generator Filter



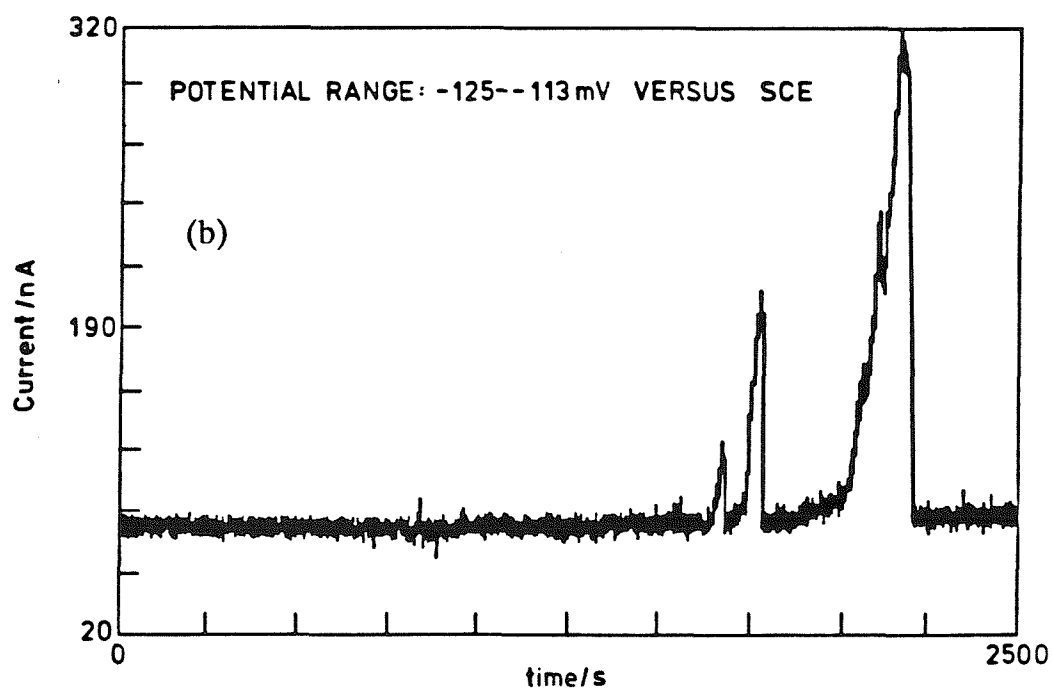
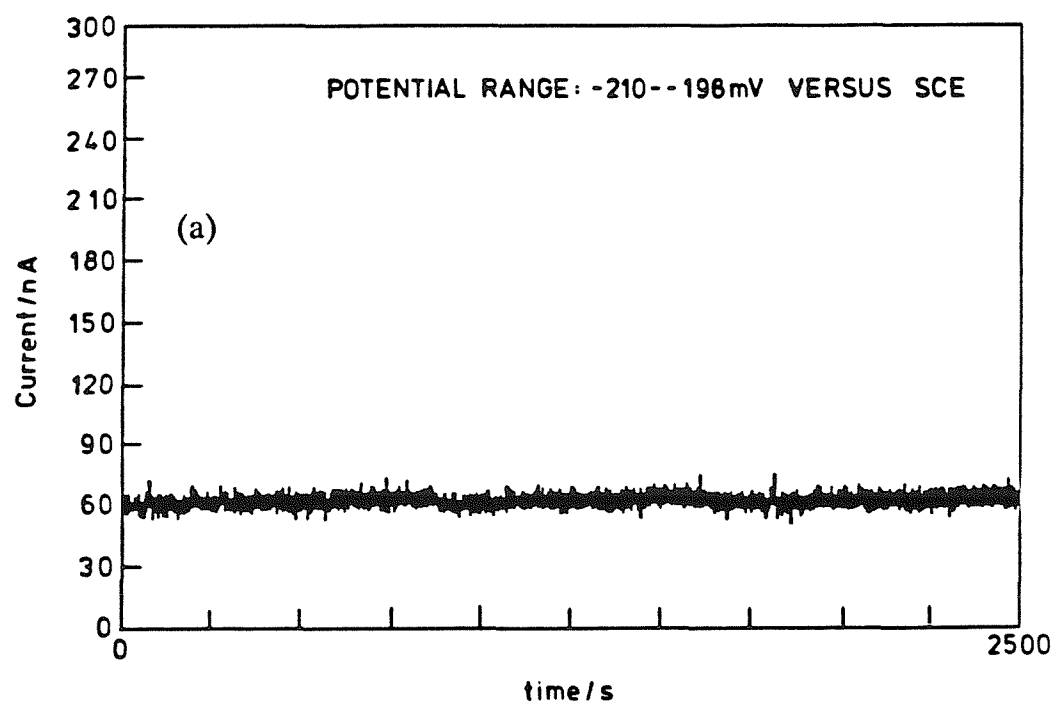


Figure 3.3 Typical current-time sequences across a range of potentials (with ramp generator filter).

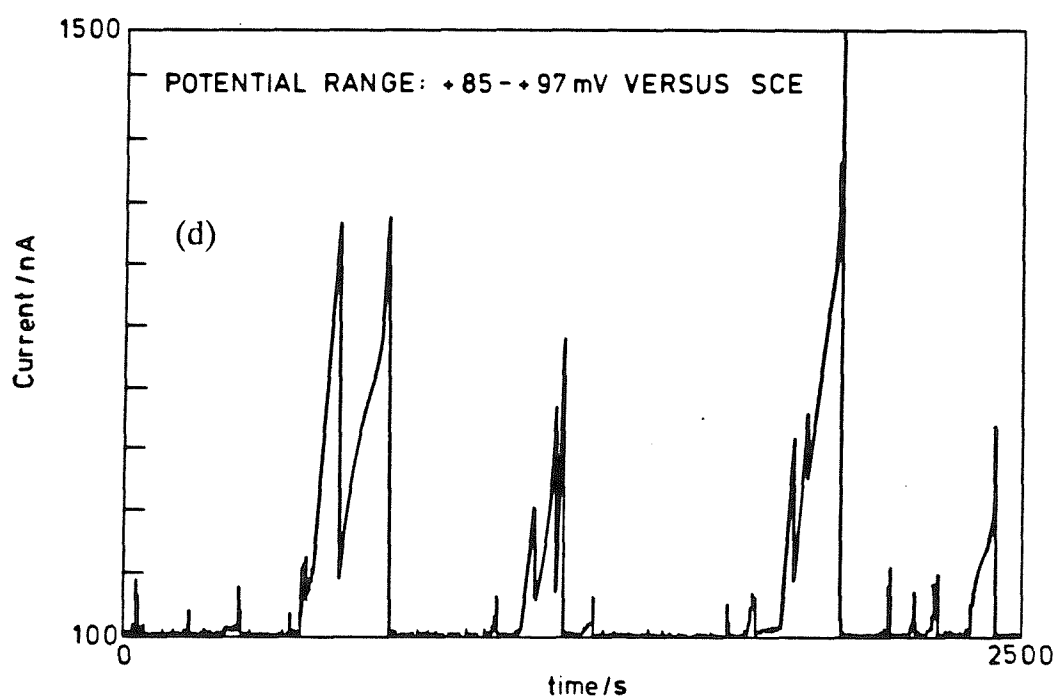
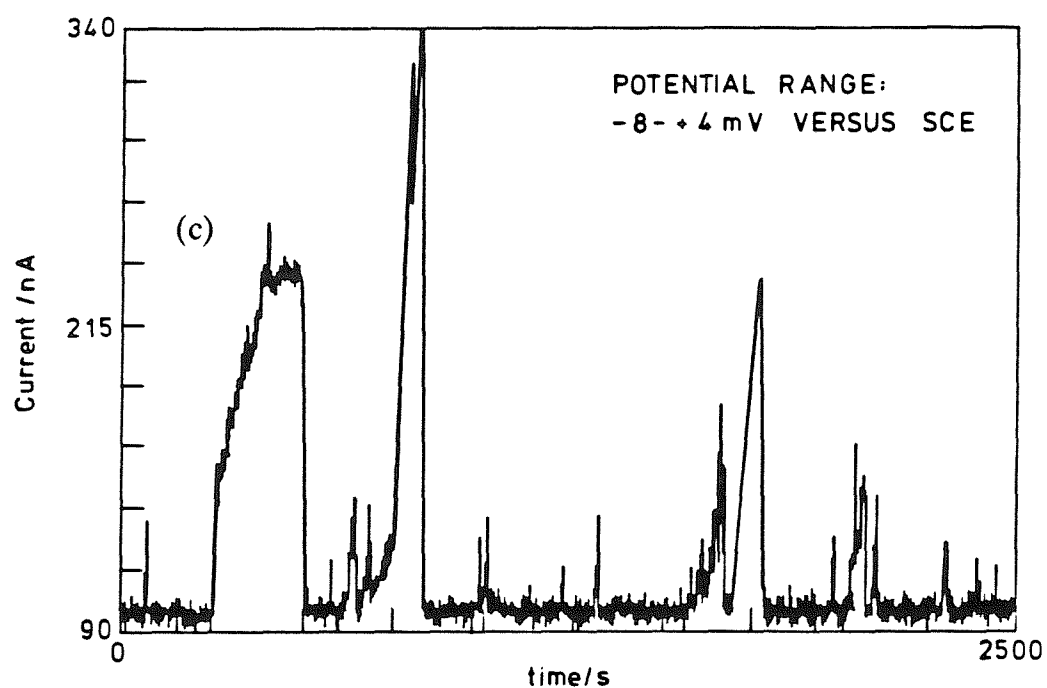


Figure 3.3 (continued)

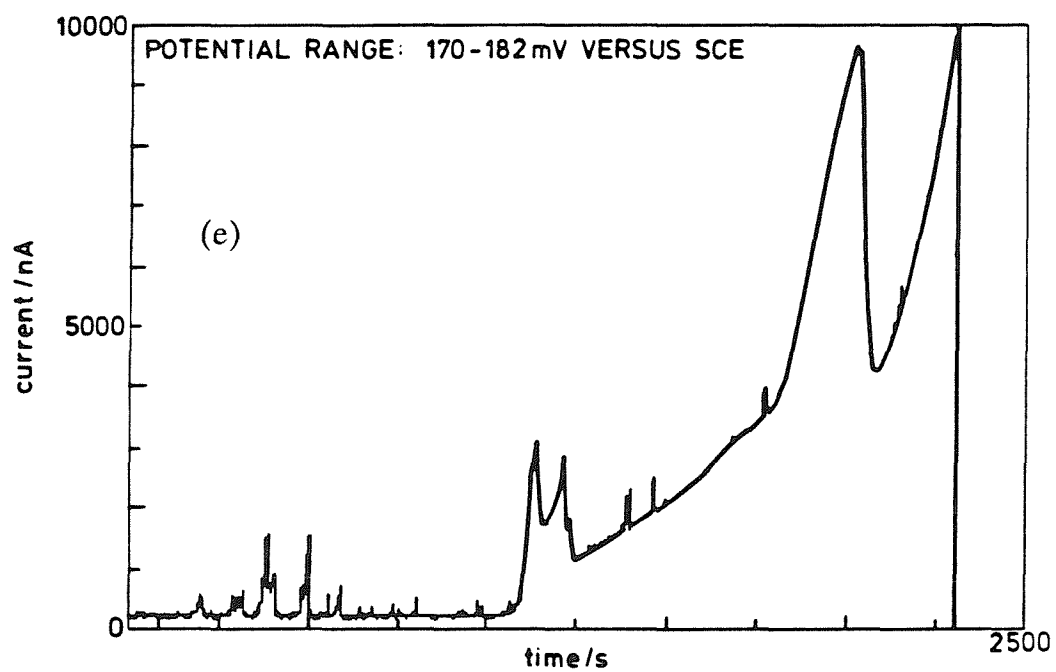


Figure 3.3 (continued)

as in Figure 3.3b, but sometimes at considerably lower potentials (for example Figure 3.1a). With further anodic polarisation, both the frequency of occurrence and the propagation, which was limited by a diffusion-controlled process, increased. Figure 3.3d illustrates a commonly observed feature of the current transients: they often appeared to consist of a series of current bursts on a rising background (see also Figure 3.6). This feature was sometimes apparent at the onset of pit propagation, Figure 3.4.

3.3.1.1 The Shapes of Current Transients

The current transients observed in these experiments were all basically right-triangular in shape: a relatively slow current rise was followed by a much more rapid current decay. The transients could further be sub-divided into three basic classes according to the characteristics of the current rise.

$$i \propto t^{1/2}$$

A typical event in this category is shown in Figure 3.5a. It was noted that these events tended to be quite long lived, and invariably ended with an anodic current spike.

$$i \propto t^2$$

An example of this type of event is also seen in Figure 3.5a. Again, some of these transients exhibited anodic current spikes during the current rise, often just prior to repassivation.

$$i \propto t$$

repassivation.

These events were the most commonly encountered. Examples are shown in Figure 3.5b. Some of these transients exhibited anodic spikes during the linear current rise, and often just prior to repassivation.

$$i \propto t$$

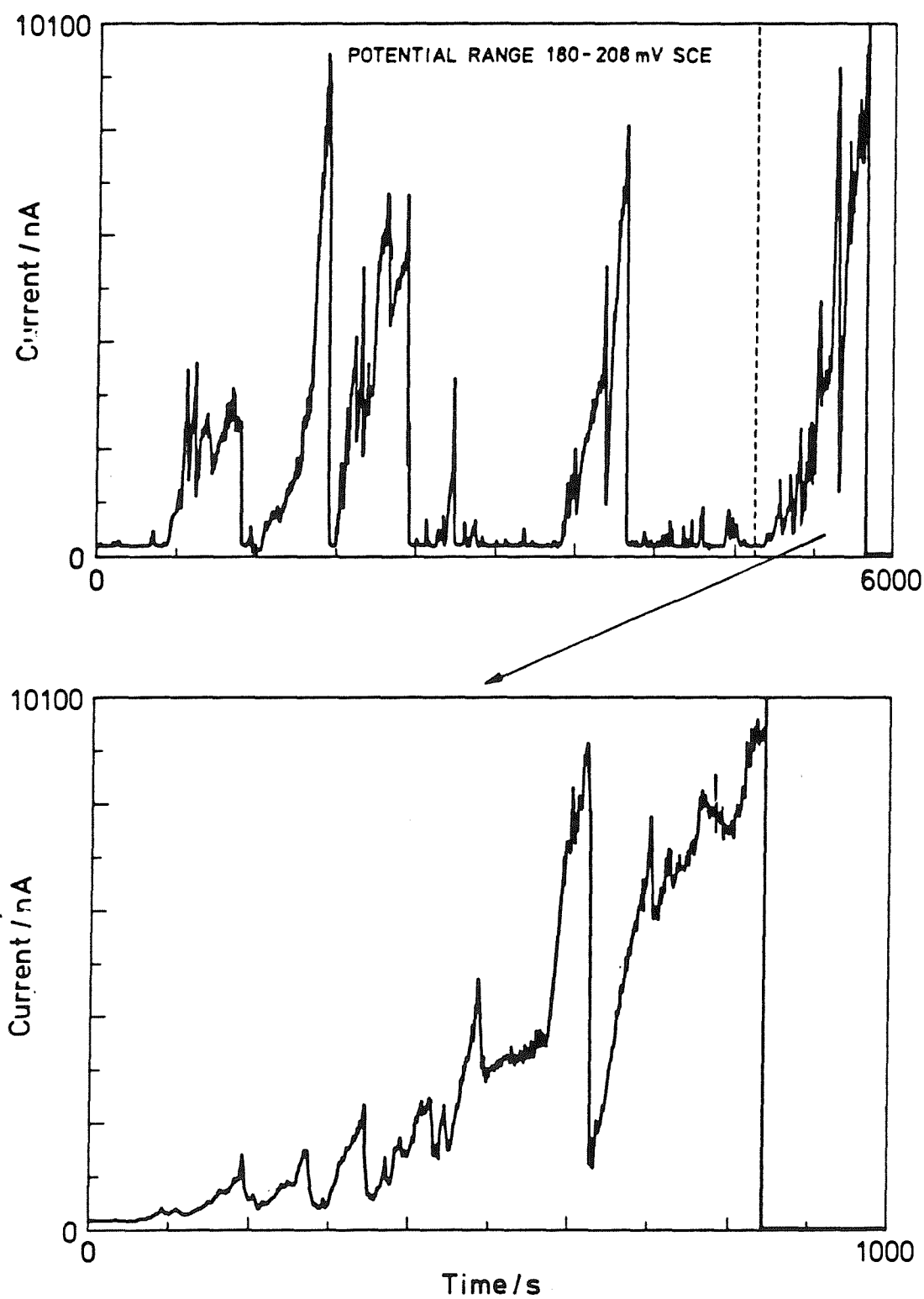


Figure 3.4 The onset of pit propagation marked by a series of anodic current bursts.

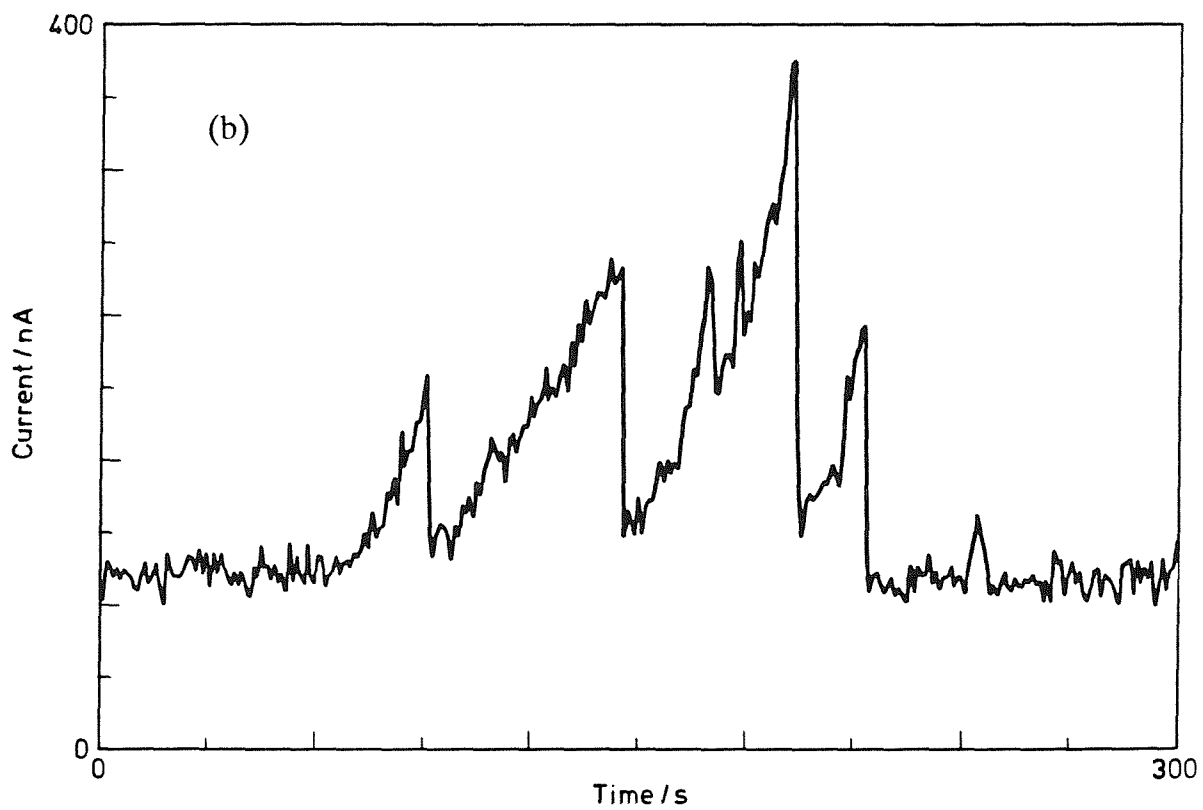
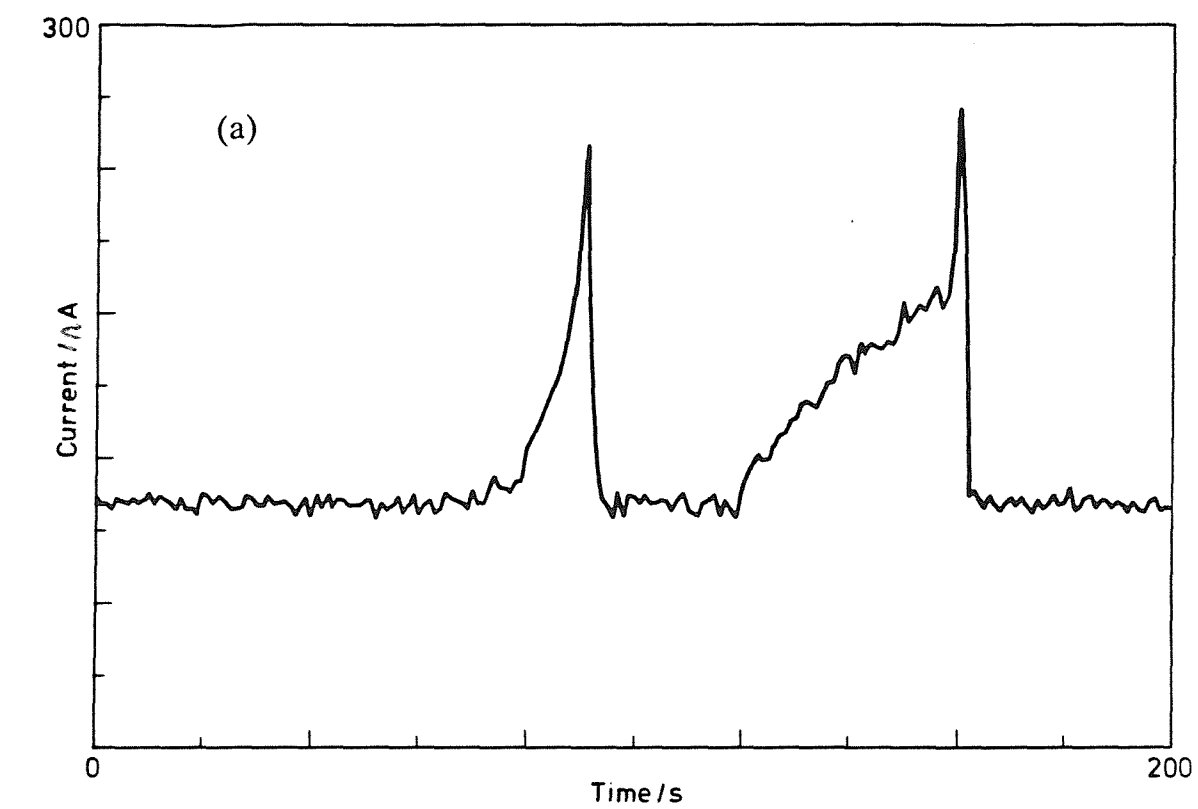


Figure 3.5 Transient shapes (a) $I \propto t^2$ and $I \propto t^{1/2}$ (b) $I \propto t$ ($E \approx 0\text{mV SCE}$)

Microscopic models which account for the observed current evolution with time ($i \propto t^n$) are discussed further in Section 3.4.

All classes of current transient were characterised by a rapid repassivation, which occurred in a few seconds, and thus could not be adequately followed using a sampling frequency of 1Hz.

The frequency of the current transients often varied widely from specimen to specimen under nominally identical experimental conditions, Figure 3.6. This variability in the data from transient to transient and from experiment to experiment is a good illustration of the need for the caution required when interpreting the data from single pitting experiments, and hence why statistical approaches are increasingly seen to be appropriate. In this work, therefore, large numbers of experiments were performed for a given set of conditions, and the results analysed collectively (that is, as an *ensemble*). Figure 3.7 shows the relationship between electrode potential and the frequency of occurrence of current transients. This figure was constructed from an ensemble of 30 individual experiments carried out on 304L stainless steel in 1,000ppm Cl^- at $5 \times 10^{-6}\text{V/s}$.

3.3.2 The Potential Ramp Rate

The majority of the experiments reported in this thesis were performed at $5 \times 10^{-6}\text{V/s}$. The effect of the potential ramp rate on the frequency of current transients can be demonstrated using data from experiments performed at $5 \times 10^{-5}\text{V/s}$ (2), using the same apparatus, 304L specimens from the same stock material and 1,000ppm Cl^- solution. Figure 3.8 shows such data, and it clearly illustrates that the nucleation frequency of the current transients increased with ramp rate. Figure 3.9 includes data from Keddam and co-workers(1) and Balkwill(2) and shows the variation in the passive current density as a function of the electrode potential for ramp rates in the range 0.005 to 1mV/s . The passive currents increased to a plateau, and the plateau currents increased with sweep rate.

3.3.3 The Relationship Between Current Transients and Observed Pitting

An assumption which is often made (but rarely substantiated) in electrochemical studies of pitting corrosion is that the observed electrochemical noise (current

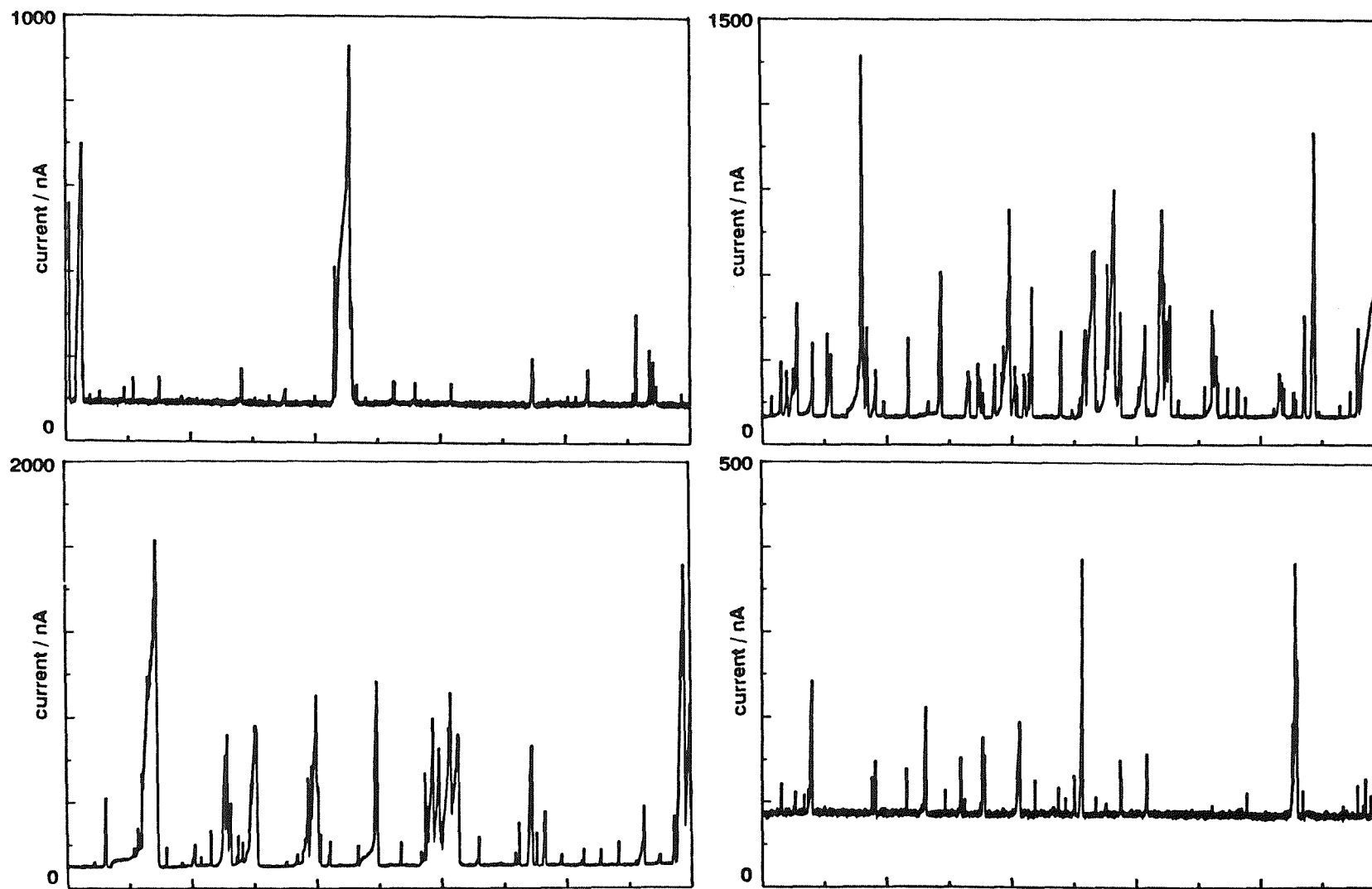


Figure 3.6 Variability in pitting response indicated by current-time sequences of 4 specimens from the same experiment.
(each frame 5,000s; $E \approx 95 - 120\text{mV SCE}$)

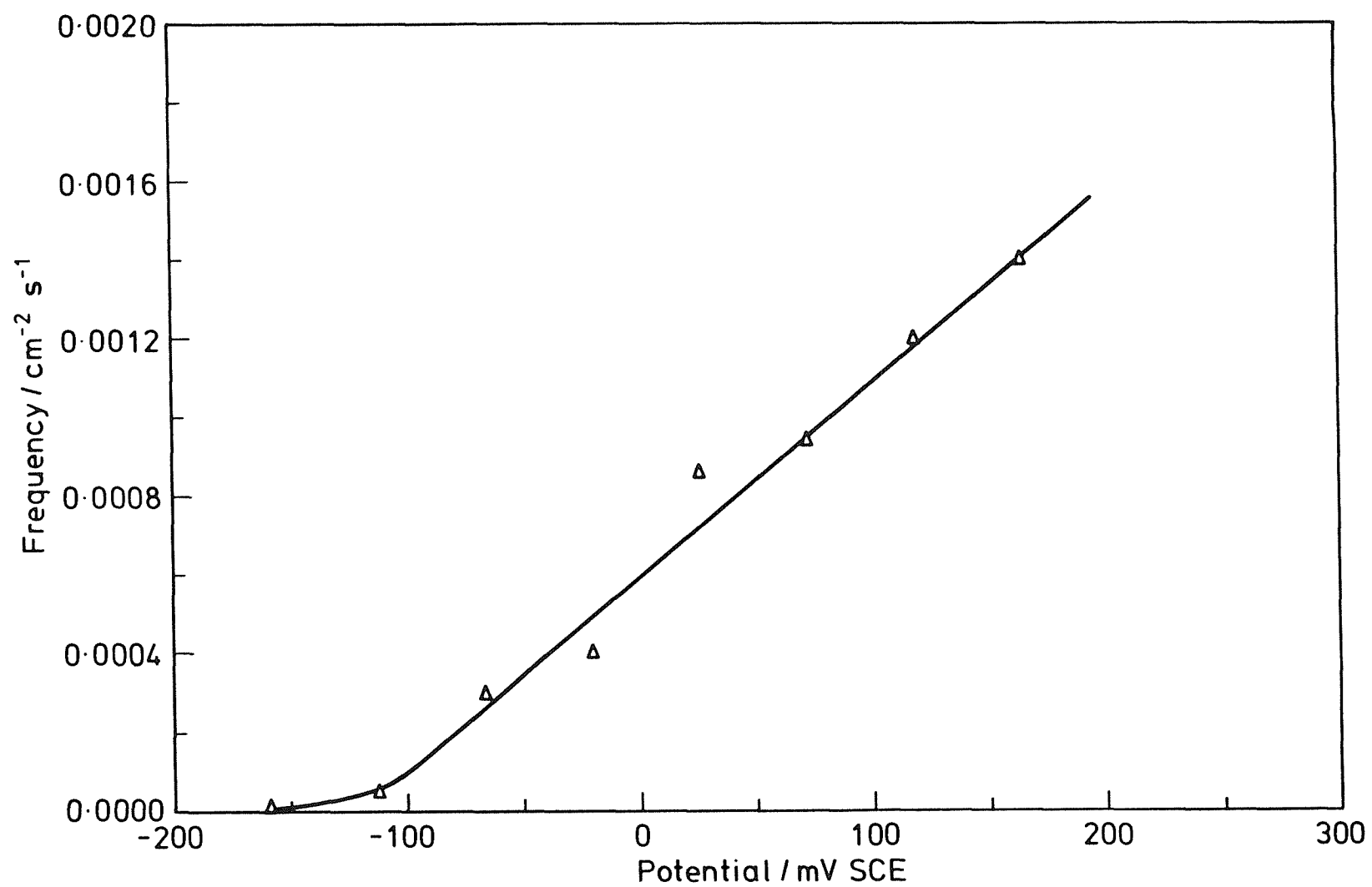


Figure 3.7 Frequency of occurrence of current transients vs. electrode potential (304L, 1000ppm chloride, 0.005mV/s)

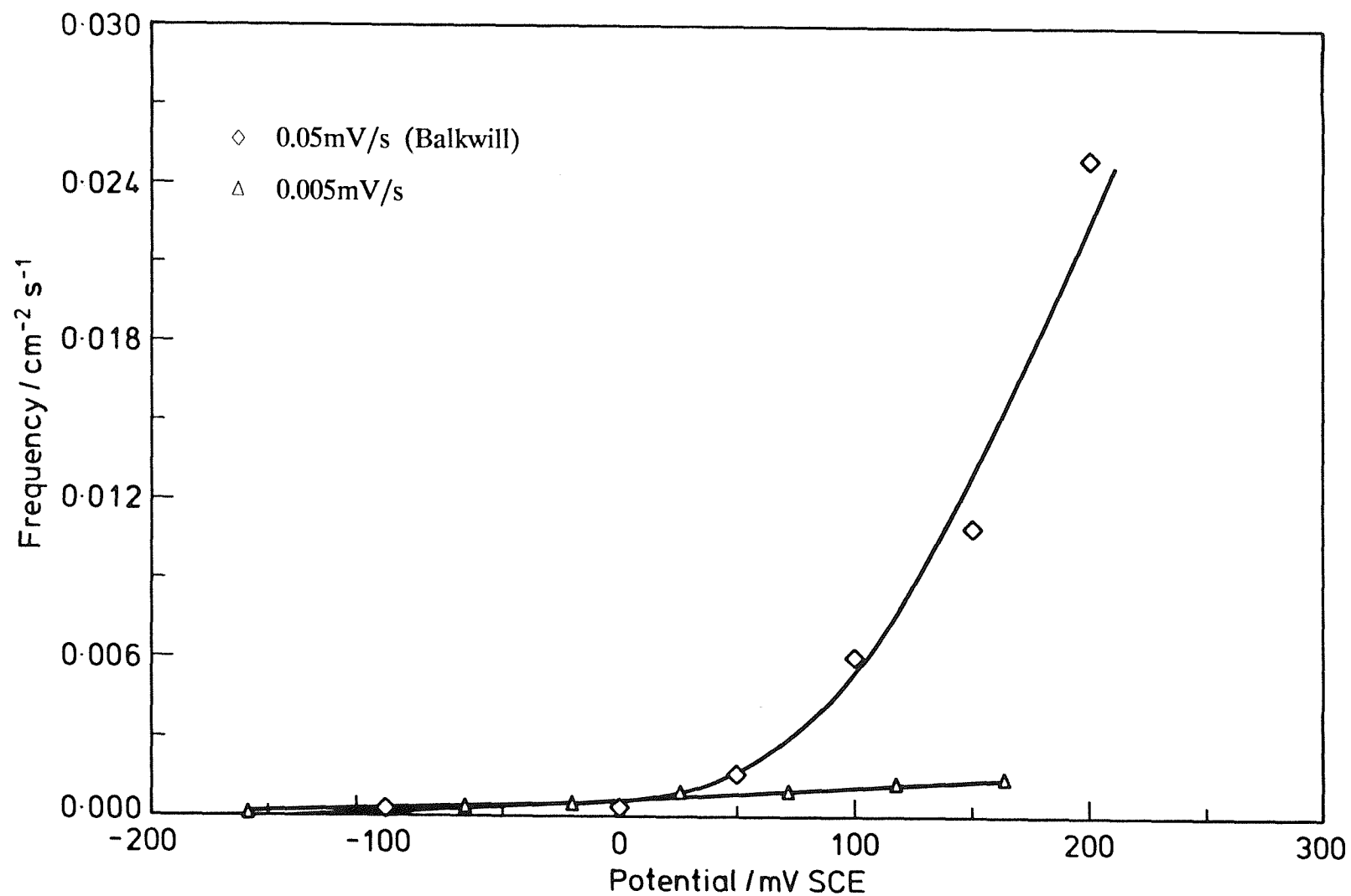


Figure 3.8 Effect of potential ramp rate on event frequency (304L, 1000ppm chloride)

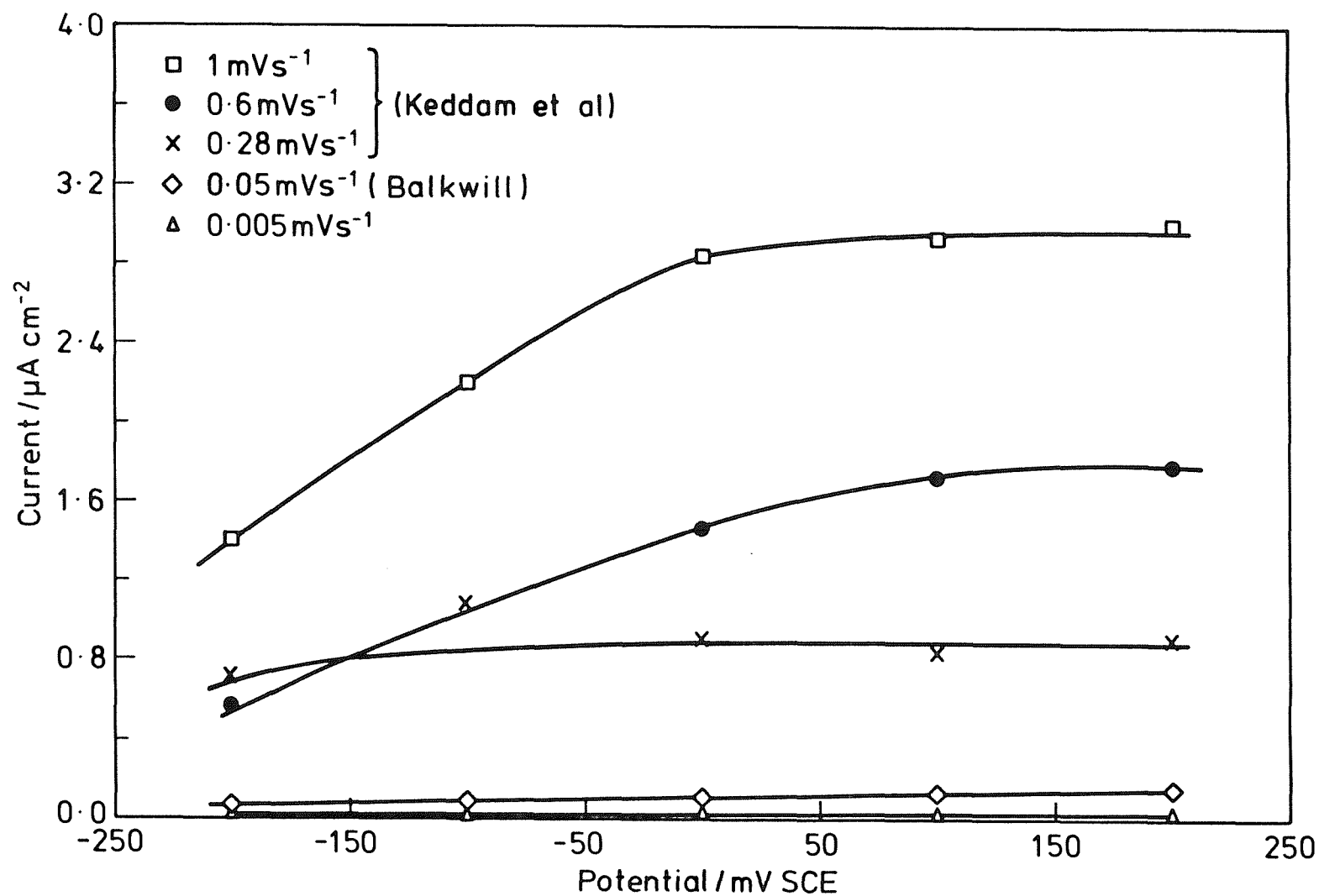


Figure 3.9(a) Effect of potential ramp rate on passive current density (304L, dilute chloride solutions).

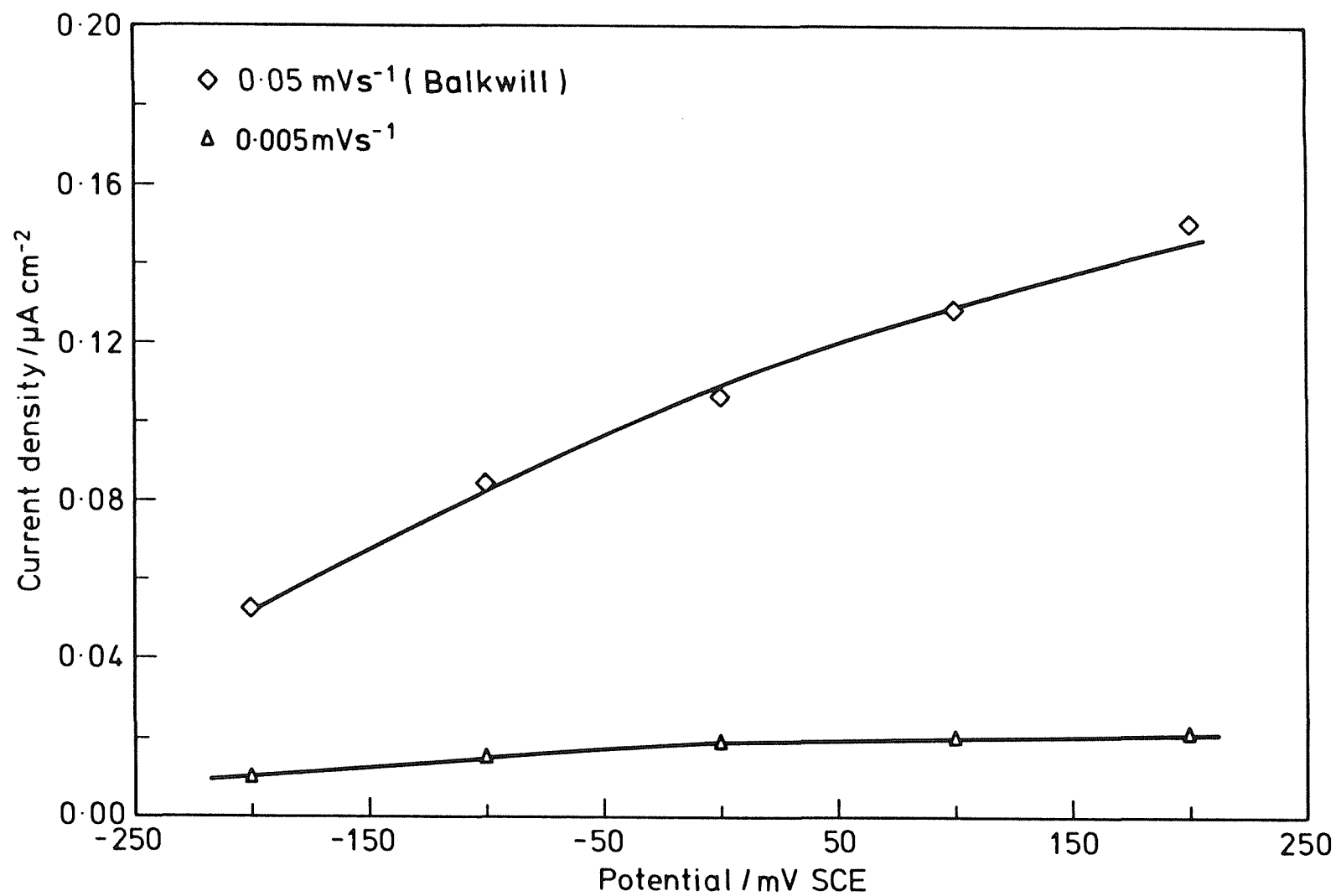


Figure 3.9(b) Detail of passive current density vs. potential at slow ramp rates (304L, 1000ppm chloride).

transients or potential fluctuations) is caused by the initiation, temporary propagation and repassivation of small, unstable pits. In this study, the validity of this assumption is tested. Post-test examination of specimens used throughout this work usually revealed the presence of very small pits. However there remained clear difficulties in proving that the current transients were due solely to the generation of pits. Such proof required a one to one correlation between pits and transients. Two further complicating factors were, (a) the anticipated small size of the pits (estimated using Faraday's law from the charge passed during the current-time transient - see below) and, (b) the fact that pits were generally only readily observable in the optical microscope with oblique illumination after light abrasion of the specimen surface.

A series of experiments were carried out with the intention of reducing the number of pits formed, to enable direct correlation with observed current transients. This was achieved by reducing the specimen area and surface roughness, and limiting the test time. Most of the specimen surface was masked from the test solution, using a resin reinforced synthetic rubber, leaving a test area of 25mm² polished to a 1 μ m diamond finish exposed to the solution. A high purity model alloy, based on 304L composition, was used for these experiments (see Chapter 5 for details), at a potential of +200mV SCE. Experiments consisted of potentiodynamic polarisation of specimens from the region of the open circuit potential to +200mV SCE at a ramp rate of 8x10⁻⁵V/s where the potential was held constant for the remainder of the test. The current was logged at 1Hz from -150mV SCE until the test was stopped after a total elapsed time of 10,000s. Of the 14 experiments carried out, crevice corrosion occurred on 4 specimens. A further 8 experiments showed no transients. Two experiments did yield current transients (numbers 8 and 13). The current-time records from both experiments are shown in Figure 3.10. From these records, all pits formed were unstable ones which had ceased to propagate before the end of the test. An estimate of the size of pit associated with these transients was made using Faraday's law:

$$V = \frac{QV_m}{zF} \quad (3.1)$$

where:

V = volume dissolved (cm³)

Q = charge passed (C)

$V_m = \frac{m}{\rho} = \text{molar volume (cm}^3/\text{mole)}$

z = electrochemical equivalent/mole

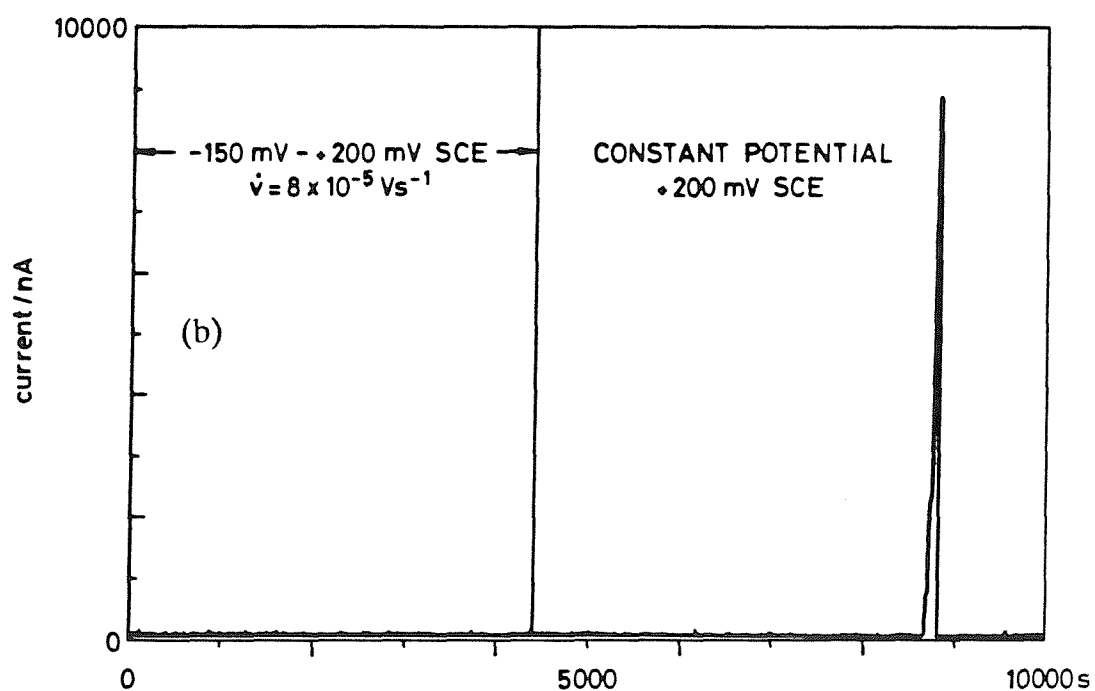
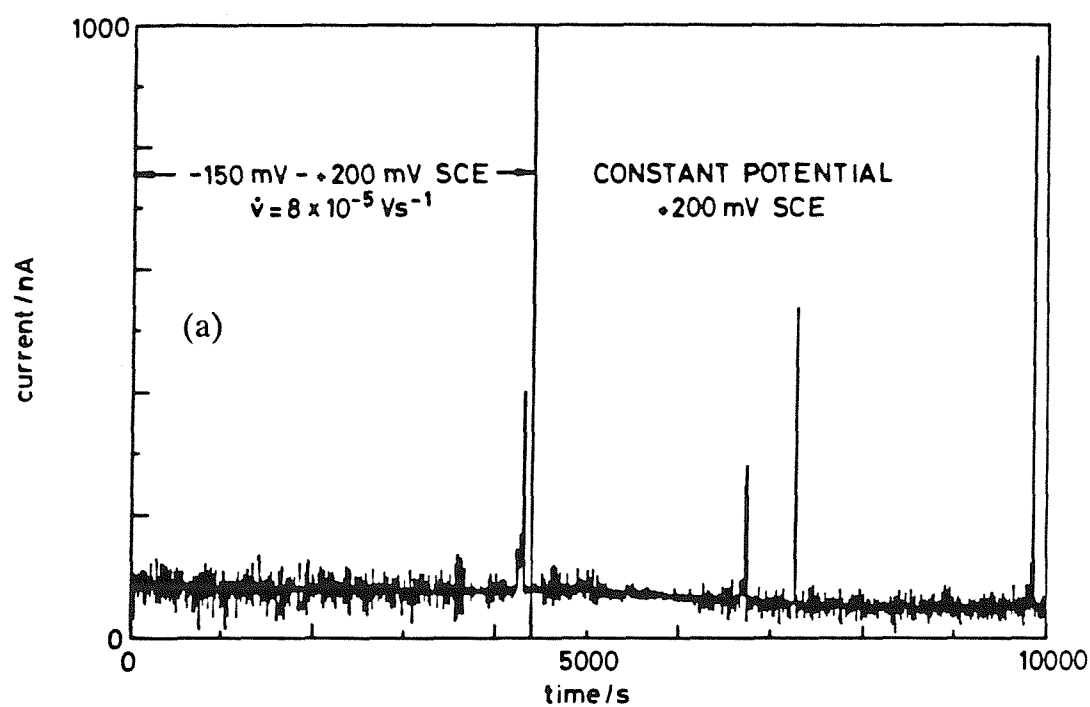


Figure 3.10 Complete current-time records for specimens on which current transients were observed in the control experiments: (a) Specimen 8, (b) Specimen 13 (see Table 3.1).

F = Faraday constant (96,500 coulombs equivalent)

ρ = density (g/cm³)

m = relative molecular mass (g/mole)

Assuming that only the major alloy constituents - iron, chromium and nickel were involved in the corrosion reaction, and that they dissolve as Fe^{2+} , Cr^{3+} and Ni^{2+} in the ratio found in the alloy (Table 2.1), then:

$$m_{\text{(average)}} = 55.41 \text{ g/mole}$$

$$\rho_{\text{(average)}} = 7.84 \text{ g/cm}^3$$

$$Z_{\text{(average)}} = 2.2 \text{ equivalent/mole}$$

Equation 3.1 then reduces to:

$$V = Q \times 3.33 \times 10^{-5} \text{ cm}^3 \quad (3.2)$$

If a hemispherical pit geometry is assumed (for convenience), then an estimate of the pit radius is given by:

$$r = \sqrt[3]{(Q \times 1.59 \times 10^{-5})} \text{ cm} \quad (3.3)$$

The transients were collected, and the area under the i vs. t curve measured, using the digitising tablet and software routine described in Chapter 2 (Section 2.5), one output of which was an estimate of pit radius, using Equation 3.3, to the nearest μm . Table 3.1 summarises the results of these experiments.

Initially, optical microscopy of all as-tested specimens (excluding the 4 creviced specimens) could not positively identify pits. The specimens were then given a light abrasion and cleaned in an ultrasonic bath. Further optical microscopy (with oblique illumination at x400) located 4 very small pits, away from the lacquer, on the test area on specimen 8 and one quite large pit in the centre of the test area on specimen 13. A scanning electron micrograph of the pit on specimen 13 is shown in Figure 3.11, along with a detailed plot of the single transient. It can be seen that the pit is faceted. This anisotropic dissolution is similar to that observed by Brauns and Schwenk⁽³⁾ who noted that, near to the pitting potential, some crystal planes (notably {111}) exhibited lower dissolution rates, attributable to closer atomic packing on these planes. The periphery of the pit appeared bright in the SEM, indicating that the metal/passive film in this region was very thin, and therefore that the pit had undercut the free surface.

**Table 3.1 Control Experiments to Correlate Current
Transients and Pits**

EXPT. NUMBER	TRANSIENTS	PITS COUNTED	PIT RADIUS (μm)	
			Estimated	Measured
2, 3, 4, 6, 7, 11, 12, 14	None	None	-	-
1, 5, 9, 10	Creviceing	-	-	-
8	4	4	4, 3, 4, 5	4 pits each of approx $5\mu\text{m}$
13	1	1	20	15 typical

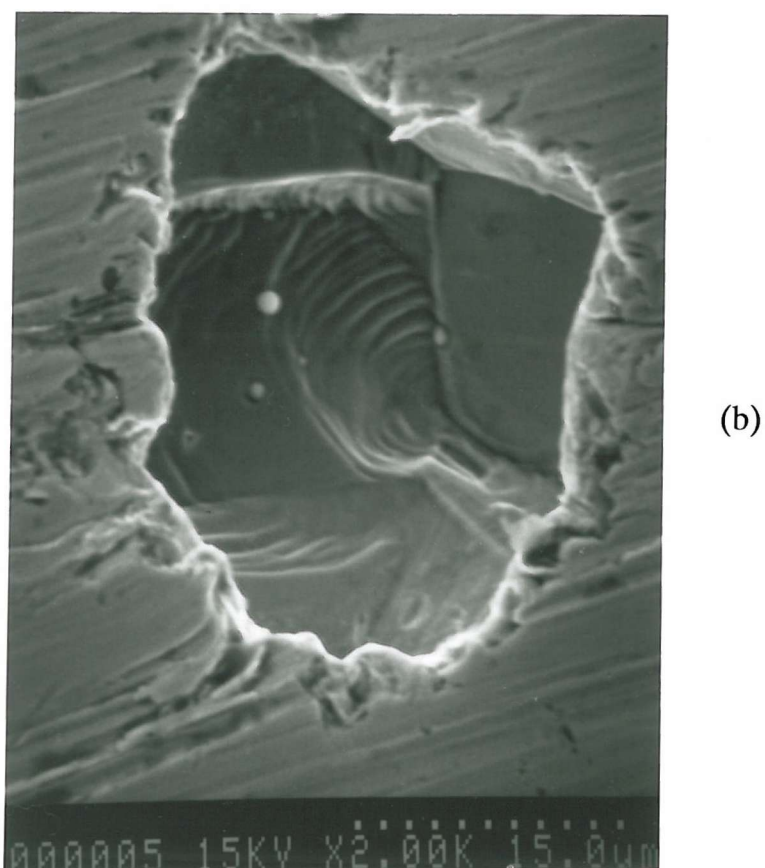
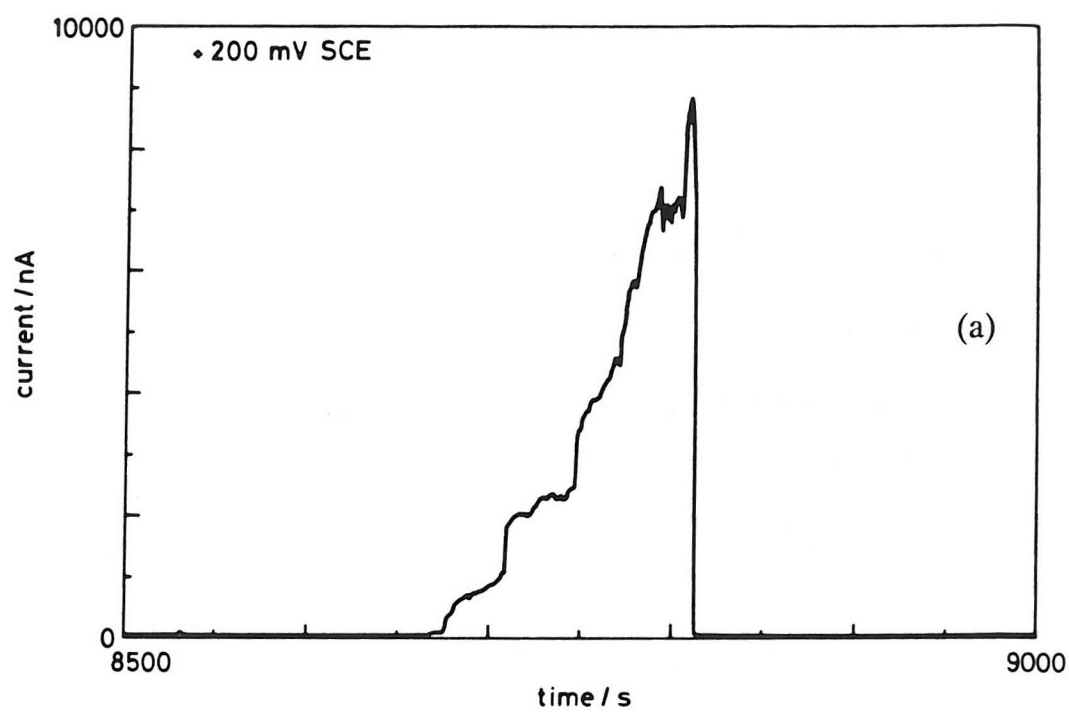


Figure 3.11 (a) Detail of the single transient observed on specimen 13. (b) Scanning electron micrograph of the single pit found on specimen 13 (see table 3.1).

A further observation was that the pit walls contained small, sub-micron particles. Energy dispersive spectroscopy of the particles was rather difficult due to their size and location. However, the presence of sulphur was not detected, (it seems likely that these were oxide particles - see Chapter 5). A comparison of the observed and calculated pit size is made in Table 3.1. Given the assumptions used in the calculation of pit size, the estimated and actual pit sizes are in good agreement. Examination of the eight specimens where current transients were not observed failed to find pits. This work confirms that the anodic current transients do in fact signal the initiation, temporary propagation and repassivation of small micropits.

3.3.4 Pit Sizes Represented by Current Transients

With increasing anodic polarisation, in addition to becoming more frequent, the magnitude, in terms of peak currents and charges of the individual transients increased, thus signifying the initiation of larger pits. This trend is summarised in Figure 3.12, which is a series of scatter diagrams showing the peak current and lifetime variation for current transients as a function of potential. Interestingly, the average lifetime of the unstable pits did not appear to increase with increasing potential. Figure 3.13 shows that the average pit radius increased rather linearly with anodic polarisation. The pit radii were calculated for many individual transients using Equation 3.3.

3.3.5 Current Densities in Unstable Pits

The current density in unstable pits during the growth stage was calculated by assuming that the pits were hemispherical (for convenience). This is the most widely assumed shape for pits and, whilst found not entirely accurate (see Figures 3.19c, 3.20c, and Section 3.4.2), it provides a reasonable working approximation.

$$i = \frac{I}{\text{surface area}} \quad (3.4)$$

where:

i = current density

I = current

Using Equation 3.3,

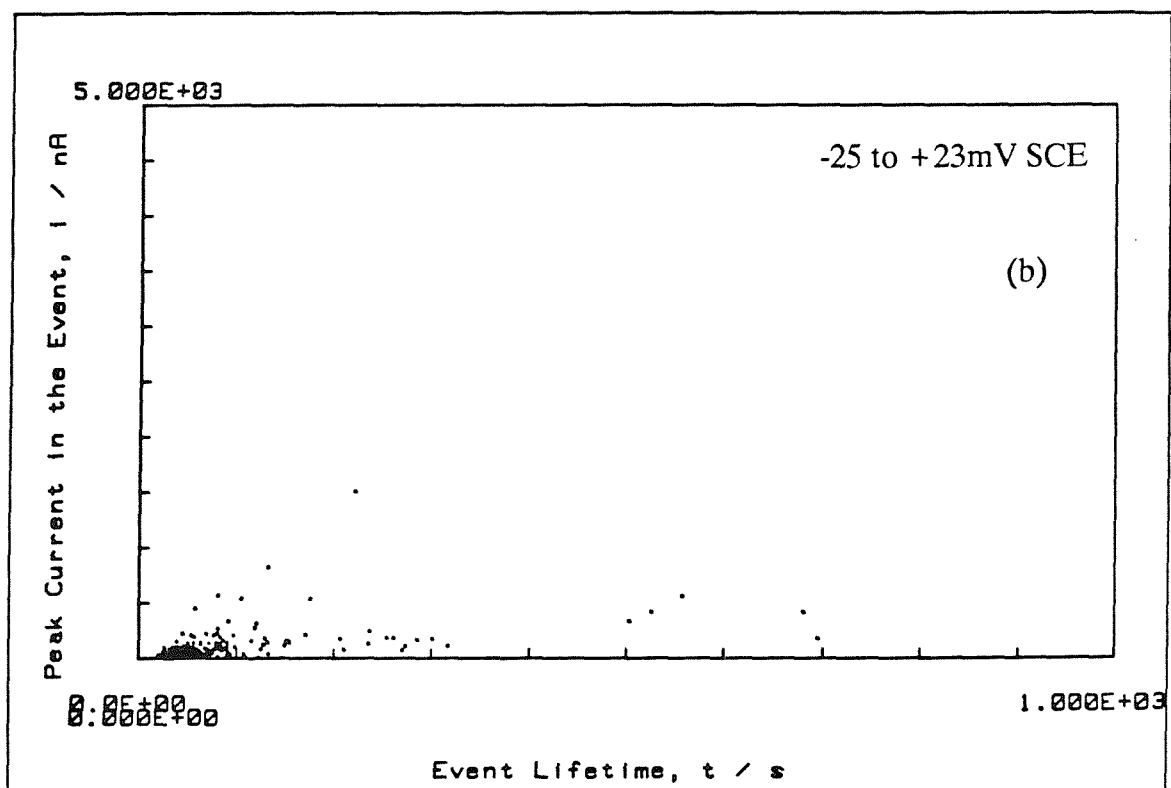
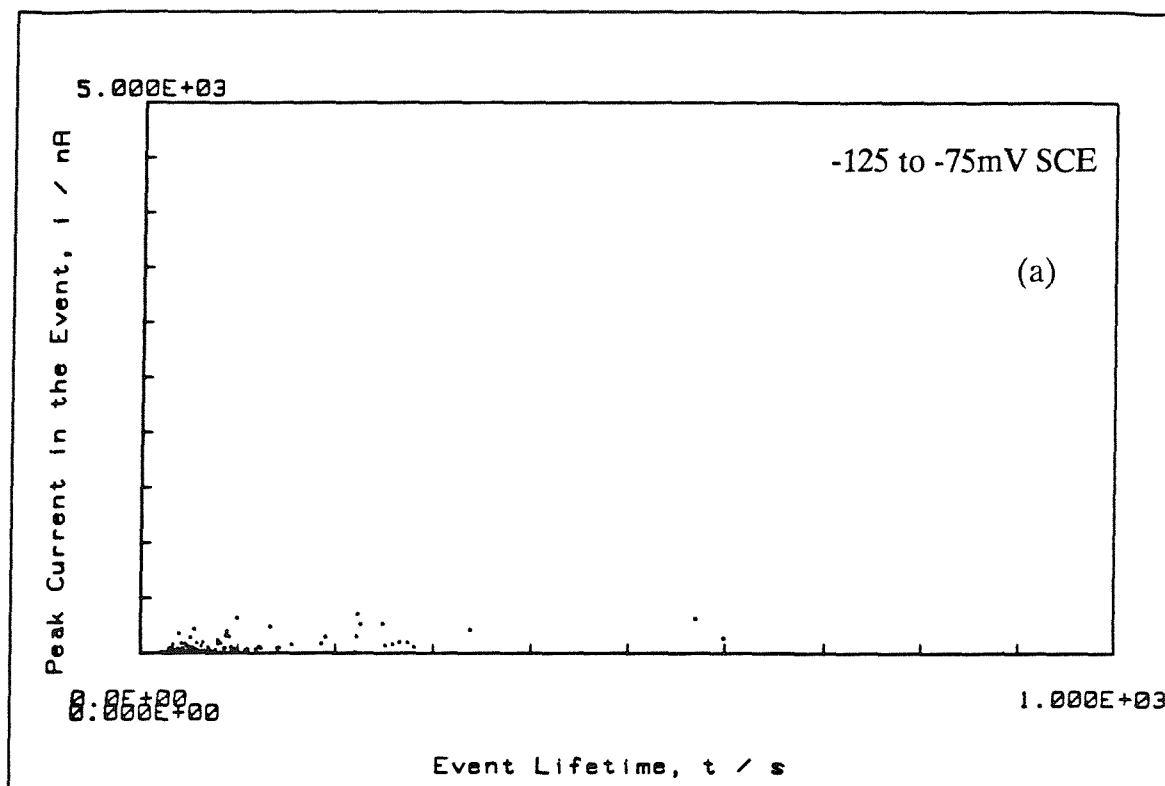


Figure 3.12 Scatter diagrams of transient peak height vs. lifetime.

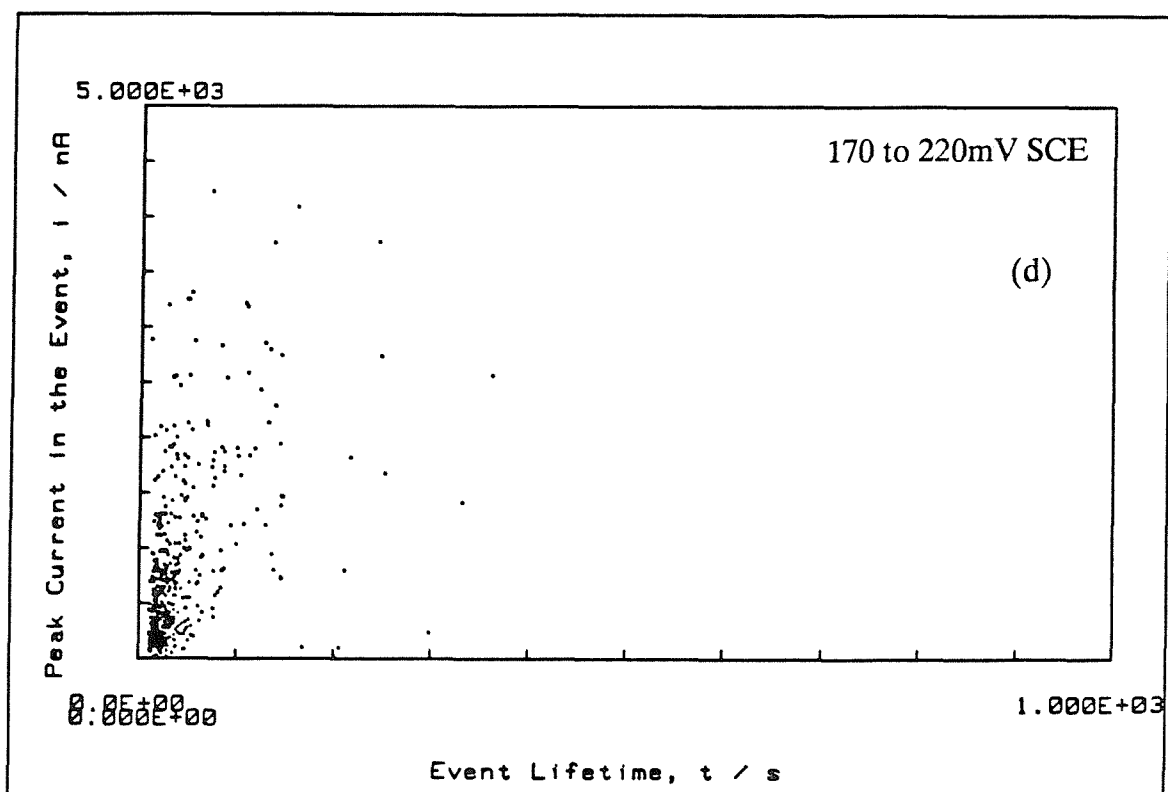
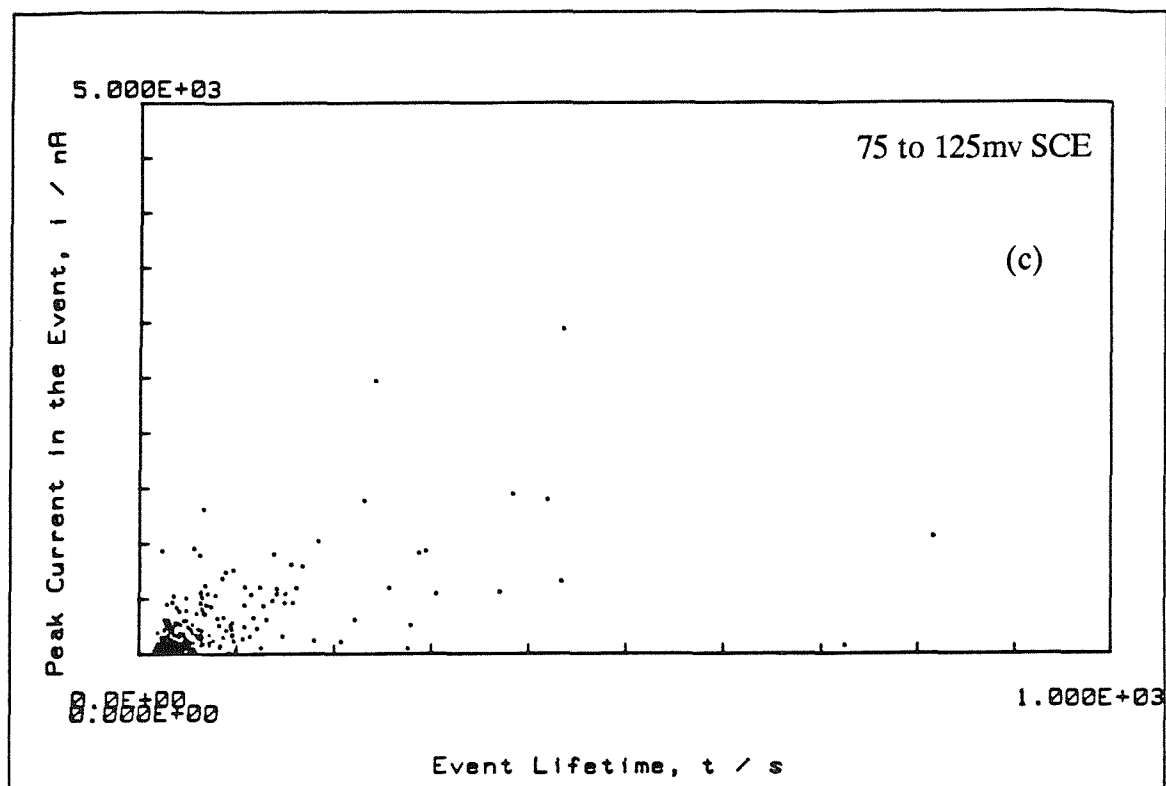
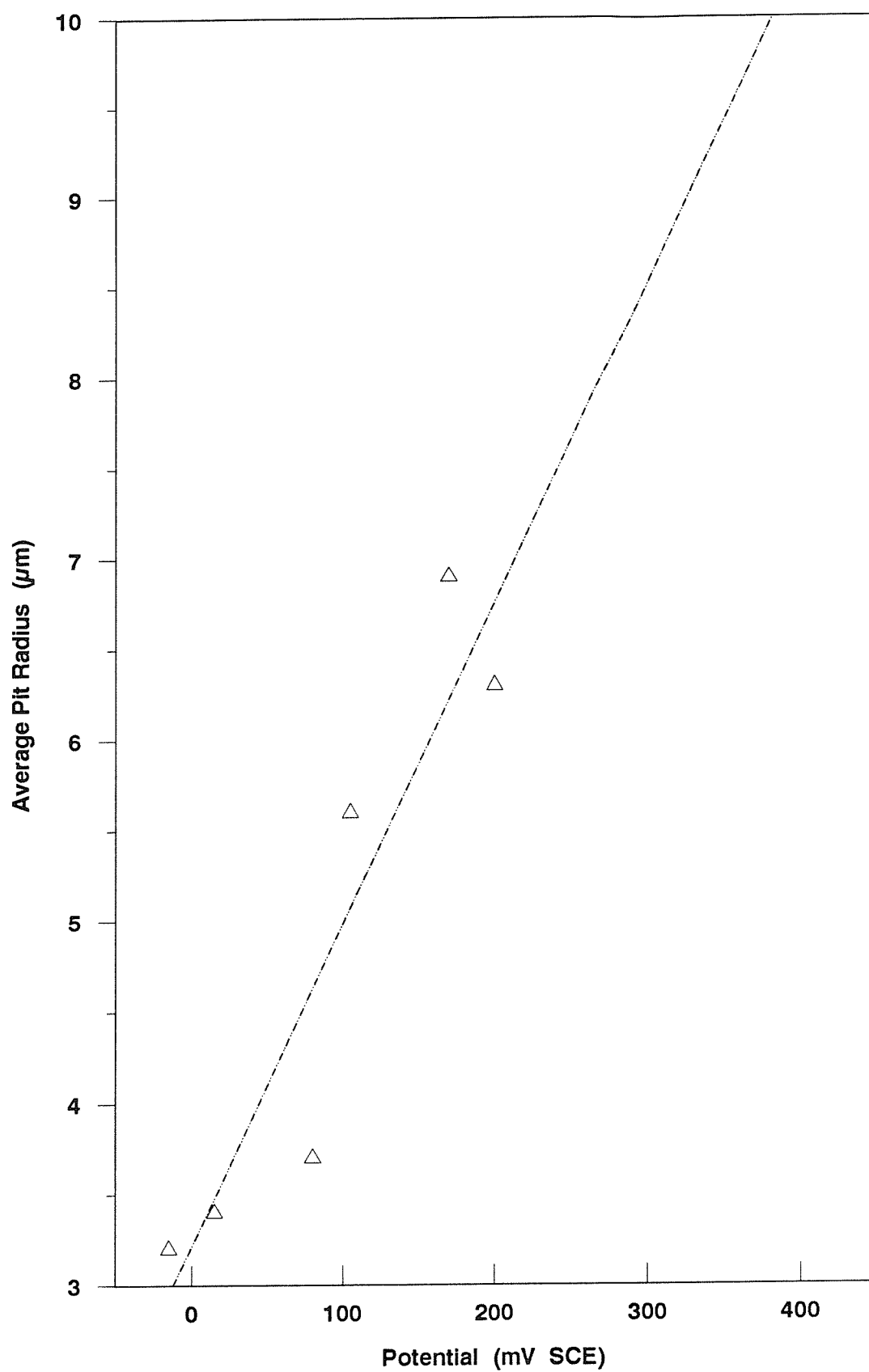


Figure 3.12 (continued)

Figure 3.13 Average Calculated Pit Radius



304L CP

—△—

$$i = \frac{I}{2 \times \pi \sqrt[3]{(Q \times 1.6 \times 10^{-5})^2}} \quad (3.5)$$

Using Equation 3.5, the current density could be calculated at any point on the current transient. In practice, the transients were digitised using 4 points (i.e. 4 current/time pairs, Chapter 2, Section 2.5) and current densities were calculated at the peak current, just before repassivation (not including the current spike, if present) and approximately halfway between the initiation of the event and the peak height. Where transients were superimposed on an existing transient, these were initially considered separately. Figure 3.14 shows, as a function of potential, the distribution of current densities for many transients calculated from the anodic current measured at the two locations. Within a given potential regime a range of current densities was observed. The range of current densities increased with increasing electrode potentials, and the peak in the distribution curves shifted to higher current densities. Figure 3.15 shows the current densities calculated for "superimposed" transients, that is the individual current bursts sometimes evident within a single transient, in the potential regime +170 to +220mV SCE. Taken overall, these transients were characterised by higher current densities than transients initiated from the background current level, although this difference was not great (compare the distributions in Figure 3.14g with Figure 3.15a and 3.14h with 3.15b).

3.3.6 Characteristics of Pit Propagation

3.3.6.1 Current vs Time

The initiation of a propagating pit was marked, as was shown in Figures 3.3e and 3.4, by a sustained current increase until the 10 μ A limit was exceeded. During the early stages of pit propagation, comparison with unstable transients obtained in the same potential regime revealed no obvious differences in the population of propagating pits to set them apart from the unstable pits. This is demonstrated in Figure 3.16, which shows the current/time relationship for the first 250s of propagating pits which nucleated in the potential range 170 to 220mV SCE, and re-plots the scatter diagram of peak current versus lifetime for unstable transients in the same potential range (from Figure 3.12d). Figure 3.17 shows the current densities after 25s and 50s of 20 propagating pits that nucleated in the range 150 to 205mV SCE. Comparison between Figures 3.14g and h with Figure 3.17 indicates that the pits which propagate are not the pits which grow fastest initially. Indeed, there are no apparent features in the

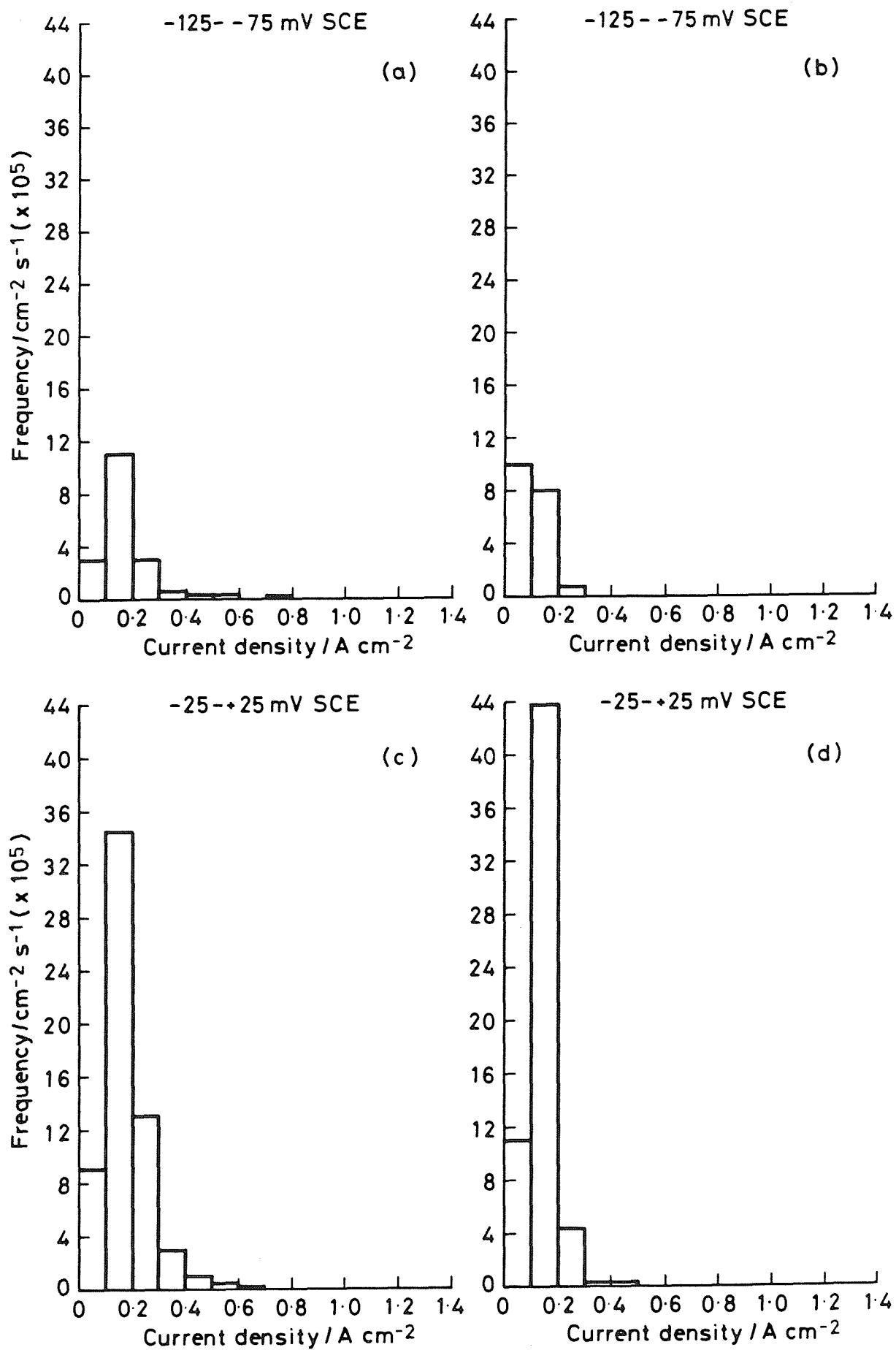


Figure 3.14 Calculated current density distributions for many individual transients (b, d, f, h were calculated at the peak current).

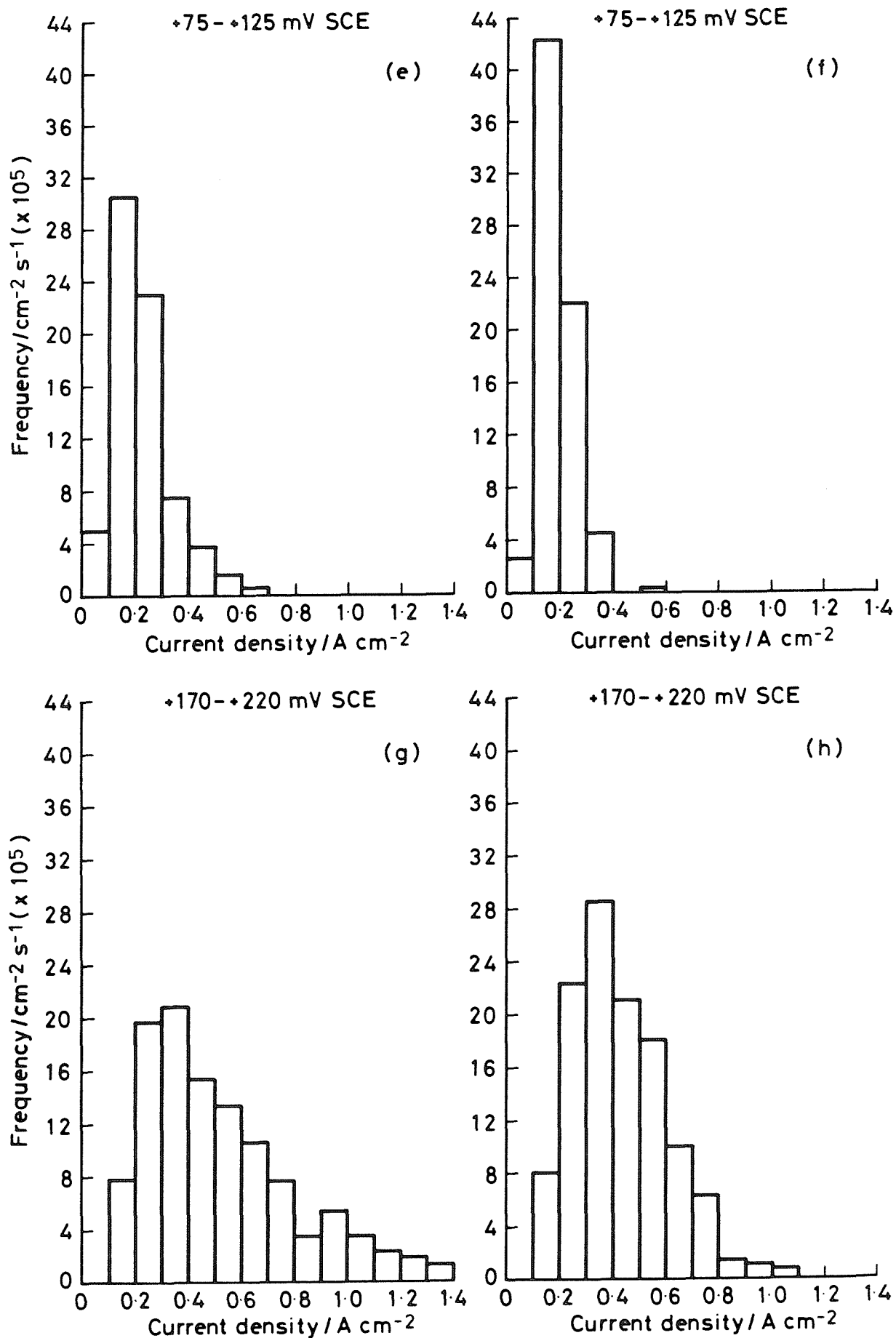


Figure 3.14 (continued)

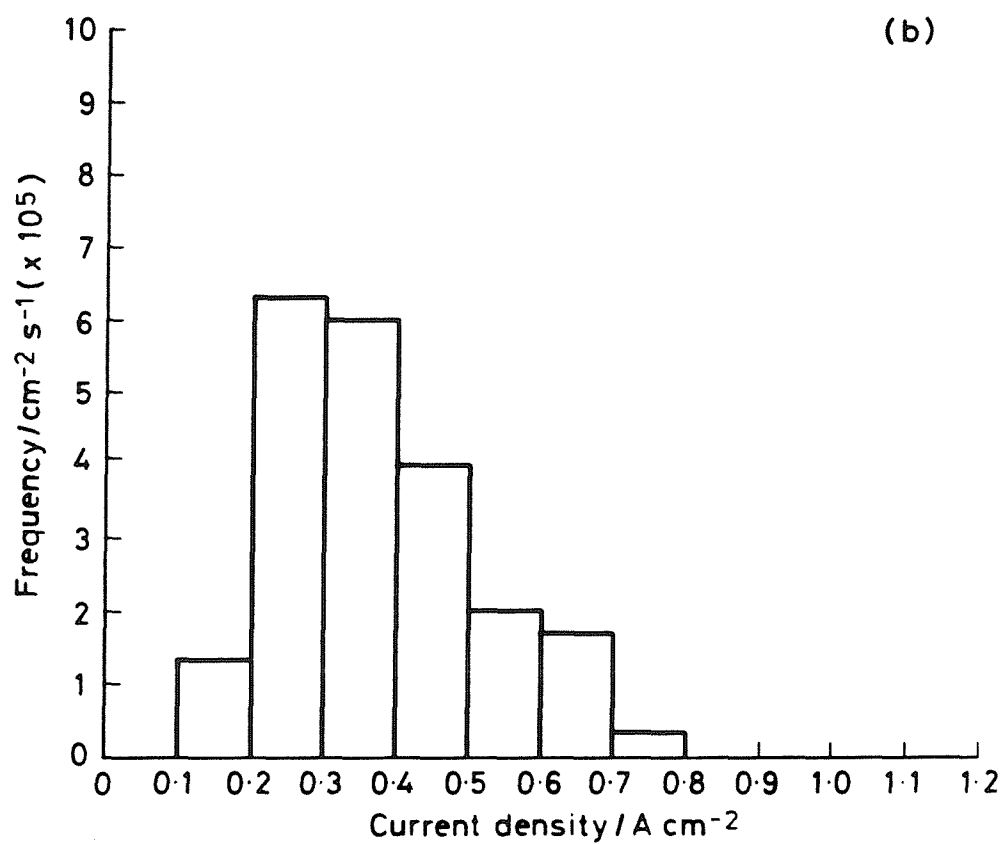
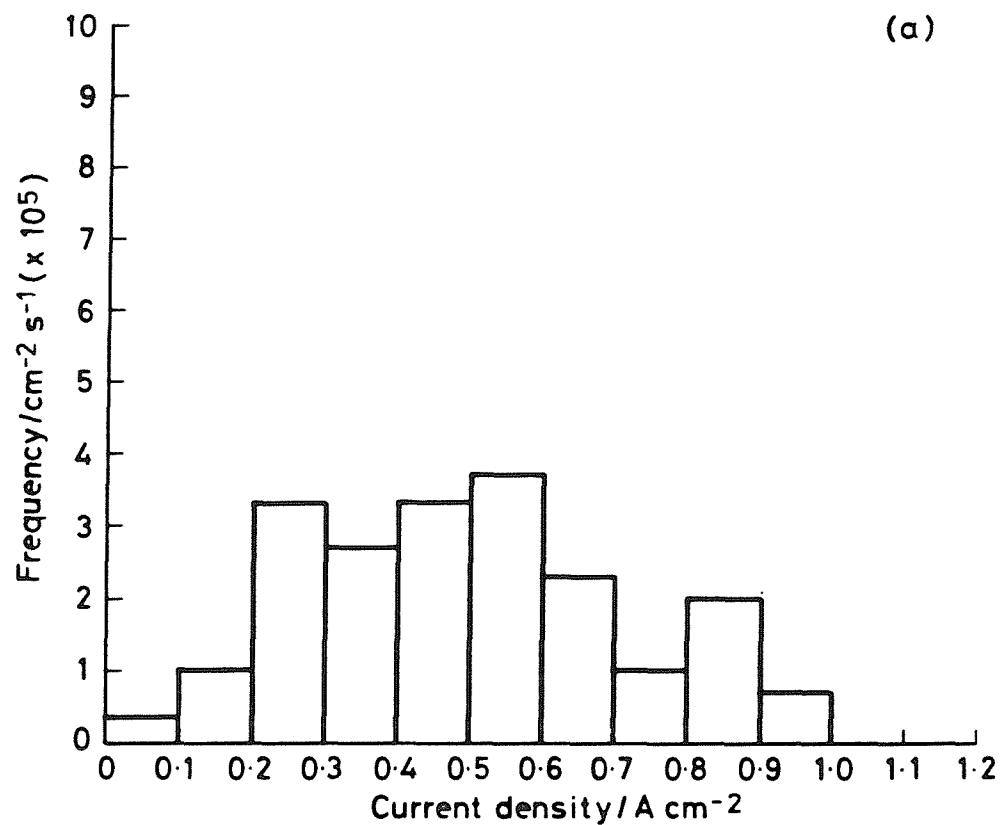


Figure 3.15 Calculated current density distributions for "superimposed" events. (\bar{E} = 170 - 220mV SCE)
(data in plot (b) calculated at peak current)

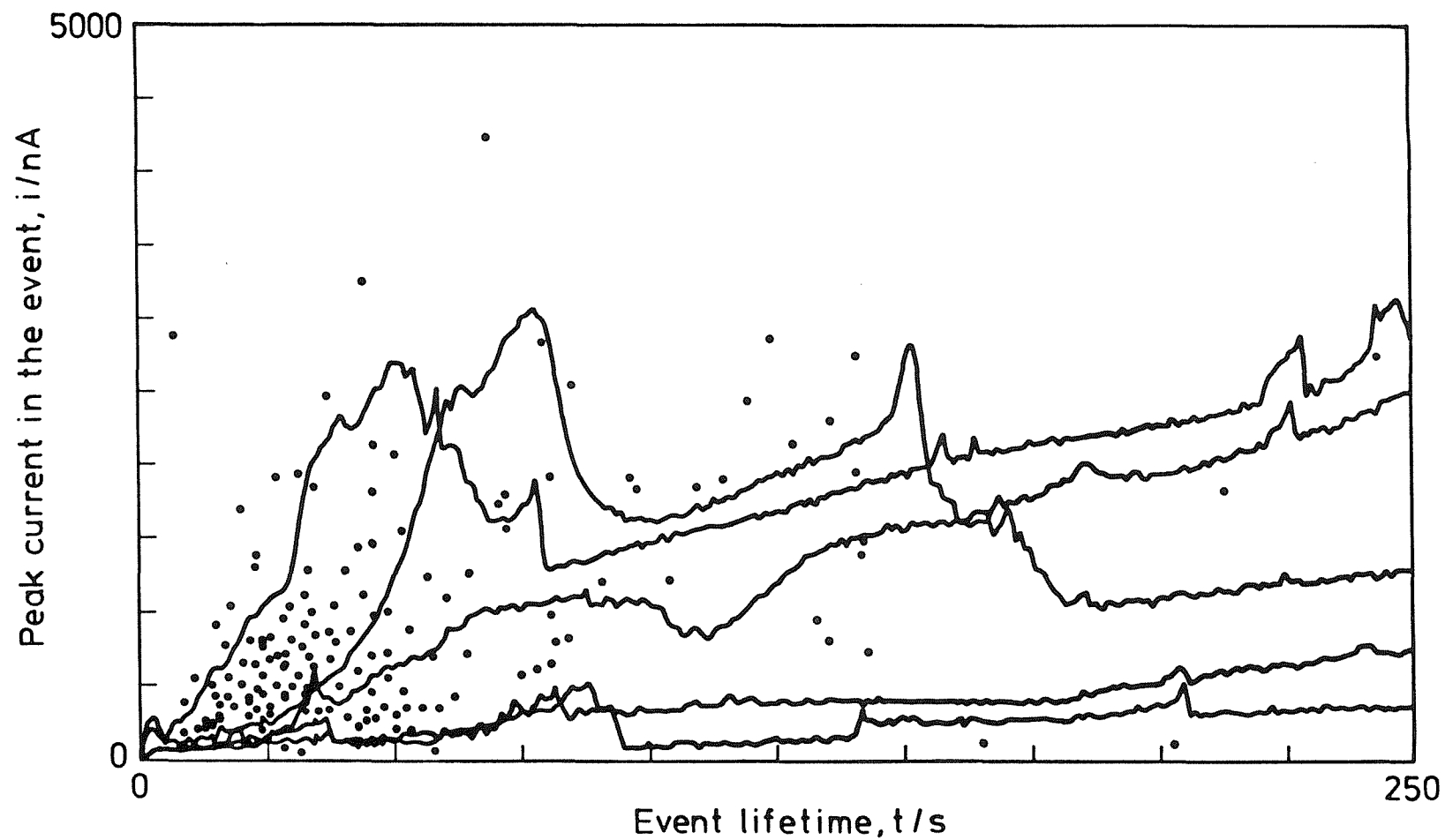


Figure 3.16 Current vs. time relationships during the initial 250s of propagation of 5 representative pits.

Also plotted are peak currents vs. lifetime of unstable pits (replotted from Figure 3.12d). $E = 170$ to 220mV SCE

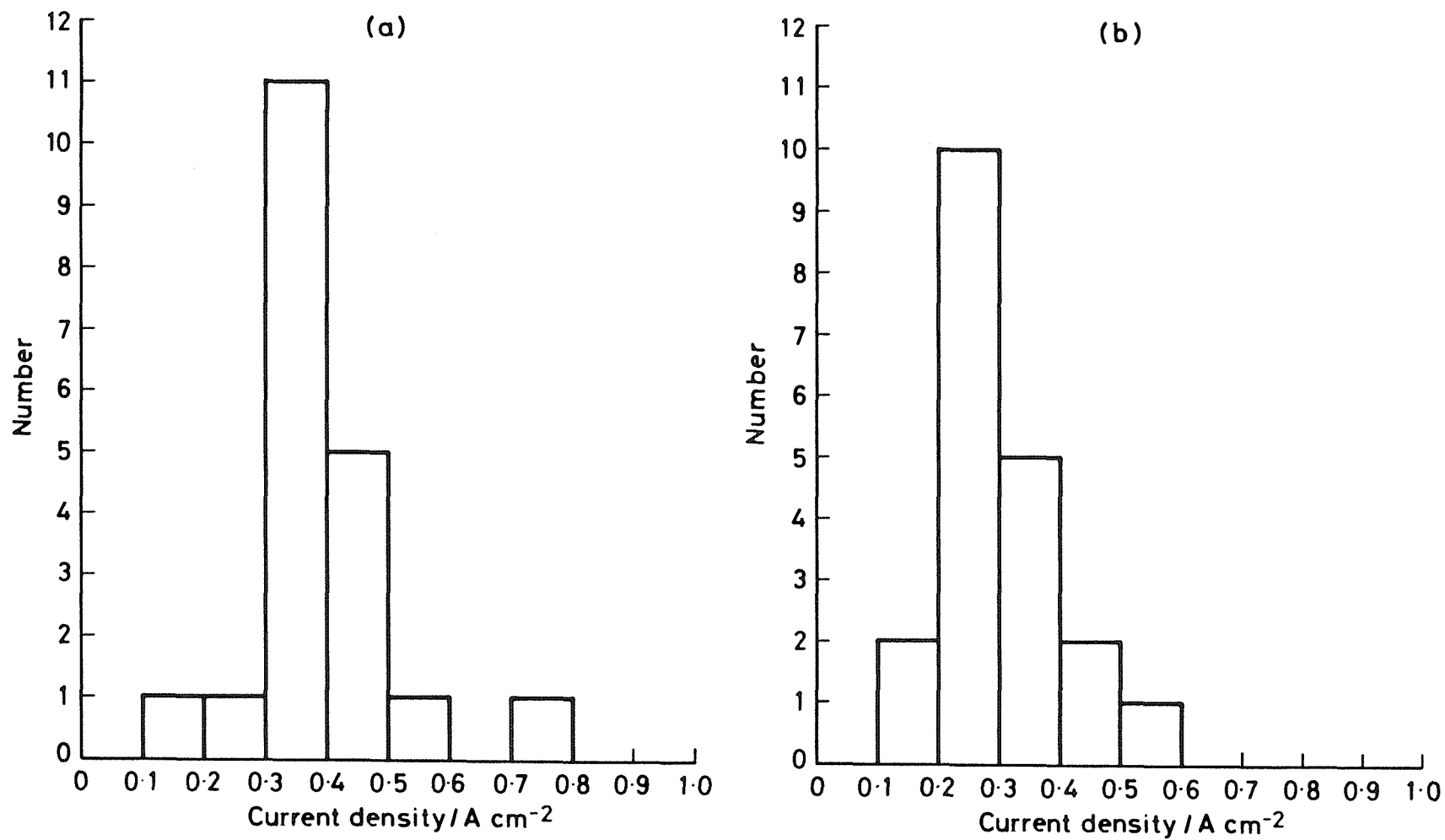


Figure 3.17 Current densities calculated after, (a) 25s and (b) 50s of growth of 20 propagating pits (potential range 150 – 205mV SCE).

current vs. time characteristics which distinguish the early stages of pit propagation from the many unstable pits. The current time records imply that there is no special characteristic distinguishing pits which eventually continue to propagate from those that do not.

The distribution of potentials at which propagating pits reached the $10\mu\text{A}$ current limit varied over about 300mV. Figure 3.18 is a plot of the cumulative frequency distribution of the breakdown potentials recorded for 36 experiments.

3.3.6.2 The Physical Characteristics of Pits

The low current limit imposed on the slow potential ramp experiments generally meant that propagating pits were still quite small when the experiment was stopped. Study of the characteristics of propagating pits was therefore supplemented with the experiments described here. A number of individual experiments were performed in which 304L specimens, ground to grade 1200 grit, were ramped at $8 \times 10^{-5}\text{V/s}$ to +200mV SCE in 10,000ppm chloride (0.28M Cl^-) and allowed to pit for a period of 2 hours. Examination of the specimens in the SEM following the test (and without further treatment) revealed a wide range of pit sizes, from a few μm diameter, and therefore typical of the pits observed in the slow potentiodynamic experiments, to $100\mu\text{m}$ and more. This provided a simple way to look at the characteristics of pits as a function of their size. Most of the larger pits ($20\mu\text{m}$ and above) were covered with what appeared to be metal remnants. These covers were invariably holed, and often contained a series of concentric cracks, Figure 3.19. It appeared that the pits had grown by undercutting the surface. Sometimes the cover was found to have fallen into the pit bottom, Figure 3.20. Pit geometry was usually nearer to a sphere or ellipse than a hemisphere and the undercut metal at the circumference of the pit appeared to provide support for the pit cover, Figure 3.20c.

Examination of the inner surface of the pits often revealed the presence of smaller pits, indicating that pit growth was non-uniform and preferential dissolution had occurred on some regions of the pit surface (Figure 3.21). These "pits within pits" were also often seen to exhibit undercutting and covers (Figure 3.21c).

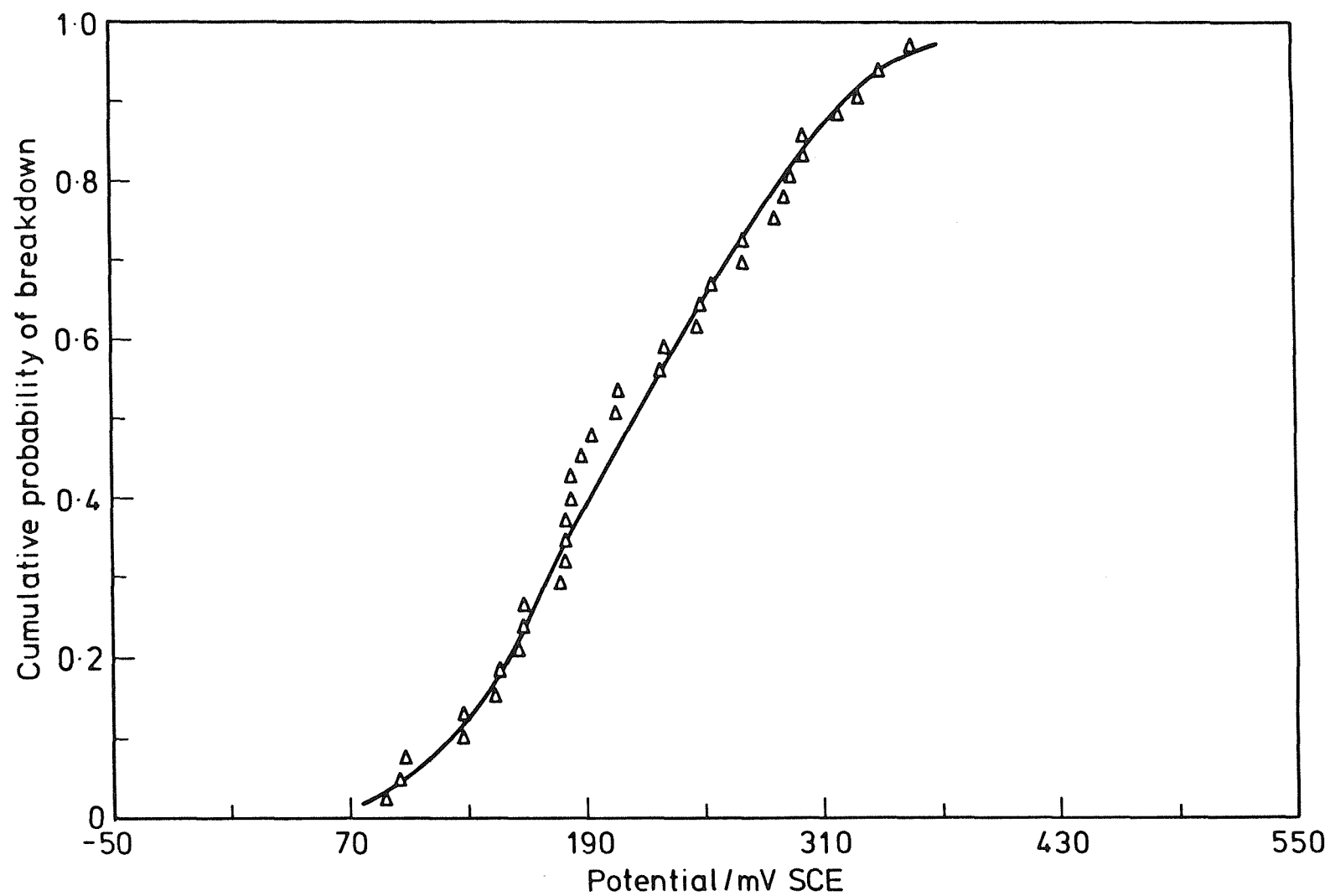


Figure 3.18 Cumulative breakdown distribution for 36 specimens (304L, 1000ppm Chloride, 0.005mV/s)

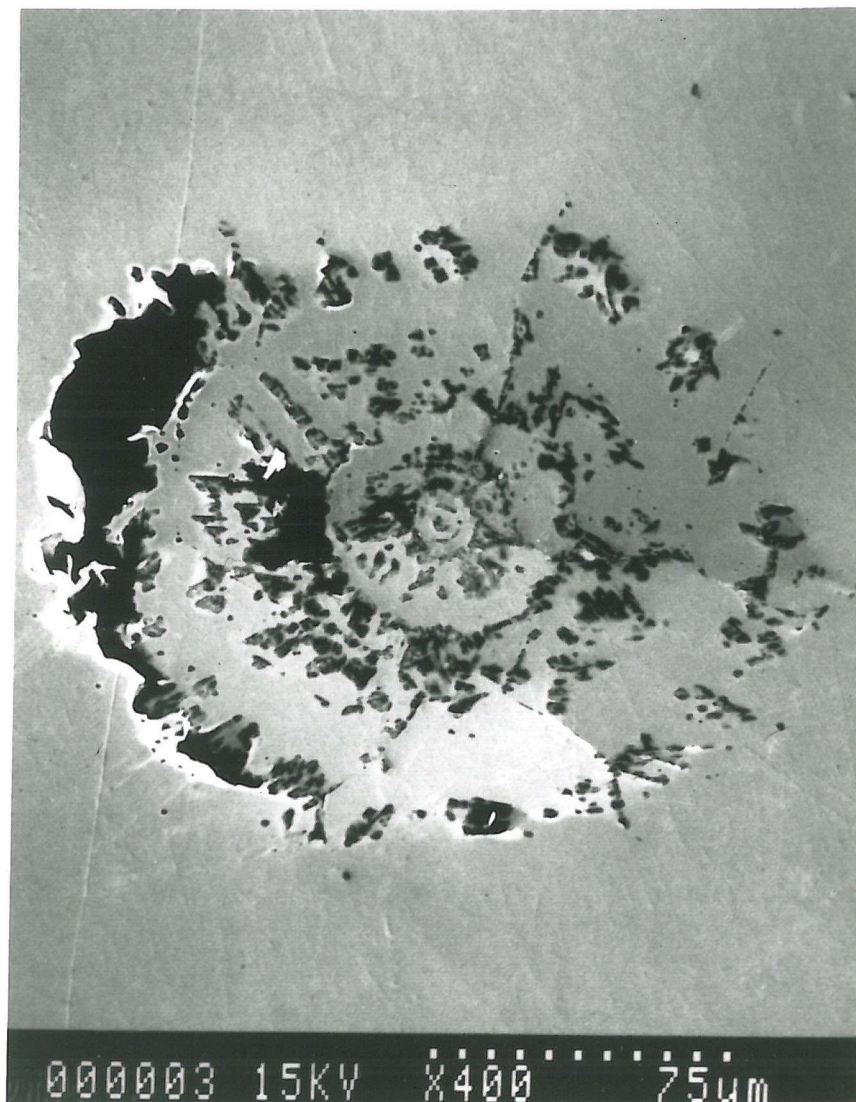


Figure 3.19 Scanning electron micrograph of a covered pit

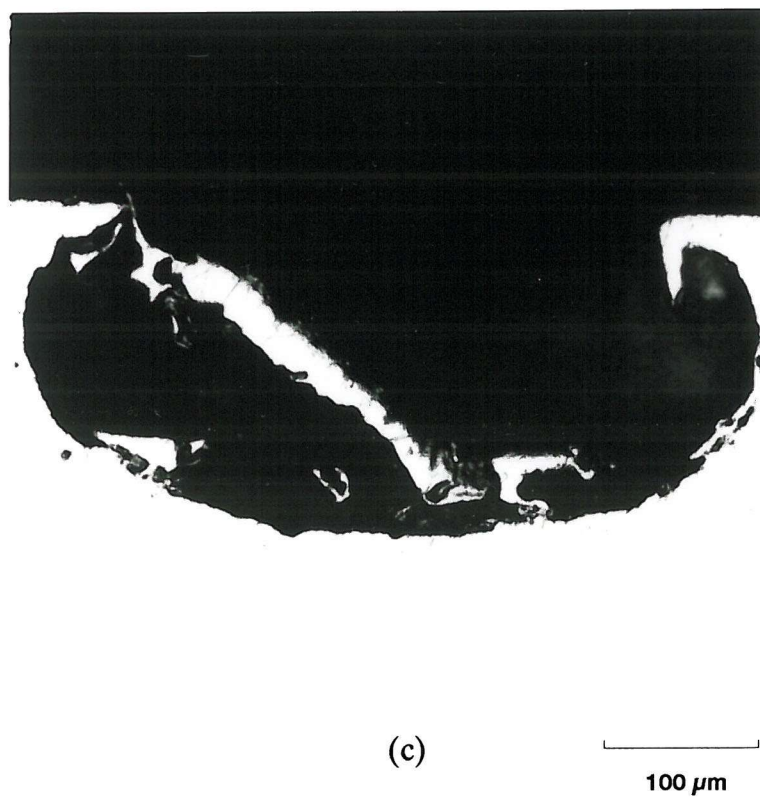
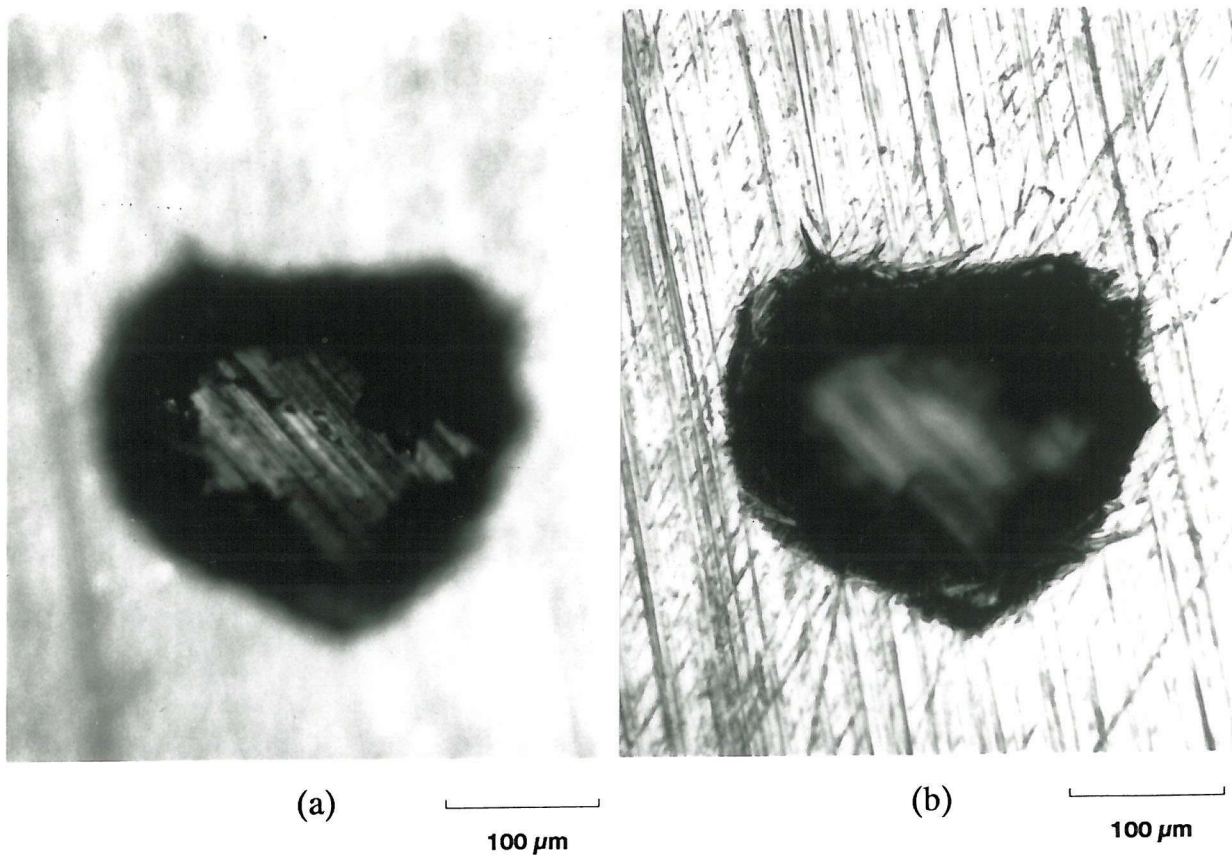
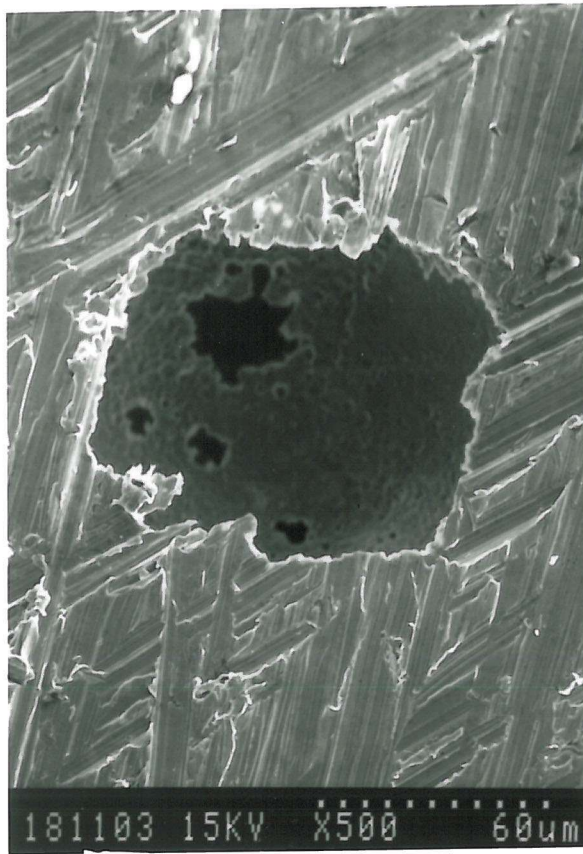
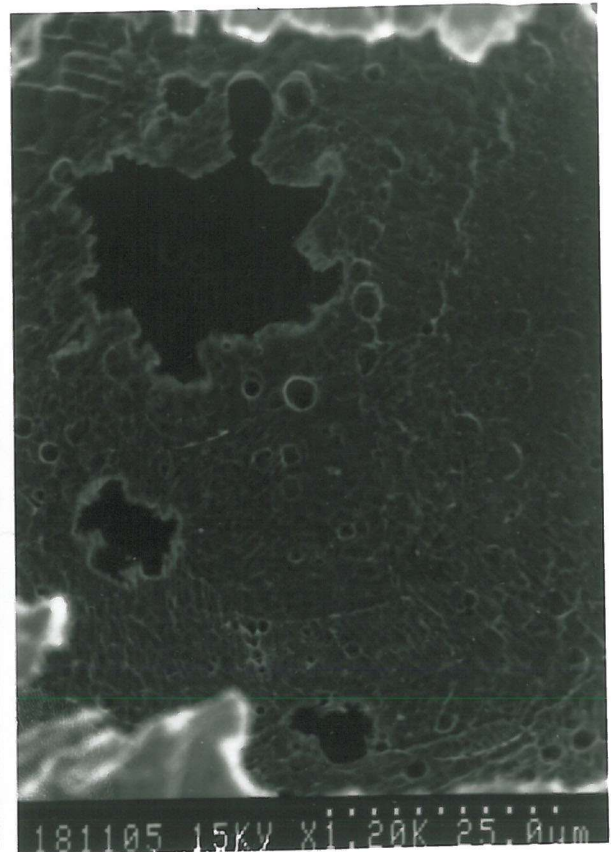


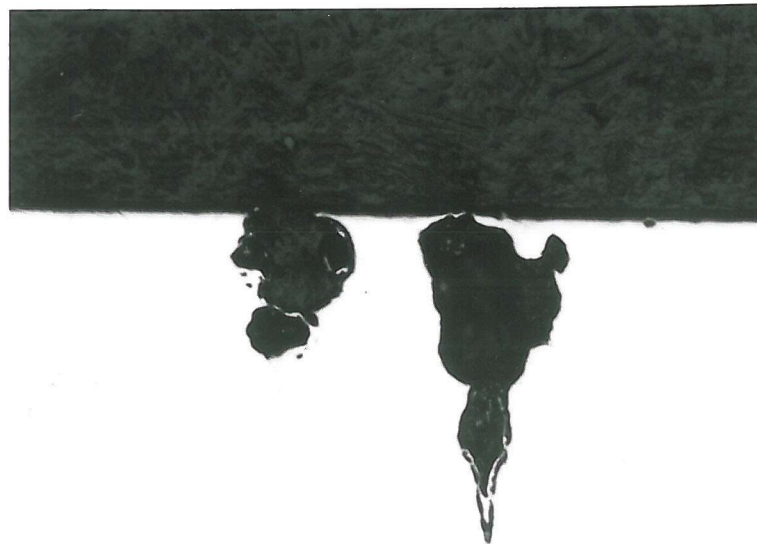
Figure 3.20 Optical micrographs of pits with the cover collapsed into the cavity.



(a)



(b)



(c)

100 μm

Figure 3.21 Scanning electron and optical micrographs illustrating non-uniform dissolution ("pits within pits").

Most of the small pits observed in this work were associated with non-metallic inclusions, particularly those containing sulphur. These pits invariably appeared to open out below the free surface. Figure 3.22a shows such a pit containing a particle, indicated by Energy Dispersive Spectroscopy (EDS) in the SEM to be sulphur-rich. Figure 3.22b shows, at the base of a small pit, a sulphur-rich particle, probably the remainder of the surface inclusion from which the pit initiated. Figure 3.23 shows a small covered pit with cracks in the cover, as had also been observed on larger pits (Figure 3.19). Significantly, EDS analysis of the central region of the pit cover produced strong sulphur and chlorine peaks, which were absent away from the pit. Occasionally, oxide particles were found within the pits, as illustrated in Figure 3.24. EDS analysis of this inclusion produced a strong peaks for silicon and aluminium: Figure 3.25 gives the EDAX spectra for the particles in Figures 3.22a and 3.24.

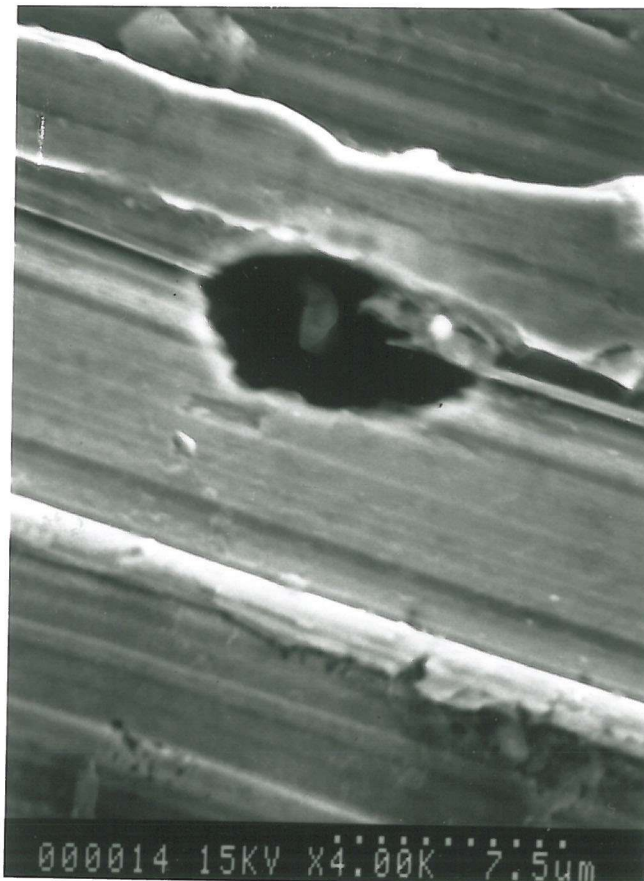
3.4 DISCUSSION

3.4.1 General

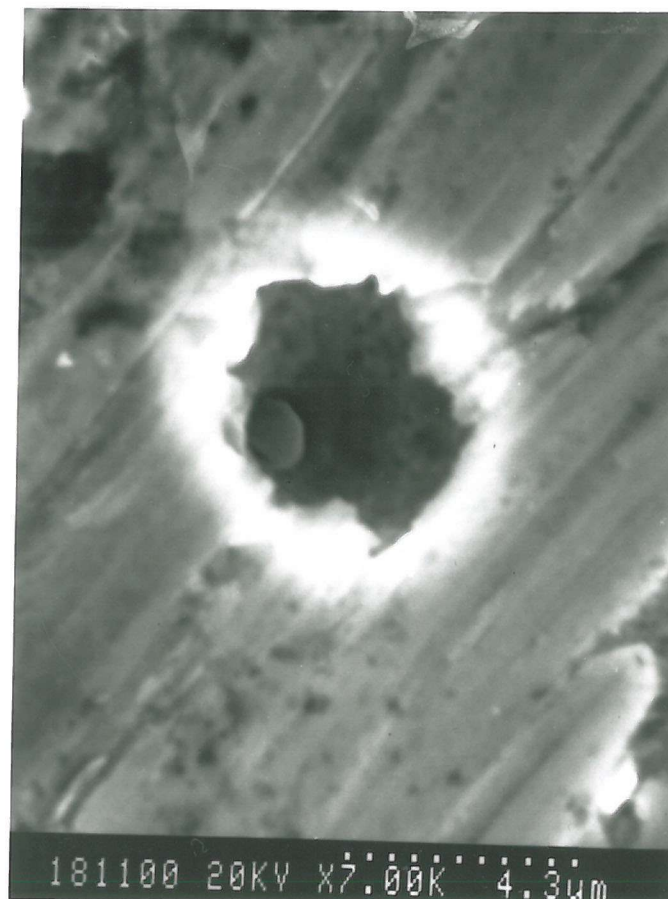
The experimental techniques developed and employed in this work have proven to be very sensitive, enabling a number of significant observations to be made. For example, anodic current transients with a peak current of a few tens of nA, superimposed on background current densities of a few nA/cm² were observed at very low electrode potentials. Secondly, a direct correspondence was established between current transients and pits, demonstrating that pits can be nucleated at potentials lower than -150mV SCE. In this work all of these pits repassivated. However, probabilistic theories of pitting would contend that there exists some non-zero probability of pitting at these potentials. For example, in the Harwell model^(4,5) a proportional relationship was proposed for the nucleation rate of unstable pits (λ), and the nucleation rate of stable pits (Λ), (see Chapter 1):

$$\Lambda = \lambda a \exp(-\mu \tau_c) \quad (3.6)$$

A basic assumption in the above model is that whilst nucleation of pits is a stochastic process, subsequent growth is then deterministic such that the more pits that are nucleated, the higher the probability that one will propagate. There is some evidence in the results presented here to support such models: the nucleation rate of unstable and stable pits both increase with potential, and the current vs. time records associated with the early stages of pit propagation were not obviously different from unstable pits



(a)



(b)

Figure 3.22 Scanning electron micrographs of micropits containing sulphur-rich particles

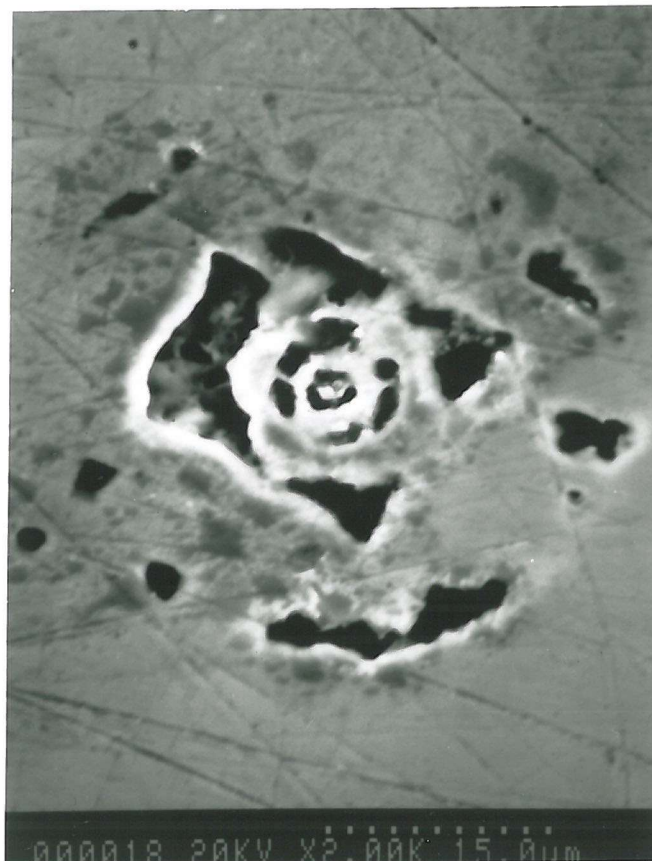


Figure 3.23 Scanning electron micrograph of a covered micropit. (compare with figure 3.19).

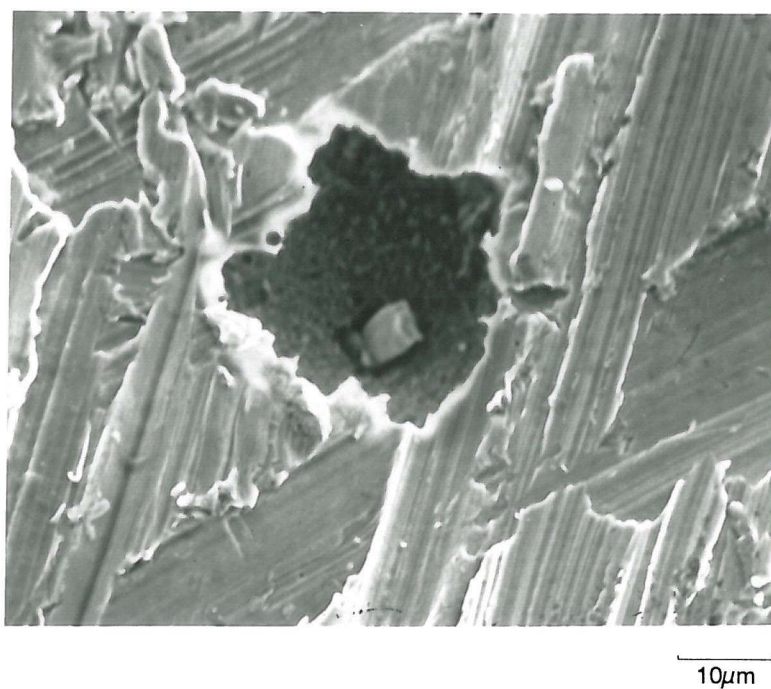


Figure 3.24 Scanning electron micrograph of micropit containing an oxide particle.

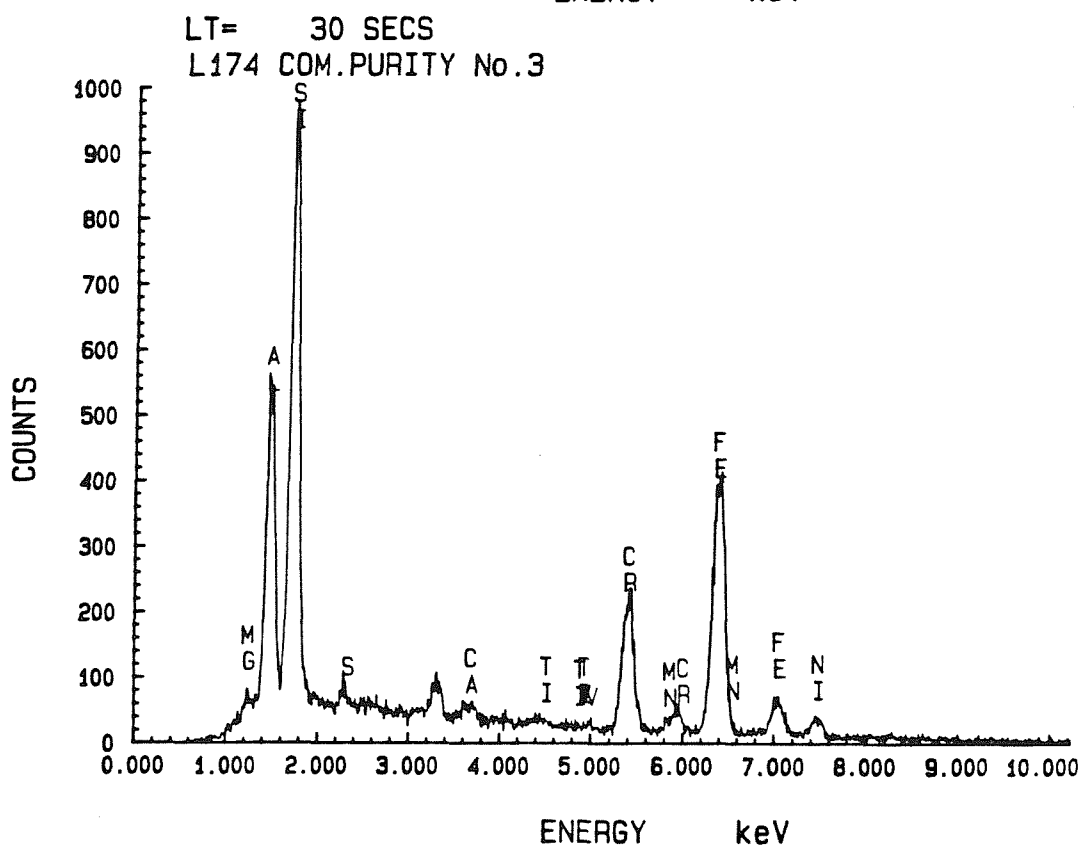
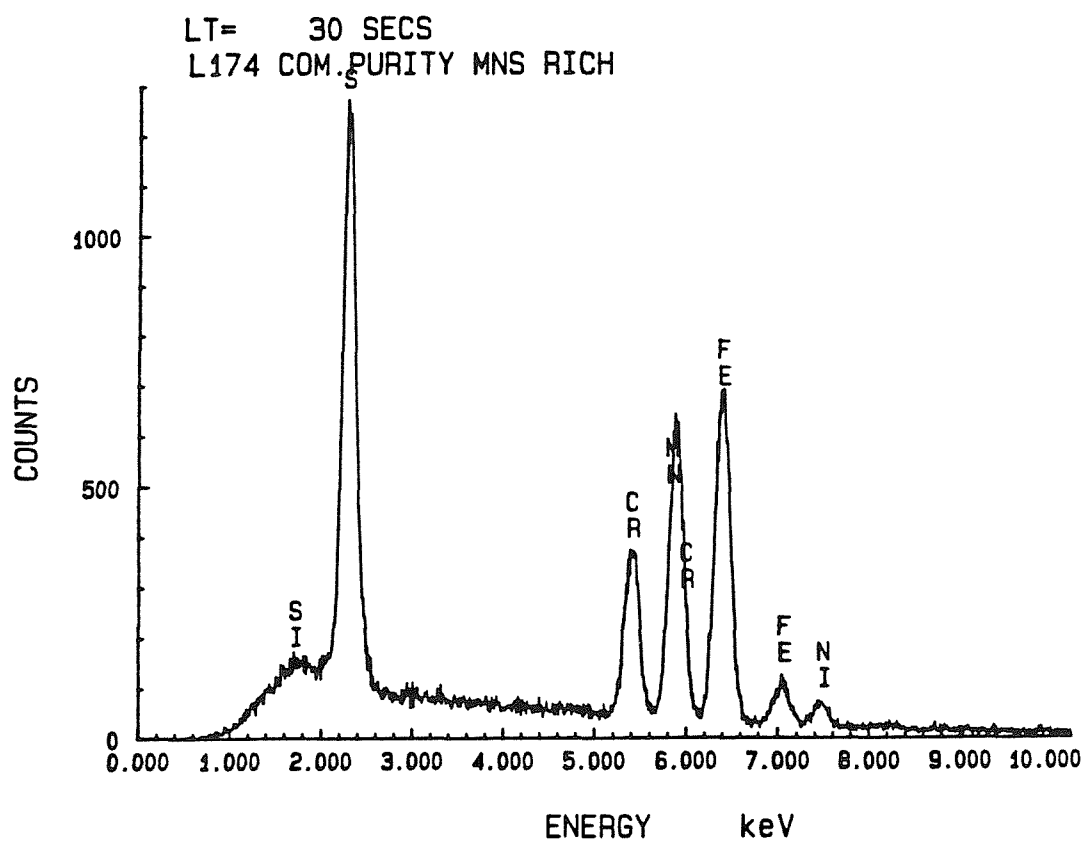


Figure 3.25 EDAX spectra for the particles in Figures 3.22(a) and 3.24.

in the same potential regime (Figure 3.16). It is noted that the reported "repassivation" potential for type 304L stainless steel in 10^{-1} to 10^{-2} M chloride solutions, determined by cyclic polarisation^(6,7) is about +50mV SCE. The results reported here therefore question the reliability of the "repassivation potential" for delineating safe and dangerous conditions in technological applications. The results also imply that a measure of the nucleation frequency of unstable pits (Λ) would provide a rapid assessment method for the probability of nucleating a stable pit. In an extension of this work, the relationship between Λ and λ was examined, and found to be rather constant as a function of potential⁽²⁾.

The Harwell stochastic approach^(4,5), and other statistical models such as the pit generation model of Baroux⁽⁸⁾ provide a general quantitative framework within which to describe the statistics of the pit initiation process. However, the assumption that pit initiation is a stochastic process requires further examination, since there are potential influences on the initiation process which should be amenable to analysis. In the remainder of this work, one intention is to identify and describe stochastic elements which influence the early stages of pitting.

3.4.2 Anodic Film Growth and Passive Current Density

The behaviour of the passive current as a function of potential and potential sweep rate, shown in Figure 3.9, is that expected for thickening of an oxide film by high field ion migration. The empirical high field growth law is:

$$i = A \cdot \exp(B\bar{E}) \quad (3.7)$$

where:

$$\bar{E} = \frac{zF}{V_m} \cdot \frac{\dot{V}}{i} \quad (3.8)$$

\bar{E} = electric field

\dot{V} = potential sweep rate

A, B are parameters of the high field growth law

In potential sweep experiments when a film of a given thickness exists prior to the experiment, the expected form is that, as the potential increases, the current will increase with increasing field in the film, until a plateau is obtained where the rate of increase of thickness balances the increase of potential:

$$\log i_{\text{plat}} = \log A + \frac{B}{2.3} \cdot \frac{zF}{V_m} \cdot \frac{\dot{v}}{i_{\text{plat}}} \quad (3.9)$$

This implies a linear plot of $\log i_{\text{plat}}$ against $\frac{\dot{v}}{i_{\text{plat}}}$, which is indeed the case, Figure 3.26. Ideally, and in the simplest model, the measurement of the background current would comprise entirely the film dissolution current at the film/solution interface (the corrosion rate of the passive metal), which under steady state conditions is equal in magnitude to the flux of ions through the passive film. Figure 3.26 shows that $B \approx 2 \times 10^{-6} \text{cm/V}$, implying fields in the oxide layer of about 10^6V/cm , which is consistent with the assumption of high field growth. Extrapolation gives the "exchange current", for the film growth process ($\log A$), of about 10^{-18}A/cm^2 : an extraordinarily low value. Although the errors involved in the extrapolation are obviously large, the conclusion that the exchange current is exceedingly small is probably sustainable. Given that the exchange current for film growth is exceedingly small, it would seem that a simple model of uniform dissolution is unlikely to apply, and that a steady state is never achieved, even under conditions of natural immersion. By minimising the perturbation to the oxide film (away from its steady state), the outcome of the experiment is less influenced by the experimental technique. That is, the slow potential ramp experiments used in this work more closely resemble real corrosion situations. This is an important point; it reinforces the decision to adopt a slow potential ramp approach to investigate the mechanisms involved in the initiation of pitting corrosion.

3.4.3 Potential Dependence of Transients

The scatter diagrams of transient peak height versus lifetime (Figure 3.12) and the plots showing the distribution of current density as a function of potential (Figure 3.14) illustrate a trend toward larger transients (and pits, Figure 3.13) with increasing anodic polarisation. This trend can be understood by consideration of the increased driving force for the corrosion reaction as the specimen is polarised further away from its equilibrium potential. When the potential ramp was commenced, the background current levels were very low, and no current transients were seen (Figure 3.3a). The current at this point was made up of the corrosion rate in the passive state (a "leakage" current due to slow dissolution of the alloy, comprising a number of small anodic sites on an otherwise passive surface) and film growth due to the application of the anodic potential. There is also a small contribution from the electrical double layer charging

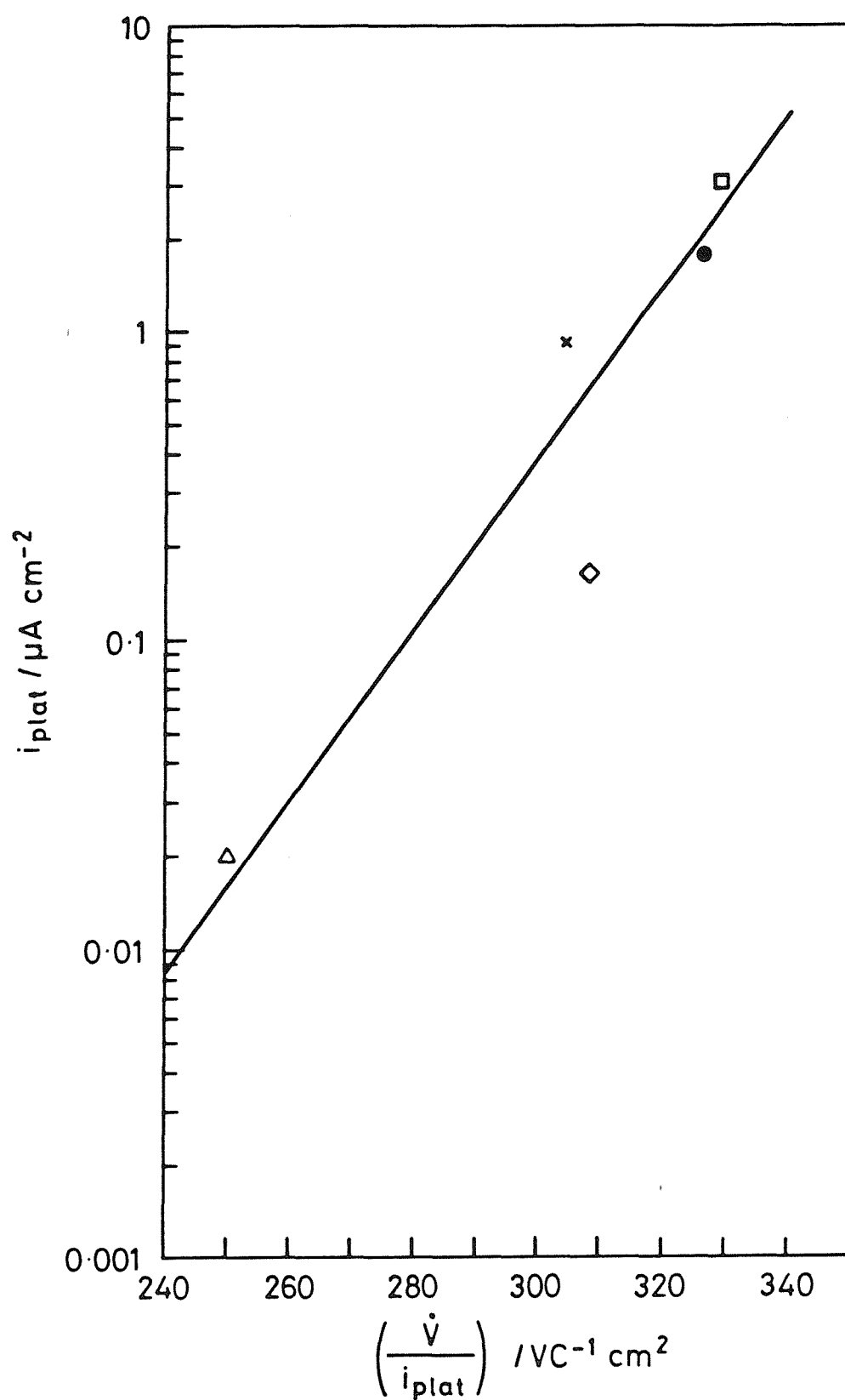


Figure 3.26 Plateau current as a function of sweep rate to test exponential growth law (using data from figure 3.9).

current, although with a ramp rate of $5 \times 10^{-6} \text{V/s}$, this is negligible (about 0.1nA/cm^2 assuming a double layer capacitance of $20 \mu\text{F/cm}^2$). At some point during the potential ramp, and still at low electrode potentials, the first current transient was observed. This, and subsequent transients was due to the localised breach of the passive film providing a low resistance path (much lower than the intact passive film) through which the current associated with metal dissolution could pass. The dissolution at this site was such that the corrosion current could be seen above the background current. It has been shown here that the propagation of these unstable micropits proceeds in an identical fashion to that of the macropits: the observations are consistent with the local acidification mechanism for pit propagation (described in Chapter 1, Section 1.2.1). At some time during the growth of this (still very small) pit, the current falls abruptly, marking the end of the localised corrosion. As the experiment continued, the number of transients and the magnitude of the associated currents increased (Figure 3.3) until at some point a stable propagating pit was initiated (Figure 3.3e). That the transients became more significant at higher potentials can be explained by the increasing driving force for the corrosion reaction as the specimen was polarised to more anodic values. Thus the intensity of the metal dissolution, and that of the localised corrosion cell, increased. This is illustrated by the shift to higher average current densities with increasing potential (Figure 3.14). Whilst the transients appear to become more frequent at higher potentials (Figure 3.7), it should be noted that this curve is to some extent determined by the level at which the measurement is made. For example, at potentials near to open circuit where the driving force for dissolution is relatively low, it is possible that transients (if they were to occur) would not be seen above the general background current. At higher potentials, where transients were observed, the difficulty in resolving detail in the background current persists. A possible way to obtain an improved resolution of the background current would be to use still slower potential ramps, although this would be impractical for most purposes. The major limitation is however the capacitive filtering effect of the specimen area, and in order to overcome this, very small specimen areas are required. The use of microelectrodes has found application in pitting studies⁽⁹⁾, and appears to offer potential for future work. It must be recognised, however, that there are practical problems in defining material state or ensuring an absence of crevices when using a $10 \mu\text{m}$ diameter wire!

3.4.4 Discussion of Pit Initiation and Propagation

The following discussion is framed by the three basic questions which are at the heart of the pit initiation process:

1. Why and where do pits initiate?
2. Why do most pits repassivate?
3. Why do some pits propagate?

3.4.4.1 Initiation

Several different mechanisms have been reported for the initiation of pitting corrosion of stainless steels⁽¹⁰⁾ (see Chapter 3): attack at weak spots of the passive film, the formation of a chloride cluster of a critical size⁽¹¹⁾, incorporation of chloride into the film⁽¹²⁾, local thinning of the film⁽¹³⁾, cracking and healing of the film^(13,14) and coalescence of point defects in the film⁽¹⁵⁾. The difficulty, however, with theoretical models which focus simply on properties of the passive film, is to explain not the instability but the stability of the system: most of the surface does not react and the pit initiation frequency is rather low.

3.4.4.1.1 Effect of Potential Sweep Rate on Pit Nucleation Frequency and Feedback Model for Initiation

A clear effect of potential sweep rate on micropit nucleation frequency has been demonstrated, Figure 3.8, which was also observed by Keddam and co-workers⁽¹⁾. They established that the pre-pitting activity at any potential in the course of a potential sweep experiment depends on a property that is not completely characterised by the charge stored in the passive film, which they found to be independent of the initial sweep rate. They went on to suggest that the properties of the (non-steady state) passive film are tightly related to the degree of disorder maintained in the film by the flux of ionic species involved in the growth process. That is, the film structure requires time to stabilise at a given potential, which involves the incorporation of charges, increase of the film density and a decay in the defects concentration. Thus, during potential ramp experiments, they postulated that the film is formed of a low density, loose material.

Here, attention is focussed on a general class of "feedback" models, which incorporate ideas implicit in some of the theories mentioned above, and which provide an alternative explanation to the hypothesis of Keddam and co-workers. The passive current, i_p , at any point on the surface is a function of the local surface concentration of Cl^- , H^+ and other "special species", denoted X. It is also directly related both to the local gradients of these species and to the time derivatives of the local surface concentrations. Similarly, the local potential, potential gradient and current are linked:

$$i_p = f(E, [\text{H}^+]_s, [\text{Cl}^-]_s, [\text{X}]_s \dots)$$

$$\frac{\partial [\text{H}^+]_s}{\partial t}, \frac{\partial [\text{Cl}^-]_s}{\partial t}, \frac{\partial [\text{X}]_s}{\partial t} \dots = f(i_p)$$

These relationships constitute a system of equations which, if the local current density fluctuates above some value, becomes unstable, leading to a large increase in the local current density, i.e. pitting. Once pitting starts, the local current is more than adequate to maintain large gradients of potential, chloride and pH, and it is the coupling between these gradients and the current which keep the corrosion localised. However, typical passive current densities ($\approx 10\text{nA}/\text{cm}^2$) are far too small to generate any local gradient of chloride, potential or pH: hence the introduction of "special species" of low diffusivity (such as point defects) or rare occurrence (such as critical clusters). Alternatively, the local current density might be far from uniform over the whole surface and in regions of very restricted access, such as underneath deposits or at the base of machining marks, sufficient gradients of Cl^- and H^+ might conceivably develop. This general class of theories implies that the "driving force" for pit initiation is the passive current density. Qualitative support for these ideas is provided by the data presented in Figures 3.8 and 3.9, where the higher current densities achieved with a faster ramp rate ($0.05\text{mV}/\text{s}$) resulted in an appreciably higher pit nucleation frequency when compared with experiments conducted at $0.005\text{mV}/\text{s}$.

3.4.4.1.2 Alloy Microstructural Effects

It will be shown, in Chapters 5 and 6, that important "special species" in the initiation of pitting on stainless steel are sulphur-rich inclusions. The effects of alloy microstructure are notably absent from most theories of pit initiation, such as those mentioned at the start of this section. Specifically, the effect of impurities and

microstructural features have at best featured peripherally in these models. This is surprising on two accounts. Firstly, there is abundant evidence linking pit initiation with microstructural features, particularly with non-metallic inclusions⁽¹⁶⁾. Secondly, it is to be expected that the passive film over microstructural features will have different (usually less protective) corrosion properties from the film covering matrix austenite (in stainless steels). Indeed, in the vicinity of inclusions which intersect the free surface, it is possible that no chromium rich protective film can form⁽¹⁷⁾. Since these "defects" - which might be inclusions, grain boundaries etc. - exist in all technologically relevant materials, the role of alloy microstructure in pit initiation should not be underestimated when constructing useful mechanistic descriptions of pitting corrosion, which by definition should suggest schemes to improve pitting resistance. The observations reported earlier in this chapter support this view: many small pits were associated with non-metallic inclusions containing sulphur. As far as the "feedback" models are concerned, the effect of the microstructural defects is to induce a local variability (which may be large) in the passive current density and in its dependence locally on potential, chloride concentration, pH, etc.. This local variability may then induce instability.

3.4.4.2 Repassivation

3.4.4.2.1 Hypotheses on Repassivation Based on Potential Gradients and Changes in Resistance to Current Flow

During the discussion of the slow potential ramp experiments (above) a stage was reached where the local acidification had led to the pit becoming self-sustaining. Why then should this localised corrosion stop? As evidenced by the large number of transients, most did. One hypothesis can be given in terms of a change to solution conditions in which the pit cannot be sustained. The dissolution process of a pit, stable and unstable, occurs at significant rates, and must be due to active dissolution. In order for a passive surface to co-exist with an active pit, then a potential gradient of up to several hundred millivolts may have to be maintained between the two areas (as shown by the polarisation curve, Figure 1.1 for example). This potential difference is equal to the product of current flow (carried in solution by anions and cations) and the solution resistance (from Ohm's Law). Thus it may be envisaged that, in high resistivity environments, potential gradients may be established over short distances, such as that between the pit base and the free surface. However, should the solution

resistance decrease, then the potential gradient may only be maintained at larger distances. Should these significantly exceed the pit dimensions, they are unlikely to be maintained. The potential difference for a given distance will decrease and so the potential at the pit bottom might move in a more anodic direction, leading to repassivation.

Environmental conditions, in particular solution convection, might be expected to influence pit growth. The application of solution flow to a growing pit would have the effect of removing the local concentration gradient established at the pit (principally within the pit, but also possibly outside the pit within the concentration boundary layer) such that the potential difference between the pit base and free surface is destroyed. This is the basis of the microscopic model proposed by Williams, Westcott and Fleischmann^(4,5) to account for the observed rapid repassivation of pits under conditions of natural convection, and the prevention of initiation when the solution was stirred. In a follow up to this work, a study of the effects of hydrodynamics on pitting is described in Chapter 4.

The concept of a concentration gradient and external solution resistance requirement to maintain pit propagation is however, one of only a number ways by which a potential drop could be maintained between the passive surface and pit bottom. For example, there is substantial support for the advocates of a salt film which when precipitated at the active pit surface, provides resistance to current flow^(18,19,20). The kinetics of the corrosion are then controlled by the dissolution of the salt film. It perhaps should be mentioned that workers who have noted salt film precipitation, and others who postulate this mechanism, tend to conduct their experiments in fairly concentrated chloride solutions at rather high (anodic) electrode potentials. In a recent paper, Frankel and co-workers⁽²⁰⁾ gave a very plausible account of the pit initiation process. They suggested that for *metastable* pits (which are the same as "unstable" pits in this work) to continue to propagate, a salt film must precipitate in the early stages of pitting, whilst the pit cover (said to be the remnants of the passive film) remains intact. They further suggested that the precipitation of the salt film could be observed in the current vs. time response of the specimens. Initially, pits grew with $i \propto t^2$ (active dissolution at constant current density, assuming hemispherical pits). When the salt film precipitated, the current dropped, and then evolved as $i \propto t^{1/2}$ (attributed to diffusion control via salt film dissolution). Whilst their analysis of metastable pitting was drawn from a large number of transients, their

analysis of the transition to stable pitting appeared to be drawn from only 4 pits, and is therefore rather less convincing.

There was no evidence in the present work that salt film precipitation differentiated unstable from stable pits. The current vs. time evolution of propagating pits varied quite widely from pit to pit, and in the early stages of growth were not obviously different from many unstable pits (Figure 3.16). Indeed, it is notable that many unstable pits exhibited higher current densities, which might be expected to favour salt film precipitation, than propagating pits within the same potential regime (compare Figures 3.14 and 3.17). The observation that the peak in the current density distributions for unstable pits shifted to higher values with increasing potential (Figure 3.14) demonstrates that the dissolution was not salt film (diffusion) limited. Furthermore, this rather linear increase of current density with potential is a good indication that the dissolution was under ohmic control.

Another possible source of resistance within pits is the formation of gas bubbles⁽²¹⁾, which could provide resistance until they detach and escape.

A suggestion from the present work is that a thin film of metal covering the pit, resulting from undercutting by the growing pit, could provide the resistive element, a possibility which has previously been considered by Vermilyea⁽²²⁾. It was noted that many pits were covered (Figures 3.19, 3.20, 3.23) and that the covers usually contained holes or cracks. Thus the actual area through which the current could flow was much less than in say an open hemispherical pit. Pit repassivation might be anticipated to occur when the cap breaks or falls into the pit (Figure 3.20c), a mechanism previously suggested by Rosenfeld and Danilov⁽²³⁾ and supported by other workers^(20,24). There is some evidence to support this assertion in the current vs. time evolution of the transients. The observation of $i \propto t^{1/2}$ transients is consistent with current flow limited by the electrical resistance of a porous pit cover. The cover would also protect the growth of the pit by isolating the pit solution from the bulk solution. That is, the rate of removal of ions from the pit would be limited by the diffusion rate through the cover.

The current vs. time evolution of the current transients is now considered in more detail.

Consider a simple model for a pit, viz a sphere of which the pit mouth is a chord. The assumption is that the pit mouth increases in radius as the sphere increases in radius:

$$a \propto r$$

where:

a = pit mouth radius

r = pit radius

and:

$$a = k_a r \quad (3.10)$$

It follows that:

$$V = k_v r^3 \quad \left(\frac{4}{3}\pi > k_v > \frac{2}{3}\pi \right) \quad (3.11)$$

$$A = \frac{dV}{dr} = 3k_v r^2 \quad (3.12)$$

where:

V = pit volume

A = pit internal area

The relationship between k_a and k_v is considered in more detail in Appendix C.

Consider the pit mouth as a microdisc of radius a . Then, the resistance for current flow to the disc is R , where⁽²⁵⁾:

$$R = \frac{1}{4\kappa a}$$

R = resistance to current flow to the pit mouth

κ = conductivity of external solution

Substituting with Equation 3.10:

$$R = \frac{k_R}{r} \quad (3.13)$$

where:

$$k_R = \frac{1}{4\kappa k_a}$$

Now, using Equation 3.10:

$$\frac{dV}{dr} = 3k_v \cdot r^2$$

multiply both sides by $\frac{dr}{dt}$:

$$\frac{dV}{dt} = 3k_v \cdot r^2 \cdot \frac{dr}{dt}$$

Now, Faraday's law for the pit growth can be written:

$$\frac{dV}{dt} = k_1 \cdot I$$

$$k_1 = \frac{m}{zF\rho} \quad (3.14)$$

where:

m = relative molecular mass

ρ = density of the metal

z = charge no. of the dissolving species

using Equation 3.12 and since:

$$I = iA \quad (3.15)$$

I = current

i = pit internal surface current density

$$\frac{dV}{dt} = k_1 \cdot i \cdot A = k_1 \cdot i \cdot 3k_v r^2 \quad (3.16)$$

Therefore, using Equations 3.14 and 3.16:

$$\frac{dr}{dt} = k_1 \cdot i \quad (3.17)$$

multiplying Equations 3.13 and 3.15 and substituting with Equation 3.12:

$$IR = 3k_R \cdot k_v \cdot i \cdot r \quad (3.18)$$

If E_a is the applied potential and E_o is the rest potential of the pit interior, in the pit interior solution, then the general equation is:

$$E_a - E_o = \Delta E = b \ln \left(\frac{i}{i_o} \right) + 3k_v k_R i r \quad (3.19)$$

where:

b = Tafel slope

i_o = exchange current density for pit base reaction in pit interior solution

The first term in the RHS of Equation 3.19 is the overvoltage for the pit dissolution reaction and the second term is the external solution resistance. The resistive drop inside the pit has been ignored.

Thus, in the resistance controlled limit, when the IR term dominates:

$$\Delta E = 3k_v k_R i r$$

and substituting for i with Equation 3.17:

$$\Delta E = \frac{3k_v k_R}{k_i} \cdot \frac{r dr}{dt}$$

by integrating:

$$\int r dr = \int \frac{\Delta E \cdot k_i}{3k_v k_R} \cdot dt$$

$$\frac{r^2}{2} = \frac{\Delta E \cdot k_i}{3k_v k_R} \cdot t + C$$

Since ΔE is constant and $r = 0$ at $t = 0$, it follows that $C = 0$. By manipulation:

$$r = \left(\frac{2 \Delta E \cdot k_i}{3k_v k_R} \right)^{1/2} \cdot t^{1/2} \quad (3.20)$$

differentiating Equation 3.20 with respect to t and substituting into Equation 3.17:

$$i = \frac{1}{2k_i} \cdot \left(\frac{2 \Delta E k_i}{3k_v k_R} \right)^{1/2} \cdot t^{-1/2} \quad (3.21)$$

i.e. the current density on the pit walls decreases with time in this limit.

Using Equations 3.12 and 3.15 and substituting with Equations 3.20 and 3.21:

$$I = 3k_v r^2 i = \frac{1}{2k_i} \cdot \left(\frac{2 \Delta E k_i}{3k_v k_R} \right)^{1/2} \cdot \frac{2 \Delta E k_i}{k_R} \cdot t^{1/2}$$

$I = \frac{\Delta E}{k_R} \cdot \left(\frac{2 \Delta E k_i}{3k_v k_R} \right)^{1/2} \cdot t^{1/2} \quad (3.22)$
--

Now, taking the general case of Equation 3.19, and substituting for i from Equation 3.17:

$$\Delta E = b \ln \left(\frac{1}{k_i i_0} \cdot \frac{dr}{dt} \right) + \frac{3k_v k_R}{k_i} \cdot r \cdot \frac{dr}{dt} \quad (3.19b)$$

with $r \rightarrow 0$, we have the surface area limiting case:

$$\begin{aligned}\frac{\Delta E}{b} &= \ln\left(\frac{1}{k_1 i_o} \cdot \frac{dr}{dt}\right) \\ \frac{1}{k_1 i_o} \cdot \frac{dr}{dt} &= \exp\left(\frac{\Delta E}{b}\right)\end{aligned}\quad (3.23)$$

By integrating:

$$\int dr = \int k_1 i_o \exp\left(\frac{\Delta E}{b}\right) dt$$

therefore, since $r = 0$ at $t = 0$:

$$r = k_1 i_o \exp\left(\frac{\Delta E}{b}\right) \cdot t \quad (3.24)$$

Let:

$$i = i_o \exp\left(\frac{\Delta E}{b}\right) \quad (3.25)$$

and from Equations 3.15 and 3.16 and substituting with Equations 3.24 and 3.25:

$$I = 3k_v r^2 i = 3k_v \left(k_1^2 i_o^3 \exp\left(\frac{3\Delta E}{b}\right) \right) \cdot t^2 \quad (3.26)$$

Thus, there are two limiting current/time forms:

- a) $I \propto t^{1/2}$: resistance limited case
- b) $I \propto t^2$: surface area limited case

Experimentally, the case $i \propto t$ is frequently observed. The question is whether this case can be derived from Equation 3.19b?

The general equation (Equation 3.19b) is:

$$\Delta E = b \ln\left(\alpha \frac{dr}{dt}\right) + \beta r \frac{dr}{dt} \quad (3.27)$$

where:

$$\alpha = \frac{1}{k_1 i_o}$$

$$\beta = \frac{3k_v k_R}{k_1}$$

If one defines:

$$r_o = \frac{b}{3k_v k_R i_o} \quad (3.28)$$

$$t_o = \frac{b}{3k_v k_R k_I i_o^2} \quad (3.29)$$

using these and Equation 3.31 then the general equation (Equation 3.19b) becomes:

$$\Delta \epsilon = \ln \left(\frac{dR}{dT} \right) + R \cdot \frac{dR}{dT} \quad (3.30)$$

where:

$$\Delta \epsilon = \frac{\Delta E}{b} \quad (3.31)$$

$$R = \frac{r}{r_o} \quad (3.32)$$

$$T = \frac{t}{t_o} \quad (3.33)$$

In order to achieve a solution of this equation, define:

$$\frac{dR}{dT} = e^y \quad (3.34)$$

thus:

$$R = \int e^y dT$$

By substitution into Equation 3.30:

$$\Delta \epsilon = y + e^y \int e^y \cdot dT \quad (3.35)$$

differentiate with respect to T:

$$0 = \frac{dy}{dT} + e^y \cdot e^y + e^y \cdot \frac{dy}{dT} \int e^y dT$$

However, from Equation 3.35:

$$e^y \int e^y dT = \Delta \epsilon - y$$

so:

$$0 = \frac{dy}{dT} + e^{2y} + \frac{dy}{dT} (\Delta \epsilon - y)$$

or

$$\frac{dy}{dT} \cdot (1 + \Delta \epsilon - y) = -e^{2y} \quad (3.36)$$

or

$$\int \frac{1 + \Delta \epsilon - y}{e^{2y}} dy = - \int dT \quad (3.37)$$

to integrate this function, let $u = 1 + \Delta \epsilon - y$ and $\frac{dv}{dy} = e^{-2y}$, it follows that:

$$\frac{du}{dy} = -1$$

$$v = -\frac{1}{2} \cdot e^{-2y}$$

integration by parts:

$$\int u \cdot \frac{dv}{dy} \cdot dy = uv - \int v \cdot \frac{du}{dy} \cdot dy$$

Substituting into this equation:

$$\begin{aligned} \int (1 + \Delta \epsilon - y) \cdot e^{-2y} \cdot dy &= (1 + \Delta \epsilon - y) \cdot \left(-\frac{1}{2} e^{-2y}\right) - \int -\frac{1}{2} e^{-2y} \cdot -1 \cdot dy \\ &= -\frac{1}{2} (1 + \Delta \epsilon - y) \cdot e^{-2y} - \left(-\frac{1}{4} e^{-2y}\right) \end{aligned}$$

Therefore:

$$e^{-2y} \cdot \left(-\frac{1}{4} - \frac{\Delta \epsilon}{2} + \frac{y}{2}\right) = -T + \text{constant} \quad (3.38)$$

as $T \rightarrow 0$ assume this is the surface limiting case and from Equations 3.32 and 3.33:

$$\frac{dr}{dt} = \frac{r_o}{t_o} \cdot \frac{dR}{dT}$$

substituting into Equation 3.23 and multiplying both sides by $\frac{t_o}{r_o}$ using Equations 3.28 and 3.29:

$$\frac{dR}{dT} = \frac{b}{3k_v k_R k_I i_o^2} \cdot \frac{3k_v k_R i_o}{b} \cdot k_I i_o \cdot \exp(\Delta \epsilon)$$

using Equation 3.34, this equation reduces to:

$$\frac{dR}{dT} = \exp(\Delta \epsilon) = e^y \quad (3.39)$$

Therefore, when $T = 0$, $y = \Delta \epsilon$, and so the constant in Equation 3.38 can be found and the equation becomes:

$$e^{-2y} \left(-\frac{1}{4} - \frac{\Delta \epsilon}{2} + \frac{y}{2}\right) + \frac{1}{4} e^{-2\Delta \epsilon} = -T \quad (3.40)$$

This equation can now be solved numerically for y as a function of T . From this solution, $\frac{dR}{dT}$ is given as $f(T)$ and hence by numerical integration R is obtained as a $f(T)$, leading to I as $f(T)$. The exponential terms cause difficulty in the numerical solution so the equation is re-arranged:

$$e^{-2y} \cdot \frac{\left(\frac{1}{4} + \frac{\Delta\epsilon}{2} - \frac{y}{2}\right)}{\left(T + \frac{1}{4} \cdot e^{-2\Delta\epsilon}\right)} = 0$$

$$-2y + \ln\left(\frac{1}{4} + \frac{\Delta\epsilon}{2} - \frac{y}{2}\right) - \ln\left(T + \frac{1}{4} \cdot e^{-2\Delta\epsilon}\right) = 0 \quad (3.41)$$

In order to decide what range of values of T to use, it was first necessary to estimate t_o , (Equation 3.29):

$$t_o = \frac{b}{3k_v k_R k_I i_o^2}$$

$3k_v$ can be estimated from Equation 3.11 as:

$$3k_v \approx 10 \quad (a)$$

The relationship between $3k_v$ and $10k_a$ is shown in Appendix C, Figure C.2. With $3k_v \approx 10$ then:

$$k_a \approx 1.0 \quad (b)$$

For the 1,000ppm Cl^- solution the conductivity was measured at:

$$\kappa = 2,700 \mu S/cm \quad (c)$$

From Equation 3.13:

$$k_R = \frac{I}{4 \kappa k_a}$$

$$k_R \approx 10^2 \quad (d)$$

Using the values from Section 3.3.3 in Equation 3.14:

$$k_I = 3.3 \times 10^{-5} \quad (e)$$

For stainless steel:

$$b \approx 90 \text{ mV/decade}^{(26)}$$

$$= \frac{90}{2.3} \approx 40 \text{ mV} \quad (f)$$

Substituting these values into Equation 3.29:

$$t_o \approx \frac{1}{i_o^2}$$

A typical exchange current density for an anodic dissolution reaction might be 1 mA/cm^2 , in this case:

$$t_o \approx 10^6 \text{ s}$$

Knowing that a typical event lifetime is around 100s, it follows from Equation 3.33:

$$T \approx 10^{-4}$$

If the exchange current density is larger, say 10 mA/cm^2 , then:

$$t_o \approx 10^4 \text{ s}$$

So in this case:

$$T \approx 10^{-2}$$

It is also likely that the conductivity of the solution just outside the pit is higher than in the bulk solution (because of the flux of material out of the pit). So if k_R is approximately 10 ohm cm , then substituting these values into Equation 3.29:

$$t_o \approx \frac{10}{i_o^2}$$

i.e t_o is longer and T is shorter.

We now have established the range of T to use in the solution of Equation 3.41 which is solved numerically using the Newton-Raphson method. The computer program for this iterative method is given in Appendix D. Sample graphical outputs of solutions are given in Figure 3.27.

The current evolution with time resulting from the numerical solutions changed, according to the input parameters, in a manner fully consistent with the

experimentally-observed current transients. This is illustrated below with reference to Figures 3.3 and 3.27.

For constant T :

- * at small $\Delta\epsilon$ (e.g. $\Delta\epsilon \leq 3$), the current is surface area limited and evolves as $i \propto t^2$, Figure 3.27(a and b)
- * at large $\Delta\epsilon$ (e.g. $\Delta\epsilon \geq 6$), the current is resistance limited and evolves as $i \propto t^{1/2}$, Figure 3.27(d and f)
- * for intermediate $\Delta\epsilon$ (e.g. $\Delta\epsilon = 4$), the current evolution is linear with time $i \propto t$, Figure 3.27(c), arising as a balance between the two limiting cases

Furthermore, the transients which evolve as $i \propto t^{1/2}$ (i.e. resistance limited), initially develop as $i \propto t^2$ (i.e. surface area limited), Figures 3.27d and e.

This results are consistent with the experimental observations given in Figures 3.1 and 3.3 and summarised in Table 3.2.

3.4.4.2 Hypothesis on Repassivation Based on "Sulphur Exhaustion"

The possibility that micropits which nucleate at sulphur-rich inclusions subsequently repassivate when the supply of sulphur is exhausted is examined in Chapters 5-7.

3.4.4.3 Propagation

The results presented in this chapter indicate that unstable pits and stable pits nucleate by the same mechanism - both types exhibit similar current versus time characteristics and current densities in the initial stages. Indeed, many unstable pits exhibited higher current densities than stable pits in the same potential range. A simple explanation of this observation might be that the condition giving rise to the resistive element in the localised corrosion cell - suggested here to be the pit cover (see above) - is sufficiently persistent to enable the pit to propagate. Two additional mechanisms are suggested by the observations reported here, although at this stage both are speculative. Firstly, non-uniform dissolution or "pits within pits" (Figure 3.21) may arise as a growing pit uncovers sites where dissolution can proceed preferentially;

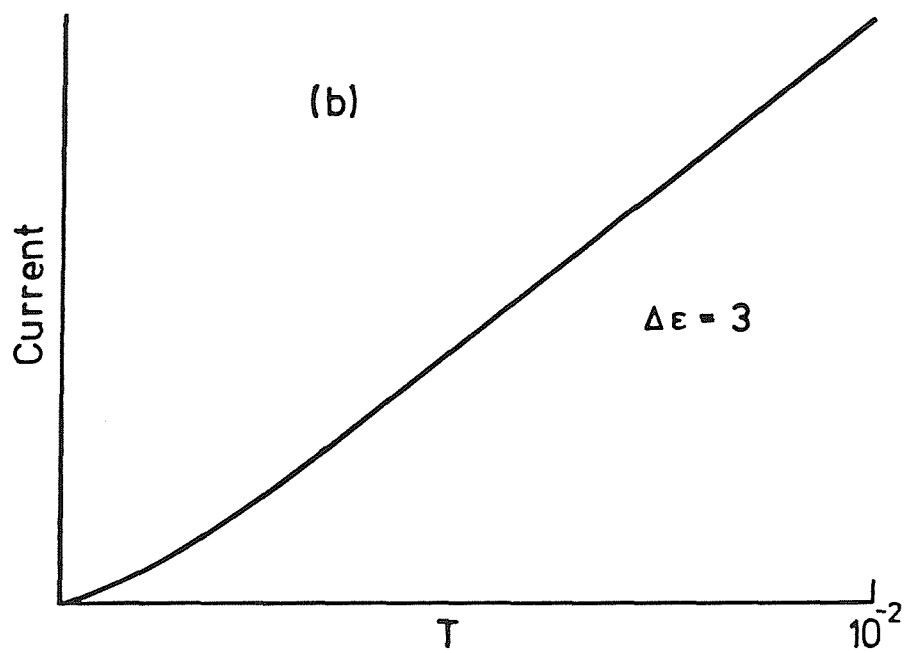
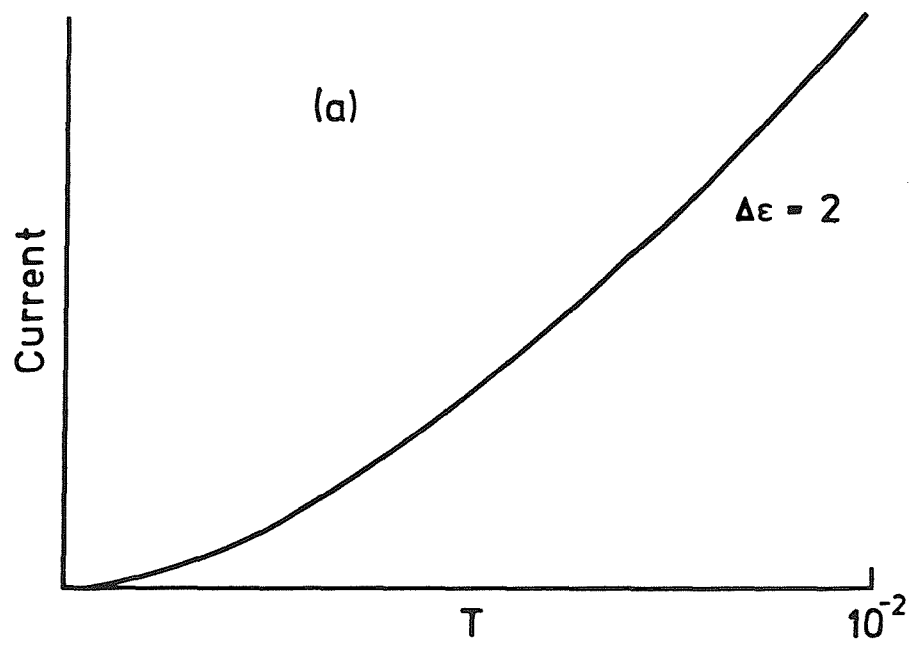


Figure 3.27 Sample outputs from numerical solutions of equation 3.41

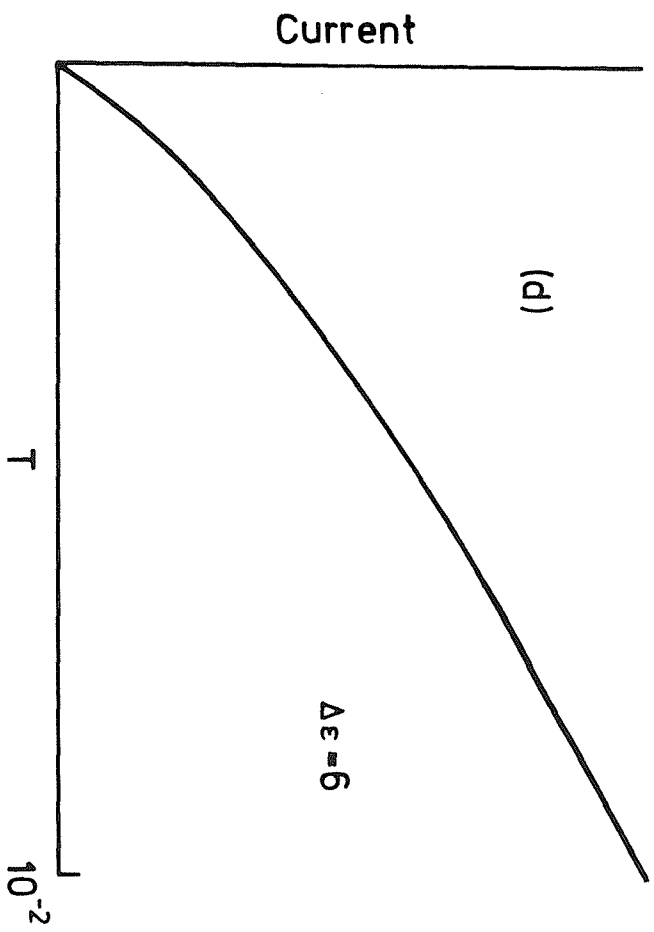
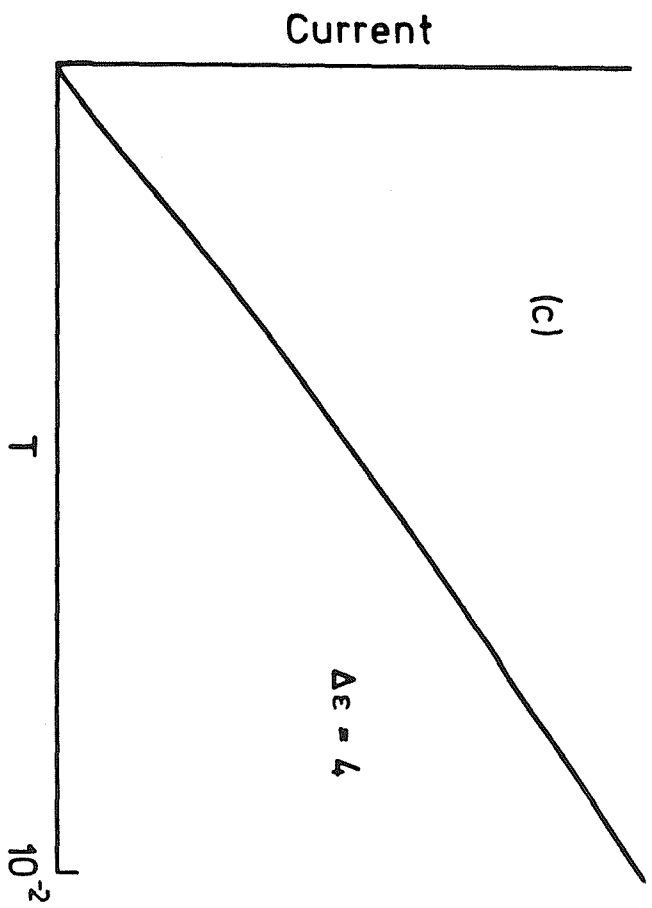


Figure 3.27 (continued)

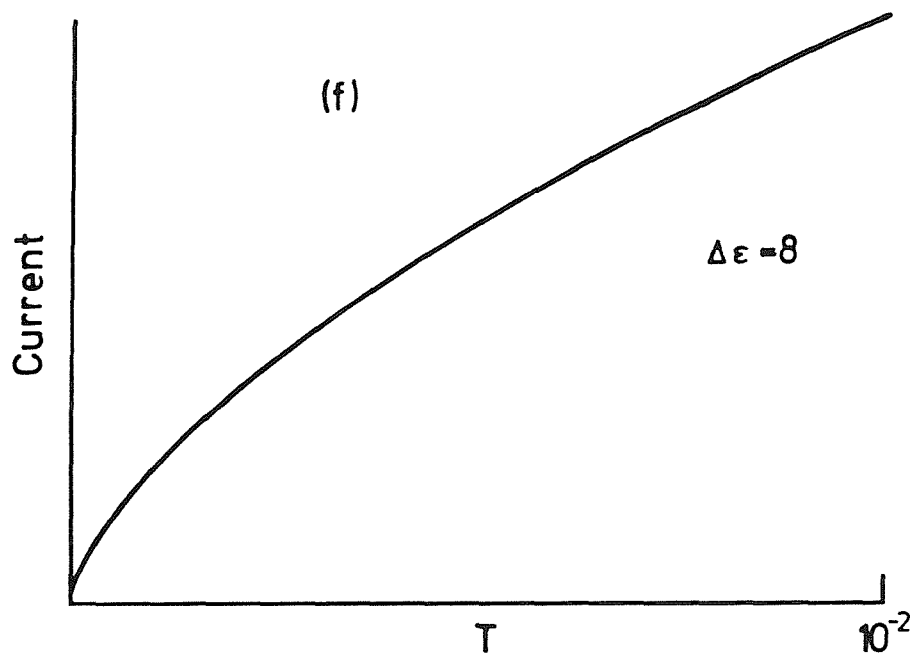
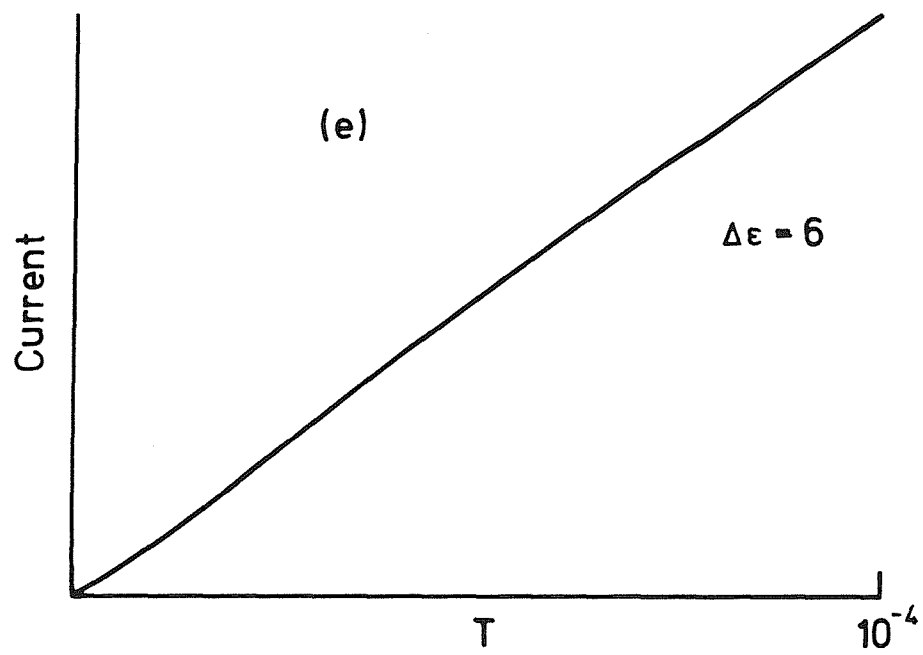



Figure 3.27 (continued)

**Table 3.2 Comparison Between Experimental and Predicted
Current-Time Evolution**

	POTENTIAL RANGE (mV SCE)	FIGURE NUMBER	COMMENTS
<div style="text-align: center;">  <p>Increasing $\Delta \epsilon$</p> </div>	-210 to -198	3.3(a)	Nothing
	-190	3.1(a)	$i \propto t^2$
	-125 to -113	3.3(b)	Linear, with curve on bottom
	-8 to +4	3.3(c)	Linear, with curve on bottom
	+85 to +97	3.3(d)	Starting to look like $i \propto t^{1/2}$
	+170 to +182	3.3(e)	$i \propto t^{1/2}$ if they last long enough

sub-surface inclusions for example. Such a process might account for the observation of "superimposed" events. Secondly, the observations of covers in the "pits within pits" (Figure 3.21) might indicate that reinitiation has occurred: if the original pit repassivated when the cover fell in or was unable to provide the resistance required to maintain an active dissolving pit, re-initiation could perhaps occur within the pre-existing cavity.

3.5 SUMMARY

This chapter has demonstrated that a high sensitivity to micropitting events can be achieved by combining high resolution equipment, suitable precautions against electrical interference and a slow potential scan rate. It has been found that the exchange current density for film growth during the slow potential ramp experiment is exceedingly small (about 10^{-18}A/cm^2 by extrapolation), indicating that a simple model of uniform dissolution is unlikely to apply, and that steady state is never achieved, even under conditions of natural immersion. A direct correspondence between the occurrence of anodic current transients and the nucleation, temporary growth and repassivation of micropits has been established. Prior to repassivation of unstable micropits, there was no difference in their current-time evolution to distinguish them from pits which continued to propagate to form macropits. Current transients were first observed at electrode potentials (e.g. $<100\text{mV SCE}$) considerably lower than reported "repassivation" potentials obtained from conventional cyclic polarisation experiments, an observation which questions the reliability and meaning of the "repassivation" potential.

Microscopy of the pitted specimens revealed that many pits were covered with what appeared to be remnants of the surface metal. It is suggested that the integrity of this film is a vital element in providing a resistance to current flow, helping to maintain the potential drop between the passive surface and the dissolving pit surface. Many small pits were associated with non-metallic inclusions containing sulphur. This observation is followed up in Chapters 5 and 6 when the importance of sulphide inclusions as pit nucleation sites is examined in detail.

An examination of the evolution of the current with time during the growth of a micropit, by considering a simple model of a pit, in which it is assumed that the pit

mouth radius increases with the radius of the pit, has shown that there are two limiting forms:

- * $i \propto t^2$, where the current is limited by the surface area of the growing pit;

- * $i \propto t^{1/2}$, the current is solution resistance limited.

A relationship between current and time was derived and solved numerically for the intermediate (and commonly observed) case of a linear increase in current with time. The experimentally observed current transients evolved in a manner fully consistent with the model predictions.

CHAPTER 4

THE EFFECTS OF SOLUTION FLOW ON THE INITIATION OF PITTING CORROSION ON STAINLESS STEELS

CHAPTER 4 - THE EFFECTS OF SOLUTION FLOW ON THE INITIATION OF PITTING CORROSION ON STAINLESS STEELS

4.1 INTRODUCTION

Most if not all corrosion processes involve some relative motion between the corroding metal and its environment. Such movement can increase or decrease the corrosion rate occurring under static conditions. In most cases of general corrosion, fluid flow increases the rate of arrival of corrosive species to the metal and the rate of removal of the corrosion product from the metal surface. Consequently, the corrosion rate increases. If, however, the metal forms a protective oxide film, an increase in velocity will increase the availability of oxygen to the surface, helping to maintain the protective film.

In plant situations, pitting of stainless steels is generally observed to occur more readily in stagnant rather than flowing electrolytes⁽¹⁾. The beneficial effect of solution flow is illustrated by the work of Moller⁽²⁾: seawater flowing at 1.2m/s did not pit welded type 316 and 310 stainless steel, whereas deep pitting occurred in stagnant seawater. A number of other workers have investigated the effects of flow on pitting resistance. Danek⁽³⁾ and LaQue⁽⁴⁾ found that stainless steel and nickel-based alloys were much more resistant to corrosion at high flow velocities compared to stagnant conditions. Such experience accounts for the recommendation of a minimum flow velocity for stainless steels in seawater of 5ft/s⁽⁵⁾.

Curiously, most studies which have addressed the effects of flow have found no effect on the breakdown potential⁽⁶⁻¹⁰⁾. Exceptions are Franz and Novak⁽¹¹⁾, who, studying aluminium found a noble shift of 50mV in flowing vs. stagnant solution. Also, the use of ultrasonics, applied to electrolytes containing stainless steel electrodes, has shown that the pitting potential is shifted in the noble direction by 200mV compared to similar tests in stagnant solutions⁽¹²⁾.

There have been few mechanistic studies of the effects of flow on pitting. The work of Beck and Chan⁽¹³⁾ studied the effect of flow velocity on the growth of single, artificial pits on zone refined iron and type 304 stainless steel. They concluded that there was a critical electrolyte velocity past the pit mouth, which was inversely proportional to pit radius, above which convection determines the current density. At

values higher than the threshold, the current density increases to an ohmic resistance limited value in high conductivity solution, and decreases to an ohmic limit in low conductivity solution (when the transport limited current is greater than the ohmic limited current). Pits were found to repassivate at the ohmic limit at a critical velocity where the salt film, present on the growing pit surface, was removed. They went on to show that, at 5ft/s, only small pits can grow before they are extinguished.

In previous work in this laboratory, pit initiation on stainless steel was shown to be inhibited when a 0.28M Cl⁻ solution was stirred, and prevented altogether when the experiments were repeated with 0.028M Cl⁻(14). This was attributed to an effect of solution flow on the diffusion boundary layer at the electrode surface.

In the present work, the effects of solution flow on pit nucleation under well defined hydrodynamic conditions have been studied. Specifically, it considers the effects of laminar and turbulent flow on pit initiation using a flow channel apparatus. It differs from the approach of Beck and Chan in that multiple pits were allowed to nucleate and grow on the specimens. The electrochemical methods described in the previous chapter were used to follow the current evolution, with time, of the individual pits.

4.1.1 Laminar and Turbulent Flow in a Closed Conduit

The flow of an incompressible fluid in a closed conduit such as a flow channel is subject to inertial and viscous forces. However, apart from forces due to piezometric pressure between different parts of the fluid, it is not normally subject to any other forces.

At low relative velocities of the channel walls and solution, the flow is laminar and at high velocities it is turbulent. The transition occurs over a velocity range and depends on the geometry of the system, the viscosity of the liquid and the roughness of the surface. The dimensionless Reynold's Number (Re) is used to take account of such effects and allows the prediction of transitions:

$$Re = \frac{ud}{\nu}$$

where:

u = velocity (m/s)

$$d = \frac{2ab}{a + b} = \text{hydraulic diameter}$$

for a rectangular duct, a and b are the sides of the duct

ν = kinematic viscosity (m^2/s)

Laminar flow, in which all the fluid particles travel parallel to the sidewalls of the channel, occurs at low Re . Turbulent flow is evident at high Re . Thus in laminar flow the viscous forces, which exert a stabilising influence, are predominant, whilst in turbulent flow it is the inertial forces which dominate.

When the flow velocity is increased, eddies begin suddenly rather than gradually, indicating that laminar flow is unstable, and a small disturbance is sufficient to bring on turbulent flow. Under normal engineering conditions, when disturbances such as vibration are always present, transition occurs for Re in the range 2,000 - 4,000.

In turbulent flow, there is still a thin viscous sub-layer (δ_h) which results from viscous drag. If mass transfer is occurring at the surface there will also be a diffusional boundary layer (δ_d). The relationship between the thickness of these two boundary layers is governed by the dimensionless Schmidt number (Sc):

$$Sc = \frac{\nu}{D}$$

where:

D = diffusivity of the relevant species (m^2/s)

With increasing values of Sc , the diffusion layer is reduced in thickness, and it forms more rapidly. If both δ_h and δ_d start to develop together then $\frac{\delta_h}{\delta_d} \approx \sqrt{Sc}$. Associated

with the velocity gradient across these boundary layers is a frictional force which may be expressed as a surface shear stress, τ_s . It is possible that this may influence the mechanical stability of surface films.

The overall transport to the surface consists of bulk convection, in which there is an overall transfer of fluid involved, and turbulent convection, where there is an exchange of fluid between the boundary layer and the bulk. Both depend on the concentration driving force, and the mass transfer coefficient is empirically derived as:



k_m = rate of reaction/concentration driving force

The mass transfer rate is also expressed in the dimensionless Sherwood number (Sh):

$$Sh = k_m \cdot \frac{d}{D}$$

Theoretical relationships can be derived for the functional relationship between Sh , Re and Sc (e.g. for the rotating disc electrode). However, they are usually obtained as empirical correlations of experimental data, of the form:

$$Sh = \text{constant} \cdot Re^x \cdot Sc^y$$

where:

x usually lies between 0.3 and 1.0, and y is typically 0.3(15)

For a reaction that is diffusion controlled,

$$\text{rate} = k_m \cdot \Delta C$$

where:

ΔC = concentration driving force

In electrochemical terms, when the rate equals the limiting current density (i_{lim}),

$$i_{lim} = k_m \cdot z \cdot F \cdot \Delta C$$

and:

$$k_m = \frac{D}{\delta_d}$$

4.2 EXPERIMENTAL

The effect of hydrodynamics on pit initiation was studied using the apparatus shown in Figure 4.1 and 4.2(16). A twin reservoir system was adopted to enable bulk solution changes to be made rapidly, a procedure facilitated by solenoid-actuated pneumatic valves. These rather sophisticated features were not required for the study described here, but were essential for a separate study(17,18). The smaller secondary reservoirs

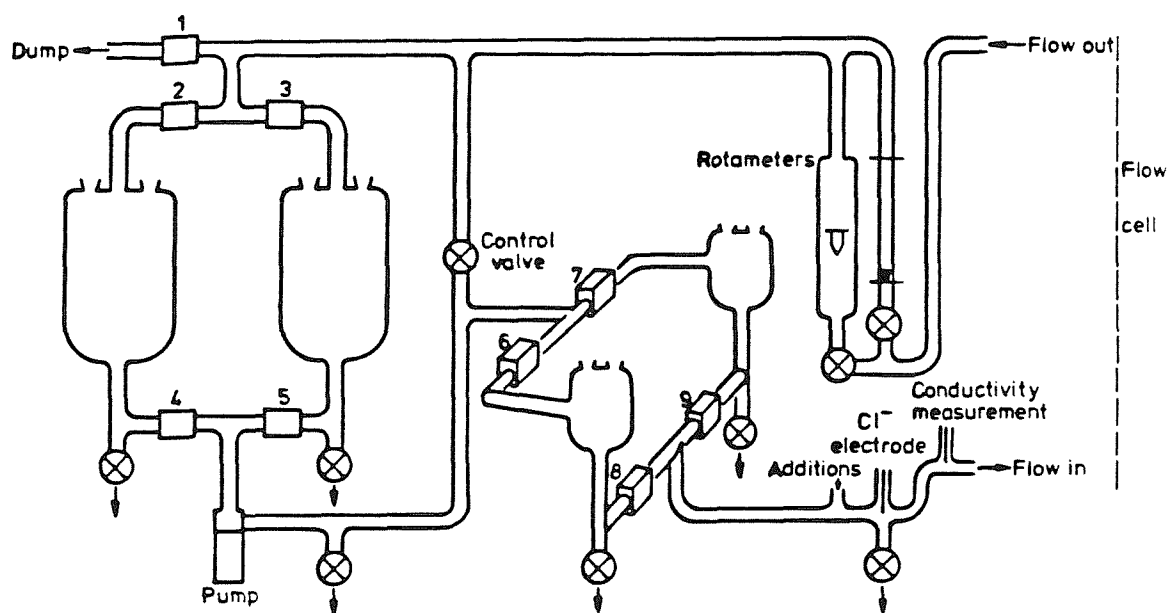


Figure 4.1 The Flow Rig

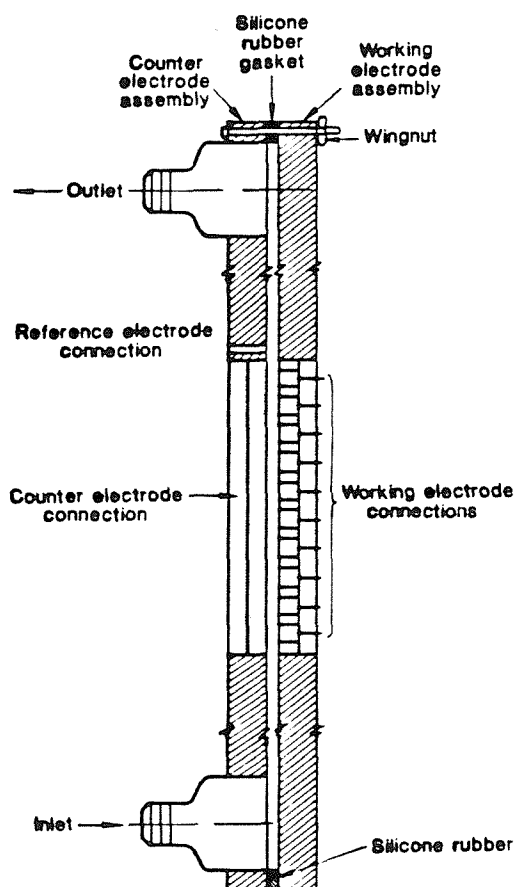


Figure 4.2 The Flow Channel

were used to remove gas bubbles, entrained during deaeration (see below) or induced by cavitation in the pump.

Borosilicate glass was used to construct the flow rig (Figure 4.1), which was designed to deliver the test solution to the flow channel at the desired flowrate. Deaeration of the test solution in the reservoirs was achieved using an argon purge, whilst the network of glass tubing was deaerated by the argon bubbles entrained in the flow. A dissolved oxygen meter located at the inlet to the flow channel monitored the efficiency of the oxygen removal, and an argon blanket was maintained above the solutions in the reservoirs. A magnetically coupled centrifugal pump, with a glass-filled polypropylene chamber and a ceramic shaft, was used for electrolyte circulation. Coarse flowrate control was achieved by a control valve in the by-pass circuit. The flowrate was measured using one of two rotameters, which had ceramic floats for solution compatibility, and were calibrated in the test solution. Fine adjustment of flowrate was accomplished using the valves on the rotameters.

The flow channel was designed for the study of pit initiation under laminar flow conditions. Figures 4.2 and 4.3 show the construction. Essentially, two acrylic sheets containing respectively the working and counter electrode assemblies were separated by a silicone rubber gasket.

The gasket, shown in Figure 4.3a, defined the flow channel from inlet to outlet (and hence the hydraulic diameter, d), and provided a seal between the working and counter electrode assemblies. From the inlet the channel was gradually widened at an angle of 3.5° (19), to the design width. The channel was then parallel sided for a lead-in length equal to $50d$ prior to the specimens. This profile was repeated downstream of the specimens.

In constructing the working and counter electrode assemblies, care was taken to provide a smooth and continuous surface to the flowing solutions, to ensure that the flow was not disrupted. Windows were cut in the acrylic sheets, into which the electrodes were set using epoxy resin. The electrodes were surface-prepared and primed, as described in Chapter 2 (Section 2.1), to prevent crevice corrosion. The whole acrylic sheet/electrode assembly was then milled to the desired flat, continuous surface.

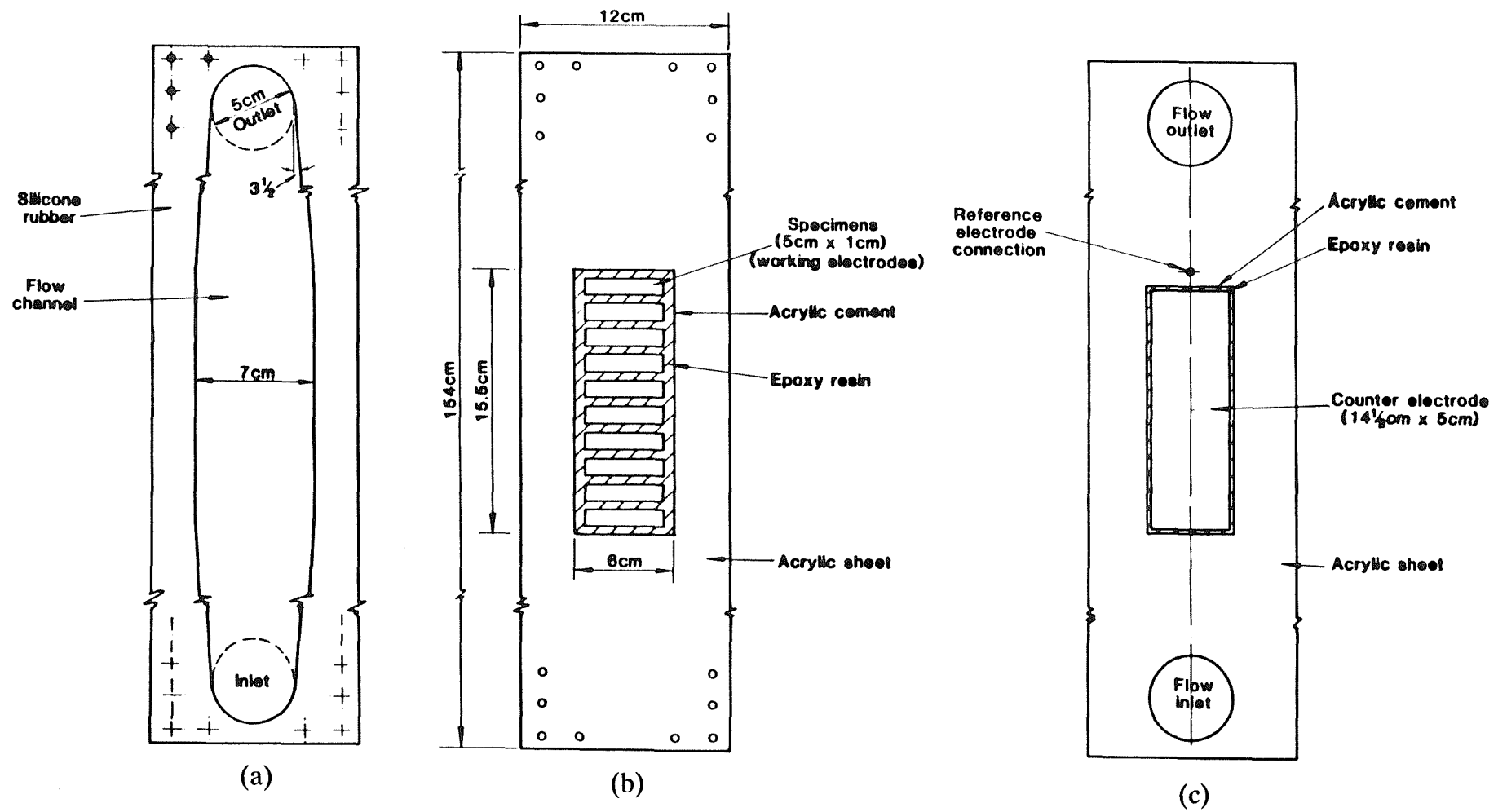


Figure 4.3 Component Parts of the Flow Channel: (a) Gasket, (b) Working Electrode Assembly, (c) Counter Electrode Assembly

The working electrode assembly, Figure 4.3b, contained 10 rectangular specimens (5cm x 1cm) mounted perpendicular to the solution flow direction. The specimens were machined from the same commercial purity AISI 304L plate stock as used throughout this study (the composition of which is given in Appendix B), and were wet ground using grade 240 grit SiC paper.

The counter electrode was a large rectangular plate (approximately 70cm²), machined from the same 304L plate stock as the specimens. This was positioned in the counter electrode assembly such that it was directly opposite the 10 specimens when the flow channel was assembled. The counter electrode assembly, Figure 4.3c, also provided an outlet to the reference electrode, located downstream of the counter electrode. Solution filled plastic tubing connected the saturated calomel electrode to the flow channel.

When turbulent flow conditions were required, turbulence promoters were mounted on the counter electrode assembly upstream of, and opposite to the 10 specimens. A plastic mesh with a wire diameter of 1mm and a mesh size of about 1cm was used for this purpose.

Electrochemical measurements were made in the flow channel using a three electrode configuration. The low noise apparatus and data acquisition routines used in the experiments in stagnant solutions, described in Chapter 2, were again used. Faraday cages were placed around the section of the flow channel containing the working, counter and reference electrodes, and again all connecting wires were shielded and kept as short as possible.

4.3 CALIBRATION

Calibration of the flow channel was carried out using the diffusion limited current in the potassium ferricyanide-ferrocyanide redox system, and is described in Appendix E. The results showed good correlation with available literature values. In the laminar flow regime, the concentration boundary layer thickness was found to vary from about 110 μ m (at $Re = 214$) to 52 μ m (at $Re = 2148$). Although transitional flow was evident above about $Re = 2150$, it was found that fully developed turbulent flow in the channel could not be induced without the use of turbulence promoters.

4.4 RESULTS

All of the experiments described here used 1,000ppm Cl^- . Oxygen levels were below the 0.1ppm limit of the oxygen meter at the inlet to the channel, and rest potentials were typically -350mV SCE. As for experiments under stagnant conditions, the flow experiments consisted of slow potential sweep experiments from the average value of the rest potential of the 10 specimens. The forms of the current transients associated with the unstable pitting were the same as those described in Chapter 3, for stagnant conditions. Figure 4.4 shows the event frequency as a function of potential, again illustrating the occurrence of unstable pits at low potentials, in this case down to -160mV SCE. The amount of data collected in this study was rather limited, but it did show that the nucleation rate of unstable pits was not strongly dependent on solution flow, Table 4.1. However, if an event had begun to propagate significantly, then the application of a solution flow in the turbulent regime had a significant influence on the further development of the event: often the event would die immediately. For events which were sufficiently well established, the rate of increase of current with time was lowered, but the event did continue to propagate. Figure 4.5 illustrates these effects of turbulent flow.

Table 4.1 - Effects of Flow on Pit Nucleation Frequency
($E = 250\text{mV SCE}$)

FLOW REGIME	FLOW VELOCITY (cm s^{-1})	NUCLEATION FREQUENCY ($\text{cm}^{-2}\text{s}^{-1}$)
Static Solution	0	0.0022
Laminar	7.9	0.0026
Turbulent	120	0.0023

In the flow channel apparatus, since large volumes of solution were required ($\approx 30\text{l}$),

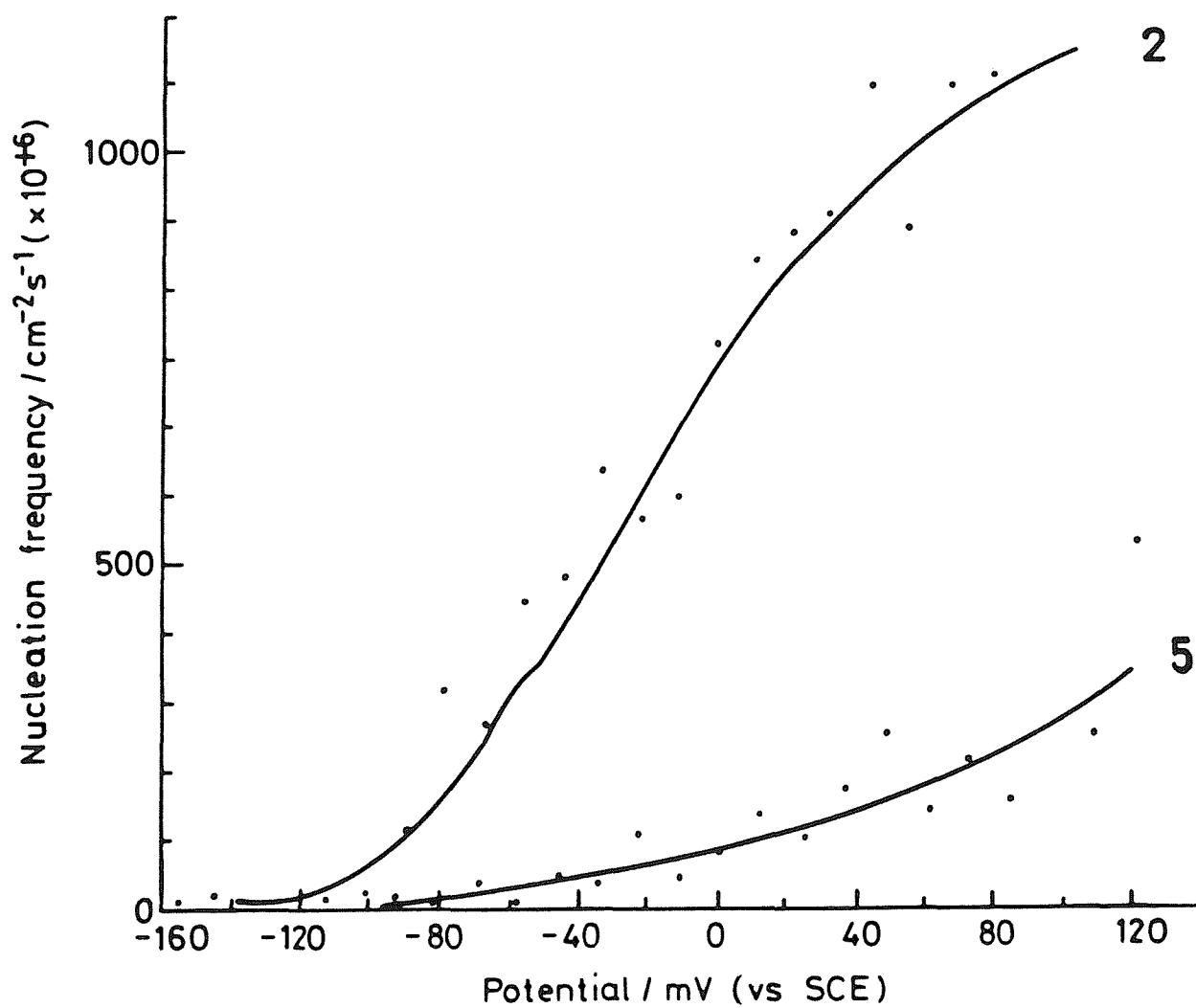


Figure 4.4 Anodic current transient frequency as a function of electrode potential.

Laminar flow Regime ($Re = 540$)

The Labels 2 and 5 on the curves are the sequence numbers of the experiments

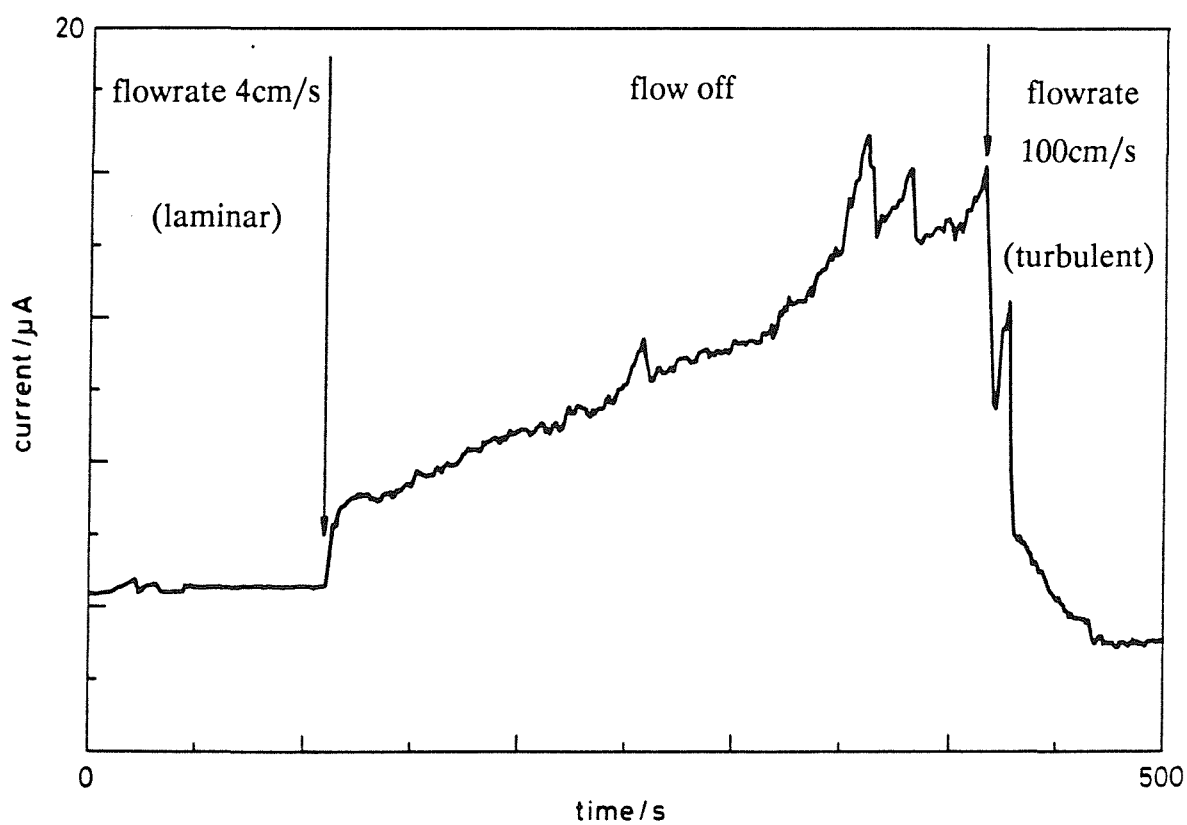
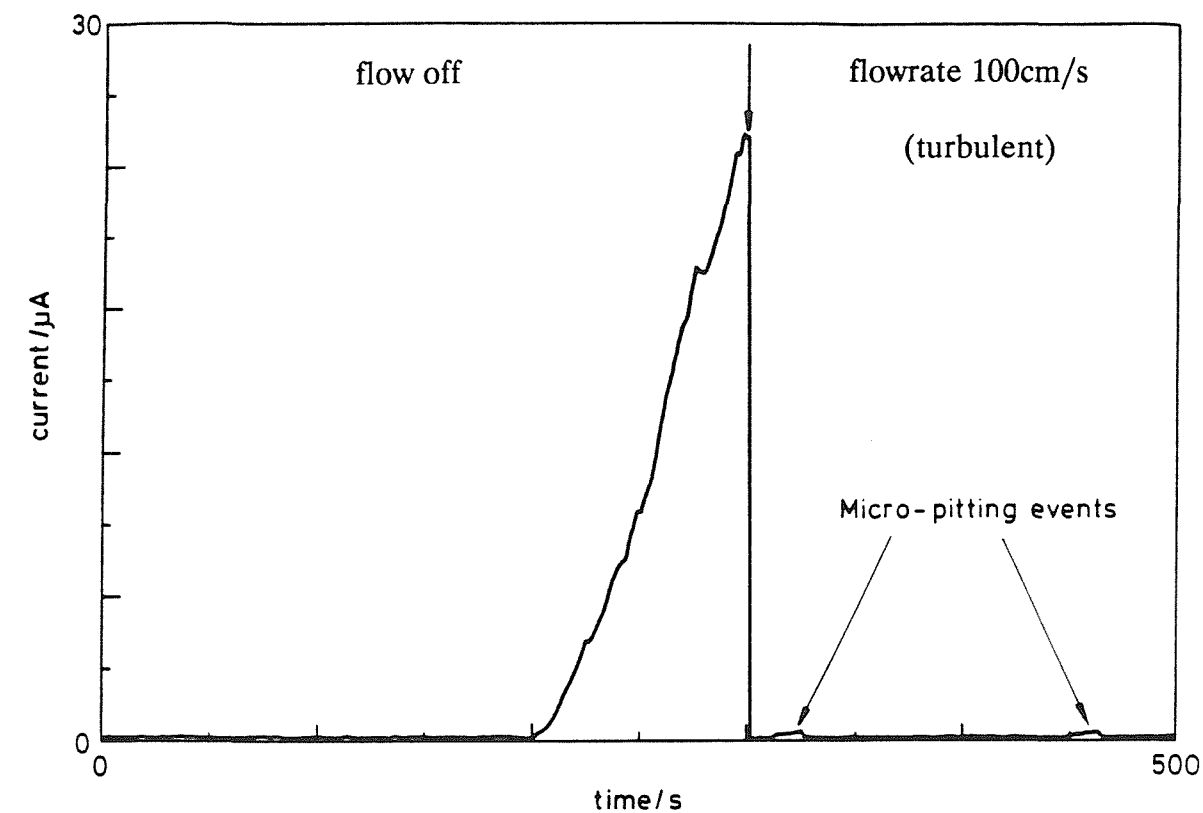


Figure 4.5 Examples of the effects of turbulent flow on pitting.

At the times marked by the arrows the flow was changed as indicated

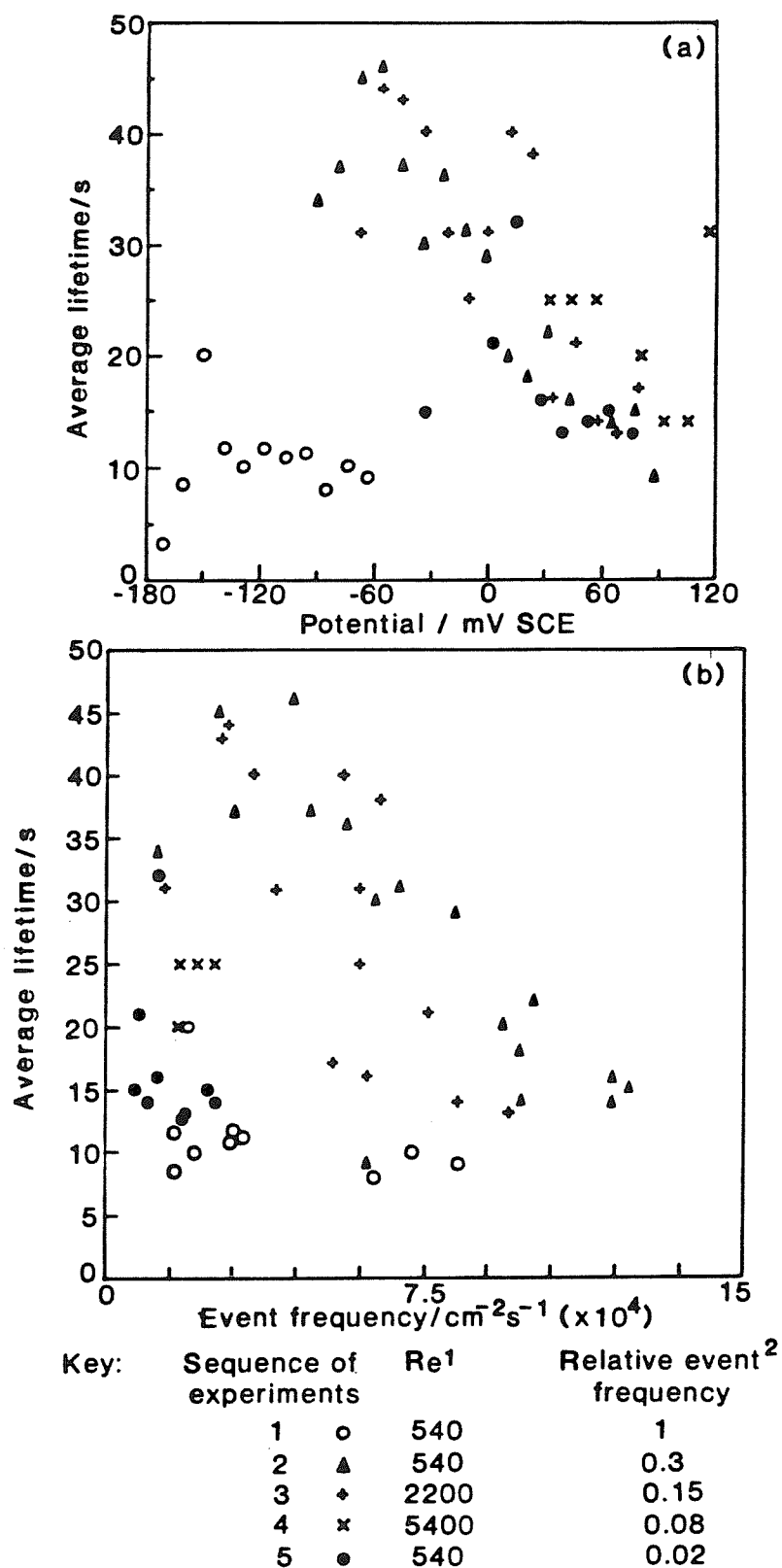
the solution stayed in the apparatus for some time. Also, since the electrode preparation involved a long procedure and in an effort to maximise the usefulness of a given electrode, it was used for a number of experiments before being replaced. It was observed that the frequency of unstable pitting events declined steadily over this series of repeat experiments, Figure 4.4. This effect persisted when the solution was partially replenished, but not wholly replaced, and is discussed later.

Figure 4.6a shows the variation in average lifetime of current transients as a function of electrode potential for a sequence of experiments at different flowrates, and Figure 4.6b shows the average lifetime vs. event frequency for the same sequence of experiments. These results indicate that as the event frequency decreased, the average lifetime tended to increase. Also, the average lifetime tended to decrease with increasing potential, but was unaffected by the solution flowrate (up to $Re = 5400$, but without turbulence promoters).

4.5 DISCUSSION

The results of this study are inconclusive. No effects of laminar flow on nucleation frequency were found. However, effects of laminar flow on pitting "breakdown" potentials were not determined (although subsequent work has shown that laminar flow does not affect the breakdown distribution).

There was no effect of turbulent flow on pit nucleation, but there was a specific effect of turbulent flow on propagating pits - they either repassivated immediately, or the propagation was initially slowed, before continuing. The following interpretation of these observations identifies two contributory factors: firstly, under stagnant or laminar flow conditions, the concentration gradient decreases from a maximum at the active pit surface, out into the concentration boundary layer outside the pit, eventually reaching the bulk solution composition. The solution outside (but near to) the pit has a much higher conductivity than the bulk solution. When turbulent flow is applied, this relatively concentrated solution is swept away by the flow (i.e. the concentration boundary layer is reduced), effectively increasing the solution resistance. This *decreases* the current and hence the material supply (e.g. chloride) by electromigration *into* the pit. Secondly, in reducing the concentration boundary layer, turbulent flow *increases* the flux of material *out* of the pit (by forced convection), and the



Notes: 1. No turbulence promoters in these experiments

2. Relative event frequencies quoted to illustrate progressive inhibition of pit nucleation during sequence of experiments 1-5

Figure 4.6 (a) Variation in average lifetime of events as a function of electrode potential for a sequence of experiments at different flowrates

(b) Average lifetime vs. frequency of events for the same sequence of experiments

concentrated solution inside the pit, which is required for continued propagation, cannot be maintained.

It may be recalled from the previous chapter that pits were often found to be covered by thin metal remnants, and it was suggested that it was necessary for these pit covers to remain intact to protect the pit during its early stages of growth (by providing a resistance to current flow). This hypothesis can be extended on the basis of the results reported in this chapter. Another specific effect of turbulent flow may be to disrupt or collapse the pit covers, removing the resistance to current flow, and allowing the pit contents to be dissipated by convection. Also, the observation that the growth of a sufficiently well established pit was retarded, but not stopped, may be associated with the observation in the previous chapter of "pits within pits": the turbulence could not penetrate far enough into the pit to disrupt all of the dissolving surfaces. The efficiency with which turbulent flow is able to stop pit propagation would be expected to increase with flowrate (all other things being equal), as the viscous sub-layer is decreased (i.e. turbulent eddies reach nearer to the surface) and the shear stress at the boundary (which might disrupt pit covers, for example) increases.

The lack of an effect of turbulent flow on pit initiation can perhaps be explained by further development of the arguments outlined above. It is possible that, in the early stages of the development of a pit, the pit size and developing concentration gradients might be small enough to be well within the viscous (hydrodynamic) sub-layer at the metal solution interface. That being so, solution flow would not greatly influence the initiation or development of a pit unless the thickness of viscous sub-layer was reduced (by increasing the flow rate) or the pit grew to a size where, (a) it was wider than the viscous sub-layer (in effect increasing the surface roughness), (b) the shear stress at the wall was sufficient to disrupt the pit cover.

Under laminar flow conditions, it could be argued that a pit developing inside the hydrodynamic boundary layer would be unaffected by the bulk solution flowrate, so long as the developing concentration gradients were on a finer scale than the hydrodynamic boundary layer.

The work reported in this chapter on the effects of flow on corrosion is rather preliminary. However, it has shown that pit nucleation is unaffected by solution flowrate, and that turbulent flow stops or retards pit propagation. This latter result is

consistent with industrial research and plant experience for stainless steels, where a minimum flowrate of 5ft/s is recommended⁽⁵⁾. In industrial plant, with much rougher surfaces than were used in this work, this undoubtedly corresponds to turbulent flow conditions. It is consistent with Beck and Chan's⁽¹³⁾ findings that pits continue to nucleate in flowing solutions, and that their size is limited by the flow velocity. However, it differs in the interpretation of the results: Beck and Chan attributed the effect of flow to removal of the salt film on the dissolving surface of the pit. In this work, at the relatively low potentials and chloride concentrations used, there was no evidence for salt film formation, and the results have been interpreted differently (see above).

The effects of flow on pitting breakdown potential distributions has not been studied and awaits further work. However, on the basis of these results it is expected that turbulent flow will result in a noble shift in the breakdown potentials: only well established pits (which had been grown initially in laminar or stagnant conditions) were able to survive the application of turbulent flow - this observation is consistent with the work of Sato and co-workers⁽⁷⁾, who found that pit growth was unaffected by flow only above a critical pit size. Under turbulent flow conditions throughout, it would be anticipated that fewer pits would survive beyond the early stages of growth.

The final section in this discussion examines the observation that the nucleation frequency of unstable pits declined steadily over a series of repeat experiments. At the time this work was done, it was suspected that this effect was caused by an inhibitor, probably leached from the apparatus, although none could be identified⁽²⁰⁾. However, in subsequent work, a strong effect of pre-polarisation of electrodes on the nucleation rate of unstable pits has been identified⁽²¹⁾: experiments were carried out on pre-pitted specimens (i.e. those which had been used in slow potential sweep experiments, and exceeded the 10 μ A current limit), which were re-used without further preparation, except for fresh solution. In the previous chapter it was shown that the current-potential behaviour during the slow potential sweep experiments was consistent with high field film growth. Therefore, with a thicker initial film, due to pre-polarisation, the initial rise in passive current should be shifted to more anodic potentials. This behaviour was indeed observed, see Figure 4.7⁽²¹⁾. Also in the previous chapter, the nucleation frequency of unstable pits was shown to increase with increasing passive current density, the latter being identified as providing some of the driving force for pit nucleation. The fresh ground vs. pre-pitted results were consistent

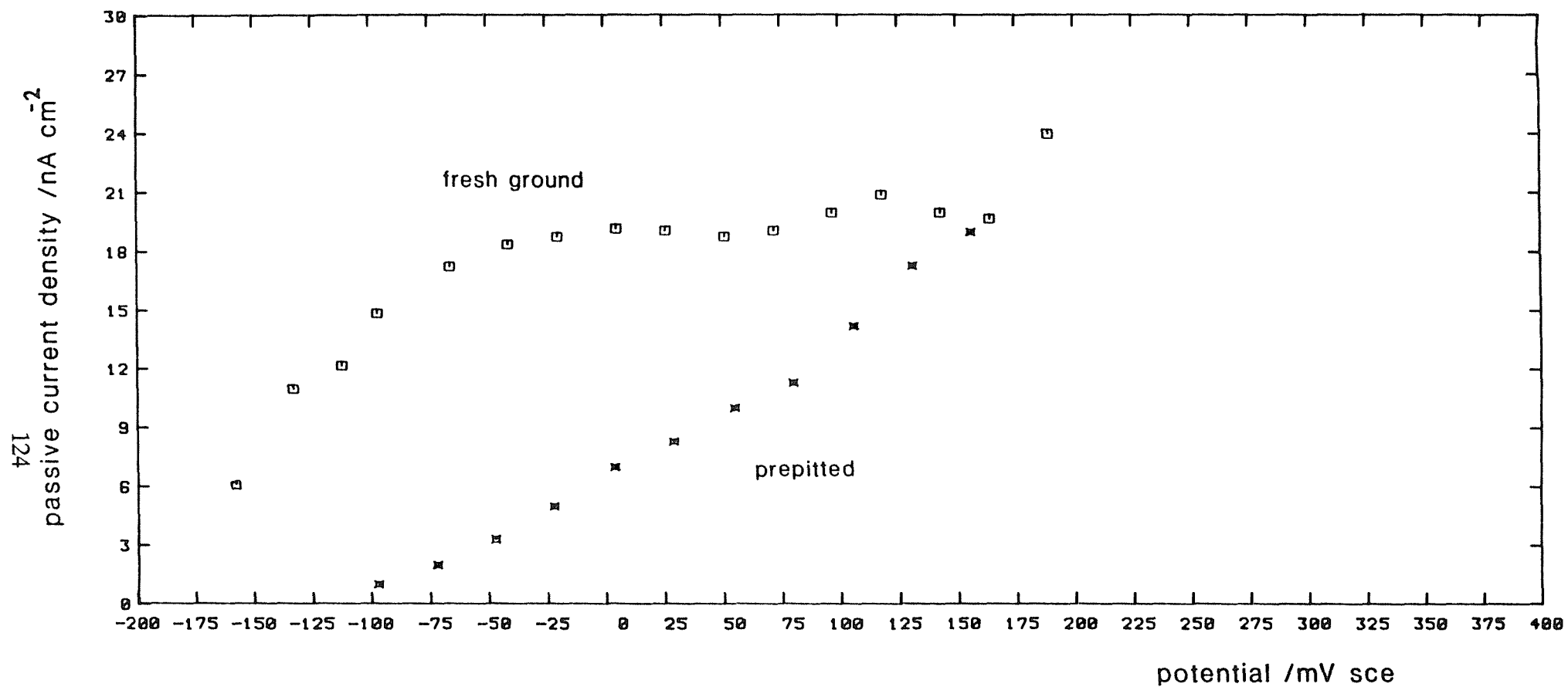


Figure 4.7 Variation in passive current density with electrode potential for fresh-ground and pre-pitted specimens (304L, 1000ppm chloride, 0.005mV/s)

with this. More recently, by using the flow rig described in this chapter to conduct experiments on progressively thicker films, it has been concluded that film thickness has a profound effect on the nucleation of unstable pits⁽¹⁷⁾ (although other possibilities, such as exhaustion of active sites, were not excluded in these experiments). Also, by plotting event frequency against passive current density, the results of all experiments were found to fall approximately on a common curve⁽¹⁸⁾, thereby lending support to the idea that passive current density provides the "driving force" for pit nucleation.

4.6 SUMMARY

This preliminary study has indicated that the initiation frequency of pits is not strongly dependent on solution flow. However, a specific effect of turbulent flow was to stop or inhibit the growth of a developing pit. This result, which is consistent with practical experience, is supportive of an interpretation based on a reduction in the thickness of the concentration boundary layer. This has two effects: an increased solution resistance outside the pit as the concentration gradient is swept away by the flow reduces electromigration (e.g. of chloride) into the pit; an increase in the flux of material out of the pit (by convection) is such that the concentrated pit solution, which is required for continued propagation, cannot be maintained.

A more speculative interpretation has been given in which it was suggested that the morphology of the pit and the strength of the pit cover may contribute to the observed effects of flow.

An observation that repeat experiments on the same specimens resulted in a steady decline in pit nucleation frequency has been found to be consistent with the presence of a progressively thicker film on the pre-polarised specimens. This reduces the passive current density, and is consistent with the hypothesis (described in the previous chapter) that the passive current provides the driving force for pit nucleation. Subsequent studies have reinforced this hypothesis^(17,18).

CHAPTER 5

THE IMPORTANCE OF SULPHIDE INCLUSIONS IN THE PITTING CORROSION OF STAINLESS STEELS

CHAPTER 5 - THE IMPORTANCE OF SULPHIDE INCLUSIONS IN THE PITTING CORROSION OF STAINLESS STEELS

5.1 INTRODUCTION

Commercially produced stainless steels contain numerous inclusions, second phases and regions of compositional heterogeneity. There have been many studies which have set out to identify where pits nucleate, many of which report that nucleation occurs at microstructural features. Figure 5.1 summarises some of the candidate locations for pit initiation⁽¹⁾. There is overwhelming evidence that the preferred sites for pit initiation are sulphide inclusions, and in particular MnS inclusions physically associated with oxides⁽²⁻⁶⁾. Further confirmation of this was found in the results reported in Chapter 3: small pits tended to be associated with sulphide inclusions, and oxide inclusions were sometimes observed at the bottom of small pits - probably residual oxide from a duplex oxide/sulphide inclusion.

In this chapter the role of inclusions, and specifically sulphur-rich inclusions, on pit initiation is examined in detail using two 304L model alloys and a commercial 304L stainless steel. The chapter is divided into three main sections. The first section surveys the literature on pit initiation at inclusions in stainless steels, particularly emphasising the role of sulphide inclusions. The second section describes the production of two model alloys, based on the AISI 304L specification. One alloy was produced with a minimum of impurities, whilst the other, although having a similar specification, was produced with increased sulphur and manganese contents, resulting in a higher volume fraction of sulphur-rich inclusions. The microstructural characterisation of these model alloys, together with a commercial 304L steel account for a substantial proportion of this chapter. The third section presents and discusses the results of pitting experiments on the three alloys.

5.1.1 The Origin and Types of Sulphide Inclusions in Stainless Steels

Sulphur is present in stainless steels as an impurity (0.03% maximum), or as an intentional addition to improve machinability, for example AISI type 303 (see Figure A.4, Appendix A). The solid solubility of sulphur in stainless steels is not known⁽⁷⁾, but is extremely low and consequently it usually precipitates as a sulphide during alloy

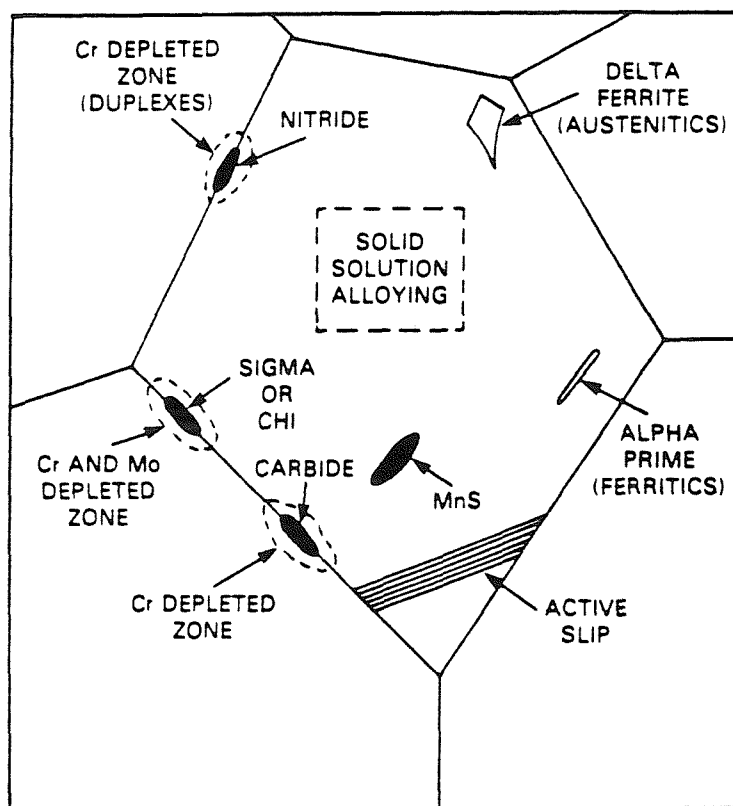


Figure 5.1 Some candidate microstructural sites for the initiation of localised corrosion⁽¹⁾

solidification. The sulphides are predominantly manganese sulphides, but they usually contain chromium, iron and other elements, and are often physically associated with oxides. When the steel solidifies, oxide particles which have not been able to escape from the melt, become trapped in interdendritic spacings. In these isolated liquid pockets, sulphur and other low solubility constituents are concentrated ahead of the solidification front. During the freezing of the rest of the melt, reactions between the melt and the oxides can take place, establishing a quasi-equilibrium. The sulphides with oxide particles present can therefore have a different composition from the single phase sulphides.

In all steels, one of the main roles of manganese is to tie up residual sulphur as manganese sulphide. This prevents the formation of FeS, which has a lower melting point and is detrimental to hot workability. In stainless steels, manganese has some additional roles: firstly, it reduces the amount of chromium lost (as sulphide) from solid solution in the alloy, and secondly, being an austenite stabilising element, it reduces the amount of nickel required to form a fully austenitic microstructure. (It is ironic therefore that MnS appears to provide optimum sites for pit initiation!). Very low sulphur contents are attainable with modern AOD practice. Consequently the amount of manganese required to combine with residual sulphur is appreciably lower than with older steelmaking methods. However, the manganese content of some AISI 300 series steels (such as type 316) is maintained at about 1.8% to ensure the solubility of nitrogen and to decrease the nickel alloying addition.

The great majority of sulphide inclusions in steel are of the α -MnS type. However, several different types of sulphide inclusion have been identified in stainless steels⁽²⁻¹⁷⁾. Analysis of inclusions from commercial steels, mainly based on isolates, show that the sulphides are MnS with various amounts of iron and chromium substitutionally dissolved^(8,9). Investigations by Sano and Inoye⁽⁹⁾ and Kiessling⁽⁷⁾ showed that iron and chromium may replace 60-70wt% of the manganese atoms in MnS without changing the lattice type. The exact amount of substitution depends on the way the steel is produced, heat treated etc.. Generally, as the manganese content of the sulphide decreases, the chromium content increases⁽¹⁰⁻¹³⁾. In a type 303 stainless steel, the iron content of the metallic sulphide was found not to vary with the chromium and manganese contents⁽¹¹⁾. Other sulphides found in stainless steels include (Al, Cr, Mn)S⁽¹⁴⁾ and mixed sulphide-silicate inclusions⁽¹⁵⁾. In a systematic

study on a 18Cr-2Mo ferritic stainless steel, Kiessling⁽⁷⁾ showed how the Ti content of sulphide inclusions could be varied by adjusting the Mn:Ti ratio.

Most studies of the composition of sulphide inclusions have been carried out on free-machining or re-sulphurised grades such as AISI type 303. There have been exceptions: Sydberger⁽¹³⁾ analysed a variety of austenitic stainless steels. In a type 304 steel containing 1.49% Mn and 0.012% S, the inclusion composition was found to be 3% Cr, 63% Mn and 34% S. In a steel with the same S content, but with the Mn reduced to 0.15%, the inclusion composition was 39% Cr, 24% Mn and 37% S; Kiessling and Lange⁽¹⁶⁾ found sulphides with the composition 26% Cr, 32% Mn, 1% Fe, 41% S in a steel containing 18% Cr, 1.47% Mn and 0.022% S. These results^(13,16), serve to illustrate the wide variation in inclusion chemistries found in steels with similar bulk alloy compositions. Li et al⁽¹⁷⁾ found that cerium additions to highly alloyed stainless steels, a common practice to improve hot workability, resulted in cerium-rich sulphides, oxy-sulphides and oxides. They also noted that calcium treated steels contained small spherical CaS particles.

5.1.2 Experimental Observations of Pit Initiation at Sulphide Inclusions in Stainless Steels

The recognition that pitting corrosion in steels may nucleate at sulphide inclusions is not recent, and dates back to the early part of this century^(18,19). The high sulphur contents and strong segregations of the alloys of those days assisted these observations (particularly during "sulphur-printing"). Evans⁽²⁰⁾ expressed the view that the detrimental influence of sulphur on the corrosion properties of steel was better recognised at the beginning of this century than decades later! In the 1930s, Tronstad and Sejersted⁽²¹⁾ and Homer⁽²²⁾ demonstrated that certain sulphide inclusions, designated as *active*, were more effective than others, termed *inactive*, in nucleating corrosion attack. These investigations were the forerunners to the many studies undertaken subsequently to address the role of sulphide inclusions in the corrosion of steels. The following is a summary of the substantial proportion of the literature which is devoted to austenitic stainless steels.

There have long been indications that pitting in stainless steels starts at sulphide inclusions⁽²³⁻²⁶⁾. The majority of studies have employed simple corrosion tests and microscopy.

Wilde and Armijo⁽²⁷⁾ performed pitting tests on high purity 14Cr-14Ni stainless steels with sulphur additions in the range 0.008-0.17%, in a 10% FeCl₃ solution. Pits nucleated at sulphide inclusions, and the intensity of the localised attack increased with increasing sulphur content.

Steinemann⁽²⁸⁾, using a Cr-Ni-Mo alloy also found that sulphide inclusions were particularly effective as pit nucleation sites in 0.16M NaCl (pH 7), and further commented that oxide inclusions were not.

Smialowska et al⁽¹⁴⁾ studied the effect of sulphide inclusions on the nucleation of pits in a commercial 18Cr-9Ni stainless steel at constant potential (0.5V SCE) in 0.5N NaCl solution. Using electron probe microanalysis, they showed that corrosion pits initiated at mixed manganese and iron sulphide inclusions, present either in the form of separate particles, or as shells surrounding oxides. Similar observations were reported by Eklund⁽²⁹⁾, who asserted that pits start exclusively at sulphide inclusions, with the duplex oxide-sulphide inclusions being especially active. No pitting was found to occur at purely oxide particles.

In an extension to their earlier work, Smialowska et al⁽³⁰⁾, used a combination of pitting tests and electron probe microanalysis to study pit nucleation in some other commercial stainless steels, including a 25Cr-20Ni austenitic stainless steel. They again observed that sulphide inclusions which formed shells around oxides were preferential pit nucleation sites. However, where sulphide inclusions occurred independent of oxides, they dissolved but did not nucleate pits. They suggested that the probable reason for this behaviour was that the geometry of the holes produced by the dissolution of the sulphides was unfavourable for pit formation, i.e. the holes were insufficiently narrow and deep. They further noted that not all sulphide inclusions nucleated pits, suggesting that some inclusion sites were more preferred than others, depending on geometry and composition. Studies of this type continue to appear in the literature. Despite major advances in analytical techniques, much of this work has not greatly improved on the earlier observations in furthering the understanding of pit initiation at sulphide inclusions. For example, the recent work of Ives et al⁽³¹⁾, using SEM and Auger Electron Spectroscopy, merely confirmed that morphology and composition were key components in determining the propensity with which inclusions initiate pits.

5.1.3 Proposed Mechanisms of Pit Initiation at Sulphides

The preferential nucleation of pits at sulphides has been interpreted in a number of ways in the literature. Some of these studies fall conveniently into one of two categories: those which identify the physical properties of the inclusions as being the predominant feature, and those which assert that the corrosion behaviour of the inclusion governs its ability to provide a site for pit initiation. A number of theories include aspects of each. A common conclusion appears to be that pit initiation occurs as a result of crevice formation at the inclusion/metal interface.

5.1.3.1 Physical Nature of Sulphide

In some steels, MnS has a much higher thermal expansion coefficient than a steel matrix⁽³²⁾. Therefore, during cooling, for example following solidification or hot rolling operations, the sulphides contract in volume more than the surrounding alloy. This results in the formation of voids at the inclusion/metal interface. Brooksbank and Andrews^(32,33), in addition to showing that voids may form between MnS and the adjacent metal in rapidly cooled low alloy steels, suggested that the creation of triaxial stresses in certain oxide inclusions (which have distinctly lower thermal expansion coefficients than steel), such as silica or alumina, could influence the protective ability of oxide films on steel. These factors are at the heart of Tronstad and Sejersted's⁽²¹⁾ theory. They assumed that the breakdown of a passive film at the boundary of certain inclusions occurs because of differing thermal expansions of the inclusion and metals, or by poor interfacial cohesion, resulting in crevice formation.

The notion that a crevice between a sulphide and the matrix might explain why pits initiate at sulphide inclusions is rather convenient (and has been adopted for this purpose in some studies). However, it should be noted that the work of Brooksbank and Andrews was concerned with steels undergoing phase transitions, when for example the volume expansion associated with the austenite to martensite transformation might be expected to result in inclusion-matrix decohesion. In austenitic stainless steels, no such transformation occurs, and there is no evidence to suppose that such decohesion occurs during cooling or working of these steels.

A number of studies have considered the influence of inclusion morphology on the pitting susceptibility of austenitic stainless steels^(15,34-37). These studies can be

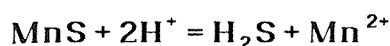
summarised as follows. For a given type of inclusion, smaller and spheroidised particles are less likely to initiate a pit than elongated, plastically deformed ones⁽¹⁵⁾. Forchhammer and Engell⁽³⁷⁾ found that pit density depended on heat treatment: when sulphide inclusions in a 24Cr-15Ni stainless steel were finely dispersed, exposure to 3% NaCl yielded numerous small pits. However, when the steel was heat treated at 1280° C for 12 hours to allow the sulphides to coagulate, the number of pits was limited, but they were more damaging. Searson and Latanision⁽³⁸⁾ found that small well dispersed inclusions in a rapidly solidified AISI type 303 stainless steel did not nucleate pits, but isolated pits did form at powder processing defects.

Manning et al⁽³⁶⁾ found that the length of sulphide inclusion/metal interface per unit area of microstructure influenced pitting susceptibility. They used this parameter to explain the decreased resistance to pit initiation at rough surfaces and sheet specimen edges. By assuming that sulphide dissolution begins at the metal/sulphide interface, they asserted that the greater the length of the interface, the greater the probability that local environmental and geometrical conditions for pit propagation exist. However, in further work⁽³⁹⁾ they appeared to concede that composition of the matrix and sulphide were more important governors of pit initiation. Li et al⁽¹⁷⁾ found that controlled additions of the rare earth metal (REM) cerium to highly alloyed austenitic stainless steels improved pitting resistance by modifying both the morphology and the chemistry of inclusions. The inclusion shape was changed from stringers to globules. The stability of inclusions in chloride environments increased in the order MnS - RE_xS_y - RE₂O₂S - RE_xO_y. They noticed in passing that a stainless steel containing small, spherical CaS inclusions displayed an even better pitting resistance than the REM-treated steels.

5.1.3.2 Sulphide Dissolution

Sulphides tend to be less noble than the passive film on stainless steels, consequently they act as small local anodes, in a large passive stainless steel surface. Of the main sulphide forming elements present in stainless steels, MnS has the most negative, and therefore favourable, free energy of formation (-209kJ/mole S at 25° C, compared with -95.5kJ/mole and -150kJ/mole for FeS and CrS respectively). Also, in acid solutions, including active localised corrosion cells, MnS readily dissolves forming H₂S and various manganese ions⁽⁵⁾. The combination of these two factors has led to a

number of studies involving stainless steel in acid solutions, when H_2S can be produced (a third property of MnS , its electrical conductivity, is considered later):



These studies, briefly discussed below, also have relevance to pit propagation: large propagating pits must encounter and dissolve sub-surface inclusions, releasing more H_2S into the occluded geometry of the pit. Many investigators have established an accelerating effect of H_2S on the corrosion rate of iron, steel and nickel, in addition to studies on stainless steels. They invariably conclude that H_2S impedes the formation of passive films. For example using an 18Cr-10Ni stainless steel, Crolet et al⁽⁴⁰⁾ measured anodic polarisation curves in $\text{H}_2\text{SO}_4 + \text{HF}$ solutions with different concentrations of H_2S . The experiments were repeated on similar steels, containing different sulphur concentrations. They found that critical passivation potentials were increased as the H_2S content of the solution, or the sulphur content of the steel, was increased. Indeed, with a high enough concentration (0.01M) of H_2S in the solution, the steel did not passivate. These results were interpreted to indicate that in the presence of adsorbed H_2S molecules (or HS^- ions) on the metal surface, the formation of the passive film is hampered. Brennert⁽⁴¹⁾ reported similar findings for an 18Cr-8Ni-(0.01-2.6Mo) steel with various sulphur additions during polarisation tests in 0.1M HCl and 0.1M NaCl solutions: the active range was extended to include more anodic and cathodic potentials. A similar effect was observed if H_2S was added to the solution. Riedel and co-workers⁽⁴²⁾ looked at the influence of acid soluble inclusions on the passivation behaviour of austenitic stainless steels, finding that, by increasing the amounts of H_2S or HS^- ions in solution, the hydrogen overvoltage was increased, with a coincidental decrease in the cathodic Tafel slope, and enhanced stimulation of the anodic metal dissolution reaction.

In the mechanism proposed by Smialowska and co-workers^(2,43) they attempted to encompass most of what is known about pit initiation at inclusions into a single theory. They assumed that at sites on the metal surface when non-metallic inclusions are present, the film is inhomogeneous either chemically or physically. They presumed that, at the metal-inclusion interface that the oxide film is defective, stressed and susceptible to failure by localised attack. Through such a defective oxide film, transport of metal ions is easier than through a more perfect film. At these defective spots, there occurs a critical agglomeration of chloride ions, which occurs at a potential slightly less positive than the pitting potential, while pit nucleation takes

place at a more noble potential. The metal ions, transported through the defective film react with the chloride to form (in the case of stainless steel) iron and metal chlorides. Acidification occurs locally due to the hydrolysis of the metal chloride, the acid attacks the defective film, and the aggressive environment now has access to the metal surface. The pit develops when the local chemistry is such that repassivation cannot occur. The presence of H_2S additionally prevents the steel from passivation.

The above hypothesis is probably at least partially valid, as it incorporates the findings of many phenomenological studies. However, without a more detailed knowledge of the processes involved, the mechanism suggested is difficult to prove. The remainder of this review section concentrates on the handful of papers which have addressed in detail the question of what it is about sulphide inclusions, embedded in a stainless steel surface, that may cause them to initiate a pit when exposed to a suitably corrosive environment.

The electronic conductivity of sulphide inclusions, which varies with composition⁽⁴⁴⁾, has featured strongly in the theories of Wranglen⁽⁴⁵⁾ and Eklund⁽⁴⁶⁾. For stainless steels immersed in aqueous chloride solutions, Wranglen suggests that, because sulphides have a higher electronic conductivity than the passive oxide film, chloride anions are selectively adsorbed onto the surface of sulphide inclusions, facilitating anodic dissolution of the sulphide. This process occurs preferentially at the edges of the sulphide inclusions (where the current density is highest), leading to exposure of bare metal underneath the adjacent oxide, making it vulnerable to attack.

Eklund's^(29,46) theory was somewhat different. It merits a more detailed discussion, since until recently⁽⁴⁷⁾ it was the only work which addressed the mechanisms of sulphide dissolution and gave a convincing account of its role in pit initiation. He reasoned that because manganese sulphides are electronic conductors, they can be polarised to a potential at which stainless steel is in its passive state. He calculated potential-pH diagrams which suggested that in this potential regime, the sulphides are thermodynamically unstable and should tend to dissolve: Figure 5.2 shows the potential-pH diagram calculated for the $MnS-H_2O-Cl^-$ system⁽⁴⁶⁾. It is applicable only to relatively concentrated solutions (e.g. 0.1M Mn species), but it is useful in defining the dissolution behaviour of MnS. In the pH range 4.8-13.8, the highest potential at which MnS can exist is about -100mV (SHE) at pH 5; at more noble potentials MnS dissolves to sulphur. Below pH 4.8, MnS dissolve to form H_2S and various manganese

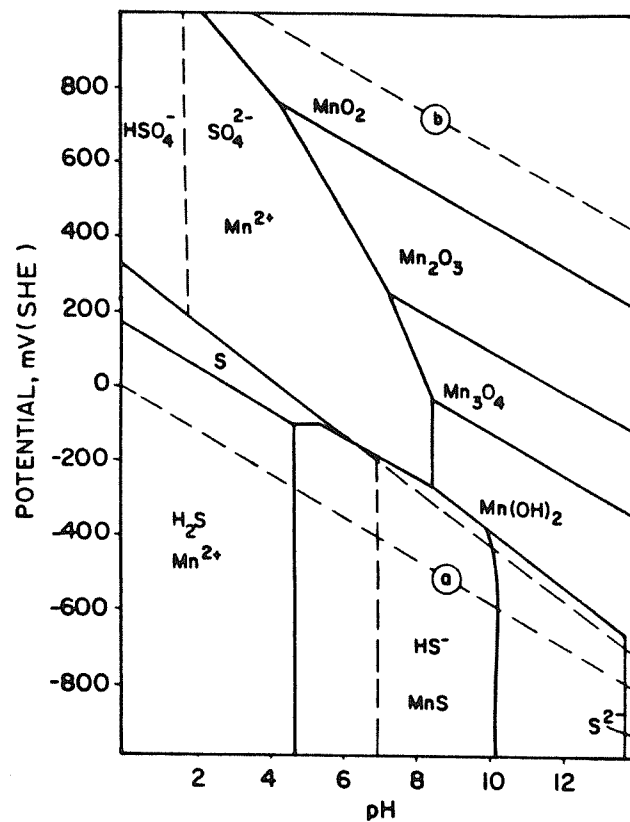


Figure 5.2 Potential-pH diagram for the MnS-H₂O-Cl⁻ system⁽⁴⁶⁾
 Calculated on the basis of 0.1M SO₄²⁻, Cl⁻ and Mn²⁺, respectively

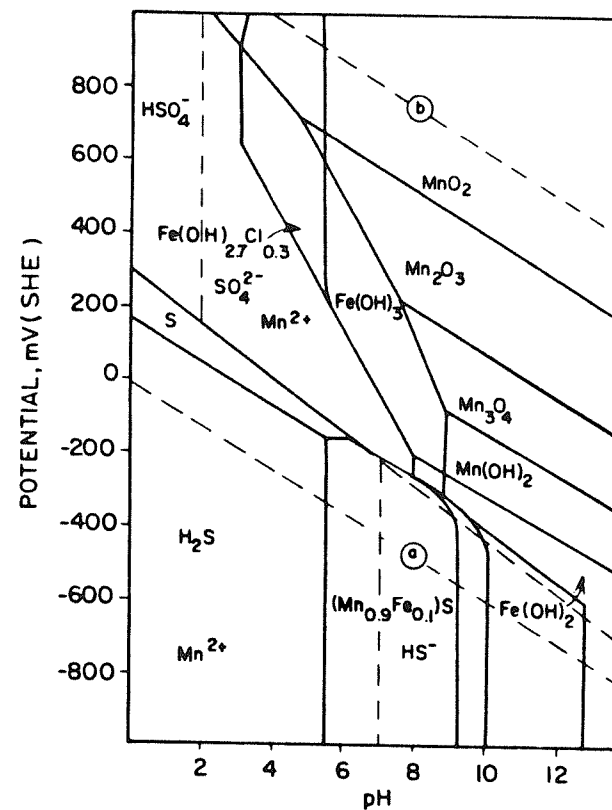
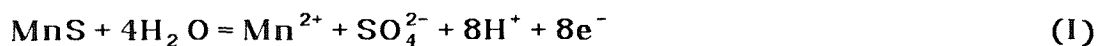


Figure 5.3 Potential-pH diagram for (Mn_{0.9}Fe_{0.1})S-H₂O-Cl⁻ system⁽⁴⁶⁾
 Calculated on the basis of 0.09M Mn²⁺, 0.01M Fe²⁺, 0.1M SO₄²⁻, and 0.1M Cl⁻

ions. The potential-pH diagram calculated for $(\text{Mn}_{0.9}\text{Fe}_{0.1})\text{S}-\text{H}_2\text{O}-\text{Cl}^-$ (46), Figure 5.3, indicates that substitution of Mn by Fe decreases the domain over which the sulphide is stable. Eklund further suggested that the low (relative to the metal) electronic conductivity of the sulphide helps to localise the attack at the inclusion/metal interface. The dissolution and resulting crevice formation was proposed to occur by the following reaction sequence:



The form of the elemental sulphur observed on the MnS (discrete loosely packed particles) suggested to Eklund that it is precipitated from solution. Initially, the exposed metal surface may passivate, but as dissolution proceeds an acid solution is formed in the microarea due to hydrolysis of the metal ions from the sulphides. When the solution has reached a certain composition, the exposed metal surface can no longer passivate and metal atoms from the lattice enter solution causing a sharp potential drop as a pit is initiated. The electrochemical dissolution of the sulphide will then stop since the potential is now within the domain of thermodynamic stability.

A pit will continue to propagate if the rate of formation of hydrogen ions from metal matrix hydrolysis exceeds that of the rate of consumption by chemical dissolution of the sulphide. The bared metal matrix will, on the other hand, passivate if the hydrogen ions are neutralised through the formation of H_2S . This hypothesis is not consistent with the observations of other workers (described above) where H_2S was found to *inhibit* passivation. During open circuit experiments on a high sulphur 18Cr 8Ni stainless steel, Eklund observed potential fluctuations which he attributed to "unsuccessful pitting attempts" at numerous inclusions on the stainless steel surface.

In observing that geometrical considerations are important in determining whether or not a pit will propagate (- crevices down the sides of inclusions are less easily diluted) Eklund reported that, when pits nucleate at the inclusion/matrix interface, the sulphide may be only partly dissolved. He suggested that the pit then propagates under the passive metal surface, and may occasionally reach the surface, resulting in

an irregular network⁽⁴⁶⁾. This is consistent with the observations reported in Chapter 3 (Figure 3.19 and 3.23).

It is evident that the electrochemical dissolution properties of the sulphide inclusions depend on their composition, which in turn depends on where and when in the steel ingot the inclusions were formed. Therefore, even in the same steel sample, there will be *active* and *inactive* sulphides.

In a very recent study, Lott and Alkire⁽⁴⁷⁾ examined the role of MnS inclusions on the initiation of crevice corrosion of type 304 stainless steel. First of all, they carried out a series of qualitative potentiostatic experiments on MnS electrodes immersed in deaerated 0.1N NaCl solution at various initial pH values (5 to 8.5). When MnS was anodically polarised to potentials in the range -125 to 0mV SCE, the only species found in solution was thiosulphate ion. They were surprised by this, since on thermodynamic grounds sulphite would be expected for the experiments conducted at a neutral pH and a relatively high potential⁽⁴⁸⁾. Their investigations into why thiosulphate was not oxidised to sulphite concluded that this was not a kinetically favourable reaction on MnS. Following anodic polarisation, analysis of the solution and surface analysis of the MnS showed that the Mn went into solution, whilst yellow islands, 90% S-rich, were found on the normally green MnS electrode surface. In-situ spectro-electrochemical experiments confirmed that only thiosulphate ions were present. In a sequence of experiments they showed that:

- (1) the production of elemental sulphur was not as an intermediate reaction step in the formation of thiosulphate: the presence of sulphur did not reduce the number of coulombs required to produce thiosulphate from MnS (8C). Therefore, sulphur must be produced by a separate reaction.
- (2) no other reaction that was a net consumer or producer of coulombs occurred at the MnS surface to any appreciable extent: the value of z for the electrochemical reaction of MnS producing thiosulphate was found to be approximately 8 for a range of potential and pH conditions. This result supported the finding that only thiosulphate was found in solution, and also that sulphur results from a chemical, not an electrochemical reaction.
- (3) elemental sulphur could be produced from MnS with a consumption of protons and without net passage of charge: MnS powder was added to a series of 0.1N NaCl solutions, with a pH range from 2 to 6. Sulphur precipitated in the near

neutral solutions (pH 4,5,6) and the final pH was about 8 in all 3 cases. The pH 2 and pH 3 solutions gave off H_2S .

- (4) the pH in the solutions actually rose: had protons been produced and not consumed, the pH should have dropped.

On the basis of these experimental observations they proposed the following reaction sequence:



They went on to show that the MnS anodic dissolution reaction was irreversible. Then moving to a stainless steel electrode, they showed that H_2 , which according to reaction (2) should have been present, would not have been oxidised at the stainless steel surface due to kinetic limitations.

In a series of galvanostatic experiments, Lott and Alkire showed that above certain critical ratios of chloride ion concentration to thiosulphate ion concentration, the stainless steel became active, Figure 5.4. The nature of this passive film breakdown remains unknown. The effect of ferrous ions and dissolved oxygen had little effect on the depassivation.

Their proposed mechanism for crevice initiation therefore requires the dissolution of MnS to produce thiosulphate. If the concentration of thiosulphate and chloride ions can build up sufficiently to exceed the critical concentrations in Figure 5.4, then breakdown of passivity can occur at the steel surface adjoining the inclusion. Due to the potential distribution within the crevice, both the migration of chloride and the electrochemical production of thiosulphate varies with position. After breakdown of the passive film, the dissolution increases by many orders of magnitude. Dissolution of the metal matrix, and hydrolysis of (particularly) the chromium ions, causes the local crevice pH to drop.

They reasoned that, if the above mechanism was correct, then inclusion density, applied potential and crevice geometry would be expected to influence initiation. This proved to be the case: with sufficiently extreme values of the three variables - a high

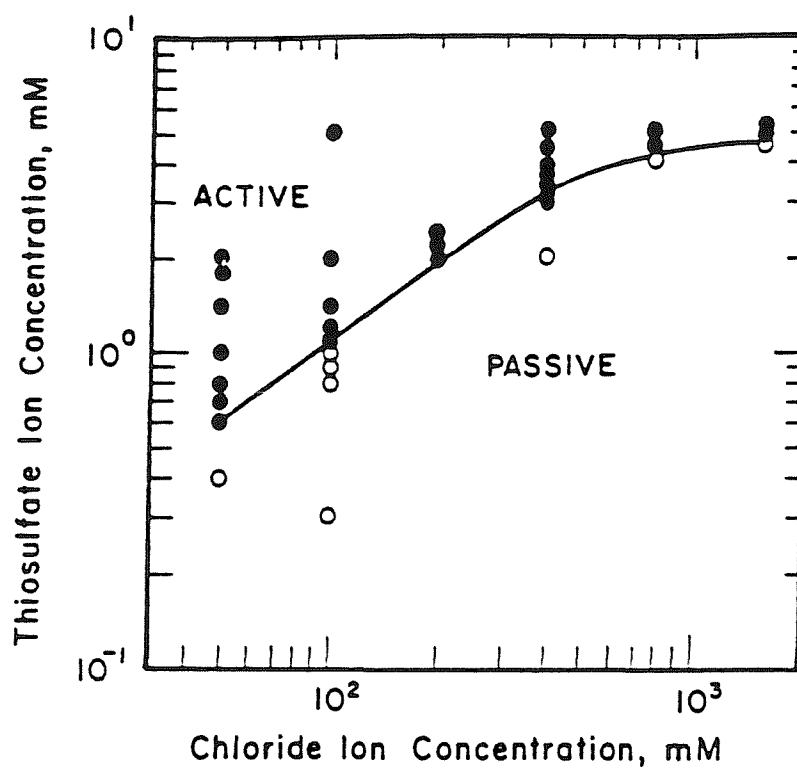


Figure 5.4 Conditions under which 304 stainless steel remains active or becomes active during dissolution at $25 \mu\text{A}/\text{cm}^2$ in deaerated sodium chloride/sodium thiosulphate electrolytes⁽⁴⁷⁾

purity steel with few inclusions, cathodic protection and a wide crevice respectively - crevice initiation could be slowed or even prevented.

In two experiments, the crevice was opened before breakdown occurred. In both cases the average crevice solution pH was found to be nearly neutral (pH 5 to 7). They made the point that had chromium been dissolving in proportion to its bulk metal composition (18%), then the pH should have been much lower. Mechanisms which require local acidification to occur in order to cause depassivation are clearly questioned by this work.

Lott and Alkire's work on crevice corrosion should be directly applicable to the nucleation of pitting corrosion at the sulphide inclusion/matrix interface in stainless steel in neutral aqueous chloride solutions. It is consistent with Eklund's studies⁽⁴⁶⁾, but essentially examines the early stages of nucleation in finer detail. Their (well supported) claim that thiosulphate ions play an important role in the initiation of localised corrosion is an attractive one, since thiosulphate is well known, under certain conditions, to greatly promote localised corrosion of stainless steels.

Thiosulphate is metastable in aqueous, room temperature solutions, and so is not found on the potential-pH diagram for the S-H₂O system. However, an informative metastable diagram can be prepared by omitting sulphate, as shown in Figure 5.5⁽⁴⁹⁾. For simplicity, this diagram considers only one polythionate ion (tetrathionate), and omits polysulphides which are important in neutral or alkaline solutions.

The extremely potent nature of the thiosulphate ion in promoting localised corrosion of stainless steels is well known⁽⁵⁰⁻⁵⁶⁾, and is thought to be due to its reduction to adsorbed sulphur (or a sulphide) on the bare metal surface, activating the anodic dissolution and hindering passivation (see below). In 304 stainless steels, this has been demonstrated in chloride solutions^(50,51) and in sulphate solutions in the absence of chlorides⁽⁵²⁾. Cr³⁺ hydrolysis can then lower the pH to a low enough value to sustain the very high rates of anodic dissolution required for pit initiation.

Pure thiosulphate does not cause pitting because the reduction or disproportionation of thiosulphate consumes protons, which tends to maintain the pH at about 3, which is too high to initiate a pit:

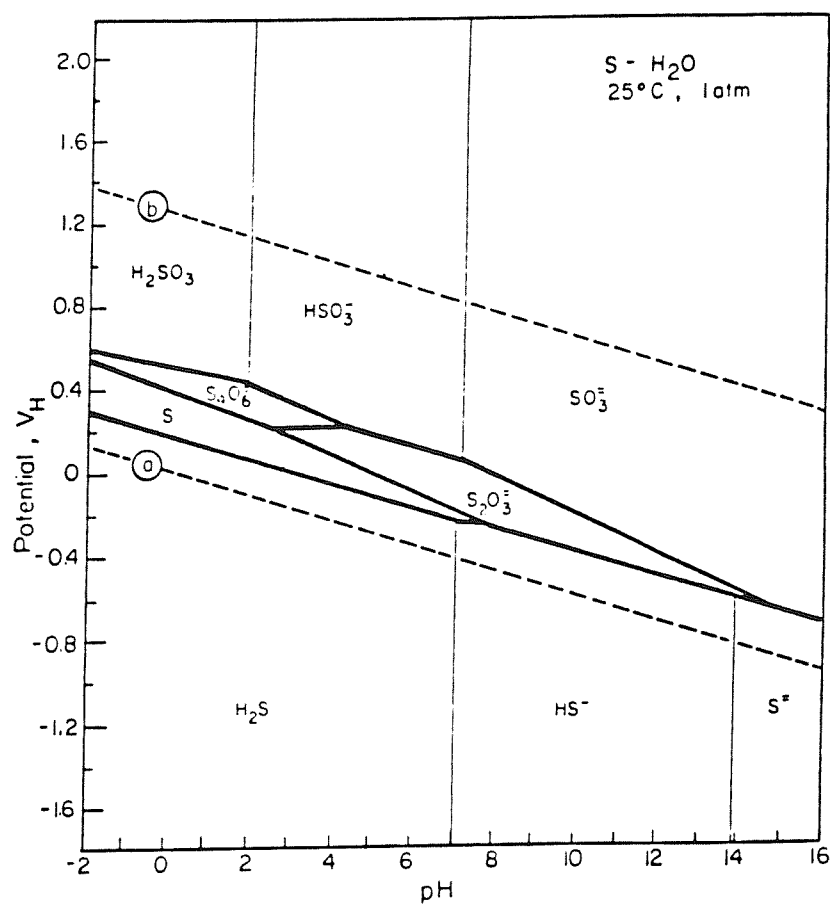
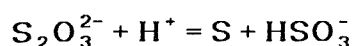


Figure 5.5 Metastable potential-pH diagram for the S-H₂O system at 298K, omitting sulphate⁽⁴⁹⁾
Lines are drawn for 0.2g of S/litre



The corrosion behaviour of sulphur-covered surfaces has been studied in a series of papers by Marcus and Oudar⁽⁵⁷⁻⁶⁰⁾ using pure nickel and Ni-Fe alloys with and without sulphur-doping. These studies on nickel are relevant to the pitting corrosion of stainless steels: of the major alloying elements, nickel is the most noble and during active corrosion (i.e. when no passive film is present) nickel is enriched at the corroding surface. Their findings on the effects of sulphur can be summarised as follows.

1. **A catalytic effect on the dissolution rate:** suggested to be due to a disruption by sulphur of the metallic bonds, which lowers the activation energy required to break the bonds. This was consistent with a shift to lower potentials observed in the active region of the i-E curves.
2. **A poisoning effect on passive film formation:** as long as the surface is covered with a complete monolayer of adsorbed sulphur, the passive film is not formed. The formation of an oxide is delayed until 20-30% of a monolayer is removed, which occurs at a higher potential than the normal passivation potential of the sulphur-free surface.
3. **Protective nature of passive film reduced:** on surfaces partially covered by sulphur, the sulphur is responsible for structure changes in the passive film, which reduces the protective character of the film.

They went on to suggest that, where sulphur can be accumulated locally on a surface - dislocations, grain boundaries etc - the concentration of sulphur may reach the critical concentration (about 80% of a monolayer) where passivation is prevented, and localised corrosion can occur. On the remainder of the surface, the sulphur coverage remains below the critical value. Clearly these ideas can be extended to include sulphur containing inclusions which, on dissolution, yield elemental sulphur or thiosulphate.

The critical ratio of chloride to thiosulphate reported by Lott and Alkire was consistent with the findings of Newman and co-workers, who found that the maximum detrimental effect of thiosulphate occurred at about 1/20 of the molar concentration of the major anion, which in their work was chloride or sulphate. This effect was also found to be highly potential dependent. Discussing his observations of pitting in

sulphate/thiosulphate solutions, Newman⁽⁵²⁾ concluded that, for pitting to occur, a potential is required that is low enough for adsorbed sulphur to be stable (and generated at sufficient rate), but sufficiently high that the metal can be dissolved rapidly enough to retain the concentrated pit solution. There must be a small but sufficient amount of thiosulphate and a larger amount of inert ion (such as sulphate or perchlorate) so that the inert ion is the predominant ion transported into the pit nucleus. Pitting could be prevented by cathodic or anodic protection, or by having the major anion present in sufficient excess (including chloride, within reason!). These ideas are shown schematically in Figure 5.6⁽⁶¹⁾.

To summarise, the theory of the involvement of thiosulphate (and adsorbed sulphur), formed by the dissolution of MnS, in the initiation of pitting corrosion of type 304L stainless steel is both attractive and feasible. The situation for more highly alloyed grades is at present unclear, since these alloys pit at potentials where thiosulphate may not be reduced to elemental sulphur. The indication from Newman and co-workers⁽⁵⁰⁾ was that thiosulphate does not have much of an effect on more highly alloyed materials. However, since the more highly alloyed steels often contain molybdenum, it is possible that Mo^{3+} ion reacts with adsorbed or dissolved sulphur species, rendering it harmless⁽⁶²⁾.

5.1.4 Methods of Improving Pitting Resistance

The recognition that MnS inclusions are the most favoured pit initiation sites has led to exploration of ways to remove them, modify their composition and change their morphology.

Removal techniques include the so-called *passivation* treatment, often used for resulphurised stainless steels which consists of immersion for 30 minutes in a solution containing 50% nitric acid and 2% sodium dichromate at 50 °C⁽¹²⁾. The improved pitting resistance following this treatment is attributed to removal of surface sulphides^(63,64). The surface holes left after the removal of the sulphides may then be rinsed with sodium hydroxide to remove any entrapped acid. Electrochemical studies using type 316 stainless steels have shown that this treatment raises the pitting potential in deaerated seawater by +250mV⁽⁶⁵⁾.

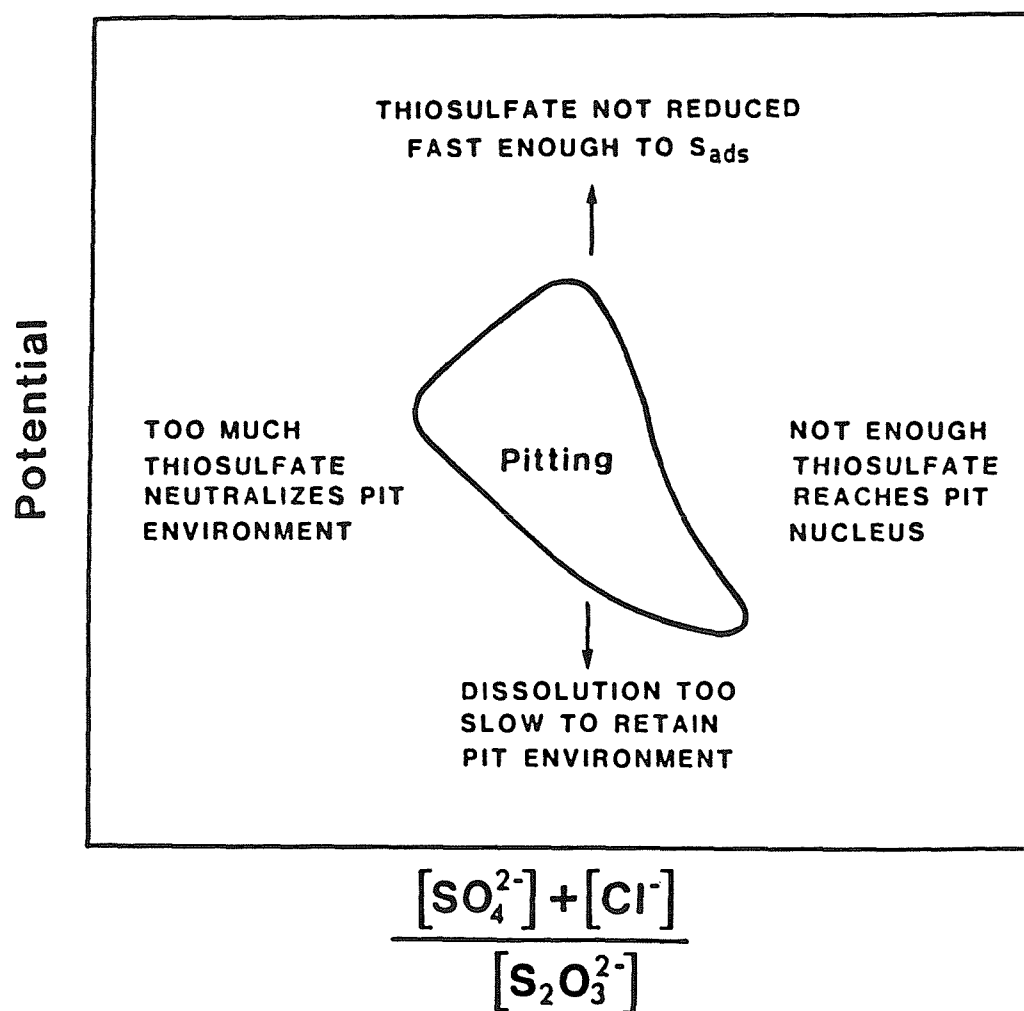


Figure 5.6 Summary of reasons for limited zone of pitting in sulphate + thiosulphate solutions⁽⁶¹⁾

The main emphasis on compositional modifications of sulphides has been to reduce the manganese content of the steel. A low manganese bulk steel, in which the pitting resistance is improved by the presence of higher chromium contents in the sulphides (which are less soluble than MnS), is now produced commercially in Europe⁽⁶⁶⁾. Another approach has been to make cerium additions (up to a maximum of 0.07%) to highly alloyed stainless steels⁽¹⁷⁾, which significantly increases the pitting resistance. However since the additions change the volume fraction, chemistry and morphology of inclusions, it is difficult to ascribe the pitting resistance to a single cause.

In experiments on conventional and rapidly solidified type 303 stainless steel, produced by the powder route, Searson and Latanision⁽³⁸⁾ demonstrated the enhanced general and pitting corrosion resistance of the rapidly solidified alloy. This improvement in pitting resistance was attributed to the size of the sulphide inclusions, i.e. that they were "too small to nucleate pits successfully".

Recently, studies of the effect of laser melting of surface layers of type 304 stainless steel suggest that this improves pitting resistance⁽⁶⁷⁻⁷⁰⁾. Potentiostatic polarisation curves taken from the laser-melted surfaces show a complex curve, indicative of pit nucleation and rapid repassivation. No sustained current rise was observed, suggesting that sustained pitting did not occur. This was confirmed in post-test examinations, when no pits were found. These observations were subsequently attributed to the removal of manganese sulphide from the laser melted layers^(67,70). The use of laser surface treatment to improve corrosion resistance is the subject of Chapter 6 in this thesis.

5.1.5 The Experimental Work Presented in this Chapter

In this chapter, experiments were performed on three variants of AISI type 304L stainless steel. Two model alloys were made specifically for this work, produced with respectively high and low volume fractions of sulphide inclusions. The production of these alloys is summarised. The commercial purity type 304L stainless steel used in the studies in Chapters 3 and 4, provided the third alloy variant.

The microstructures of the three alloy variants were characterised using a

combination of quantitative image analysis, and chemical analysis of inclusions using the scanning electron microscope (SEM) and electron probe microanalyser (EPMA).

The results of pitting corrosion tests on the two model alloys are then described, and the discussion which follows incorporates the results obtained for the commercial purity steel (from Chapter 3).

5.2 EXPERIMENTAL

5.2.1 Model Alloy Production¹

The model alloys were produced to the AISI 304L specification. For each, requisite amounts of high purity electrolytic iron and chromium, low carbon nickel shot, ferro-manganese and calcium silicide were induction melted in a vacuum furnace and cast into 10kg ingots. The ingots were hot-rolled in an inert gas atmosphere, and then cold-rolled to produce 5mm thick plates. Finally, the plates were annealed at 1100 °C for 1 hour in vacuum. The analysis of the steels is given in Table 5.1, which also includes the analysis of the commercial alloy and the AISI specification. 25mm diameter disc specimens were milled from the plates for microscopy and pitting experiments. The microstructures of the two model alloys consisted of single phase austenite, with equiaxed grains of approximately 50 μ m, determined using the mean linear intercept (m.l.i.) method⁽⁷¹⁾. The commercial alloy was predominantly austenite, with approximately 5% δ -ferrite present as discrete islands. The grain size of the commercial steel was 60 μ m (m.l.i.).

5.2.2 Characterisation of Inclusions

Two analytical techniques were used to characterise the inclusions in the two model alloys and the commercial purity 304L. Firstly, an optical microscope coupled to an image analyser was used to determine the volume fraction and size distribution of inclusions. Secondly, the chemical composition of inclusions was established using a scanning electron microscope (SEM) equipped with energy dispersive X-ray analysis (EDAX), and an electron probe microanalyser (EPMA) equipped with both wavelength and energy dispersive spectrometers.

¹ The model alloys were produced by Sheffield University (Metals Advisory Centre)

Table 5.1 Composition of Steels¹

STEEL TYPE	Weight % (Fe Balance)									
	Cr	Ni	Mn	Si	C	P	S	Mo	Cu	Ti
AISI 304L - Spec. ²	18-20	8-12	2.00	1.0	0.030	0.045	0.030			
304L - HiP	18.4	10.4	0.55	0.30	0.003	<0.01	0.003	<0.02	<0.02	<0.02
304L - HiS	18.4	10.4	0.82	0.28	0.004	<0.01	0.080	<0.02	<0.02	<0.02
304L - CP	18.2	9.3	1.13	0.42	0.020	0.026	0.011	0.038	0.21	<0.02

NOTES

- 1 - Analysis determined by X-ray fluorescence, except S and C (LECO)
- 2 - Single figures are maximum values
- CP = Commercial Purity
- HiP = High Purity
- HiS = High Sulphur

5.2.2.1 Image Analysis

Specimens of each 304L stainless steel variant were metallographically prepared to a $1\text{ }\mu\text{m}$ diamond polish. The analysis was performed on unetched specimens, and particular care was taken to ensure the removal of dust etc. prior to the analysis. An optical microscope (Carl Zeiss Universal) was used in conjunction with a high resolution television camera and a sophisticated image analysis system (Cambridge Instruments Quantimet 970) to count and measure the inclusions at a magnification of $\times 1700$ on 225 randomly chosen fields on each sample. Once a field had been selected, the analysis sequence was controlled using a software routine written specifically for the task, a flow diagram of which is given in Figure 5.7. Standard measurements were made over 500,000 pixels, each with an area of $0.17\text{ }\mu\text{m}^2$, giving a field size of 0.014mm^2 . Microstructural features were detected on a grey level threshold. The Quantimet uses 64 grey levels, and therefore had the capability of distinguishing inclusions from the matrix, and also different types of particles, from their grey scale. Limits on feature size were imposed on the analysis such that only features in the range $0.5 - 1000\text{ }\mu\text{m}^2$ were recorded. The lower limit was imposed because of limitations in the resolution of the microscope:

$$\text{Resolution} = \frac{\lambda}{2 \times \text{N.A.}}$$

Where:

λ = wavelength of light

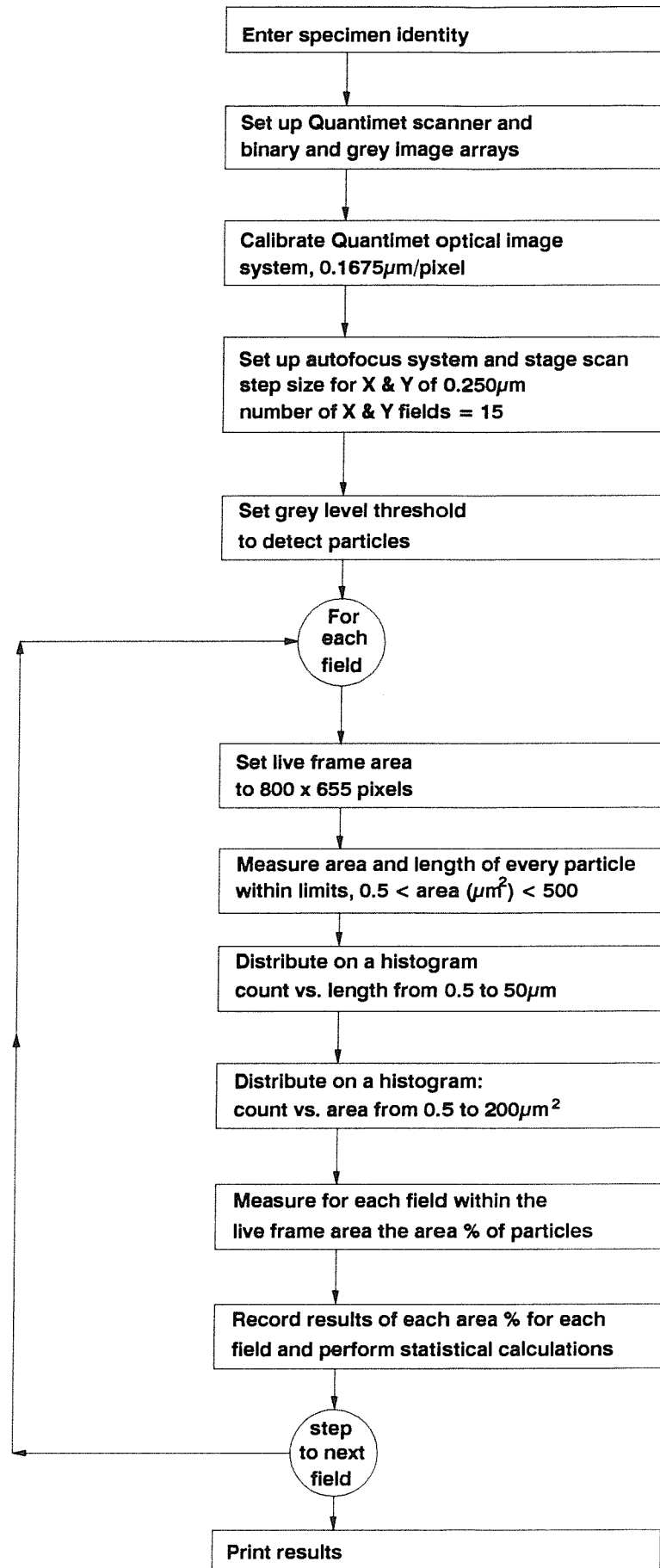
N.A. = Numerical Aperture of objective lens

This expression assumes that the numerical aperture of the condenser lens is identical to that of the objective lens. This is not the case in practice, and the equation is modified:

$$\text{Resolution} = 0.61 \frac{\lambda}{\text{N.A.}}$$

In this work, a green filter was used ($\lambda = 550\text{nm}$) and the numerical aperture of the objective lens was 0.85, such that the resolving power of the microscope was limited to $0.39\text{ }\mu\text{m}$. Also, the "useful" magnification (in terms of resolution) of a microscope is limited to about $(1000 \times \text{N.A.})$, corresponding to $\times 850$ in this work. The additional

Figure 5.7 Flow Diagram of Image Analysis Routine



magnification used in the image analysis, derived from the television camera, was used simply to enlarge the resolvable particles.

The image analysis routine (Figure 5.7) measured the area and the longest axis of individual particles, and also the average area fraction of particles for all fields. The basic principle employed here is that the volume fraction (V_f) of a phase is equal to the area fraction in random planar section through the three dimensional microstructure⁽⁷¹⁾:

$$V_f = \frac{V_\alpha}{V} = A_f = \frac{A_\alpha}{A}$$

where:

V_f = volume fraction of α - phase

V_α = volume of α - phase in specimen

V = total volume of the specimen

A_f = area fraction of α - phase

A_α = area fraction of α - phase in random planar section.

A = total area of random planar section

5.2.2.2 Chemical Composition of Inclusions

The types and compositions of inclusions present in the three steels was established by combining qualitative energy dispersive spectroscopy (EDS or EDAX) analysis in the SEM with quantitative analysis using wavelength dispersive spectroscopy (WDS) in the EPMA.

EDS analysis in the SEM - These analyses were performed on specimens polished to a $1\mu\text{m}$ diamond polish. The back scattered electron image was used to improve contrast between inclusions and the matrix. For each steel type, at least 100 inclusions were chosen at random and EDAX analysis was performed using an accelerating voltage of 15kV at magnifications in the range x2000 - x5000, according to the size of the inclusion. The characteristic X-ray spectra from each inclusion were recorded along with the size and shape of the inclusion.

EDS and WDS analysis in the EPMA - Having obtained qualitative information on the chemical compositions of inclusions present in the three steels, the specimens were then transferred to the EPMA for quantitative analysis of the range of inclusion types. The EPMA used for this work (JEOL 8600 Super Probe) was equipped with 4 wavelength spectrometers, in addition to full EDAX facilities. A typical analysis sequence consisted of:

- i) EDAX analysis to locate the inclusions of interest;
- ii) on the selected inclusions, WDS was performed for Cr, Fe, Mn, O, and S, and was supplemented by a full EDAX spectrum to show which, if any, other elements were present.

Analyses were performed using an accelerating voltage of 15kV and a beam current of 41nA, such that the analysis volume was restricted to about $1\mu\text{m}^2$.

5.2.3 Pitting Experiments

The pitting experiments performed on the model alloys were of two types:

- (1) identical experiments to those described previously for the commercial purity 304L (Section 3.2, Chapter 3), comprising slow potentiodynamic experiments ($5 \times 10^{-6}\text{V/s}$) in dilute (1,000ppm) chloride solution, and logging the current at 1Hz; these experiments therefore provided information on current transients associated with unstable pitting in the potential regime prior to pit propagation;
- (2) similar experiments to the above, except for the data acquisition; the current was measured every 30s until the $10\mu\text{A}$ limit was exceeded, at which point the potential was recorded and the experiment stopped. The current was monitored on some specimens using a chart recorder. These experiments provided pitting "breakdown" statistics without the requirement for sophisticated data acquisition equipment.

At least 30 pitting experiments were carried out on each alloy variant.

5.3 RESULTS

5.3.1 Image Analysis

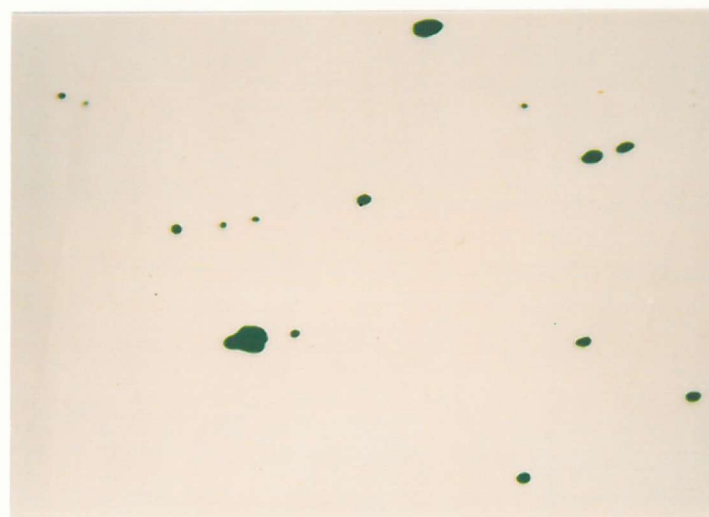
A typical sequence of image analysis operations is illustrated in Figure 5.8, which was obtained during analysis of the high sulphur steel. The photographs were taken directly from the Quantimet screen, which was set up for the purpose at a magnification of x850. In this particular sequence, Figure 5.8a shows the "grey" image, which is the optical image captured by Quantimet's high resolution television camera. Inclusions were then detected by virtue of their contrast with the matrix, observed as green particles in Figure 5.8b. Since inclusions were sometimes dual phase, it was possible to detect the two phases separately. The first phase was coloured blue, Figure 5.8c. This was followed by detection of a second phase (if present), coloured red in Figure 5.8d. The area and longest dimension of the inclusions was then measured, Figures 5.8e and 5.8f, for which the single phase and duplex inclusions were considered together.

The results from the image analysis work are presented in Figures 5.9 to 5.11, which respectively show the inclusion volume fraction, the inclusion length distributions and the inclusion area distributions for all three steels. Table 5.2 provides an overall summary of the work.

From the results of the image analysis, a number of observations can be made. Firstly, the commercial purity steel appears to be cleaner, both in terms of the number and volume fraction of inclusions, than the high purity model alloy (Figure 5.9). Secondly, inclusions in the high sulphur model alloy were more numerous, and represented a greater volume fraction (V_v) by a factor of two or so than the other steels. In terms of inclusion size, the mean values of the high sulphur and commercial purity steels were very similar at $2.34 \mu m^2$ and $2.46 \mu m^2$ respectively, and both noticeably larger than the high purity steel ($1.77 \mu m^2$). The particle size distributions on the model alloys were skewed to smaller particle sizes when compared to the commercial alloy (Figures 5.10 and 5.11). An indication of the average shape of inclusions can be obtained from the image analysis data. By making the (reasonable) assumption that the inclusions are elliptical, the average particle area and average particle length (= longest dimension, D) for the three alloys measured by image analysis (Table 5.2) enables a shape factor to be determined:



(a)



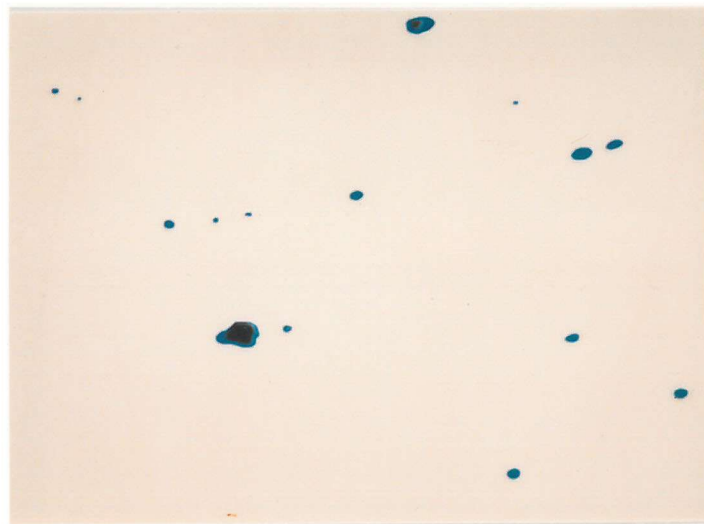
(b)

20 μm

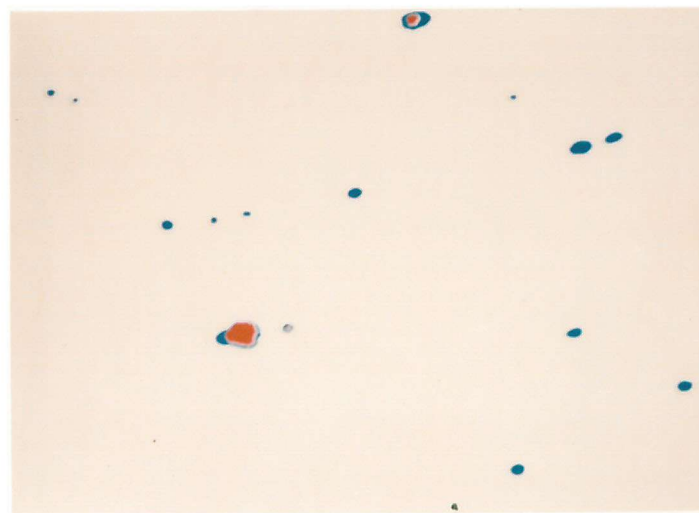
Figure 5.8 Typical sequence of image analysis operations illustrated for the high sulphur 304L model alloy.

(a) "Grey"- the optical image captured by the analyser.

(b) Features detected by level of contrast (green particles) with the matrix.



(c)



(d)

20 μm

Figure 5.8 (continued)

Detection of two-phase particles

(c) 1st phase coloured blue

(d) 2nd phase coloured red



(e)



(f)

20 μm

Figure 5.8 (continued)

Measurement of individual particle size.

(e) Area of particles.

(f) Longest axis of particles.

Figure 5.9 Volume Fraction of Inclusions

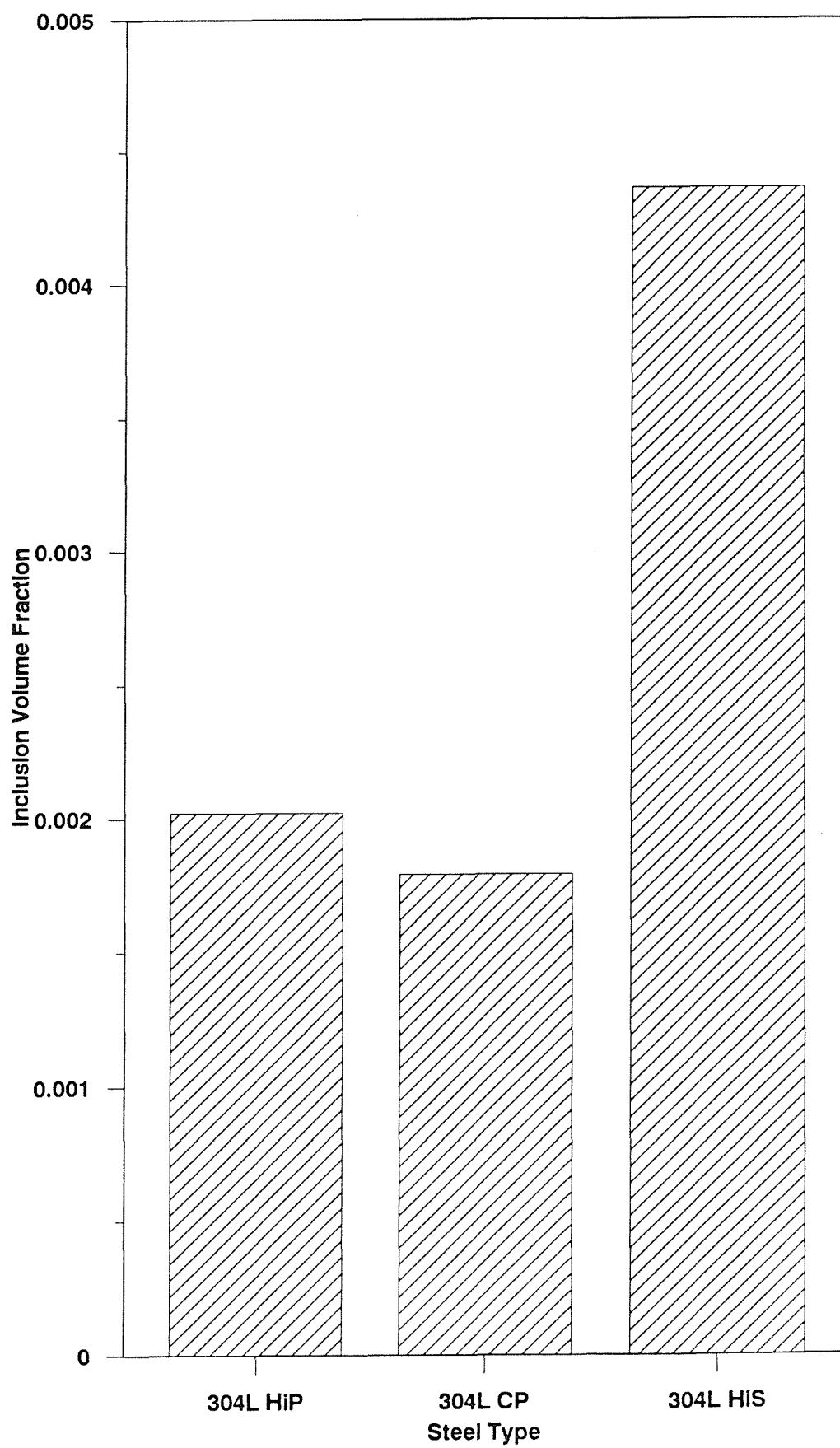
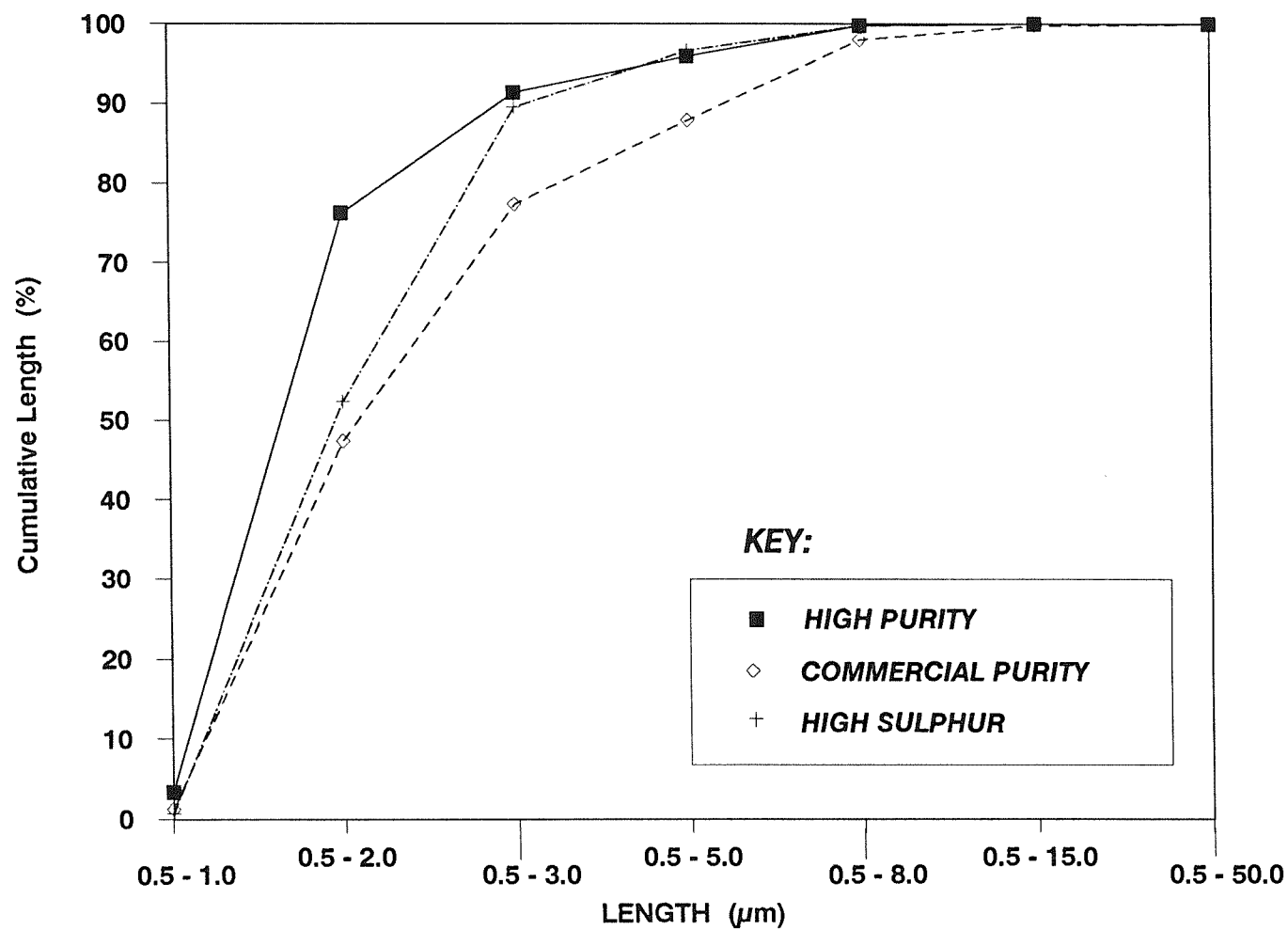


Figure 5.10 Cumulative Length Distribution of Inclusions
Measured by Image Analysis: 304L Steels



**Figure 5.11 Cumulative Area Distribution of Inclusions
Measured by Image Analysis**

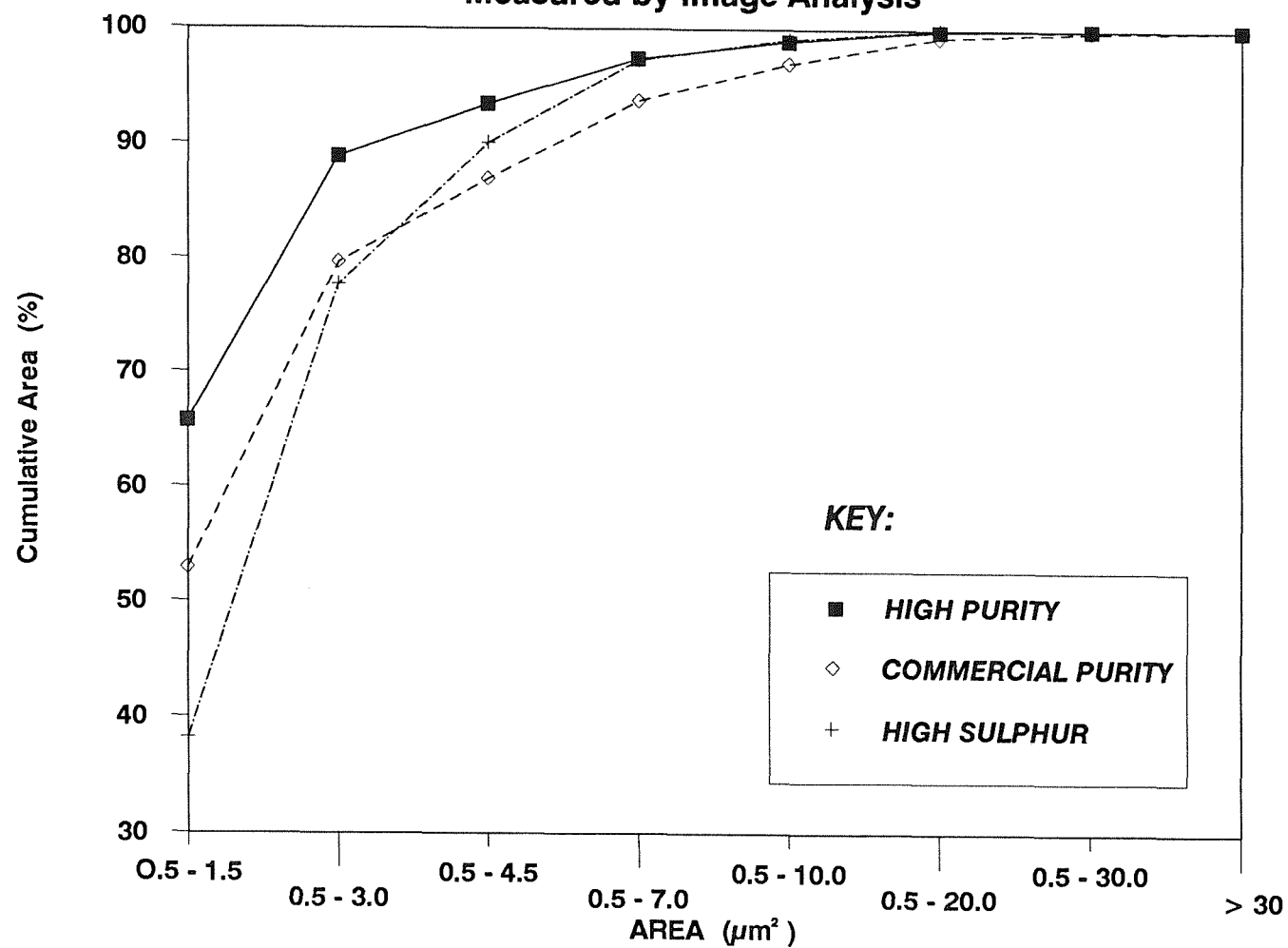


Table 5.2 Summary of Image Analysis Results

	304L HiS	304L CP	304L HiP
Total Number of Fields	225	225	225
Field Size (mm²)	0.0146	0.0146	0.0146
Total Number of Particles	6,069	2,456	3,832
Area % of Particles	0.436	0.178	0.202
Standard Deviation	0.200	0.116	0.108
Mean Length (μ m)	2.15	2.63	1.83
Standard Deviation	1.02	1.96	1.03
Mean Area (μ m²)	2.34	2.46	1.77
Standard Deviation	2.24	3.60	2.79

HiS = High Sulphur 304L

CP = Commercial Purity 304L

HiP = High Purity 304L

$\frac{D}{a}$ = degree of "roundness", or shape factor.

$\frac{D}{a} = 1.1$ (high purity steel)

$\frac{D}{a} = 2.2$ (commercial purity steel)

$\frac{D}{a} = 1.5$ (high sulphur steel)

(See also Appendix F)

where:

$$\text{area of ellipse} = 0.785 dD$$

From the length distributions (Figure 5.10), it would appear that inclusion stringers were not common in these steels. To check this further, the specimens were traversed manually at lower magnifications. This analysis revealed the occasional occurrence of stringers in the commercial purity steel. Figure 5.12 shows a typical inclusion stringer, some $60\mu\text{m}$ in length, illustrating the invariably duplex nature of these inclusions. The absence of large inclusion stringers was confirmed in the model alloys, where the inclusions were all $<20\mu\text{m}$ in length.

5.3.2 Chemical Composition of the Inclusions

5.3.2.1 EDS Analysis in the SEM

From the qualitative analysis in the SEM, the inclusions were split into two populations, according to whether or not sulphur was detected. The results of this analysis are summarised in Figure 5.13 which shows the proportion of sulphur-containing inclusions in each of the three steels. A summary of the SEM study is given in Table 5.3. Comparison of these data with those in Figure 5.9 indicates that, whilst the commercial steel contained fewer inclusions than the high purity steel, a higher proportion contained sulphur - about 25% compared to 12.5%. It is also notable that the high sulphur steel contained the desired large number of sulphur-rich inclusions, which comprised 81% of the total inclusion population.



20 μm

Figure 5.12 Duplex inclusion stringer in commercial purity 304L.

Figure 5.13 Proportion of Sulphur Containing Inclusions

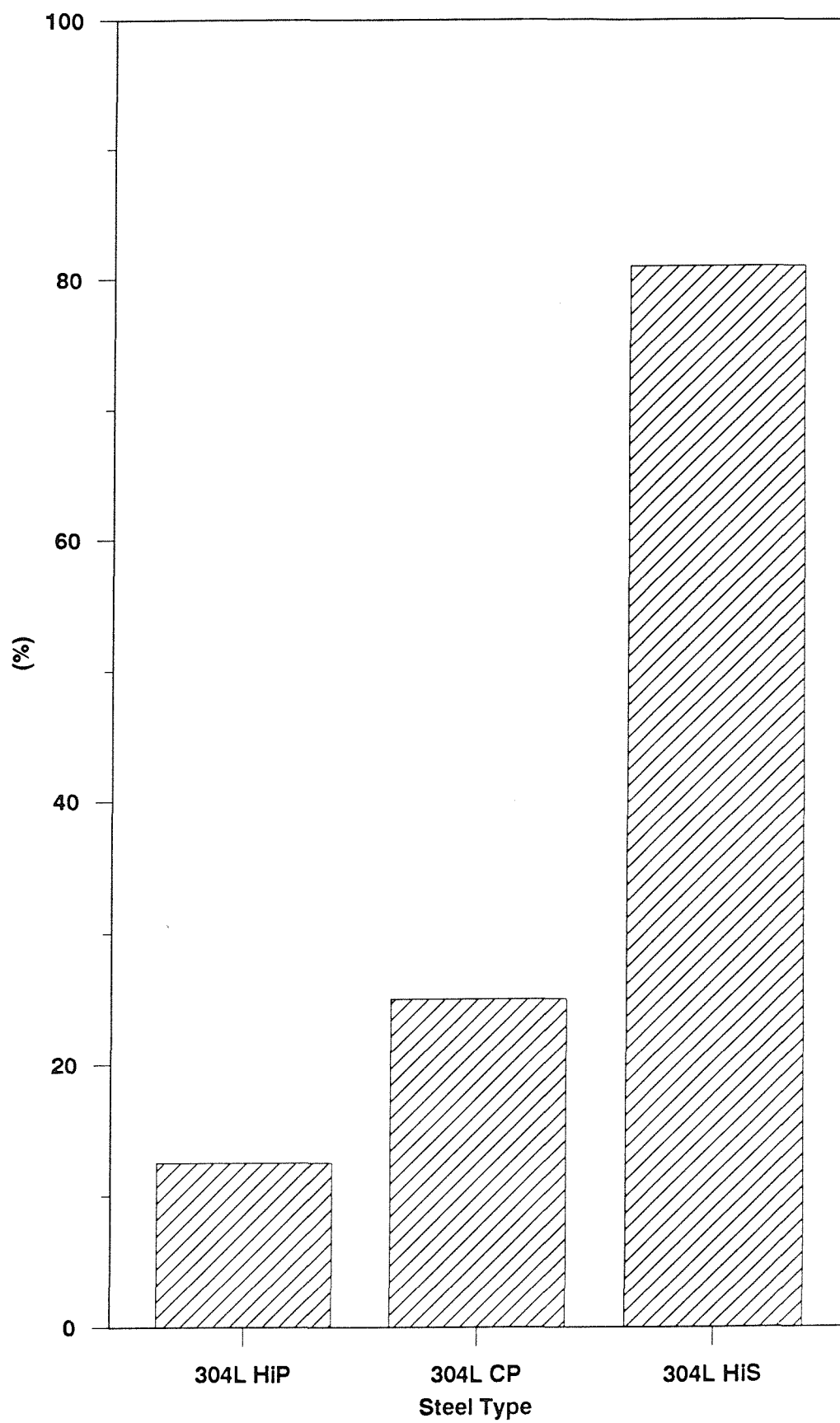


Table 5.3 Summary of SEM Analysis of Inclusions

	Total	<1 μ m	1-5 μ m	5-10 μ m	10-20 μ m	>20 μ m
HiS alloy: total	110	16	81	12	1	0
S-containing	89	12	66	10	1	0
HiP alloy: total	104	29	65	10	0	0
S-containing	13	3	10	0	0	0
CP alloy: total	100	21	67	9	3	0
S-containing	25	1	17	4	3	0
Si-containing	19	4	14	1	0	0
Ti-containing	50	7	36	7	0	0
Ca-containing	7	3	4	0	0	0
Ce-containing	14	1	12	1	0	0

HiS = High Sulphur 304L

CP = Commercial Purity 304L

HiP = High Purity 304L

Analysis of inclusions in the model alloys generally did not detect elements other than Cr, Fe, Mn or S, apart from a small peak for nickel from the matrix. The only exceptions were occasional (<2% of all inclusions) small peaks for silicon. A different picture emerged from the analysis of the commercially produced steel, in which many inclusions were found to contain minor alloying or trace elements: silicon, calcium, cerium, and titanium, in addition to combinations of chromium, iron and manganese. The presence of these trace elements in the steel arises from the scrap metal used in the commercial production process (Appendix A).

Analysis of inclusion sizes, (Table 5.3) revealed distributions largely in agreement with the optical image analysis results: most of the inclusions were in the size range 1 to 5 μm (nominal diameter of longest axis). Inclusions in this size range comprised S-containing and purely oxide inclusions in proportion with the overall analysis results (as expected since this size range accounted for >60% of the total for all three alloys). In the commercial purity steel, inclusions <1 μm were disproportionately sulphur-free (only about 5% contained sulphur). For the two model alloys, S-containing inclusions were slightly reduced in number, but generally remained in proportion with the overall analysis. A different picture emerges from the analysis of the larger inclusions. In all three steels, relatively few inclusions were longer than 5 μm . In the high purity alloy, none of these inclusions (10% of the total) contained sulphur. In the high sulphur model alloy, 12% of the inclusions measured were longer than 5 μm , of which 85% were sulphur-bearing, which represents a small increase compared to the overall analysis. In the commercial alloy, 12% of the inclusions measured were >5 μm , 58% of which contained sulphur, which represents a substantial increase when compared to the overall analysis. In the analysis of all 3 alloys, no inclusions exceeded 20 μm in length, and only 4 inclusions fell within the range 10 to 20 μm . All 4 inclusions contained sulphur.

To summarise the SEM analysis, in terms of the size distribution of inclusions, the results were consistent with the optical image analysis results, with a high proportion of inclusions found in all three steels measuring 1 to 5 μm . From the results of the chemical analysis of inclusions, there is a suggestion for the commercial purity and high sulphur steels that the larger inclusions in the distribution tended to be sulphur containing, whilst for all three steels disproportionately fewer of the smaller inclusions (<1 μm) contain sulphur.

5.3.2.2 EDS and WDS Analysis in the EPMA

Following the SEM analysis, the specimens were transferred to the EPMA to enable a more quantitative chemical analysis of inclusions. From this analysis, 6 inclusions from each alloy have been chosen to illustrate the range of inclusion compositions found in the three steels. The detailed analyses of these inclusions, using a combination of WDS and EDS in the EPMA, are presented in Table 5.4. These results indicate that, in all three alloys, few sulphide inclusions were purely MnS, with both chromium and iron having replaced manganese to some extent. The replacement of manganese with these elements in sulphides in stainless steels is to be expected^(7,9), although the values found for iron sometimes appeared to be rather high. This may have arisen due to secondary emissions from the metal matrix (although a 1 μ m analytical spot size was used to minimise this effect), or due to the presence of Fe in an associated oxide particle. Certainly, most sulphur-containing inclusions also appeared to be associated with oxides. Purely oxide inclusions were found in all three steels, and were most prevalent in the high purity steel. These oxides were mostly of the FeO.Cr₂O₃ type, often containing some manganese.

The inclusions in the commercial purity and high sulphur steels exhibited a wide range of sulphur contents, whilst in the high purity steel, those inclusions which did contain sulphur, invariably exhibited very low levels.

It is clear from this detailed analysis of inclusions that the compositional variation of inclusions may quite marked even within the same steel specimen.

5.3.2.2.1 Corrections Applied to EPMA Data In order to arrive at a quantitative, weight % figure from the counts obtained for each element, a ZAF correction was applied to the WDS data. This corrects the counts obtained for a given element in the alloy against a standard for the following sources of error:

- i. atomic number Z effect, which arises from two sources - electron backscattering and electron retardation - both of which depend on the average atomic number of the target;
- ii. absorption of X-rays by other elements - probably the most significant; absorption coefficients for lighter elements are not well known;

Table 5.4 Summary of EPMA Analysis

	Inclusion Length (μ m)	Element (Weight %)					Others (EDS)
		Fe	O	Cr	S	Mn	
HiS:							
Inclusion 1	7.0	71.92	12.48	15.22	0.04	0.34	Ca
2	2.0	73.38	0.00	18.30	5.39	2.93	
3	2.5	19.14	1.51	18.29	32.40	28.66	
4	4.0	39.30	19.65	29.95	1.92	10.18	
5	1.0	73.08	3.92	21.25	0.18	1.57	
6	8.5	00.00	2.82	19.01	38.78	39.39	
HiP:							
Inclusion 1	2.0	51.30	14.30	23.60	4.27	6.54	Al, Si
2	1.5	49.47	16.56	30.77	0.05	4.65	
3	1.0	56.59	11.68	28.35	0.03	3.34	
4	1.5	48.15	15.42	30.99	0.67	4.78	
5	1.0	71.31	2.88	21.71	1.57	2.54	
6	1.0	65.03	6.38	20.29	0.02	2.28	
CP:							
Inclusion 1	5.5	40.91	14.65	22.18	8.12	14.13	Al,Si,Ti,Ca
2	2.0	56.21	12.06	21.10	0.00	10.63	Al,Si,Ti,Ca
3	4.0	55.83	34.68	8.47	0.44	0.59	Al, Si
4	10.0	33.74	0.00	16.61	29.78	19.86	
5	1.5	70.95	5.89	20.63	0.21	2.33	Al, Si, Ca
6	3.0	71.28	4.27	22.84	0.81	0.90	Si, Ca

HiS = High Sulphur 304L

CP = Commercial Purity 304L

HiP = High Purity 304L

- iii. fluorescence - the energising of further X-rays by X-rays generated by heavier elements.

5.3.3 Pitting Experiments

5.3.3.1 Nucleation Frequency of Unstable Pits

Figure 5.14 shows clearly that the nucleation frequency of unstable pits is strongly affected by the type of inclusions present in the steel, and by the applied potential. In the high sulphur steel, unstable pits were first observed at very low electrode potentials, and the frequency curve showed a steep rise to values not previously attained in the experiments involving the commercial purity steel. In contrast, the high purity steel exhibited little pitting activity even at quite high electrode potentials. The curve for the commercial purity steel fell between the curves for the model alloys.

Inspection of the current-time series for the model alloys revealed differences in the transients observed when compared to the commercial purity steel: for both the high sulphur and high purity steels, transients tended to be very short lived. They often lasted for less than 10s, and usually consisted of one or two current pulses.

A typical current vs. time sequence for the high sulphur steel is shown in Figure 5.15, and illustrates the high frequency but discrete nature of the events. Multiple bursts of current within a single transient, such as those shown in Chapter 3 (Figure 3.3d) for the commercial steel, were not usually seen during unstable pitting on this steel. Scatter diagrams of transient peak height versus lifetime in the potential ranges -22mV to +23mV SCE and +69mV to +115mV SCE are shown in Figure 5.16, and emphasise the short-lived nature of the individual events. These figures can be compared directly with Figures 3.12b and 3.12c for the commercial steel.

Experiments on the high purity steel were characterised by a very low level of unstable pitting activity, even at high electrode potentials. Figure 5.17 shows a current vs. time sequence for this steel at electrode potentials in excess of +400mV SCE. Again the large majority of current transients comprised only one and sometimes two current bursts. Occasional transients, however, comprised multiple current bursts, Figure 5.18. The scarcity of events meant that peak height vs. lifetime plots contained too few data at potentials to enable comparison with the other steels. Such a diagram was,

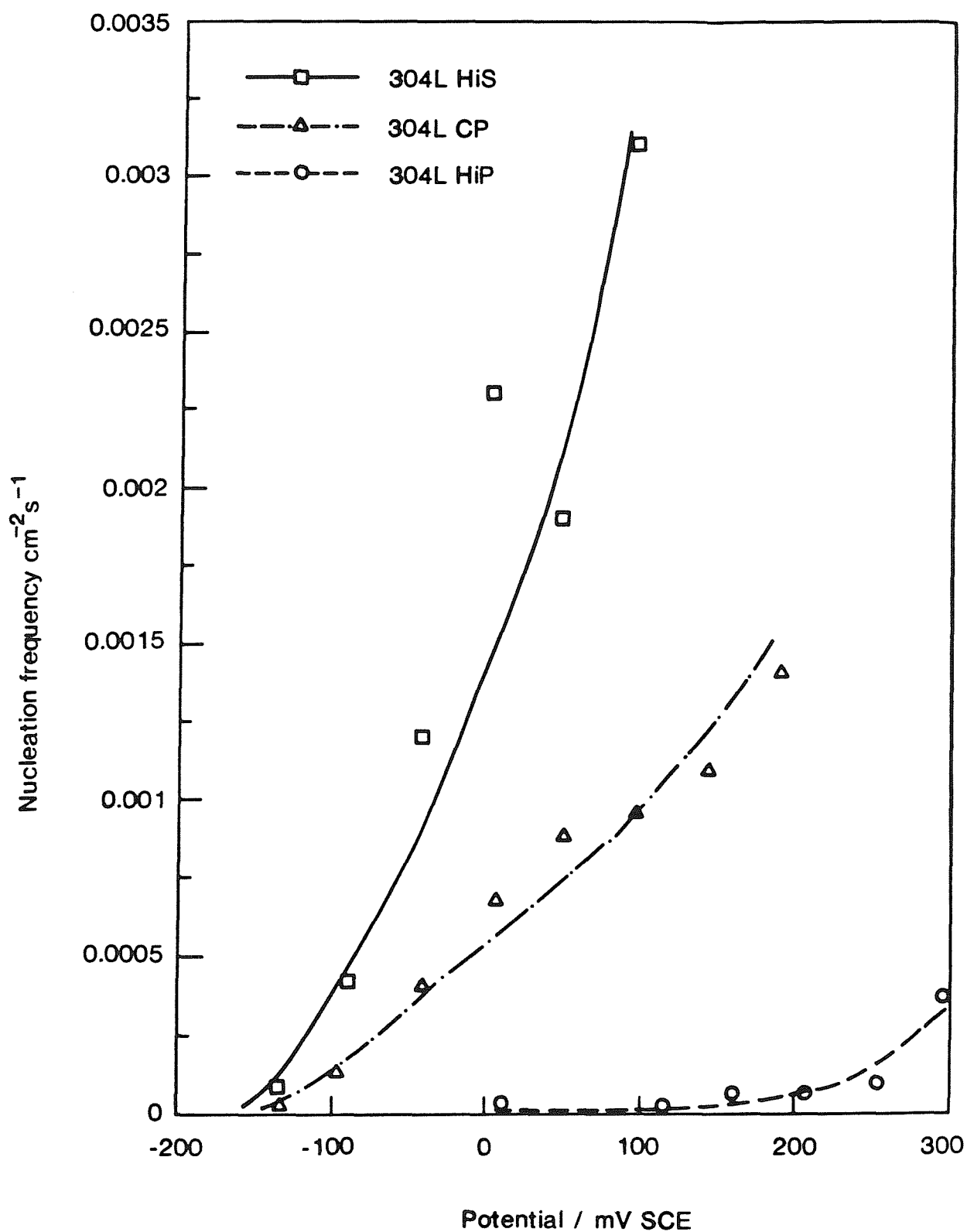


Figure 5.14 Nucleation frequency of unstable pits as a function of electrode potential for commercial 304L and two 304L model alloys (1000ppm chloride, 0.005mV/s)

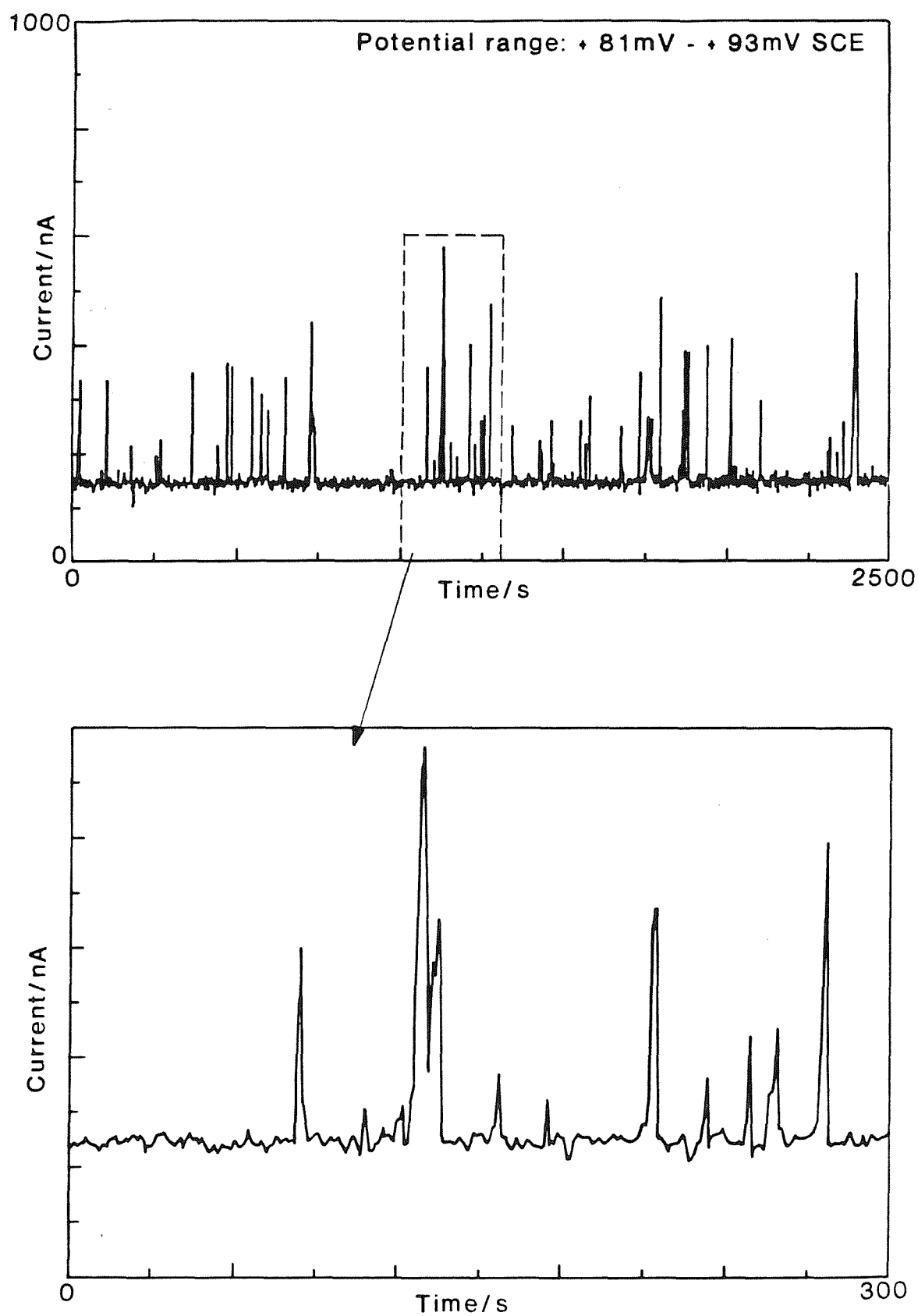


Figure 5.15 Typical current-time sequence for high sulphur 304L (model alloy) illustrating the short-lived, discrete nature of the anodic current transients.

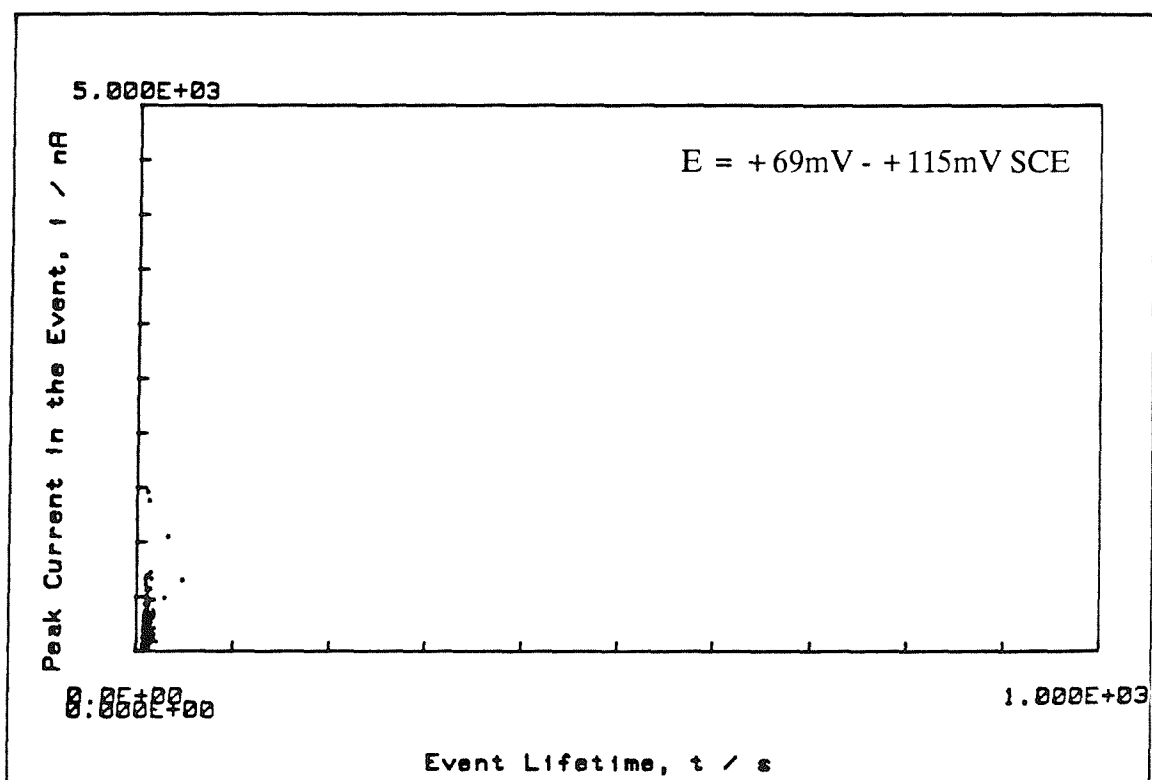
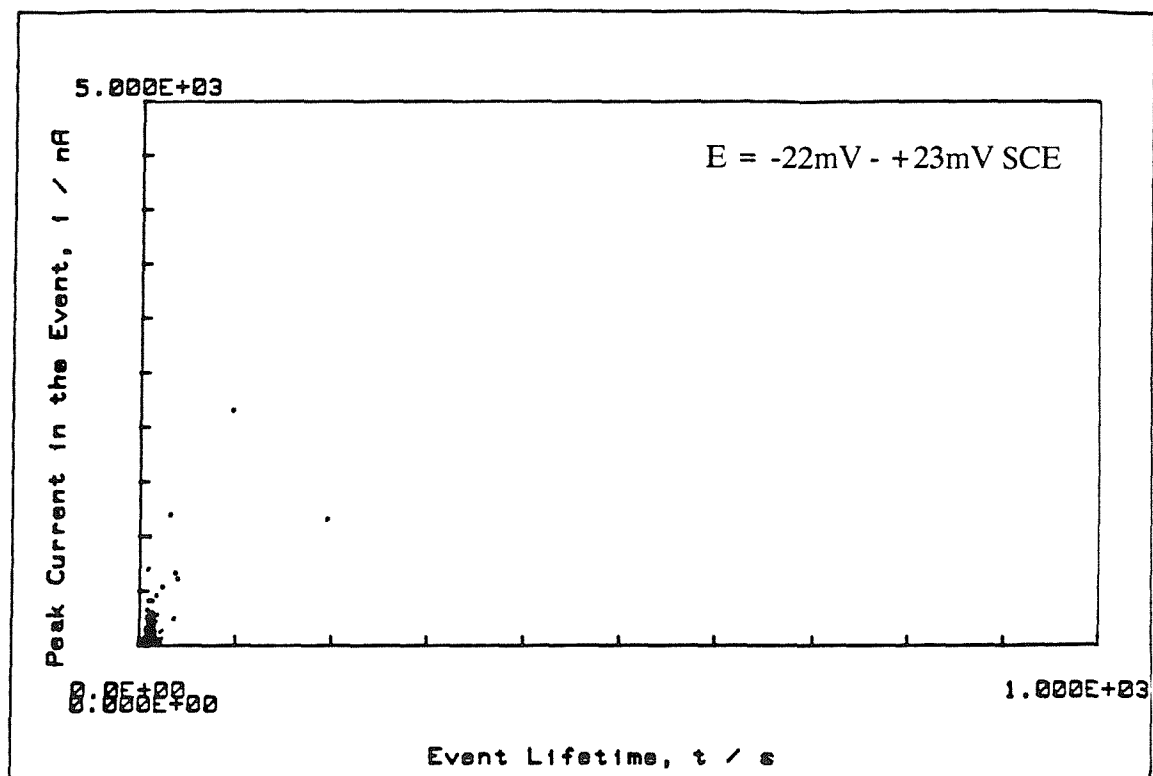


Figure 5.16 Scatter diagrams of transient peak height vs. lifetime for high sulphur 304L (model alloy).

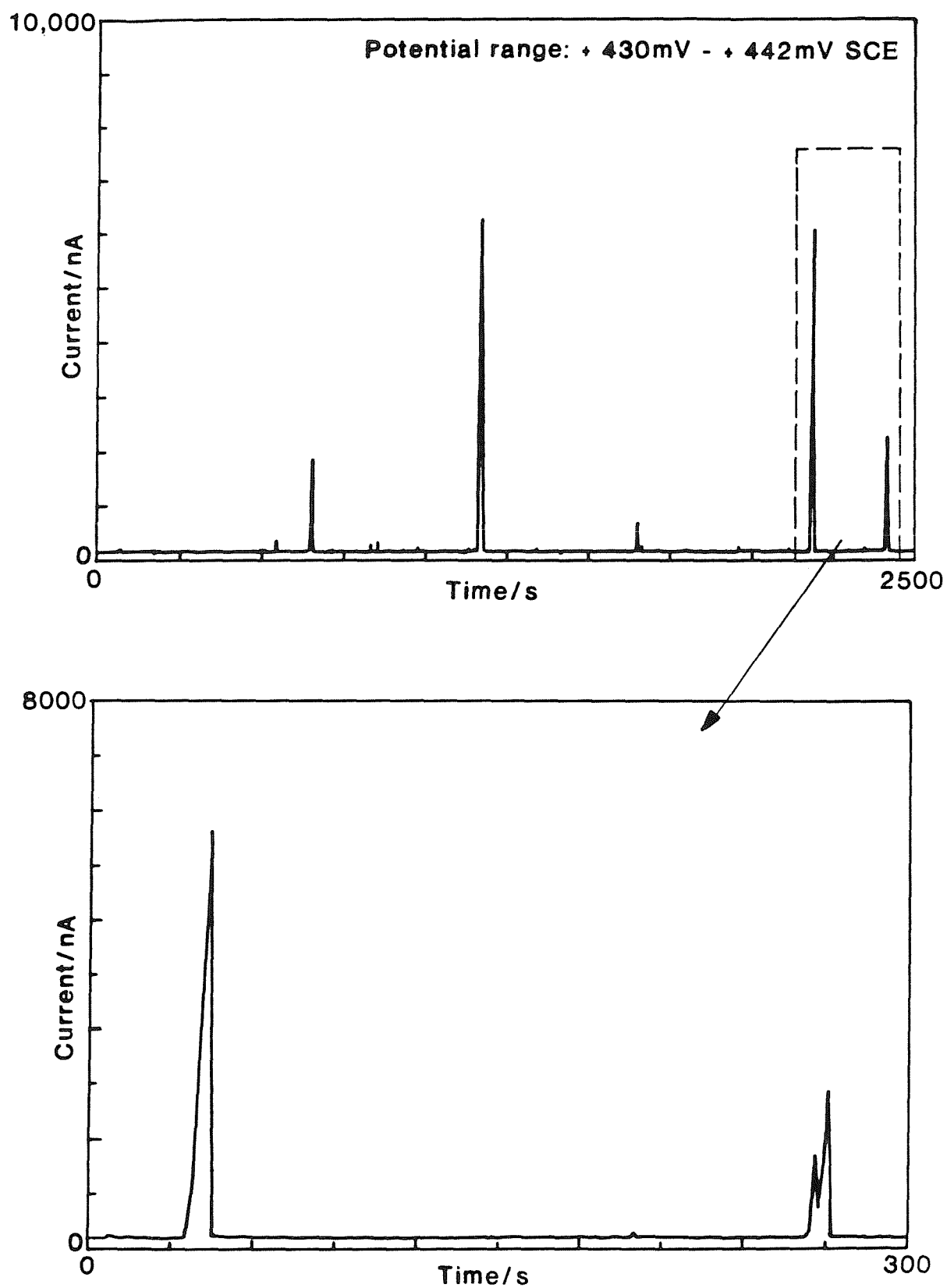


Figure 5.17 Typical current-time sequence for high purity 304L (model alloy) at electrode potentials in excess of +400 mV SCE.

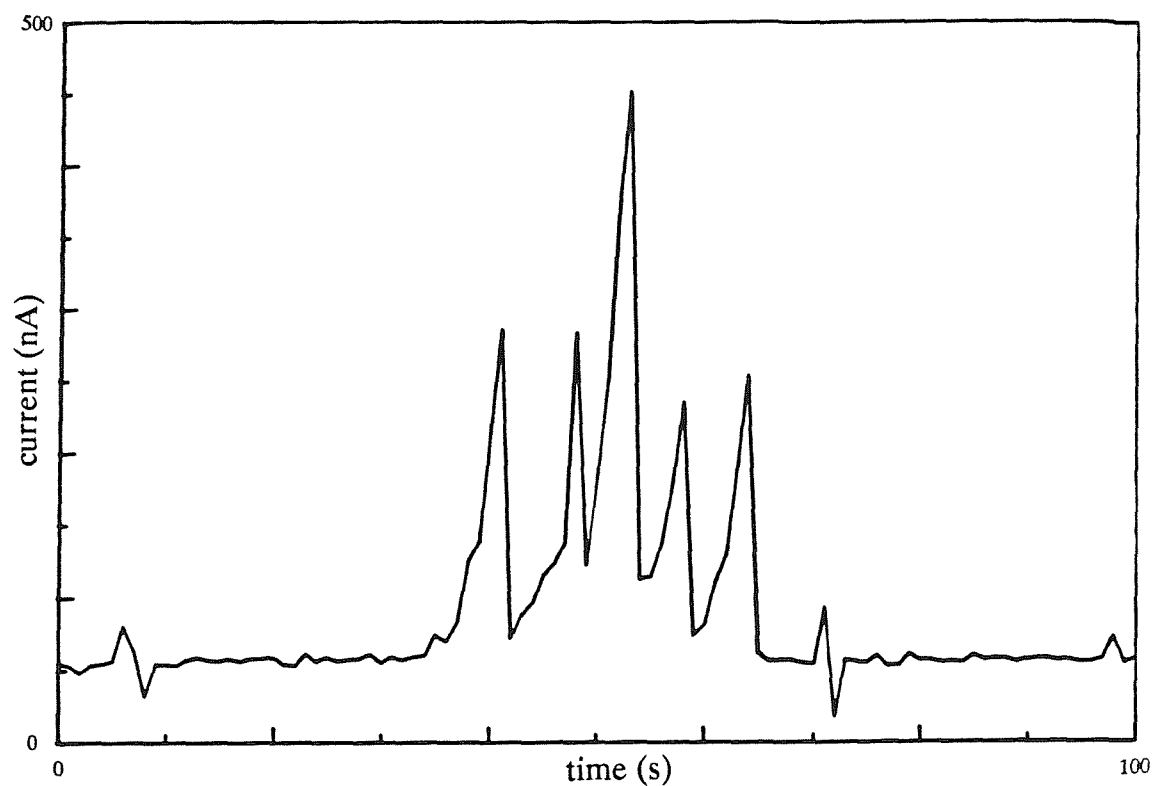


Figure 5.18 Multiple current bursts within a single transient - high purity 304L (model alloy). $E \approx +250$ mV SCE.

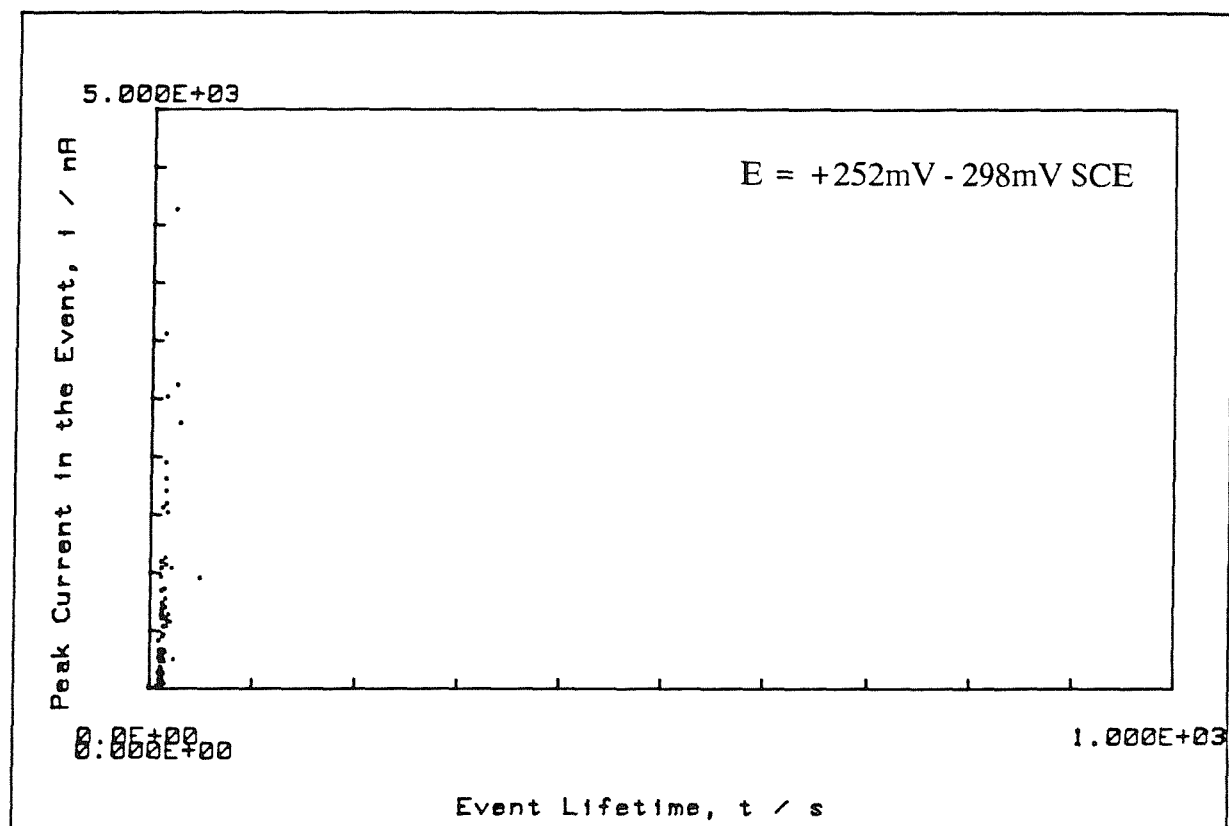


Figure 5.19 Scatter diagram of transient peak height vs. lifetime for high purity 304L (model alloy).

however, constructed for the potential regime +252mV to +298mV SCE, and is shown in Figure 5.19. This figure again illustrates the nature of the transients observed: most were short-lived and reached quite low peak currents, although occasionally individual transients reached high peak currents in a short time, before repassivating.

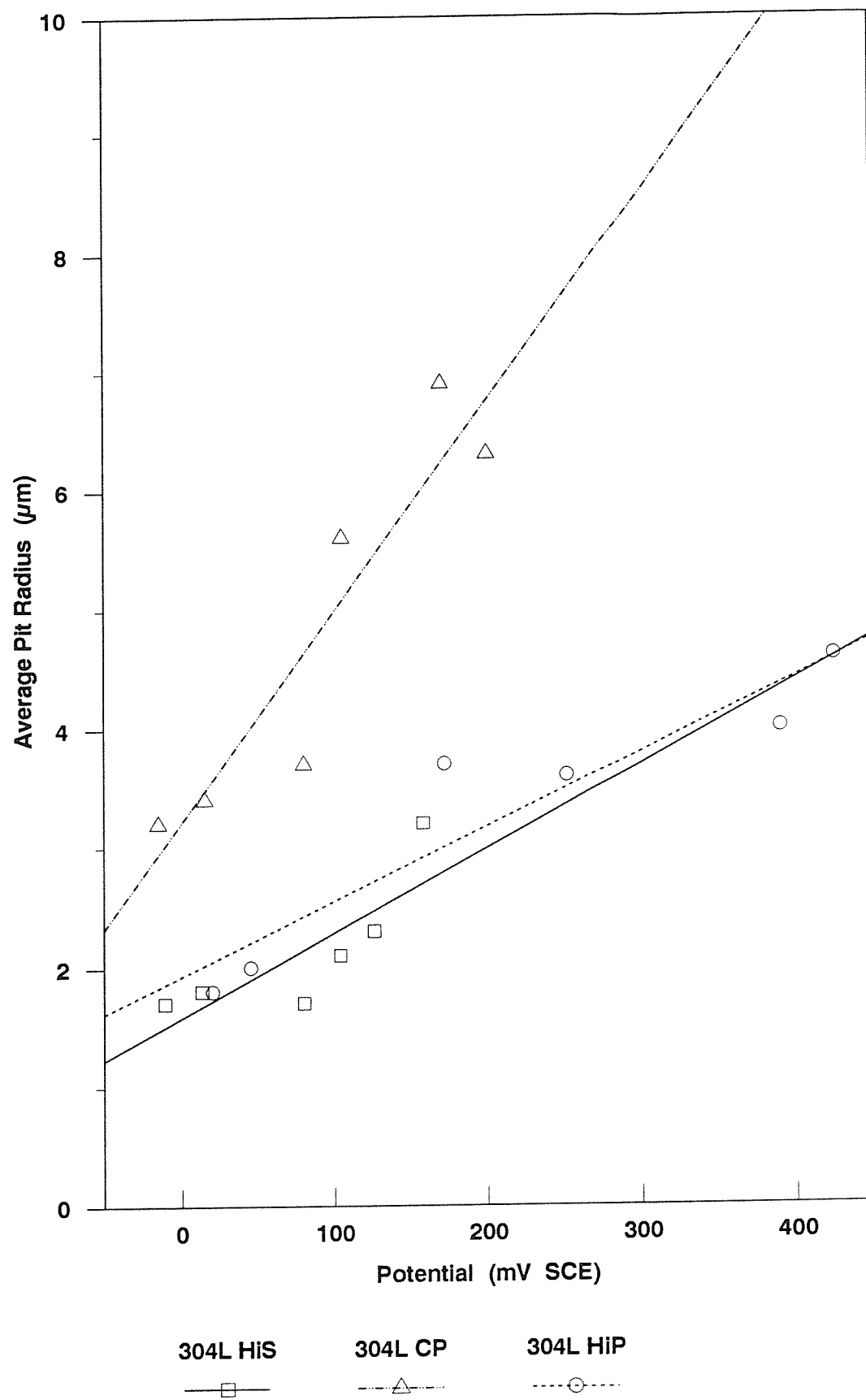
The current densities in pits calculated for the model alloys were much higher than for the commercial steel. For example, the mean values at the peak current for the high sulphur steel at +100 and +150mV SCE were 0.75A/cm² and 0.9A/cm² respectively (compare with Figures 3.14f and 3.14h). However, direct comparison requires the calculations to be made at constant time, which is not possible with the present data.

Figure 5.20 shows the average pit radius, calculated from the individual current transients, as a function of potential for the two model alloys. It is notable that although the nucleation frequency of transients (and therefore of pits) was much higher on the high sulphur steel compared to the high purity steel (Figure 5.14), the average pit size was very similar for both steels over a wide range of potentials. Also plotted on Figure 5.20 are the data for the commercial steel, presented previously in Figure 3.13. At a given potential, it is evident that the average pit size on the commercial steel was substantially larger than on the model alloys. As a further illustration of the similarities in the transients observed on the model alloys, despite the marked difference in their frequency of occurrence, Figure 5.21 shows that the lifetime distribution of the events on the two steels were very similar. Also plotted are the data for the commercial purity steel, for which two observations can be commented on. Firstly, the lifetime distribution is notably different from that of the model alloys. Secondly, there are two event populations for this steel, whilst only one is apparent on the model alloys. Figure 5.22 shows that, at a given electrode potential, the passive current densities measured on the three alloys were in the order 304 HiS > 304 CP > 304 HiP, and so showed a consistent trend with both the sulphide inclusion volume fraction and the frequency of unstable pitting events.

5.3.3.2 Pit Propagation

Figure 5.23 shows the cumulative probability of breakdown for the three steels as a function of electrode potential. The plot for each steel was constructed from more than 30 individual experiments. As a function of electrode potential, stable pits

Figure 5.20 Average Calculated Pit Radius



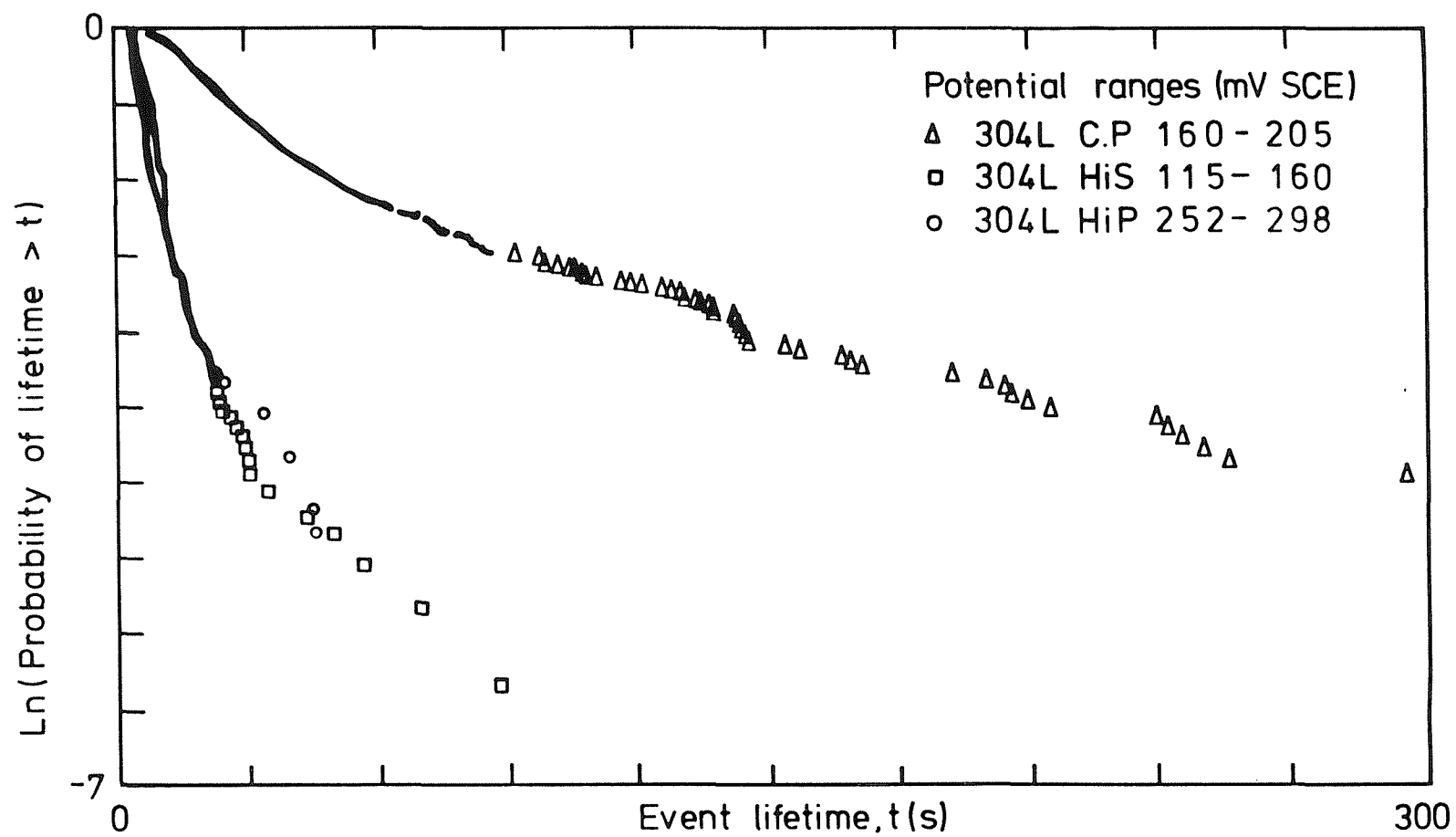
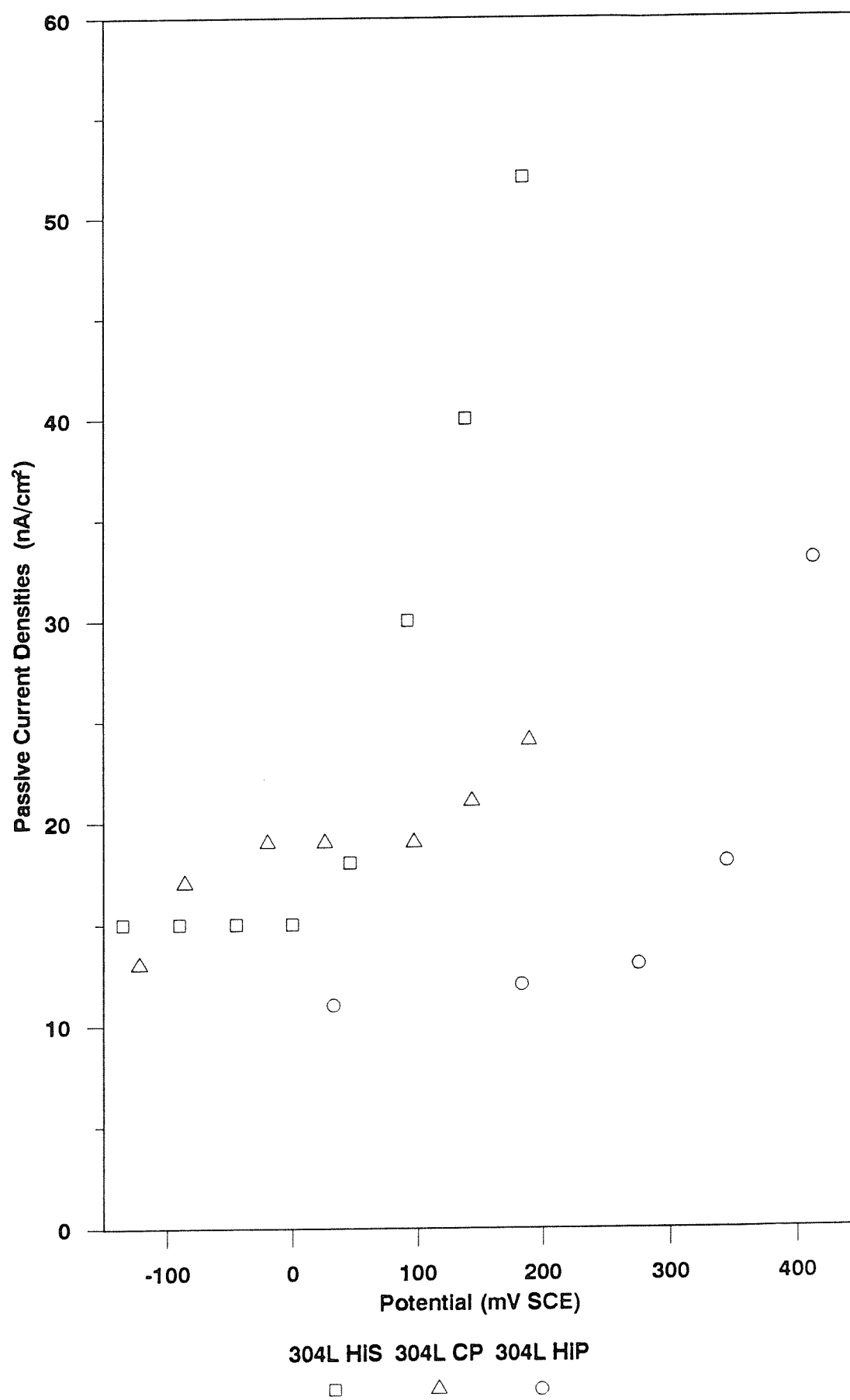
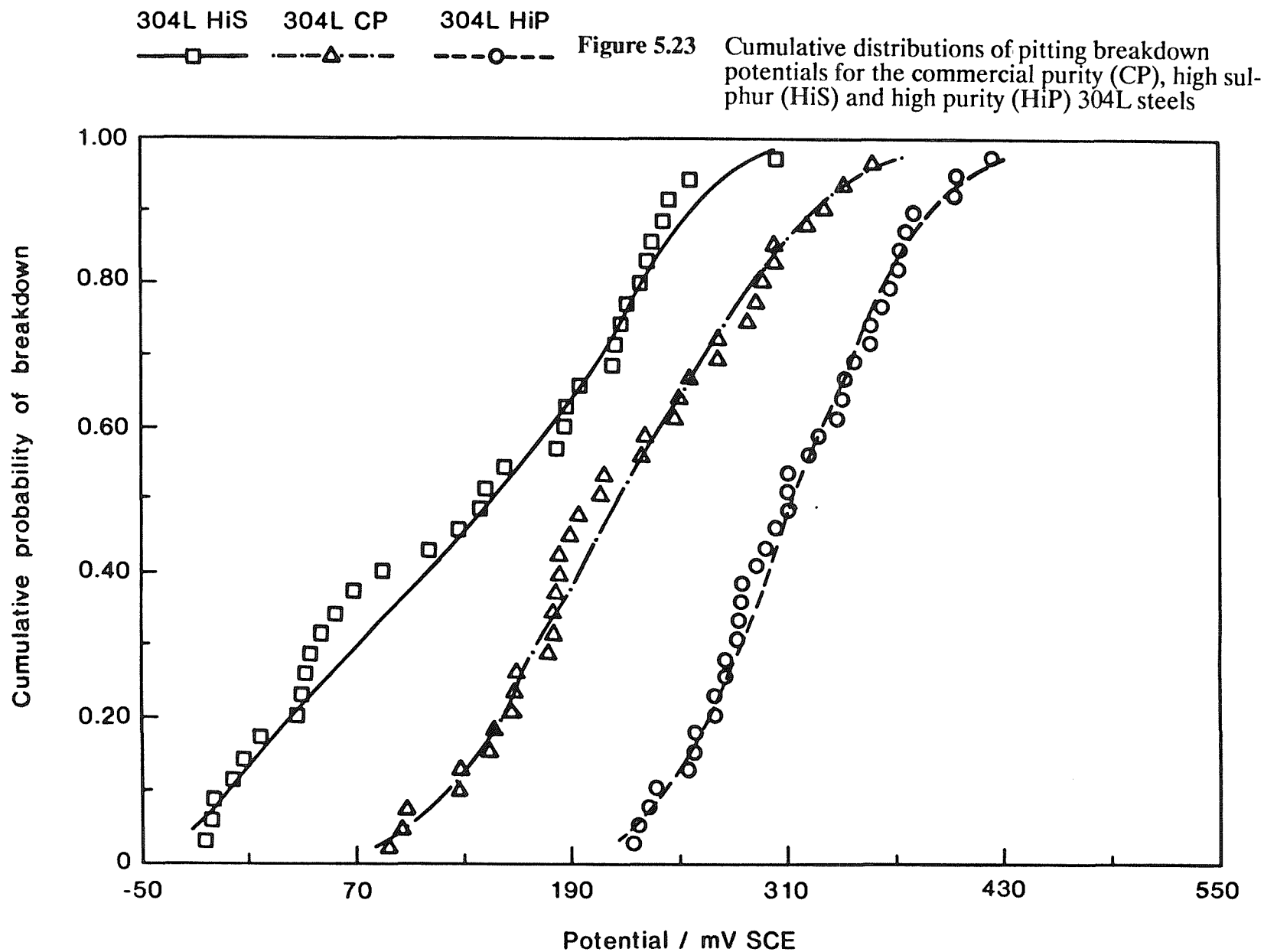


Figure 5.21 Distribution of lifetimes of current transients on commercial purity (CP), high sulphur (HiS), and high purity (HiP) 304L steels

Figure 5.22 Passive Current Densities





nucleated in the order 304 HiS < 304 CP < 304 HiP. An indication of the extent of the improvement gained by progressively reducing the sulphur content of the alloys is possible by considering, for example, the potential at which 50% of the specimens for each of the three alloys had pitted. This reveals that the commercial alloy ($p_{0.5} = 215\text{mV SCE}$) gives about a 70mV improvement over the high sulphur steel ($p_{0.5} = 144\text{mV SCE}$). Also, the high purity steel ($p_{0.5} = 310\text{mV SCE}$) gives a 95mV improvement over the commercial purity steel, and over 160mV improvement over the high sulphur steel. Figure 5.23 further indicates that the range of potential over which sustained pitting occurs decreases with decreasing sulphur content. It should be mentioned that two of the high purity 304L specimens did not pit at all (the anodic potential limit on the ramp generator was $+460\text{mV SCE}$).

Figure 5.24 shows a typical current vs. time sequence for the high sulphur steel at the onset of pit propagation: invariably the rise in background current occurred as a series of current bursts. This behaviour had been observed previously on some commercial 304L specimens (Figure 3.4).

At the onset of sustained pit propagation on the high purity steel, the current rise to the $10\mu\text{A}$ limit was usually very rapid, Figure 5.25a. Occasionally, the current limit was reached through a sequence of current bursts, Figure 5.25b.

The observations on the high purity steel suggested that further experiments should be carried out to test the accuracy of the current switch-off level for this steel: current transients associated with unstable pits sometimes approached the $10\mu\text{A}$ current level very rapidly, before repassivating. Also, the rapid current rise to the current limit observed for "propagating" pits introduced some doubt as to whether these pits would in fact have continued to propagate. Seven experiments were carried out in which the potential was recorded at the old current limit, $10\mu\text{A}$, but the experiment was continued until a higher limit, $70\mu\text{A}$, was reached, when the potential was again recorded and the experiment stopped. The results of these experiments showed differences in the "breakdown" potentials recorded at the two current levels of between $<1\text{mV}$ and 40mV . These results indicate that the $10\mu\text{A}$ current limit is too low for this steel, as sometimes unstable pits were counted as propagating pits. Of course, this is rather a good thing from the point of view of the improvement in the pitting resistance of this alloy - the results in Figure 5.23 are if anything, pessimistic.

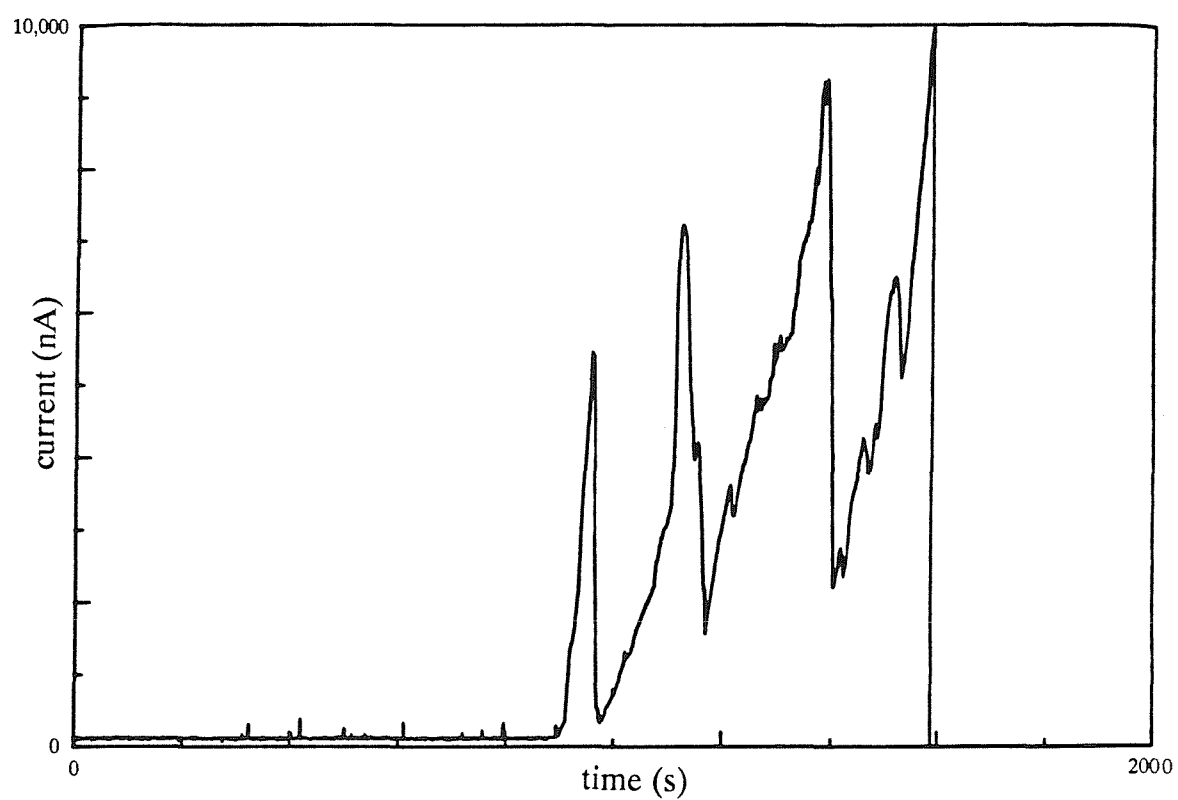


Figure 5.24 Current-time sequence for high sulphur 304L (model alloy) at the onset of sustained pitting. ($E \approx +50$ mV SCE).

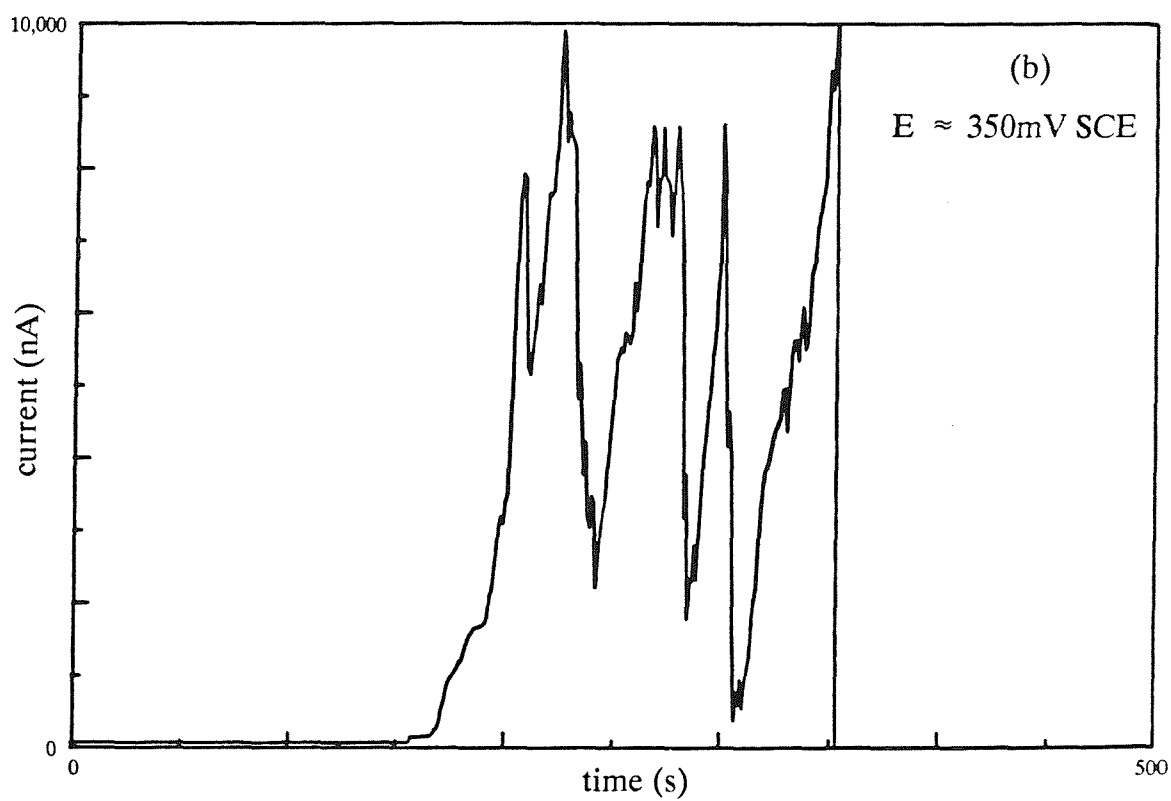
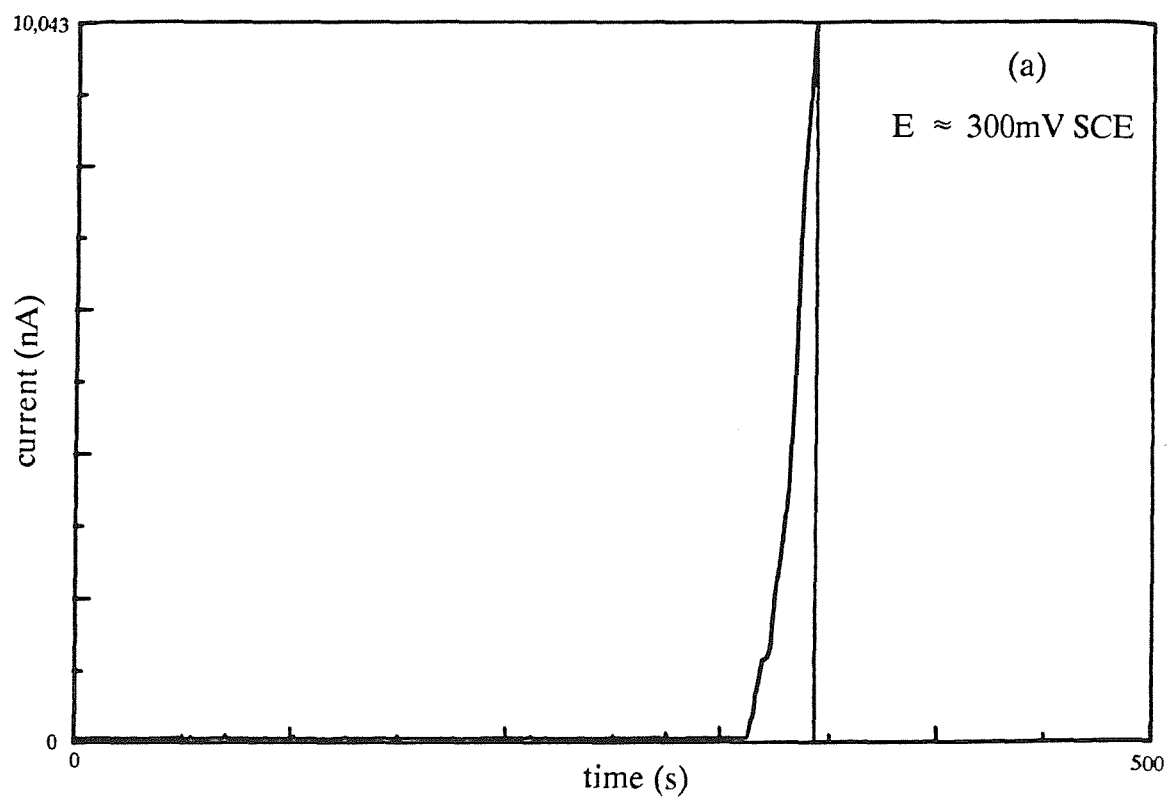


Figure 5.25 Current-time sequences for high purity 304L at the onset of sustained pitting: (a) the current rise to the $10\mu\text{A}$ limit was usually rapid (b) occasionally the current rise consisted of a sequence of current bursts

5.4 DISCUSSION

The results of this study provide clear evidence that of the possible pit nucleation sites on type 304L stainless steel, sulphur-rich inclusions dominate. There was a clear ranking order of the alloys in terms of pitting resistance: 304L high purity > 304L commercial purity > 304L high sulphur. The single most important factor in producing this improvement was probably the reduction in bulk sulphur content of the alloy, which in turn reduced the volume fraction of sulphide inclusions in the steel. However, in the following discussion the results of the pitting experiments and microscopy studies are used to illustrate that the characteristics of the inclusions - their size, chemistry and distribution - have an important influence on the nucleation of propagating pits.

To illustrate the effects of chemistry and distribution of inclusions, the discussion initially focuses on the model alloys, which were produced from the same high purity raw materials, only the sulphur content being different.

In the high purity alloy, a large number of small inclusions were present. Only a small proportion of these inclusions contained sulphur, and they were well separated spatially. Analysis of the current transients observed during the pitting tests on this steel indicated that only a few small pits were nucleated until high anodic potentials were reached, when the transients, still few in number and mostly consisting of a single current burst, sometimes attained high current levels in a short time. As described previously, this resulted in some unstable pits exceeding the current limit and being counted as propagating pits when in fact some would have repassivated.

The high sulphur alloy contained a large number of small inclusions, but most of these were sulphur-rich. The results of the pitting experiments reflected this microstructure - the occurrence of many discrete transients indicated the nucleation of many of small pits. During the initial stages of pit propagation, the associated current rise was often characterised by multiple anodic bursts (Figure 5.24).

The majority of events observed on both the model alloys were characterised by a short and quite well defined lifetime (Figures 5.16 and 5.19). Additionally, the form of these events was predominantly $i \propto t^2$, suggesting that the current was unimpeded by resistive elements such as pit covers. It should be remembered that these pits were

all rather small. Analysis of the shape of the inclusions in the model alloys suggests that these too were small, and mostly rounded (Section 5.3.1). This was particularly the case for the high purity steel. Dissolution of these inclusions during pitting might therefore be expected to produce relatively shallow, open pits. It may be envisaged that the majority of the current transients observed on the model alloys occurred at small, individual sulphide inclusions. The presence of a well defined transient lifetime (Figures 5.16 and 5.20) can perhaps be understood in terms of the supply of sulphur to the active pit surface. The work of both Lott and Alkire⁽⁴⁷⁾ and Eklund⁽⁴⁶⁾ showed that elemental sulphur is produced on polarised artificial MnS electrodes, although the mechanism by which it was produced differed slightly. However, whilst they did not report the presence of sulphur on the stainless steel surface during their respective crevice and pitting tests, in recent work using a combination of immersion pitting tests and X-ray photoelectron spectroscopy (XPS), sulphur has been found to be adsorbed on the metal adjacent to sulphide inclusions⁽⁷²⁾. The work of Marcus and Oudar⁽⁵⁷⁻⁶⁰⁾ clearly shows that adsorbed sulphur at corroding metal surfaces greatly enhances dissolution, and poisons the repassivation processes. As the pit grows a circumstance can be envisaged in which the supply of sulphur from the inclusion can no longer maintain sufficient coverage of sulphur (found by Marcus and Oudar to be 70-80% of a monolayer) due to the increasing size of the pit. The small pit may then repassivate. A further contributory factor to the repassivation of these small pits is the shape of the inclusions: the aggressive pit environment may be more easily lost from shallow hemispherical pits than from a deep, narrow pit for example,^(30,37,46) a point which is returned to later in this discussion.

The current transients observed on the commercial purity alloy were often different to those on the model alloys, generally tending to be longer-lived (compare Figures 5.15 and 5.17 with Figure 3.3). A series of current oscillations within a given transient was quite common (Figure 3.3d). Microstructural characterisation of the commercial steel perhaps provides a clue to the reasons for this difference. The tail of the particle size distribution was longer (to larger particle sizes) than for the model alloys (Figures 5.10 and 5.11). The presence of occasional inclusion stringers in this material, which were absent in the model alloys, was also noted, (Figure 5.12). These inclusion stringers were invariably sulphides. It may be postulated that the longer-lived events seen on this steel (c.f. model alloys) were the result of pit initiation at large sulphide inclusions. The plots of pit radius versus potential for all 3 alloys in Figure 5.20 are based on the calculated mean pit radius. This figure indicates that unstable pits on the

commercial steel were, on average, much larger than those on the model alloys at a given electrode potential. Also noticeable is the similarity in the average pit size for the two model alloys across the potential range. These results are consistent with the findings of other workers^(37,38) - small, well dispersed sulphide inclusions result in small, non-propagating pits, whilst a few large sulphide inclusions produced larger, more damaging pits.

For the three steels used in this study, the points raised in the above discussion are consistent with the analysis of inclusion shape and composition, and with the shape of the electrochemical current transients. The passive current densities reflected the sulphur content of the alloys, indicating that the dissolution of sulphide inclusions contributes significantly to the magnitude of the passive current. In the general class of feedback theories introduced in Chapter 3, sulphur was suggested as a "special species" which could trigger pits. That dissolution of sulphide does indeed contribute to the passive current is confirmed here.

Consideration is now briefly given to the differences between the commercial steel and the two model alloys. Apart from a slightly larger grain size, the commercial steel was different on two accounts. Firstly, it contained a variety of additional elements, mostly in trace quantities (Table 5.1), and secondly it contained some δ -ferrite. Of the additional alloying elements, molybdenum is known to be beneficial, but at 0.38% was probably not present in sufficient quantity to exert a great influence on the pitting resistance. The effect of copper on pitting resistance is less certain, but in the amounts present in this steel (0.24%) it has been reported to be beneficial to the corrosion resistance of stainless steels⁽⁷³⁾. When δ -ferrite is present in small amounts, such as the 5% or so in this commercial alloy, the adjacent austenite may be depleted in chromium (and molybdenum, if present). Dundas and Bond⁽⁷⁴⁾ found that pitting can occur in this depleted austenite. However, in duplex stainless steels, the large amounts of δ -ferrite present (e.g. 50%) can not be regarded as detrimental to pitting resistance. In summary, the commercial steel contained additional alloying elements which have been reported to improve pitting resistance, and a small amount of δ -ferrite, which has been reported to be detrimental to pitting resistance. However, it is unlikely that any of these differences were sufficient to have been greatly influential in the results obtained in this study. The remainder of this discussion focuses on the role of sulphur and sulphides in the pitting resistance of the three alloys.

5.4.1 A Suggested Mechanism for the Nucleation of a Propagating Pit

The results of this study suggest that it is the larger sources of sulphur which nucleate propagating pits: if a large enough supply of sulphur is available to maintain the rapid active dissolution, the pit might then become self-sustaining, even when all of the sulphur has been used up. The source of sulphur could be a single large sulphide inclusion. Alternatively, if a number of small sulphide inclusions were located sufficiently close together, then a growing pit could "tap" a new supply of sulphur as it expanded. Wranglen⁽⁴⁵⁾, in discussing the nucleation of pits on carbon steels identified active sulphides as those in which the adjacent matrix was "sulphur-infected" (as a result of the solidification process). These areas very easily formed anodic sites during the corrosion process. After a short while, the active sulphide was undermined and fell away, and the micropits ceased to grow. However, if a number of active sulphide inclusions occurred close to and below one another, a larger volume of the steel was "infected" with sulphur, so that a macroscopic self-generating pit could form. A similar mechanism may be operating here, with the inclusions providing a source of sulphur. It can be estimated that if all of the sulphide particles in the high sulphur steel were to be evenly distributed, then the inter-particle distance would be about $50\text{ }\mu\text{m}$, assuming that all the particles were the same (the mean) particle size. However, during the image analysis and EPMA examinations the presence of clusters of sulphides, sometimes only a few μm apart, was apparent on the specimens (Figure 5.8, for example). Also, there may be evidence in the current transients of this mechanism operating. For example, Figure 5.24 shows that the onset of pit propagation on the high sulphur steel was usually marked by a series of current bursts on a rising background. Similar observations were made on all three steels (Figures 3.4 and 5.25b). It is possible that these current bursts occurred when the growing pit encountered new regions where growth was enhanced, suggested here to be sub-surface inclusions which dissolve with the production of aggressive species such as H_2S in the acidic environment. Further supporting evidence may be derived from the optical metallography of quite large pits, where "pits within pits", presumably due to preferred growth on some areas of the advancing dissolution front, were regularly observed, Figure 3.21. Thus a propagating pit may be protected by the previous pit chambers during growth. In order to proceed on a more quantitative basis with this hypothesis, knowledge of the *spatial* distribution of sulphide inclusions is required. This information is not available, and would probably be rather difficult to acquire. At

the present time, the qualitative arguments given above are consistent with the observations.

Of course, repassivation of the pit might then still occur by some other mechanism. For example, in Chapter 3, it was suggested that the collapse of the pit cover might lead to dilution of the pit, and in Chapter 4 it was shown that solution flow rate can have an important effect on preventing a pit from developing. It is also conceivable that some growing pits bring about their own demise. For example, it has been shown by a number of authors that, growing pits undercut the metal surface (see Figures 3.20c and 3.21c), the attack can reach the surface in certain places, and the pit cover may in fact break down mechanically when the sub-surface pit becomes too great^(75,46). Certainly, the pit covers on large pits observed in this work often contained concentric cracks emanating from a prior sulphide location (Figures 3.19 and 3.23). Clearly, should the pit grow preferentially away from the surface, it is less likely to bring the roof in on itself, and more likely to continue to propagate. A technological example of the importance of the directionality of pit is the so-called "end-grain corrosion" found in some stainless steel chemical process plant fabrications. This problem arises when short transverse sections through wrought products are exposed to a corrosive medium, such as nitric acid. Exposed inclusion stringers are aligned perpendicular to the end-grain, such that when corrosion starts, the pit becomes narrow and deep, and penetration of a component can be rapid. This effect has also been noticed in laboratory tests^(35,36).

The lifetime distributions for the 3 alloys, presented in Figure 5.21, may be interpreted as follows. Pits falling into the first lifetime population (i.e. the only population on the model alloys) repassivate because the supply of sulphur is exhausted. Some of the second population of pits, observed on the commercial steel only, may in fact have been pits which had propagated beyond the sulphur exhaustion stage, but had then stopped for some other reason, such as those cited above.

The transition from unstable to stable pitting merits further discussion. It was pointed out in Chapter 3 that there was no obvious differences in the initial current rise to distinguish a pit which went on to propagate from numerous others which repassivated, and therefore that the initiation mechanism is the same for both. The recent work of Lott and Alkire⁽⁴⁷⁾ on the initiation of crevice corrosion asserts that the conditions for initiation are produced by the dissolution of MnS *prior* to local

acidification, and prior to the observation of large current increases associated with localised corrosion. Therefore, if Lott and Alkire's hypothesis was directly applicable to pit initiation, at the point at which the unstable pits repassivated in the present study, they would already have been propagating, in view of the substantial currents observed. Clearly, some other process is important in sustaining the nucleated pit. Eklund⁽⁴⁶⁾ proposes that initially the metal ions in the crevice between the inclusion and matrix come mainly from the inclusion, as the metal at that stage is able to passivate. Then, as dissolution proceeds, the dissolution of the sulphide in the crevice will increase the metal ion content, and ion complexing hydrolysis reactions can take place in the microarea. The result is a drop in pH which makes repassivation of the exposed metal difficult. Then, the electrochemical dissolution of the inclusion stops, since the electrode potential has dropped to a point where the sulphide is within its domain of thermodynamic stability (Figure 5.2). Sustained pit propagation would require that the metal ion hydrolysis exceeds that of the chemical dissolution reaction of the sulphide itself, otherwise the hydrogen ions will be neutralised by the formation of H_2S and the bared metal will passivate. He interpreted rapid potential drops in open circuit experiments to signal the onset of the metal matrix activation, or "pitting attempts". This theory does account for why nucleated pits might repassivate, but no specific role of sulphur species is required - the only requirement of the metal sulphide appears to be that it dissolves to release metal ions. However in this study, the current density of transients at the point of repassivation was usually very high, indicating that pitting according to Eklund's theory, i.e. metal dissolution outstripping chemical dissolution of the sulphide, was already well underway. A further implication of Eklund's work must be that large acid soluble inclusions such as MnS could provide pit initiation sites, but might then stop the pit growth as it chemically dissolved to produce H_2S in the acid produced from metal hydrolysis. There is no evidence to suggest a possible beneficial role of large acid soluble inclusions. On the contrary, the present work suggests that pitting is promoted by the increased availability of sulphur at larger sulphides.

5.4.2 The Relationship Between Pit Lifetime and Inclusion Size Distribution

The suggestion from the foregoing discussion is that the variability of the lifetime of a pit is related to the variability in the size (volume) of the sulphide inclusions at which pits nucleate. That is, the pit may stop when the supply of sulphur is exhausted. Whether a stable pit is formed then depends upon whether the resulting micropit is

large enough and is propagating fast enough to maintain the local aggressive environment. If the pit lifetime is indeed determined by the availability of sulphur, then the pit lifetime distribution (assuming that the inclusion dissolves at a constant rate during the lifetime of the pit) and the inclusion volume distribution should be related. To facilitate this comparison, the particle area distribution (which is directly proportional to the volume distribution assuming that the areas were measured on a random planar section through the microstructure) and the event lifetime distributions for the model alloys were scaled: if x is the variable, μ is the mean and σ the standard deviation, then the scaled variable is:

$$\frac{(x - \mu)}{\sigma}$$

Figure 5.26 shows, for the same number of standard deviation classes about the mean, the normalised distributions of particle area and event lifetime for the high purity steel. The short, apparently potential independent lifetime of events recorded for the model alloys (confirmed using the high sulphur alloy, see below) was taken into account here, and the lifetime distribution was constructed from events recorded in the potential range 10 - 460mV SCE. Figures 5.27 and 5.28 show similar diagrams for the high sulphur and commercial purity steels, respectively. For these diagrams the lifetime distributions were constructed for two potential ranges, and illustrate the consistency and largely potential-independent lifetime distributions. For each of the three alloys, the distributions of inclusion area and transient lifetime distributions are similar. These results provide strong support for the assertion that the lifetime of a pit is related to the inclusion size.

5.4.3 Some Comments on the Discrepancy Between the Total Number of Pits Observed and the Total Number of Sulphide Inclusions

Whilst the studies reported here have clearly established that sulphide inclusions are the optimum sites for pit nucleation, the number of sulphides (potential pit nucleation sites?) far exceeds the number of transients observed. Apparently then, not all sulphides nucleate pits. There are however, a number of other possible explanations for this discrepancy, three of which are briefly discussed here.

**Figure 5.26 Distributions of Particle Areas and Current Transient Lifetimes:
High Purity 304L**

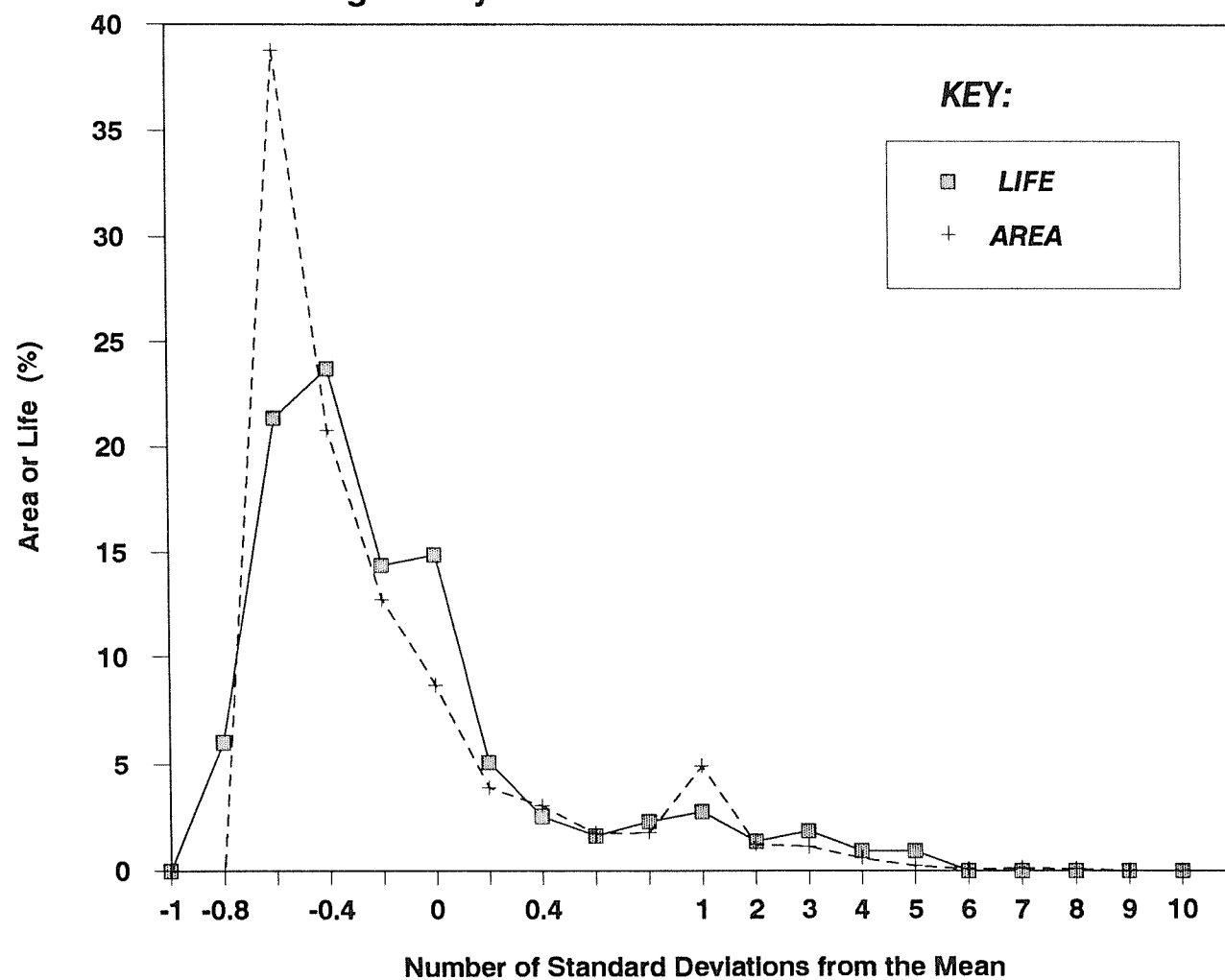


Figure 5.27 Distributions of Particle Areas and Current Transient Lifetimes:
High Sulphur 304L

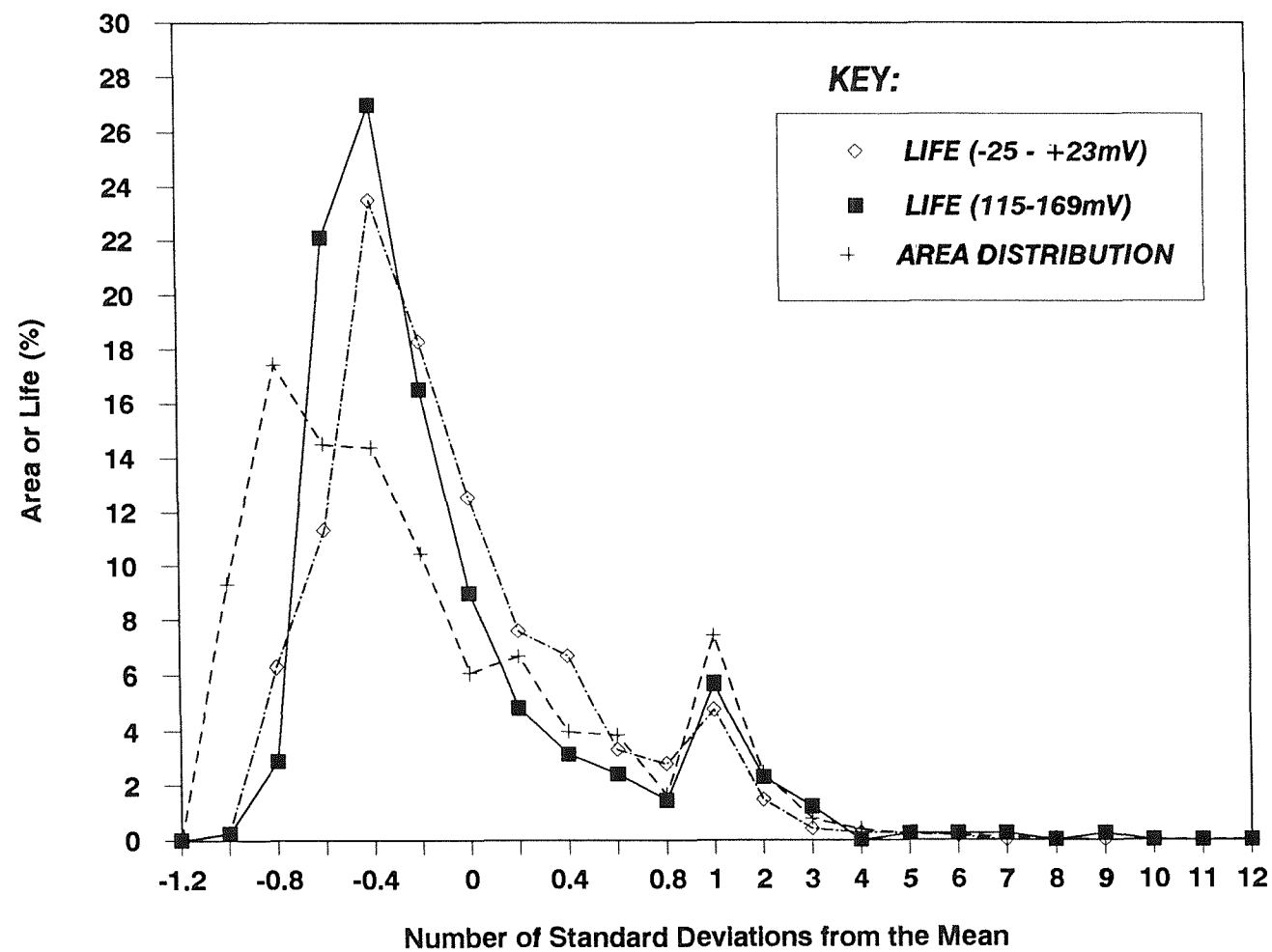
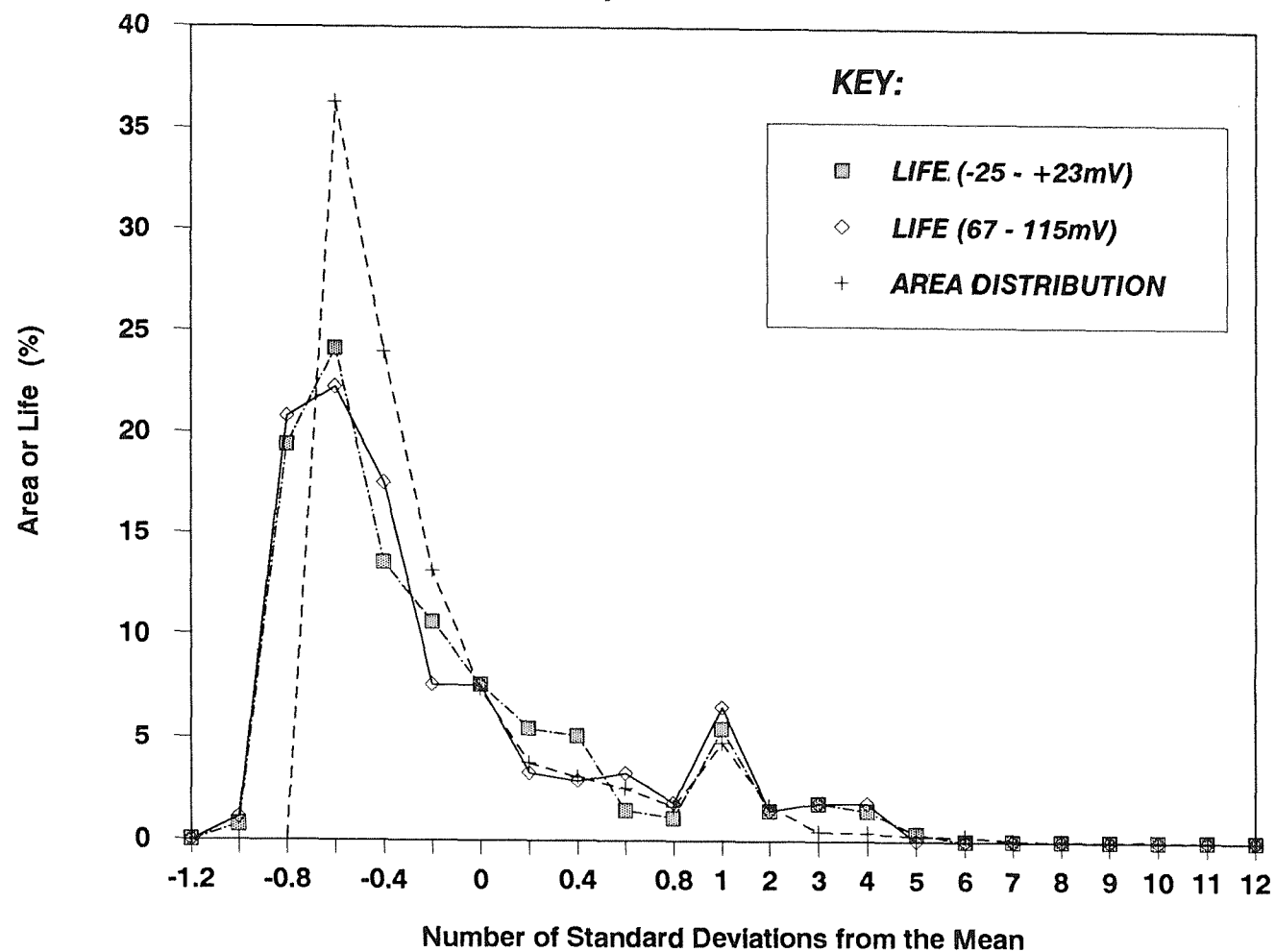


Figure 5.28 Distributions of Particle Areas and Current Transient Lifetimes:
Commercial Purity 304L



Sedriks⁽⁵⁾ pointed out in his review that there is likely to be a "pecking order" of pit initiation sites. For example, when the most susceptible sites (MnS) are eliminated - by procedures such as lowering the manganese content - the pitting resistance is increased but the susceptibility to pitting is not removed: as the oxidising power of the corrodent increases, chromium sulphides⁽²⁷⁾, oxides⁽⁷⁶⁾ or silicates⁽⁷⁶⁾ may offer sites for pit initiation. This list of susceptible sites can be extended to include other inclusions, dislocations etc., which would not nucleate pits under circumstances where sulphur-rich inclusions are present. Extending this idea of a ranking order of susceptibility, and given the wide variation of sulphide inclusion composition apparent in the steels used in this study, it is reasonable to postulate a similar spectrum of susceptibilities within the sulphide group. Susceptibility within this group is then likely to depend primarily on chemical composition (i.e. sulphur content and solubility) and also on size and shape.

It is also likely that some pits which did nucleate were not detected due to limitations of the sensitivity of the technique, that is, they repassivated before being seen above the background current. For example, if the background noise band was 20nA wide (which it usually was) then if a pit generated a current of say 30nA for 10s, this current probably would not have been detected as a pit, yet the volume of metal dissolved would have been sufficient to produce a pit 3 μ m or so in diameter. At this point it perhaps should be pointed out that the *mean* diameter of inclusions was less than this value, on all three steels. Obviously, many inclusions were much smaller than this.

A third possibility is that the nucleation of a pit at one sulphide inclusion then protects the surrounding (cathodic) area, although in the experiments reported here, this is not valid since the current was supplied by the potentiostat.

5.5 SUMMARY

By combining rigorous microstructural characterisation and multiple slow potentiodynamic sweep experiments on commercial purity 304L and two high purity 304L model alloys, one of which was doped with sulphur, it has been shown conclusively that pits nucleate predominantly at sulphur-rich inclusions. The nucleation frequency of unstable pits at a given potential reflected the sulphur content of the alloy. The size and shape of inclusions influenced the size of pits, and their shape dictated the current-time evolution of the transients. Also, the distribution of

pitting breakdown potentials was shifted to higher (more anodic) values as the sulphur content of the alloy was decreased. The different sulphide inclusion volume fraction of the alloys was also reflected in the passive current densities, being lowest in the high purity alloy and highest in the high sulphur alloy at a given potential, a result which indicates that electrochemical dissolution at sulphide inclusions contributed to the current measured in the passive state.

A suggestion from this work is that in order to nucleate a propagating pit, initiation must occur at an inclusion with a sufficiently large supply of sulphur - either a single inclusion or a cluster of smaller inclusions. Otherwise the pit may repassivate when the supply of sulphur is exhausted. In support of this, for each of the three steels, the distribution of particle sizes showed a good correspondence with the distribution of lifetimes of current transients.

CHAPTER 6

THE IMPROVEMENT OF THE LOCALISED CORROSION RESISTANCE OF STAINLESS STEEL BY LASER SURFACE TREATMENT

CHAPTER 6 - THE IMPROVEMENT OF THE LOCALISED CORROSION RESISTANCE OF STAINLESS STEEL BY LASER SURFACE TREATMENT

6.1 INTRODUCTION

Laser beams with high power density provide a method for rapidly melting and alloying selected areas on a metal surface. The attendant rapid solidification rates due to substrate self-quenching offer the possibility of modifying surfaces by, for example transformation hardening. Such procedures may also be used to modify the corrosion resistance of an alloy.

A number of studies concerning the electrochemical properties of laser processed ferrous alloys have been reported. Laser surface alloying has been used to produce stainless steel surfaces on carbon steel substrates^(1,2) which exhibited similar passivation behaviour to bulk stainless steel in 1N H₂SO₄. In addition, the work of McCafferty et al^(1,3,4) and Lumsden et al⁽⁵⁾ has shown that laser surface melting of AISI type 304 stainless steel substantially increases its pitting resistance. This, they suggested, may be due to a removal or redistribution of large sulphide inclusions.

This chapter demonstrates that the corrosion properties of an alloy can be greatly enhanced by modifying the surface microstructure by melting a thin surface layer using a laser. This is illustrated using examples of two well known failure modes of stainless steels: pitting and intergranular stress corrosion cracking (IGSCC).

In the study of pitting corrosion, the work described in the previous chapters is extended. It was shown there that the volume fraction and distribution of sulphur-rich inclusions are dominant factors in determining the pitting resistance of type 304L stainless steel, and asserted that the observed transient lifetimes are related to inclusion size. Here, it is demonstrated that laser melting improves pitting resistance primarily by removing large sulphur-rich inclusions. Most of the sulphur is retained following laser treatment, and transmission electron microscopy revealed the presence of small, rounded sulphide particles. This is a significant finding, since it indicates that below a certain size, sulphides are too small to nucleate a detectable pit. Some inclusions were also found using image analysis, and these too were generally small and rounded. These factors are thought to further contribute to the improved pitting resistance. Data from experiments on 316L stainless steel are introduced and

used in a speculative discussion on the role of molybdenum, and specifically the interaction of Mo and S on the pit surface, in improving the pitting resistance of stainless steels. This work is then extended in Chapter 7.

The second example is concerned with the prevention of intergranular stress corrosion cracking of sensitised stainless steel, and shows that by introducing a thin surface layer ($100\mu\text{m}$, for example) of unsensitised stainless steel between the corrosive environment and the underlying susceptible microstructure, cracking is prevented.

6.2 THE IMPROVEMENT OF PITTING RESISTANCE USING LASER SURFACE MELTING

6.2.1 Experimental

The effect of laser treatment on pitting resistance is studied using the electrochemical and quantitative metallographic techniques described in the previous chapter. Disc specimens (5cm^2) of the commercial purity 304L and the high sulphur 304L model alloy, were used for this work (the compositions are given in Appendix B). Prior to the laser surface treatment, specimens were ground to a grade 240 grit finish. A Culham Laboratory carbon dioxide laser operating continuously at 4kW was used for this work. A schematic diagram of the laser beam path is shown in Figure 6.1. The laser beam was defocussed 20mm to produce melt tracks approximately 2mm wide (average energy density approximately $130\text{kW}/\text{cm}^2$). The specimen was moved beneath the laser beam at 50mm/s, producing a melt depth for each track of $150\text{--}300\mu\text{m}$. Melt tracks were overlapped by approximately 50% until the entire surface had been treated. A helium atmosphere was maintained around the specimen to prevent excessive oxidation. Figure 6.2 shows a specimen following laser treatment. Specimens were surface-primed and mounted in cold setting epoxy resin, using the same methodology as described previously for the untreated specimens (Section 2.1, Chapter 2). To enable a direct comparison between the pitting resistance of laser treated specimens with untreated specimens (Chapters 3 and 5), the as-melted surface was removed by wet grinding to a depth of $50\mu\text{m}$ - still well within the laser melt zone - and then ground to a grade 240 grit finish prior to the pitting experiments. One laser treated specimen from each of the commercial purity and the high sulphur steels was prepared to a $1\mu\text{m}$ diamond polish for image analysis and SEM analysis.

Figure 6.1 - Schematic Diagram of Laser Processing Apparatus

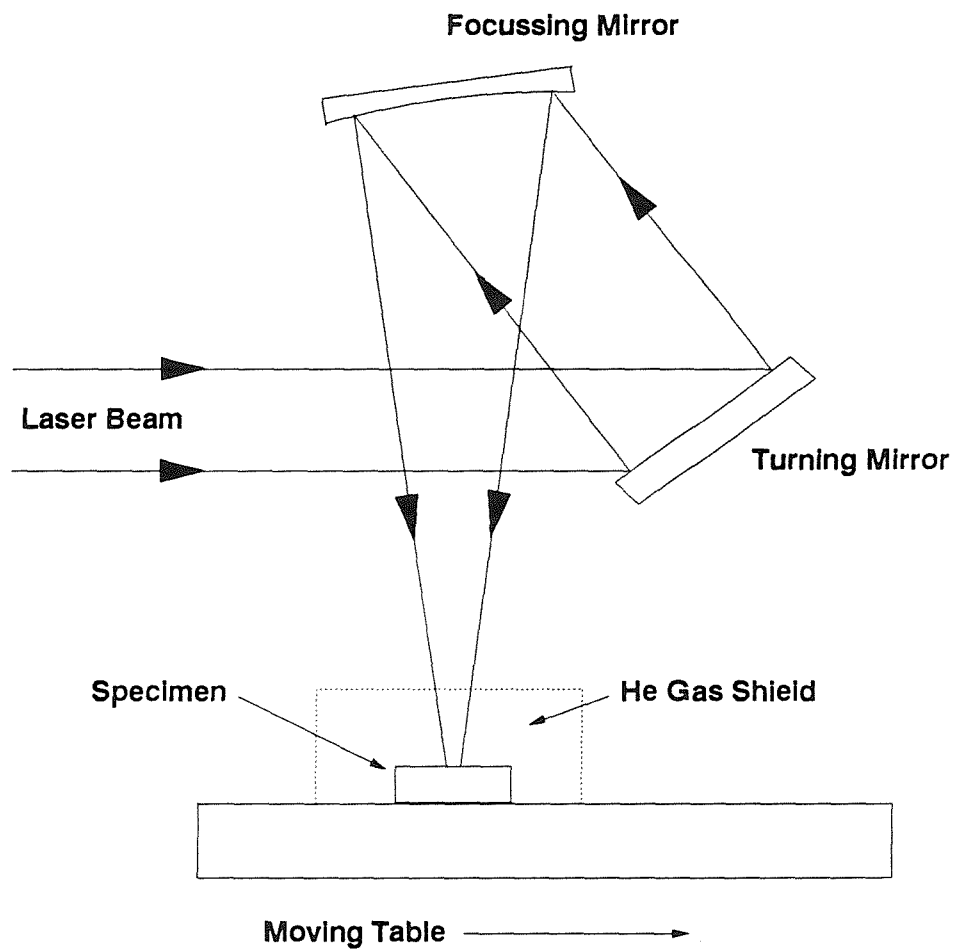




Figure 6.2 Laser-treated specimen

Pitting experiments were again carried out in 1000ppm chloride solutions. They consisted of very slow anodic sweeps ($5 \times 10^{-6} \text{V/s}$) from the region of the rest potential on multiple specimens, using the apparatus described previously (Chapter 2).

Image analysis of the laser treated specimens used the routine described in Chapter 5 (Figure 5.7) for measuring the total area fraction of inclusions, and in addition the individual particle length and particle area distributions.

Qualitative chemical analysis of individual particles was performed using EDS analysis in the SEM.

6.2.2 Results

6.2.2.1 Pitting Experiments

Figure 6.3 shows the variation in the nucleation frequency of unstable pits as a function of potential for both the high sulphur and commercial purity steels before (Figure 6.3a) and after (Figure 6.3b) laser surface treatment. The reduction in the nucleation frequency following laser treatment was dramatic, although it is notable that the differential in the pitting activity of the two alloys was maintained. This result is further illustrated in Figures 6.4 and 6.5, which show representative current vs. time sequences for the two steels, before and after laser surface treatment, in the same potential regimes. These figures also enable a comparison to be made between the shape of transients before and after laser treatment. For the high sulphur steel, there was no marked change in transient shapes following laser treatment, Figure 6.4. However, the transients on the laser treated commercial steel were, in general, much shorter lived than for the untreated steel, and indeed resembled the transients common to the model alloys (compare Figures 5.15 and 5.17 with 6.5b), as they usually consisted of single current-burst events and were much shorter lived than those on the untreated steel. Occasionally, bursts of current in a single transient, resembling those seen previously on the high purity steel (Figure 5.18), were observed, Figure 6.6. Figure 6.7 shows the lifetime distribution of current transients on the high sulphur and commercial 304L steels before and after laser treatment, and also includes data for the high purity steel (from Chapter 5). The diagram highlights three clear observations. Firstly, the lifetime distribution of current transients on the laser treated commercial steel is very different to that of the untreated steel, and is similar

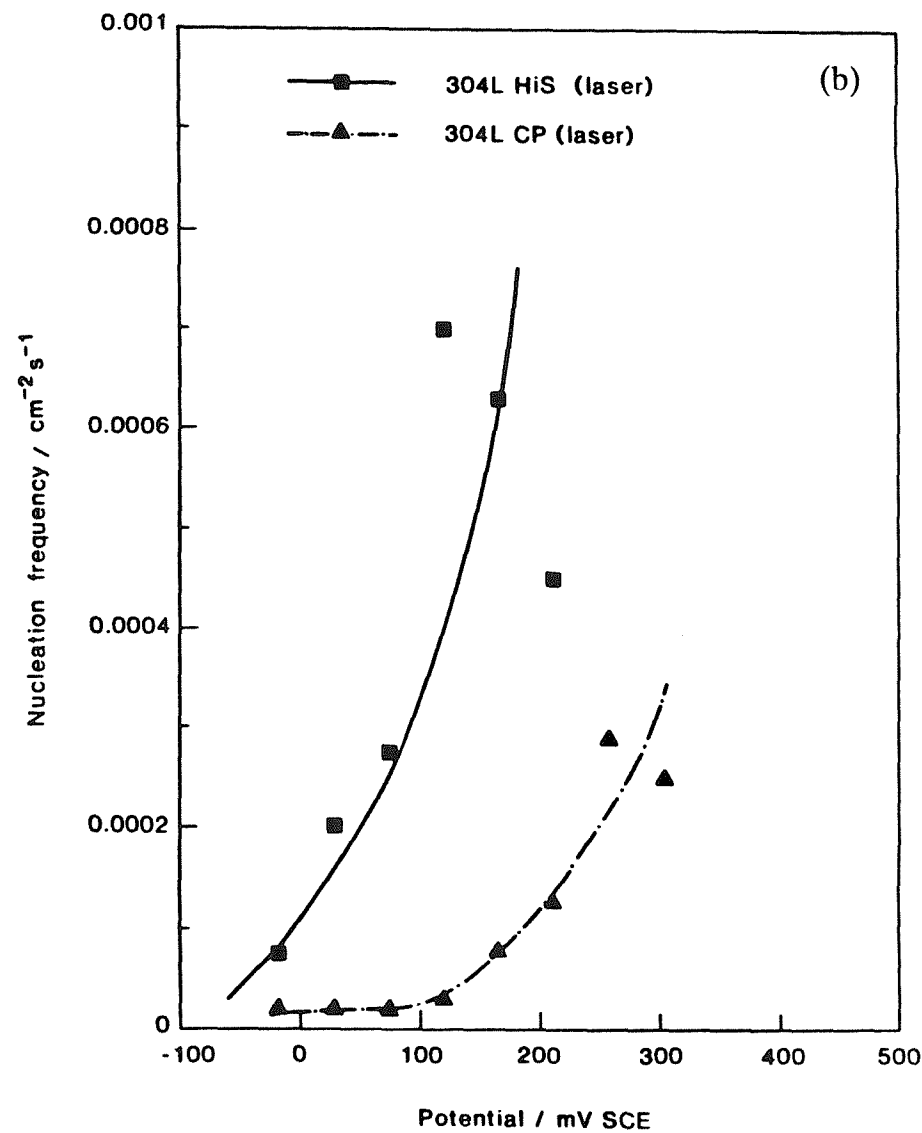
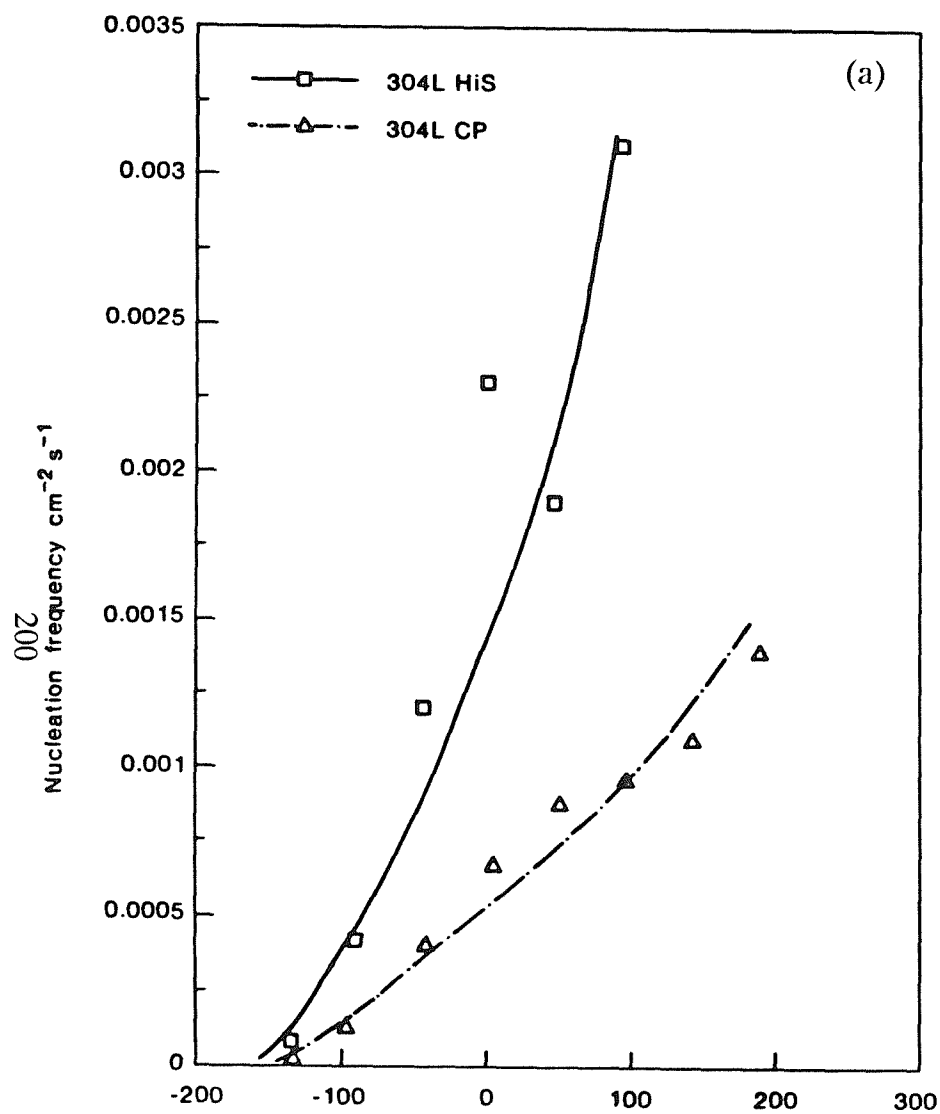
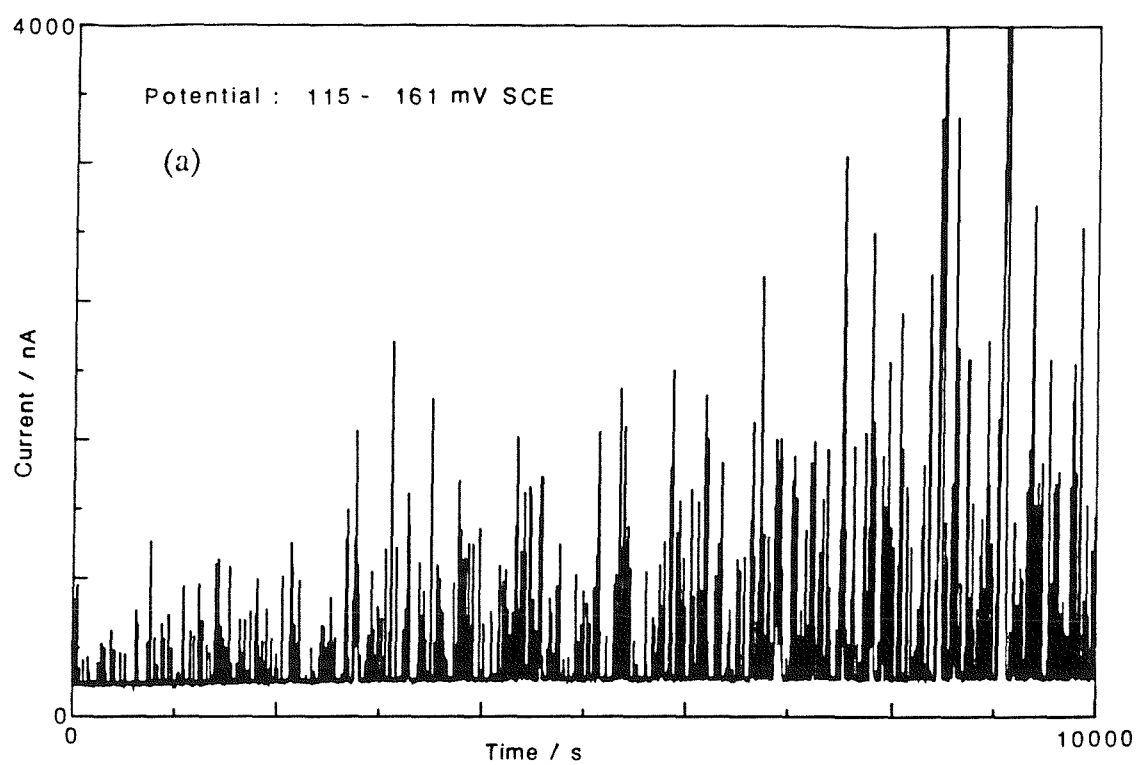


Figure 6.3

Nucleation frequency of unstable pits as a function of electrode potential for commercial purity 304L and high sulphur 304L (model alloy) (a) before and (b) after laser surface treatment.

304L High Sulphur



304L High Sulphur Laser Treated

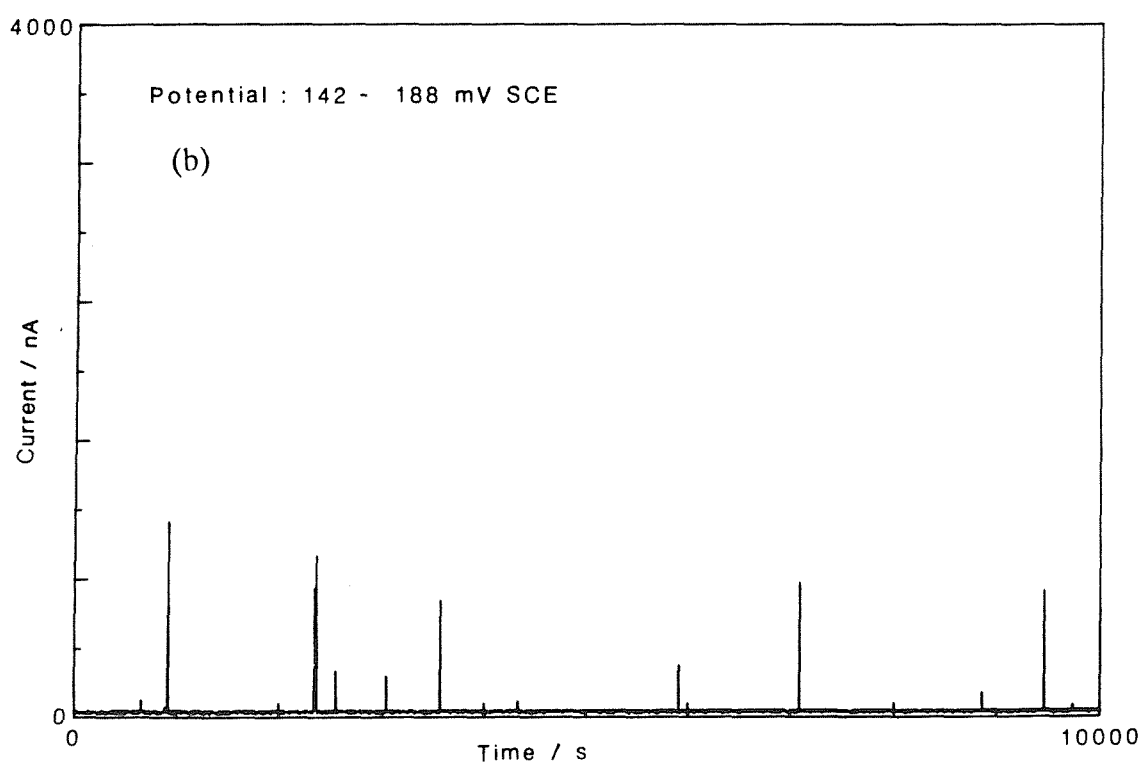
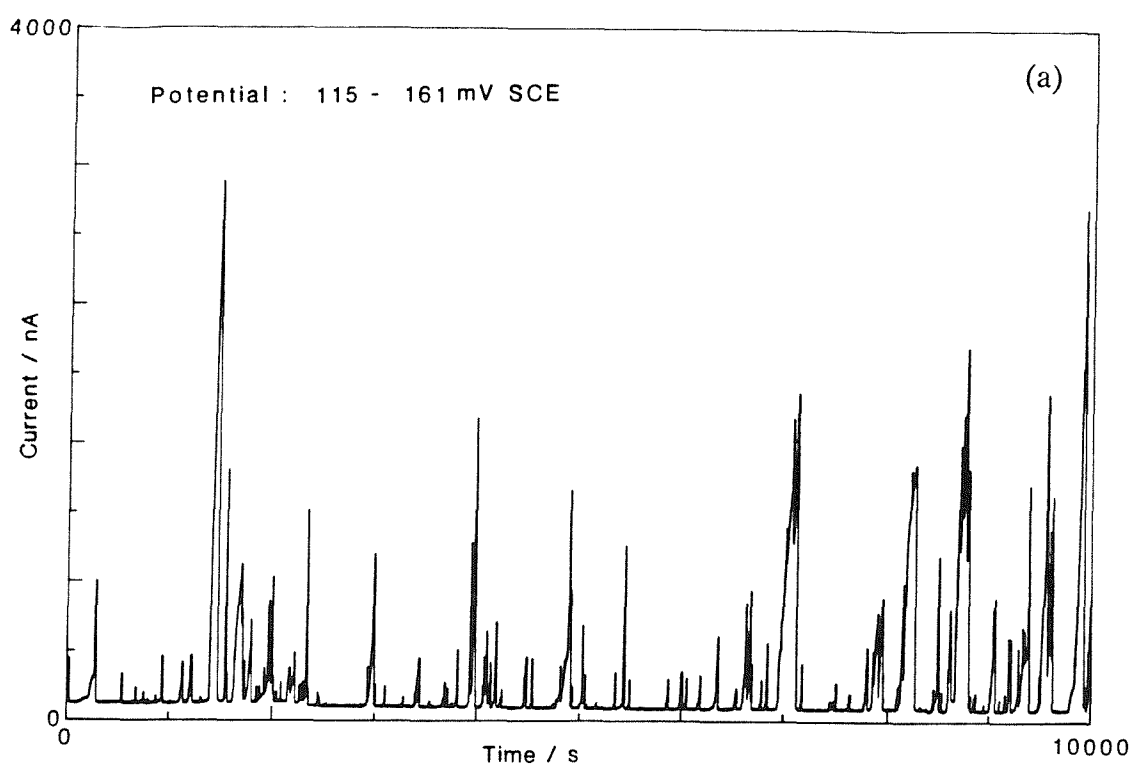


Figure 6.4 Typical current-time sequences showing anodic current transients on high sulphur 304L (a) before and (b) after laser treatment.

304L Commercial Purity



304L Commercial Purity Laser Treated

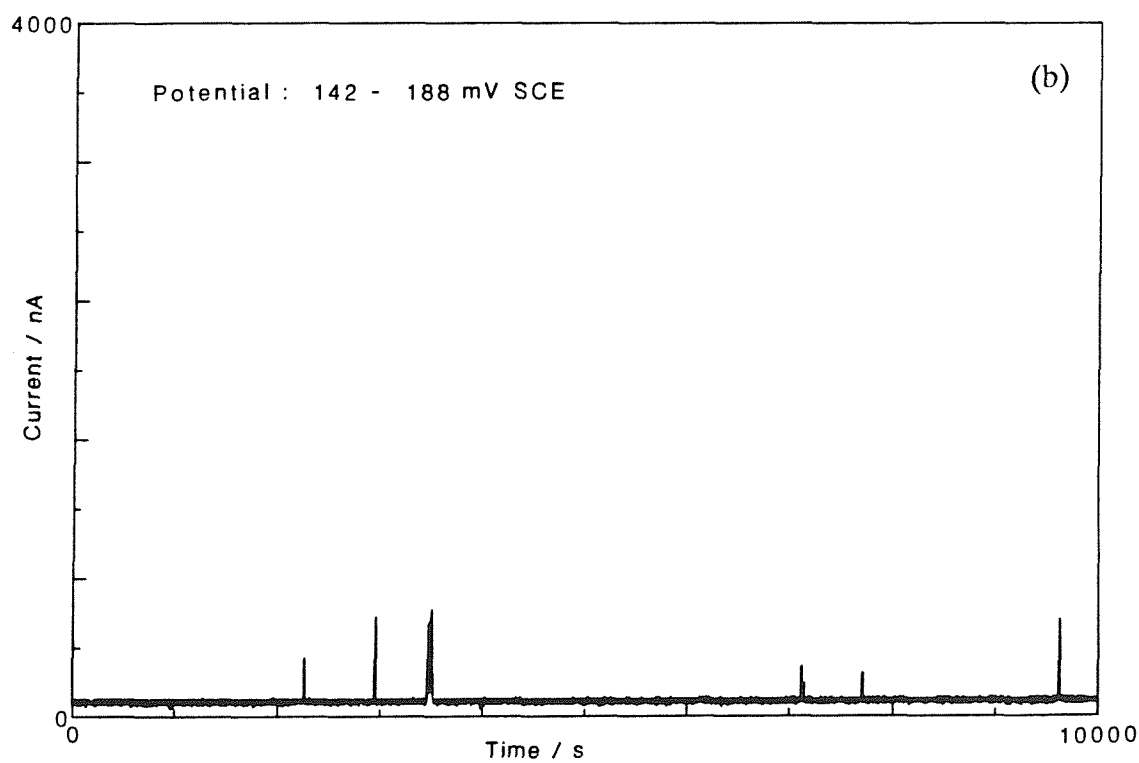


Figure 6.5 Typical current-time sequences showing anodic current transients on commercial purity 304L: (a) before and (b) after laser treatment.

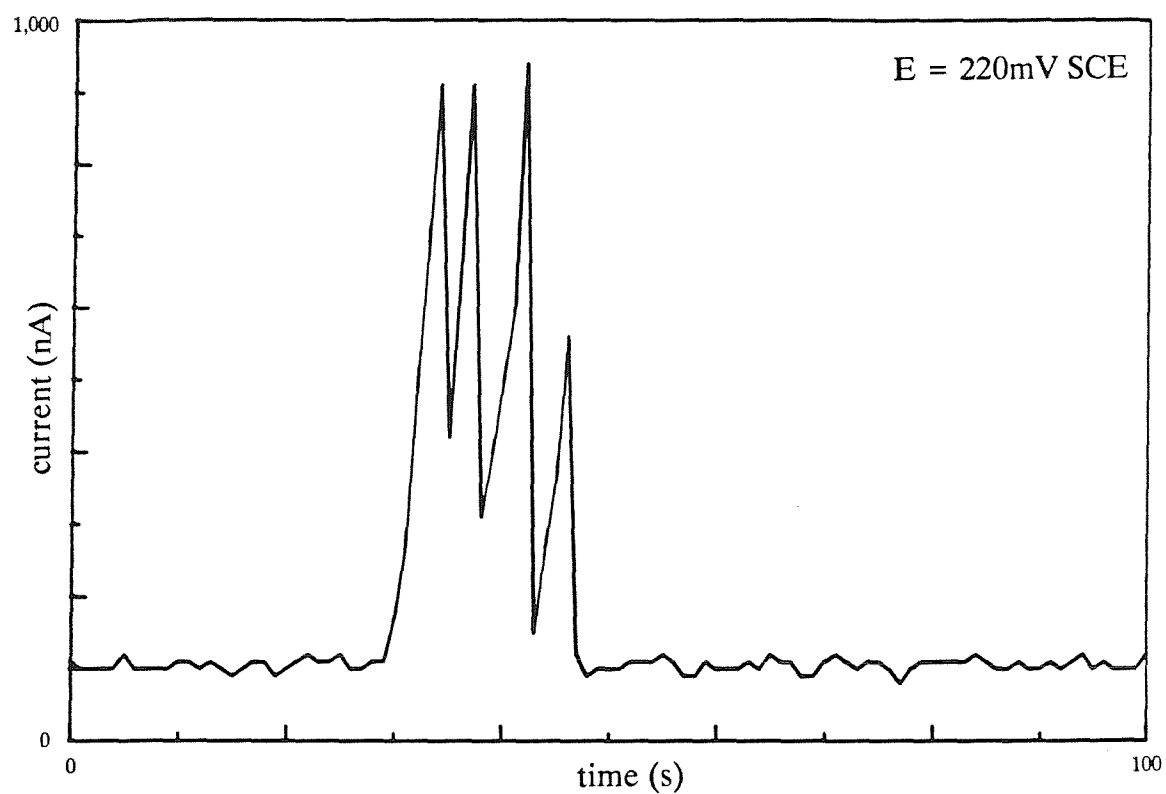


Figure 6.6 Multiple current bursts within a single transient: laser-treated commercial purity 304L (c.f. Figure 5.18)

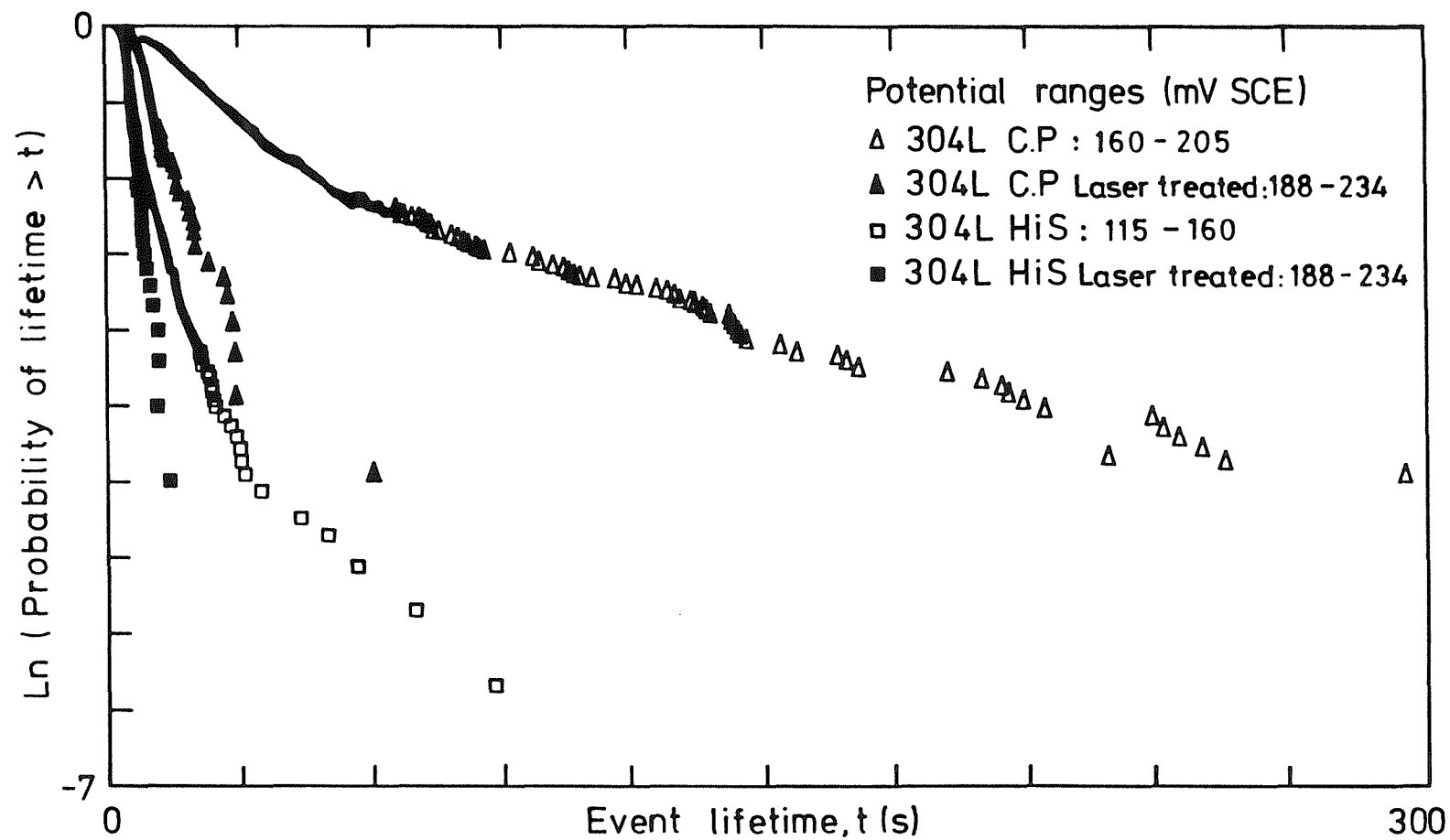


Figure 6.7 Distribution of lifetimes of current transients on commercial purity 304L and high sulphur 304L before and after laser surface treatment.

to the distribution for the model alloys. Secondly, the distributions for the high sulphur steel before and after laser treatment are similar, with a slight shift to shorter lifetimes for the laser treated steel. The third point is a re-iteration of an observation described in Chapter 5: the lifetime distributions for the high sulphur and high purity steels were very similar, which has been suggested to be related to the similar particle size distributions, despite the very appreciable differences in pit nucleation frequency and the sulphide inclusion volume fraction.

The data on pitting breakdown potentials recorded for the laser treated steels gives further clear evidence for the beneficial effect of removing sulphide inclusions. Figure 6.8 presents data for both untreated and laser treated specimens, and includes data taken from Figure 5.24. Also plotted on Figure 6.8 are some data for type 316L stainless steel, which were collected using the same apparatus and an identical experimental procedure. Although the data sets for the laser treated steels are rather limited, with 4 data points (experiments) for the high sulphur steel and 10 data points for the commercial steel, there is a clear anodic shift (indicating an improvement in corrosion resistance) in the breakdown distributions when compared to untreated specimens of the same bulk composition. An indication of the extent of this improvement is given by the proximity of the breakdown distribution for the laser treated commercial purity 304L to that for the high purity 304L. Furthermore, both distributions were close (within about 20mV) to the distribution for 316L. Two specimens, not included on the diagram, did not pit during the experiments on the laser treated specimens (the anodic potential limit was +460mV SCE). Laser treatment of the high sulphur steel would appear to improve its pitting resistance to a level comparable with that of the untreated commercial purity grade.

Inspection of current vs. time sequences at the onset of stable pitting revealed that the current rise associated with each of the 10 specimens of the laser-treated commercial 304L steel was very rapid, and appeared to consist of a single event, Figure 6.9. For the laser treated high sulphur specimens, the current rise was again rapid, but some cyclic behaviour was usually evident, Figure 6.10. These observations are discussed later.

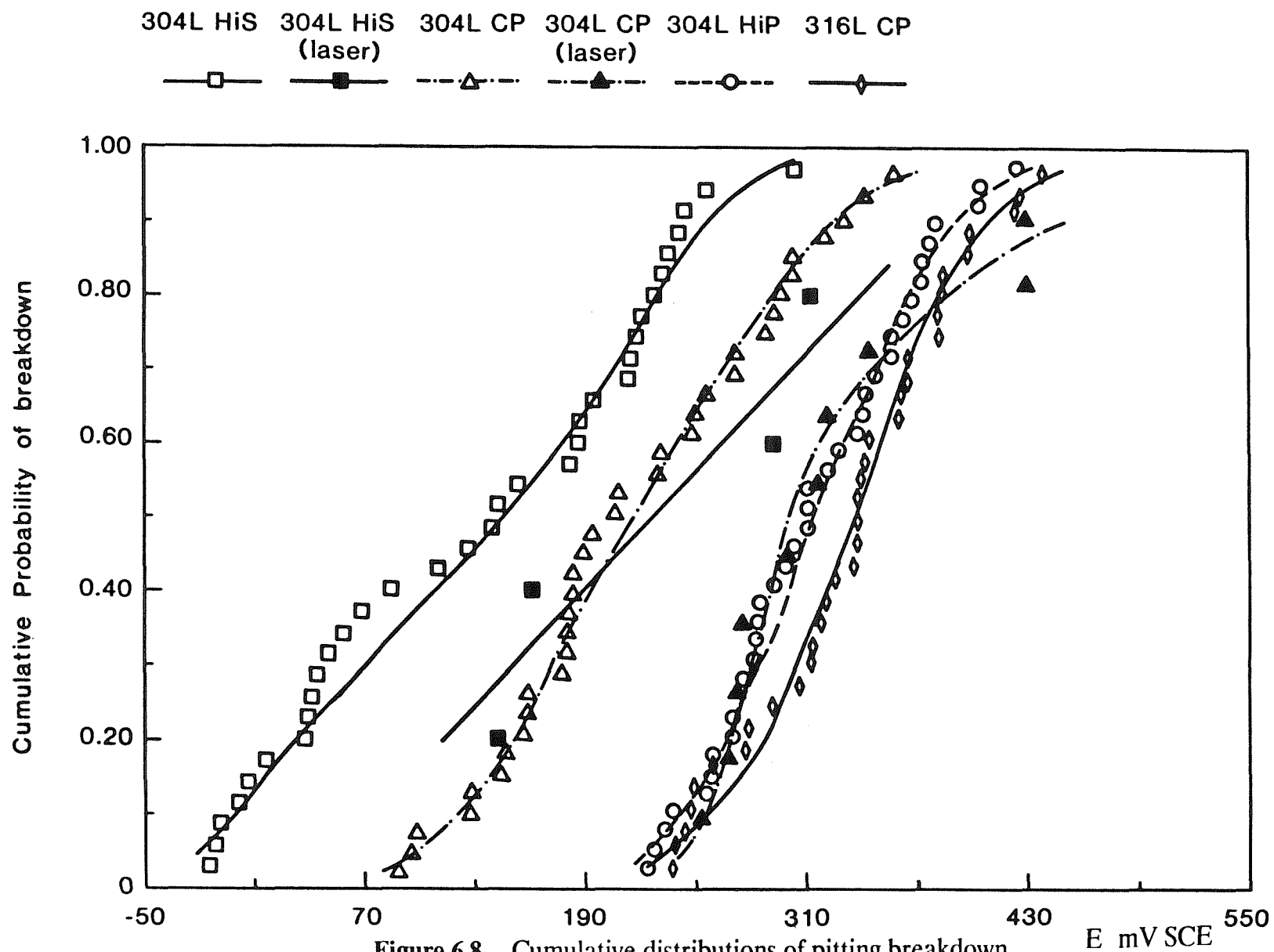


Figure 6.8 Cumulative distributions of pitting breakdown potentials for all of the steels used in this study

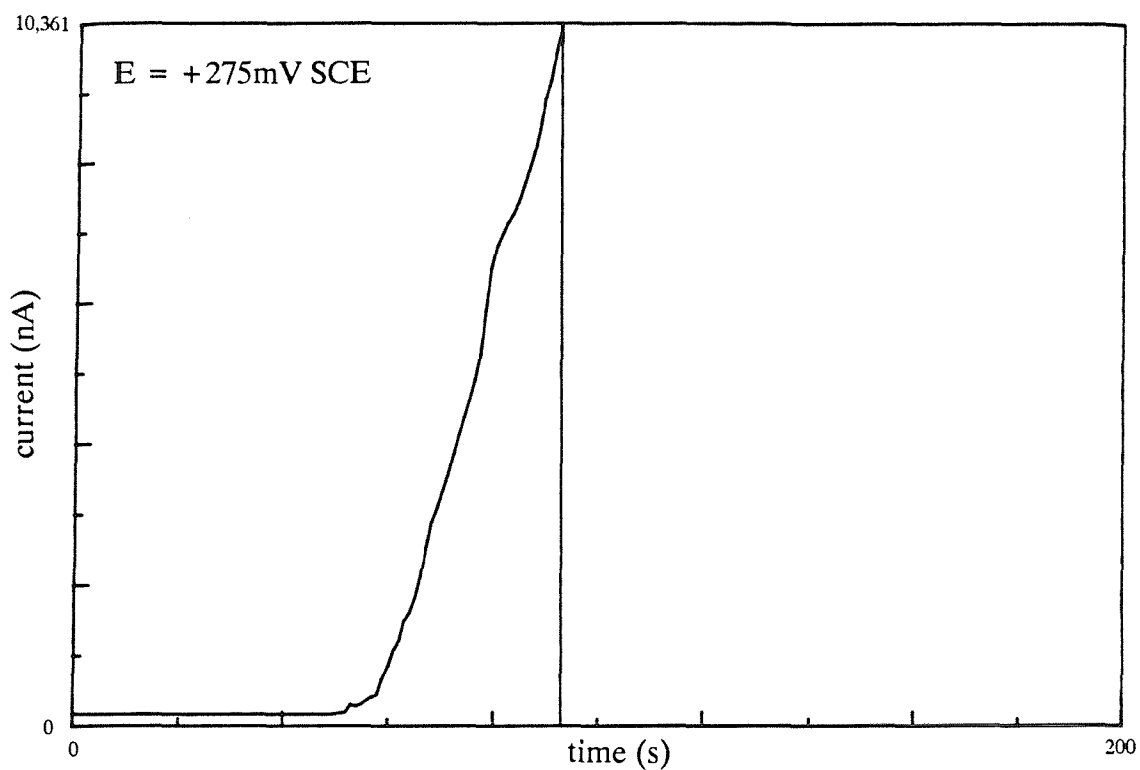


Figure 6.9 Current-time sequence illustrating the very rapid current rise to the $10\mu\text{A}$ limit, common to all of the laser-treated commercial purity 304L specimens

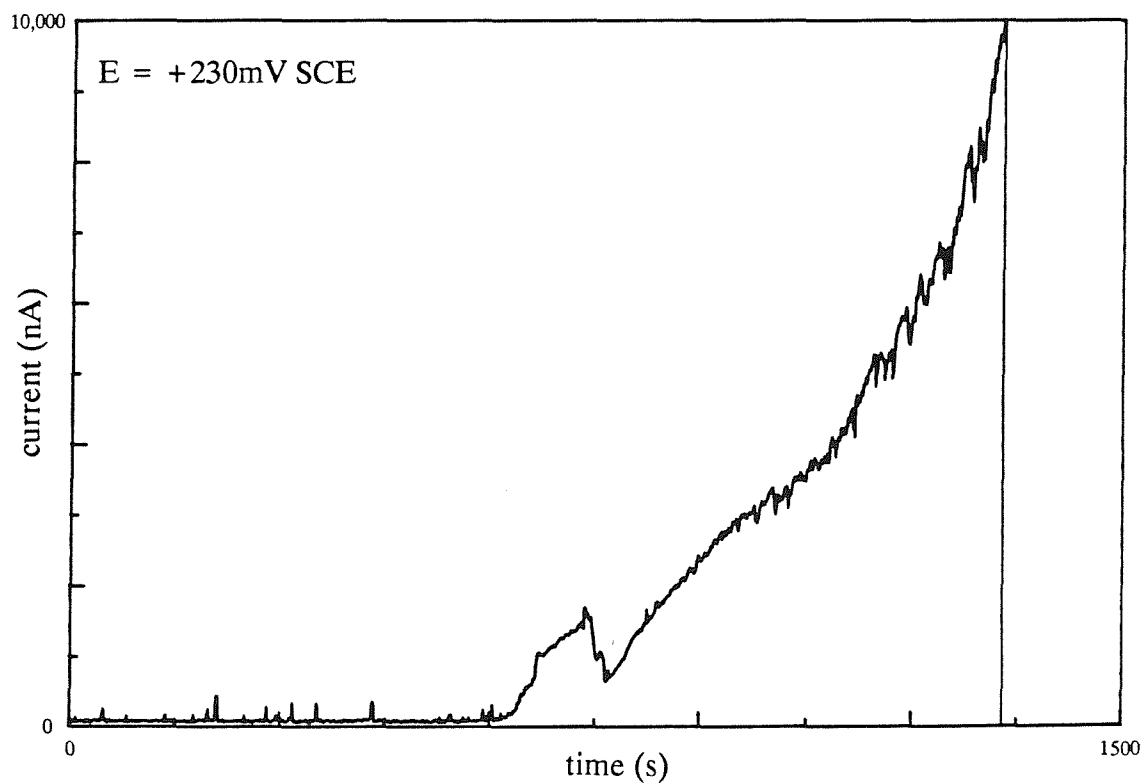


Figure 6.10 Typical current rise to the $10\mu\text{A}$ current limit at the onset of sustained pitting on the laser-treated high sulphur alloy

6.2.2.2 Microstructural Characterisation

Figures 6.11 and 6.12 show the inclusion length and area distributions for the high sulphur steel and commercial purity steel following laser treatment. Table 6.1 provides a summary of the image analysis results on the laser treated specimens, and repeats the relevant results of the analysis reported in Chapter 5 (Table 5.2) for the untreated steels. Inspection of the results for the laser treated specimens reveals a much lower volume fraction of inclusions compared to the untreated specimens for both steels - about a 70% reduction in the case of the high sulphur steel, and a reduction of about 87% for the commercial purity steel. Also, the number of inclusions found after the laser treatment was substantially reduced - by 70% for the high sulphur steel and by 81% for the commercial purity steel. Taken together, the values of volume fraction and total number of inclusions indicate that, for the high sulphur steel, the mean visible particle size stays about the same before and after laser treatment. For the commercial steel, the decrease in total volume fraction of inclusions was greater than the reduction in the total number of inclusions, indicating that the inclusions remaining after laser treatment were smaller in this steel. The values given in Table 6.1 confirm these deductions: the mean values of the area distributions were similar before and after laser treatment in the high sulphur steel. This was not the case for the commercial purity steel, where there was a marked decrease in mean particle area following laser treatment.

In addition to the image analysis work, extensive optical and scanning electron microscopy of the laser treated surfaces reached the following conclusions: on the laser treated **commercial steel** inclusions were usually spheroidal, and fairly evenly distributed throughout the microstructure. Figure 6.13 shows two such inclusions. These particular inclusions were about $60\mu\text{m}$ apart and were the closest together of the inclusions found on the specimen. On the laser treated **high sulphur steel**, regions in which clusters of inclusions were evident, Figure 6.14, were separated by large areas which were apparently inclusion free (but see Section 6.2.3). The inclusions appeared similar in shape to those on the untreated high sulphur steel (compare Figure 6.14 with 5.8).

The mean particle lengths and areas presented in Table 6.1 allow some insight into possible shape changes of inclusions associated with laser treatment. By assuming that the particles were elliptical in shape (see Appendix F), the ratio of the major axis (D)

Figure 6.11 Cumulative Length Distribution of Inclusions Measured on Laser Treated 304L Specimens by Image Analysis

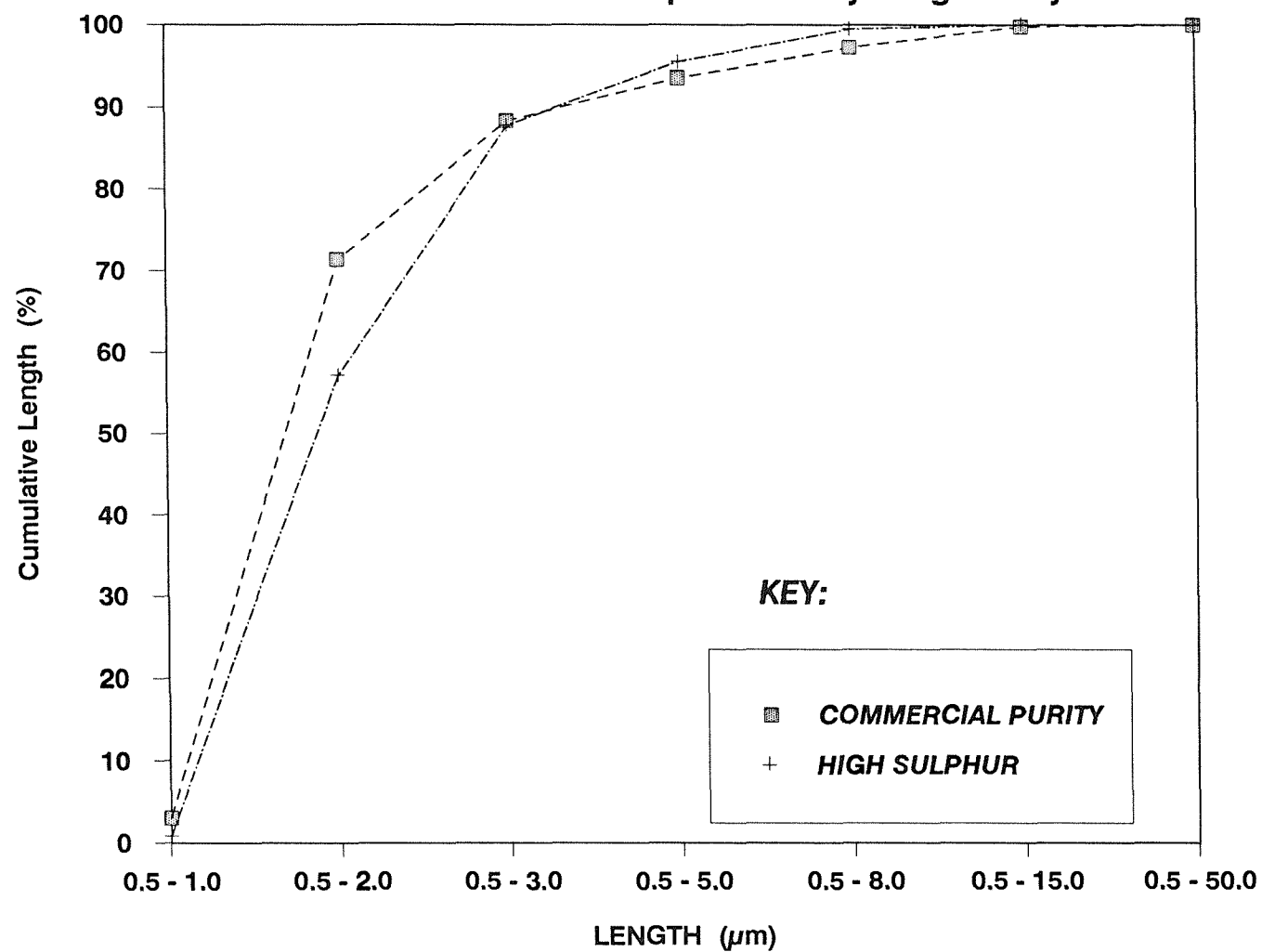


Figure 6.12 Cumulative Area Distribution of Inclusions Measured on Laser Treated 304L Specimens by Image Analysis

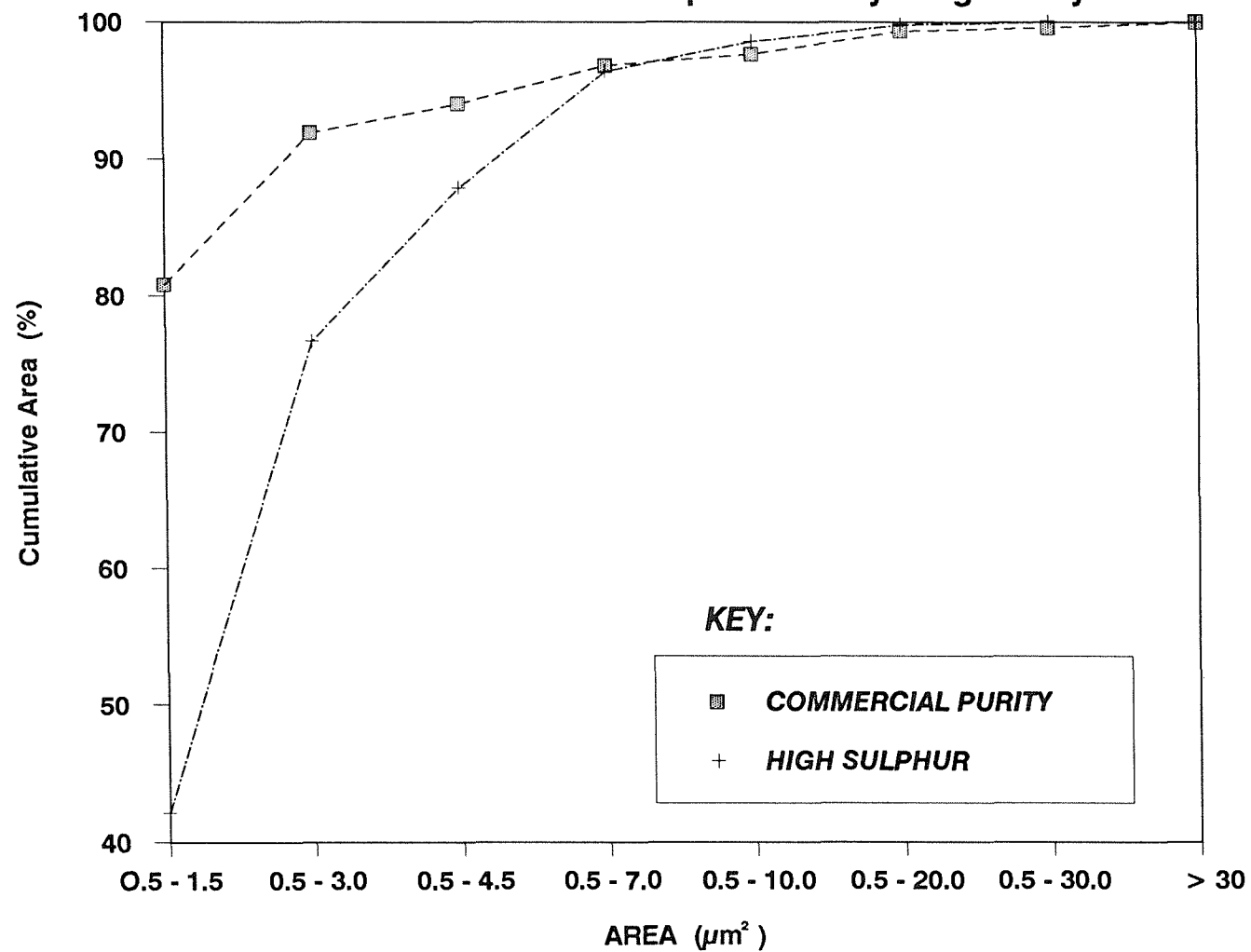


Table 6.1 Summary of Image Analysis Results

	304L HiS untreated	304L CP untreated	304L HiS laser treated	304L CP laser treated
Total No. of Fields	225	225	225	225
Field Size (mm²)	0.01459	0.01459	0.01403	0.01403
Total No. of Particles	6,069	2,456	1,807	471
Area % of Particles	0.436	0.178	0.1333	0.0234
Standard Deviation	0.200	0.116	0.180	0.1122
Mean Length (μ m)	2.15	2.63	2.16	2.32
Standard Deviation	1.02	1.96	1.02	2.82
Mean Area (μ m²)	2.34	2.46	2.37	1.64
Standard Deviation	2.24	3.60	2.22	4.4

HiS = High Sulphur 304L

CP = Commercial Purity 304L

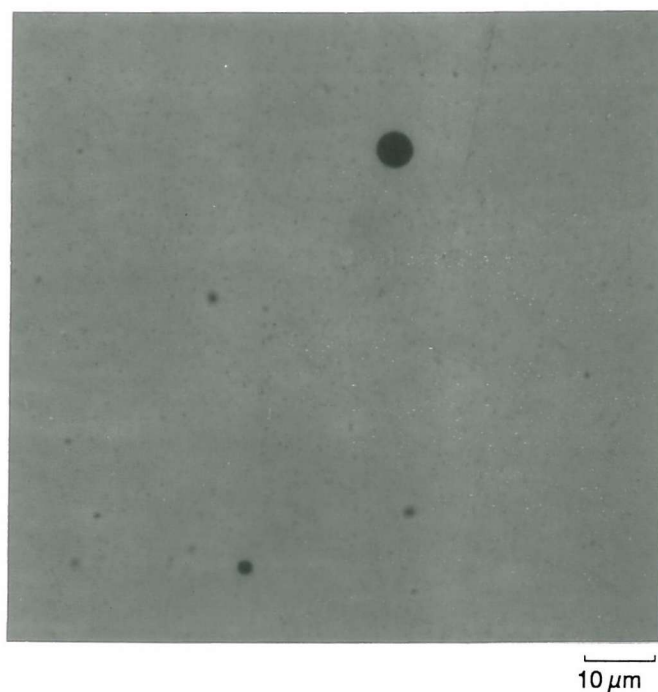


Figure 6.13 Optical micrograph showing spheroidal inclusions in the laser melt zone (commercial purity 304L)

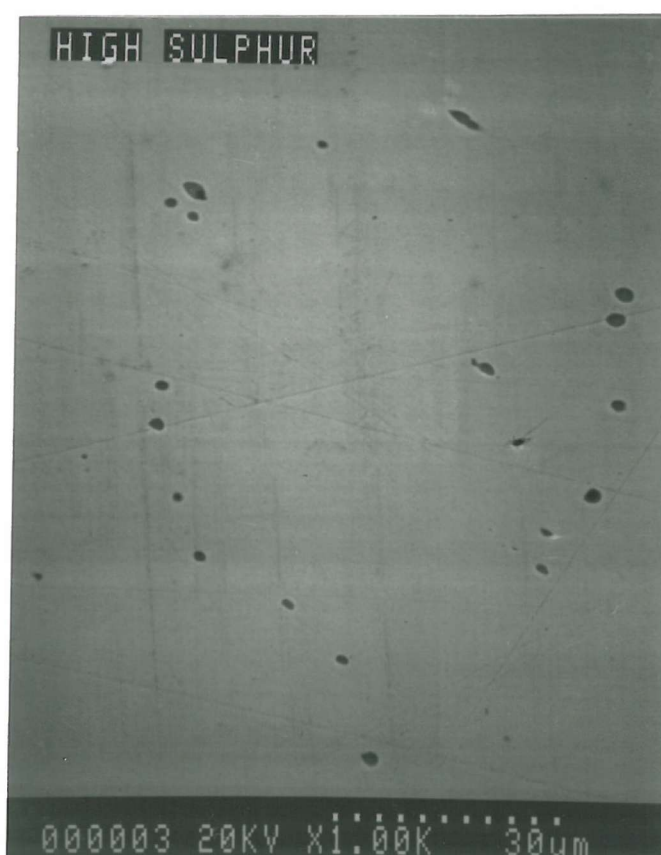


Figure 6.14 Scanning electron micrograph from a region of inclusion "clustering" in the laser melt zone of the high sulphur 304L

to the minor axis (d) gives an indication of the "roundness". When these shape factors were calculated for the two steels, before and after laser treatment, the shape of the particles in the high sulphur steel changed little ($\frac{D}{d} = 1.55$ before and 1.54 after treatment). This was consistent with the direct microscopic observations. From the image analysis of the commercial steel, the particles appeared to become slightly more elongated ($\frac{D}{d} = 2.21$ before and 2.58 after treatment). However, this analysis was not borne out by the direct microscopic observations, where the particles were found to be rounded (e.g. Figure 6.13). The reason for this anomaly is not fully clear, but may well be associated with the resolution of the image analyser, since on the laser treated commercial steel, most of the inclusions which were measured were very small (see Figures 6.11, 6.12).

If consideration is now given to the possible inclusion volume changes resulting from the laser treatment, this again can be estimated by using the values of mean particle length and mean particle area before and after laser treatment (Table 6.1). The particles in the high sulphur steel show little change. However, for the commercial steel, the decrease in volume was substantial, and has been estimated to be close to 50%, and relatively unaffected by the choice of particle shape (the shapes assumed were spheres, prolate spheroids or oblate spheroids). Further details are given in Appendix F.

EDS analysis of inclusions in the SEM found that approximately 70% of inclusions in the laser treated high sulphur 304L contained sulphur, and that approximately 20% of inclusions in the laser treated commercial steel contained sulphur. Thus for both steels, there was a small reduction in the proportion of sulphur-rich inclusions when compared to untreated specimens. However, it should be noted that, because particles were much fewer in number than on the untreated steel (only 30 particles were analysed on each laser treated steel), the apparent slight reduction in number of S-containing inclusions may be due to an error introduced by the smaller sample size. The size distribution of these particles was consistent with the optical microscopy and image analysis results. Specifically, no inclusion longer than $10\mu\text{m}$ was found.

Further, extensive, EDAX analysis found no change in the distribution of the major alloying elements between the base material and the laser melted zone (see also Section 6.3.1).

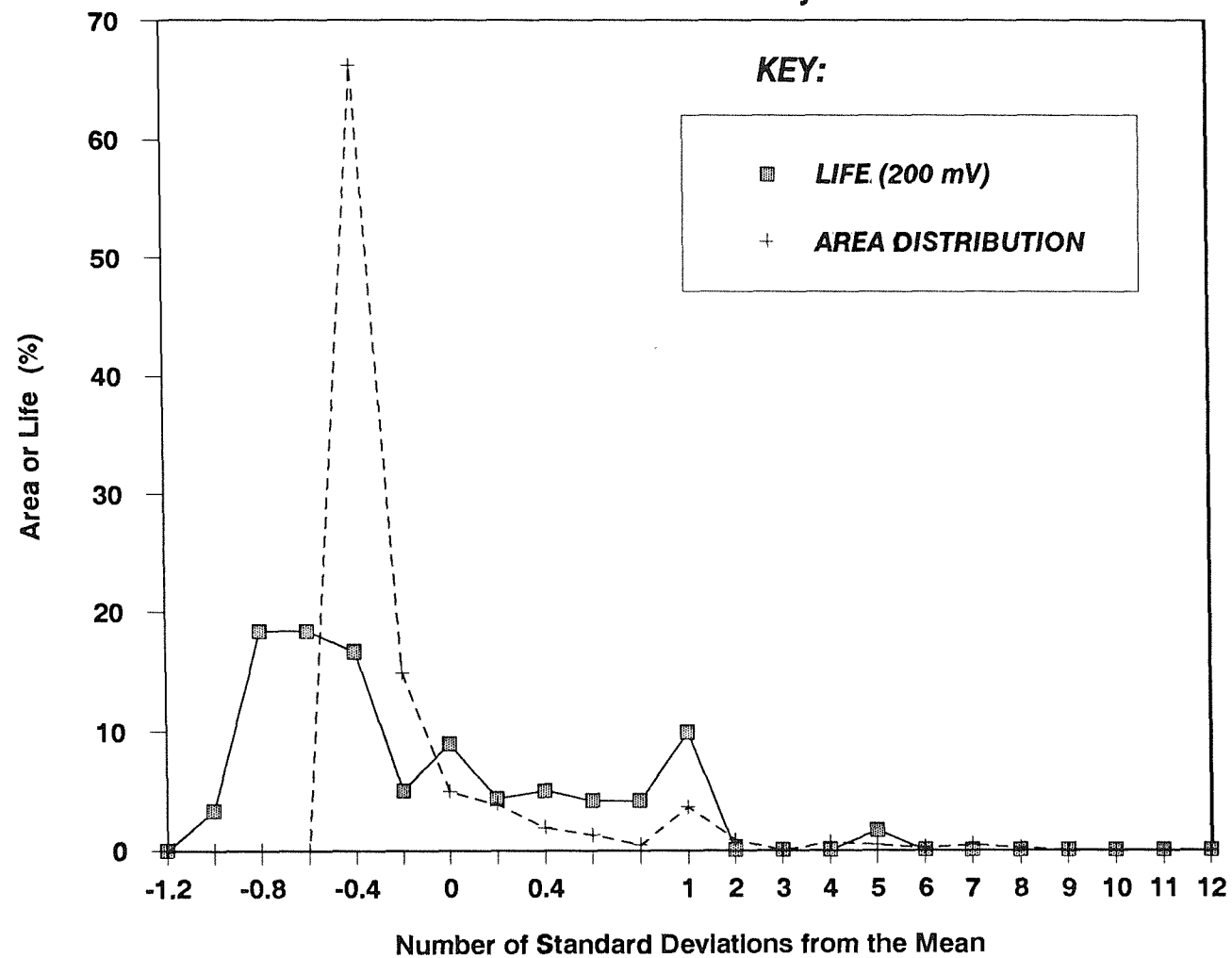
6.2.3 Discussion

In the previous chapter it was suggested that pits which propagate are those which initiate close to a plentiful supply of sulphur - either at a large sulphide inclusion or at a group of smaller sulphide inclusions. Before laser treatment, the commercial steel contained relatively few sulphide inclusions (compared to the high sulphur steel), but the measured particle size distributions indicated that the commercial steel contained a higher proportion of larger inclusions, and included some sulphide stringers. The high sulphur steel contained many sulphide inclusions, which were present in a variety of shapes and sizes, but most of which tended to be rounded or elliptical. The electrochemical noise appeared to reflect particularly the shape and spatial distribution of inclusions, and strong evidence was presented to support an assertion that pit lifetime is related to inclusion size.

From the laser treated specimens, further support was provided for the role of specific features of the sulphide particles - their size, shape and spatial distribution - on their propensity to nucleate pits. For example, on the commercial purity steel the characteristics of the current transients were markedly different: on the untreated steel the transients often comprised a number of current bursts, signalling the initiation of quite a large pit. However, following laser treatment, the transients were much shorter lived, and usually consisted of a single current rise event. This response is consistent with the metallographic observations that inclusions were reduced in size and number and were well spatially separated following laser treatment. However, a plot of the distributions of transient lifetime and particle area for the laser treated commercial steel, given in Figure 6.15, shows that the correspondence between the two distributions is not as good as noted previously on the untreated steels. A large proportion of the inclusions measured were small, pushing the limit of resolution of optical microscope, which accounts for the large peak in the area distribution. In reality, the tail of the distribution extended to smaller particle sizes (confirmed later by transmission electron microscopy), which could not be measured accurately.

The results also suggest that the *shape* of the inclusions is responsible for the shape of the transients: the sulphide inclusions in the laser treated commercial steel were invariably rounded (e.g. Figure 6.13), in common with the majority of inclusions on the high sulphur steel before and after laser treatment (and indeed the high purity steel). The current transients on these materials were also similarly shaped. It

**Figure 6.15 Distributions of Particle Areas and Current Transient Lifetimes:
Laser-Treated Commercial Purity 304L**



appears that small, rounded precipitates give rise to rapid current rises, and short lifetimes. In the previous chapter it was suggested that such precipitates were likely to form open and non-propagating pits.

Effects on the pitting resistance, if any, due to the other microstructural modifications resulting from laser treatment, would appear to be secondary to the changes associated with inclusions, since the reduction in the inclusions detected by image analysis was consistent with the reduction in the nucleation frequency of micropits. In both cases, the differential between the alloys was maintained.

By optimisation of the laser parameters, it may be possible to improve the pitting resistance still further. Evidence to support this has been provided by image analysis on specimens surface-melted to a depth of $1\text{ }\mu\text{m}$, using a pulsed *excimer* laser, which showed that a higher proportion of inclusions had been removed, and those remaining were again spheroidal but smaller than the equivalent specimens melted with the CO_2 laser⁽⁶⁾.

6.2.3.1 Further Investigations of the Laser-Melted Zone

What then, was the fate of the inclusions, and in particular the sulphide inclusions? To try to provide an answer to this question, some further investigations were carried out on the laser treated high sulphur 304L. Firstly, the laser melted surface zone was analysed using X-Ray Fluorescence (XRF). The analysis revealed no significant differences in the concentrations of the major alloying elements between the melt zone and the parent material and a sulphur level of 0.071% (compared to the bulk level of 0.080%). That is, most of the sulphur was retained in the melt zone. The small reduction in sulphur concentration in the melt zone was confirmed by "LECO" analysis.

The remainder of the sulphur was presumably lost by evaporation from the molten surface during laser processing. Evidence in support of this was provided by melting the surface of a high sulphur 304L specimen using a *excimer* laser. The specimen was polished to a $1\text{ }\mu\text{m}$ finish. A single, 15ns pulse (with a fluence of 27MJ/mm^2), melting to a depth of about $1\text{ }\mu\text{m}$, resulted in the formation of "craters" on the specimen surface, Figure 6.16. Small particles were often present at the centre of the craters,

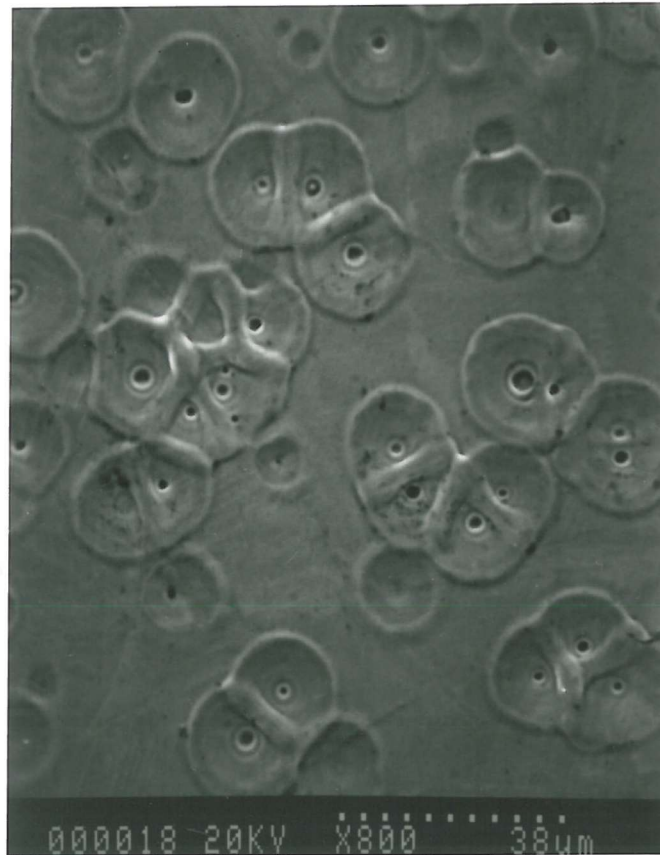


Figure 6.16 Scanning electron micrograph of high sulphur 304L following surface melting by a single 15ns laser pulse. Note the particles at centre of some "craters" (specimens were polished to $1\text{ }\mu\text{m}$ before laser treatment)

which were confirmed by EDAX analysis to be sulphur-rich. Not all craters contained particles. These observations are further illustrated in Figure 6.17, which shows a secondary electron image and a sulphur map taken from the same area. It was noted that sulphur was detected primarily in the centre of the craters, with little on the crater walls or on the surrounding surface. Presumably, the very short time for which the metal was molten was insufficient to remove all of the sulphides from the surface, and the process of removal at a given site was often "frozen" before reaching completion. In similar experiments when multiple pulses were applied to the same spot, the craters disappeared, and the surface was smoothed, which is probably because the particles from within that volume had been removed. The mechanism of crater formation is not clear, but is probably associated with differences in beam absorption properties of the particles compared to the steel. Also different physical properties, such as thermal conductivity and density, both of which are lower in the particles than in the steel, may have contributed to the volcano effect. Estimating the heating rate to be about $10^{11} \text{ }^{\circ}\text{C/s}$ (i.e. $1500 \text{ }^{\circ}\text{C}$ in 15ns), one suggestion is that localised heating in the vicinity of the particle creates a shock wave during the laser pulse, caused by the very rapid heating and melting of the surface⁽⁷⁾.

On the basis of these observations, it would seem that the reduction of sulphur content in the melt zone was brought about by evaporation during laser treatment.

Returning now to the CO_2 -melted specimens, the knowledge that most of the sulphur was retained in the melt zone posed an interesting question: what form was it in? Two possibilities presented themselves. First, the quench rates following laser melting were sufficiently rapid to maintain the sulphur in supersaturated solid solution. However, as remarked previously, the solid solubility of sulphur in austenite is extremely low, and, if the quenching conditions had permitted, the sulphur would have precipitated. The second possibility was therefore that the sulphur was present as fine sulphide precipitates. If such precipitates were in fact present, then they were too small to be detected in the image analysis and SEM work reported above. In either case the sulphur was present in a less harmful form: the pitting experiments clearly showed a reduction in unstable pit nucleation frequency, and an increase in pitting breakdown potentials. These findings presented an opportunity to test a suggestion put forward in the previous chapter, when it was speculated that there is particle size below which sulphides do not nucleate pits. If the sulphur retained in the melt zone

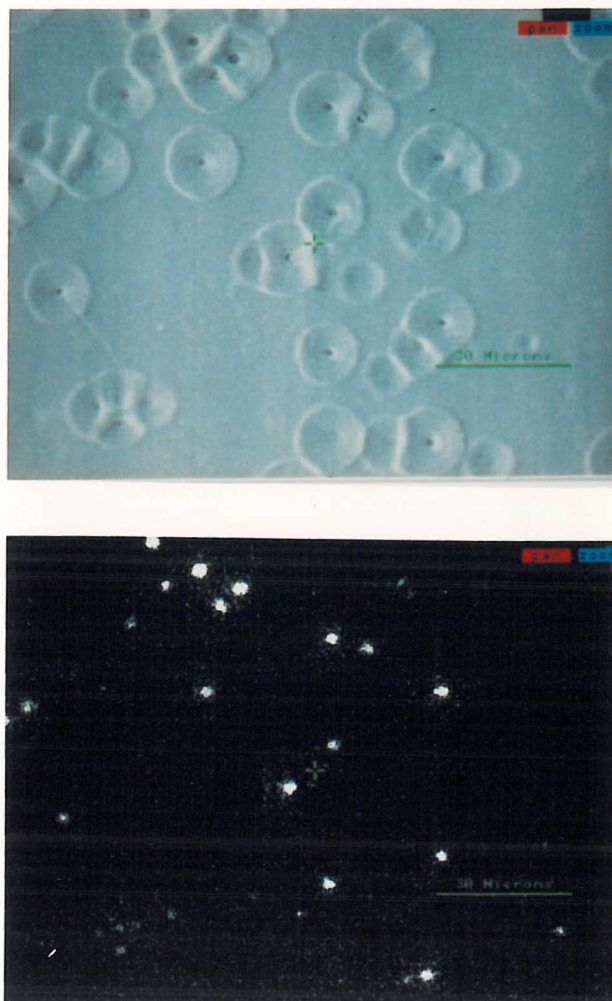


Figure 6.17 (a) secondary electron image and (b) sulphur map from the same area of the "cratered" surface following laser treatment. Note that sulphur is mostly confined to the centre of craters, and that some craters were sulphur-free (conditions as for Figure 6.16)

was present in the form of fine sulphide particles, this would provide support for a minimum cut-off size for sulphide inclusions. The transmission electron microscope (TEM) was used to investigate these possibilities.

Disc specimens (3mm diameter) were cut from the melt zone of the high sulphur steel. Samples from parent, untreated alloy were also prepared, to provide a comparison. The specimens were ion beam thinned into thin foils and then electropolished in a mixture of perchloric acid and methanol until a hole penetrated the centre of the specimen. Examination of the foil specimens from the laser treated steel, in a Phillips EM400 TEM, revealed the presence of very small sulphide inclusions - typically <100nm to 250nm - Figure 6.18. The shape of the particles was invariably close to a sphere, which was also the case for the few remaining large inclusions, noted in the optical microscope and described earlier in this chapter. The linear grouping of the particles (and the holes left by dissolved particles) is discussed in the next paragraph. Similar TEM examination of thin metal foils taken from the high sulphur steel did not find such small particles, although larger particles - typically a few μm in diameter - were in evidence. The electropolishing operation had in fact removed most of the inclusions near to the hole, and the holes left behind provided a convenient indication of the inclusion distribution, where some clustering was apparent in the parent alloy (Figure 6.19). Observations of clustering, also made in the optical and scanning electron microscopes, are of interest when considering the hypothesis, developed in Chapter 5, that a pit which nucleates at a sulphur-rich inclusion encounters another sulphur-rich inclusion during its early stages of growth, the sulphur species from the second inclusion then assisting pit growth. The opportunity was taken to analyse the metal immediately adjacent to sulphide particles (in both the laser melt zone and the untreated alloy), to see if for example, chromium depletion or sulphur enrichment had occurred. EDAX analysis in the TEM failed to detect any such compositional modifications.

The major effect of laser melting appears to be to evaporate or dissolve large inclusions^(1,3,5), which are then re-precipitated as a number of small, rounded inclusions, most of which are only visible when viewed in the transmission electron microscope. Because of the high quench rates involved, the particles did not have sufficient time at temperature to grow and coalesce, with the result that the small individual inclusions, a few μm apart, were aligned in the direction of the laser beam path. Some sulphur is evidently lost from the laser melted zone, presumably by

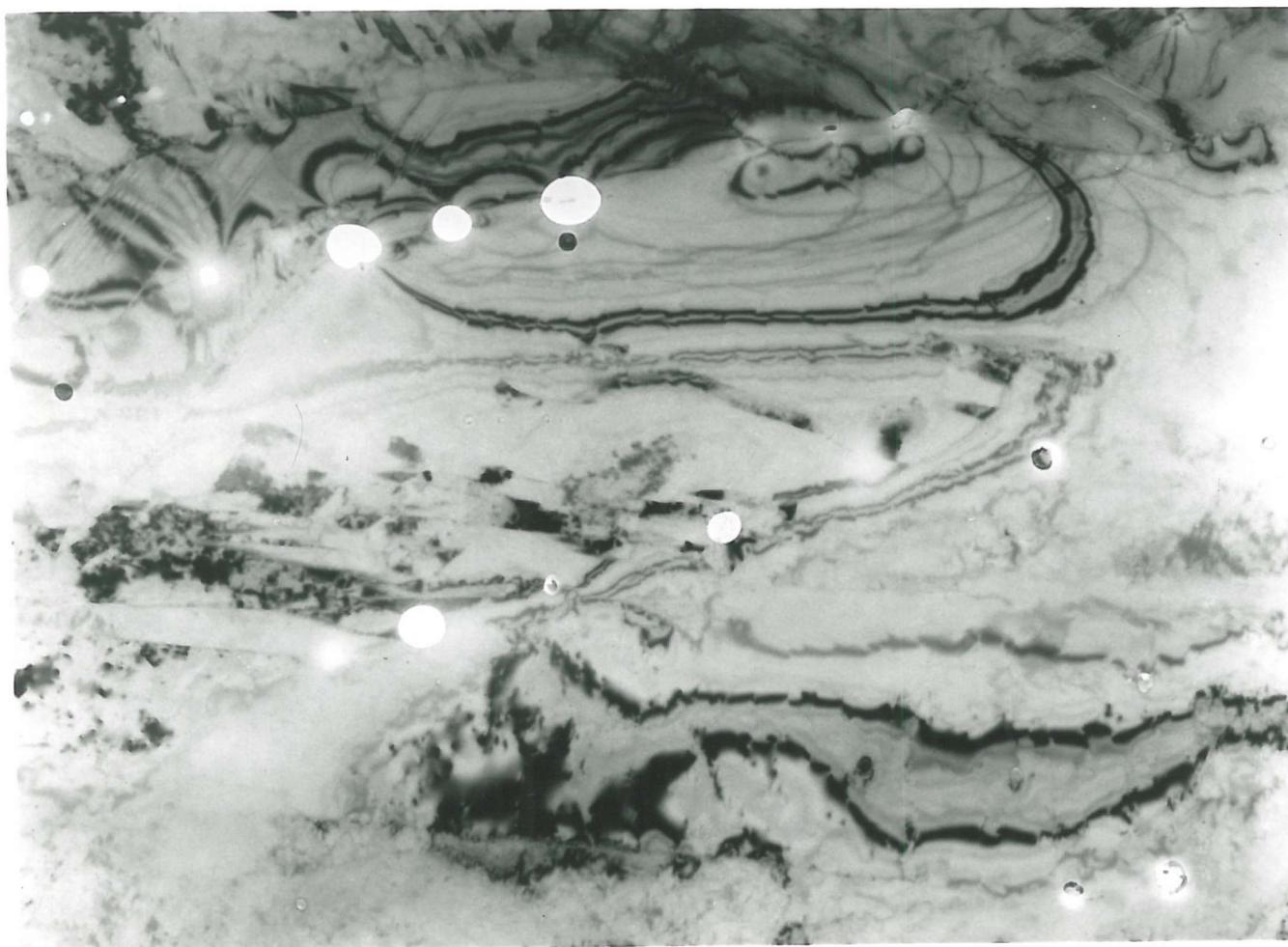


Figure 6.18 Thin metal foil transmission electron micrograph from the laser melt zone (high sulphur 304L). The holes were left by particles dissolved during specimen preparation. Note that some particles have been retained

500 nm

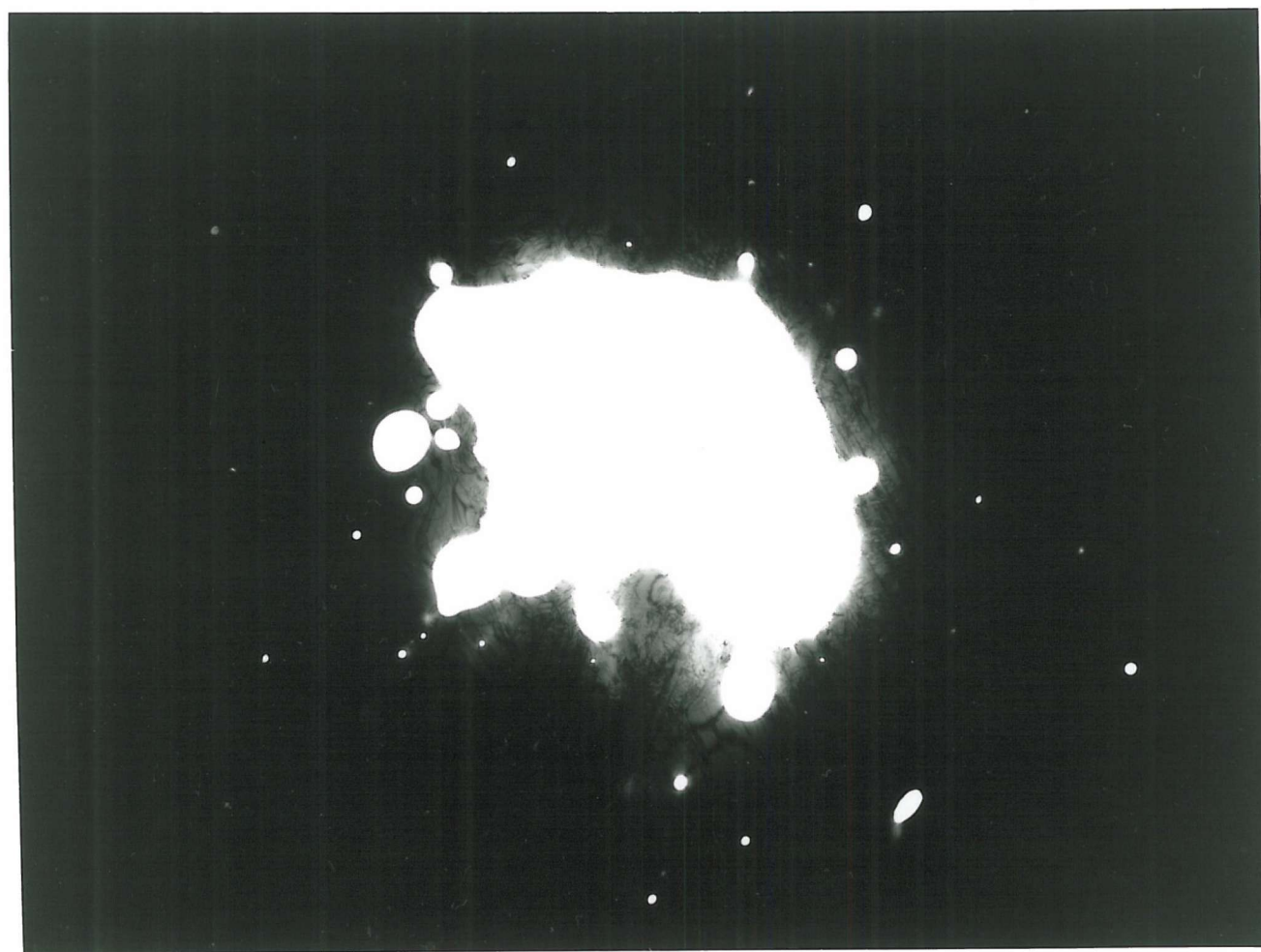


Figure 6.19 Thin metal foil transmission electron micrograph of the parent austenite (high sulphur 304L). Holes have been left in the metal adjacent to the centre hole in the foil by inclusions dissolved during specimen preparation. Note the clustering

20 μm

evaporation. In view of the enhanced pitting resistance of the laser treated alloys over the untreated steels, it is clear that the small sulphide particles, which were only detectable at high magnifications in the TEM, are too small to nucleate pits. This conclusion is consistent with the results from Searson and Latanision's⁽⁸⁾ experiments on rapidly solidified stainless steel powders in which the enhanced pitting resistance of these materials was attributed to small, well dispersed inclusions. It has been demonstrated that it is not the sulphur content of the alloy *per se* which determines its pitting resistance, rather it is the size and distribution of the sulphide particles.

Taking into account the close proximity of the breakdown distributions for the laser treated 304L, the high purity 304L and the commercial purity 316L, Figure 6.8, an interesting question now arises: if sulphides are present in a form too small to nucleate pits, as in the laser treated 304L and the high purity 304L, is the presence of Mo, as in 316L, still of benefit? If the answer to this question is no, then the potential for major cost savings for steelmakers is clear (Mo is expensive). Implicit in this question is that the beneficial effect of molybdenum is to inhibit the detrimental effect of sulphur species in pitting. In the following chapter, the effect of Mo is shown to be due to a reduction in anodic dissolution rates in a *growing* pit, and does not affect pit nucleation: the answer to the question posed above may indeed be "no" - Mo is not beneficial in the absence of aggressive sulphur species (although it is not possible, with the information available at present to distinguish between a beneficial effect of Mo on S, from a beneficial effect of Mo on its own).

Further work, to define more closely the size below which sulphur-rich inclusions are not detrimental to pitting resistance, could lay the foundations for improved alloy design based on small, well dispersed sulphide particles. Three routes could be considered to achieve this microstructure. Based on the results of this study (Chapter 5), a high purity alloy would produce the desired improved pitting resistance, although this route is impractical on the basis of cost, and also because some sulphur is desirable for improved machinability⁽⁹⁾. The second alternative, again based on the results of this study, is to laser melt the surface of the steel. This route would have advantages where fabricated, critical components could be laser treated prior to installation in plant. It would have particular advantages for "free-machining" grades of steel, which rely on sulphide stringers for their improved machinability. The main disadvantage of this method is the processing times: coverage rates would be much too slow for bulk steel products such as plates and strip. The third alternative is to

make suitable additions to the molten steel - to nucleate a large number of small inclusions rather than a fewer number of large inclusions. According to the work of Li and co-workers⁽¹⁰⁾, cerium appears to be a candidate as a suitable addition, since it has the potential to improve both the pitting resistance and hot workability of highly alloyed stainless steels. Calcium, another strong desulphuriser, might also be considered.

6.3 THE PREVENTION OF IGSCC USING LASER SURFACE MELTING

A fundamental requirement for stress corrosion cracks to initiate on passive metal surfaces is that the aqueous environment and the alloy react electrochemically at localised sites. In stainless steels and other alloys which rely on chromium for their corrosion resistance these reactive sites are often chromium depleted grain boundaries. The alloy is said to be "sensitised", and, given a suitably aggressive combination of environment and tensile stress, is susceptible to intergranular stress corrosion cracking (IGSCC).

Thermal sensitisation occurs when chromium from solid solution in an alloy heated in certain temperature-time regimes (typically 550-800 °C for austenitic stainless steels) combines with carbon in the steel to produce chromium-rich carbides at the grain boundaries, depleting the adjacent austenite in chromium. If the temperature-time conditions are such that a network of interlinking chromium depleted grain boundaries can form, extending across the entire microstructure, then the component in question is susceptible to failure by IGSCC (or intergranular corrosion, IGA). In practical situations, the boundaries can become chromium-depleted during welding or stress relieving heat treatments. With modern steelmaking practice, stainless steels can be produced with carbon contents sufficiently low that sensitisation does not occur (typically <0.03wt%, see Appendix A). However, many existing plant are fabricated from high carbon (typically 0.06wt%) sensitised stainless steels and are therefore susceptible to IGSCC or IGA.

In a recent paper⁽¹¹⁾ we presented a quantitative method for assessing the degree of sensitisation in austenitic stainless steels, based on percolation theory. The underlying assumptions were that, for a component to fail by IGSCC, a crack starts at the free surface and propagates through a connected pathway of susceptible grain boundaries. Support for this approach was provided by the close correspondence of the theoretical

results, which predicted that about 23% (= the percolation threshold, p_c) or more of the grain boundaries must be sensitised for a continuous pathway to form, and the results of slow strain rate tests, where intergranular fracture was found to occur only in microstructures sensitised above p_c .

The experiments described here illustrate a simple method for preventing IGSCC of stainless steels which have been sensitised to a level well above p_c , by destroying the connectivity of the sensitised structure. This is achieved by melting a thin surface layer using a laser, which creates a barrier of unsensitised material between the corrosive environment and the underlying, susceptible microstructure.

6.3.1 Experimental Procedure and Results

The type 304 stainless steel used for this study contained (wt%): 0.059C, 17.8Cr, 9.07Ni, 1.5Mn, 0.025S, 0.38Mo, and was supplied as 6.25mm diameter rod. Three tensile test specimens were machined from the rod to produce a smooth 20mm gauge length of rectangular (4mm x 2mm) cross-section. Specimens were solution annealed at 1070 °C for 30 minutes in vacuum, argon quenched, and then soaked at 650 °C for 24 hours in vacuum. These heat treatments produced heavily sensitised microstructures, with approximately 90% of the grain boundaries sensitised, that is, well above the percolation threshold.

Laser treatment was carried out using a CO₂ laser operating continuously at 4kW. The laser processing variables and conditions were the same as those used for the pitting studies described earlier in this chapter (Section 6.2.1). The entire gauge length on one specimen was laser treated by melting a series of tracks, which were overlapped by 50%. For the second specimen, melting was limited to a single track down the centre of each 4 mm face on the gauge length. The width of the melt zone was approximately 2mm. The depth of the melted layer was later measured at 150-300 μ m, with a further 100 μ m or so of "heat-affected zone", where the sensitisation had been removed, Figure 6.20.

The remaining tensile specimen, sensitised but not laser treated, was used as a control in the corrosion experiments.

Figure 6.20 Optical micrograph showing a cross-section through the laser-melted zone. A "heat-affected" zone is also evident (electrolytic etch)

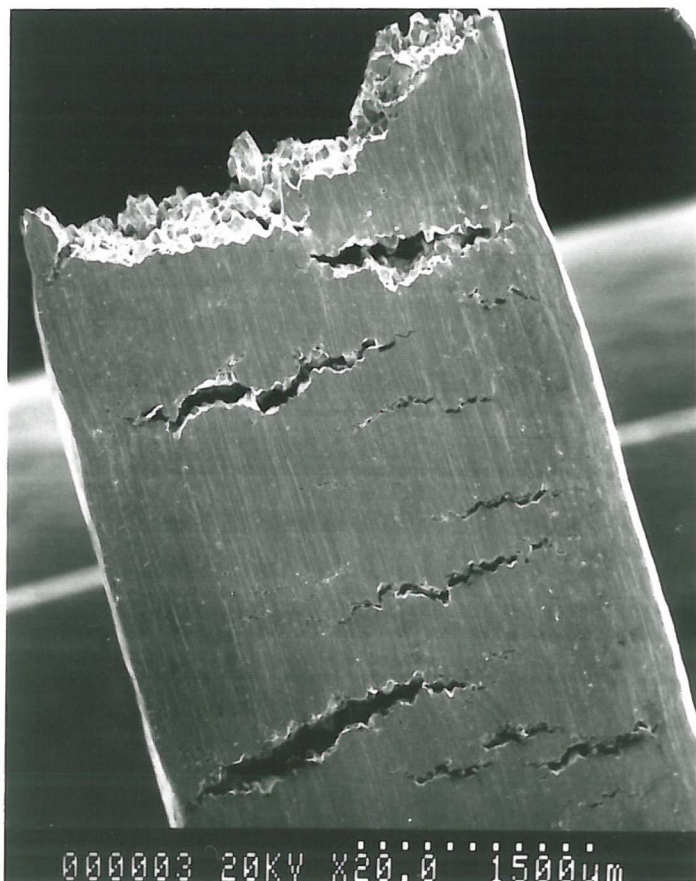
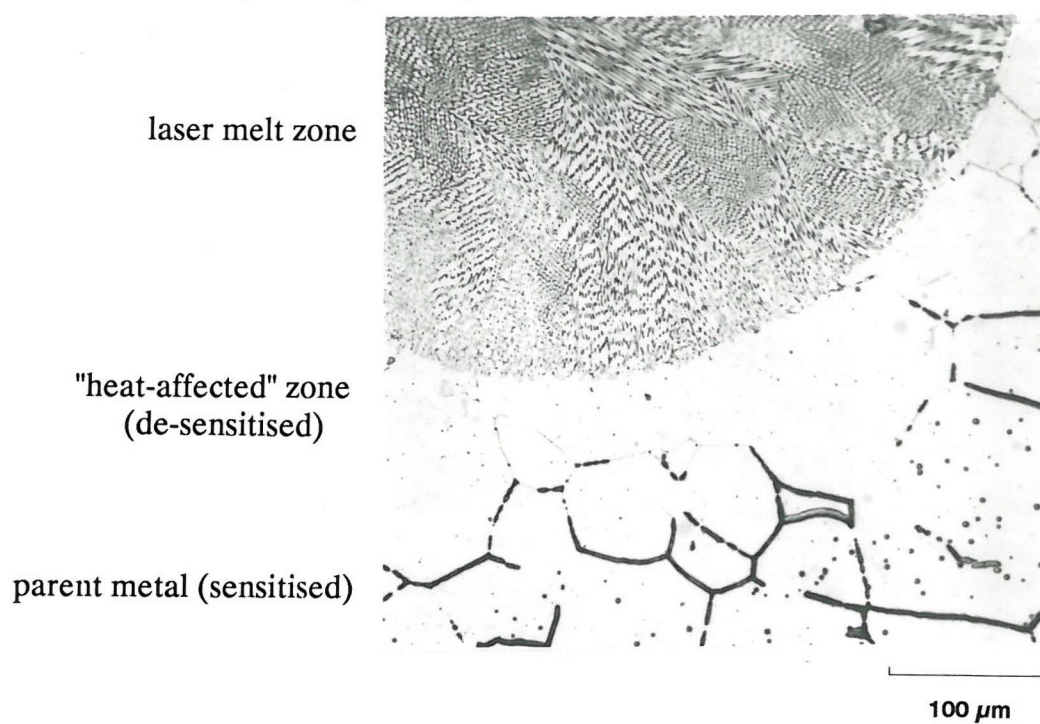


Figure 6.21 Scanning electron micrograph showing extensive cracking on the gauge length of the control specimen, and fracture due to IGSCC

The corrosion experiments consisted of slow strain rate tests (10^{-4} /s) in 0.5M sodium thiosulphate solution, in which the potential of the specimen was controlled to -200mV SCE using a potentiostat. These conditions were chosen because they are known to be very aggressive for inducing IGSCC in sensitised stainless steel⁽¹²⁾. This is demonstrated in Figure 6.21, which shows the results of the control experiment. Numerous cracks were formed, and the specimen failed catastrophically due to IGSCC, with a strain to failure of about 5%. The result of this control experiment may be contrasted with that of the specimen in which the entire gauge length was laser surface melted. This specimen failed in a ductile manner with a strain to failure of 75%.

Figure 6.22 shows the result of the slow strain rate test on the specimen where a single pass of the laser beam was made down the centre of each 4mm face on the gauge length, and clearly illustrates the effectiveness of the technique. As in the control experiment, many cracks initiated on the specimen away from the laser treated areas. However, no cracking was found in the laser melted regions. Furthermore, crack propagation was arrested at the interface with the melted zones, Figure 6.23 (Figure 6.23b also provides a good illustration of the intergranular nature of the cracking). The specimen fractured with a strain to failure of about 22%. Figure 6.24 shows a transverse section through this specimen, polished and etched to reveal the microstructure of the melt zone. At the interface between the melt zone and the parent metal, a planar region about $2\mu\text{m}$ wide was apparent. The remainder of the laser melted surface layer was cellular-dendritic, with a cell size typically of a few microns. With this composition, the microstructure on solidification would be anticipated to consist of austenite with some δ -ferrite (for example, from the Schaeffler diagram, Appendix A). The δ -ferrite results from segregation of ferrite-stabilising solute elements during the solidification process, and was present at the intercell boundaries. The usual solid-state transformation of δ -ferrite to austenite was inhibited by the high cooling rates associated with the laser treatment (which can be up to 10^7K/s ⁽¹³⁾), and about 5% δ -ferrite was retained. Electron probe microanalysis traverses from the parent alloy across into the laser melted zone found no obvious compositional variation between the parent and the melted surface layers. Similarly, a hardness traverse revealed no difference between the laser melted zone and the parent alloy (both were approximately H_v230).

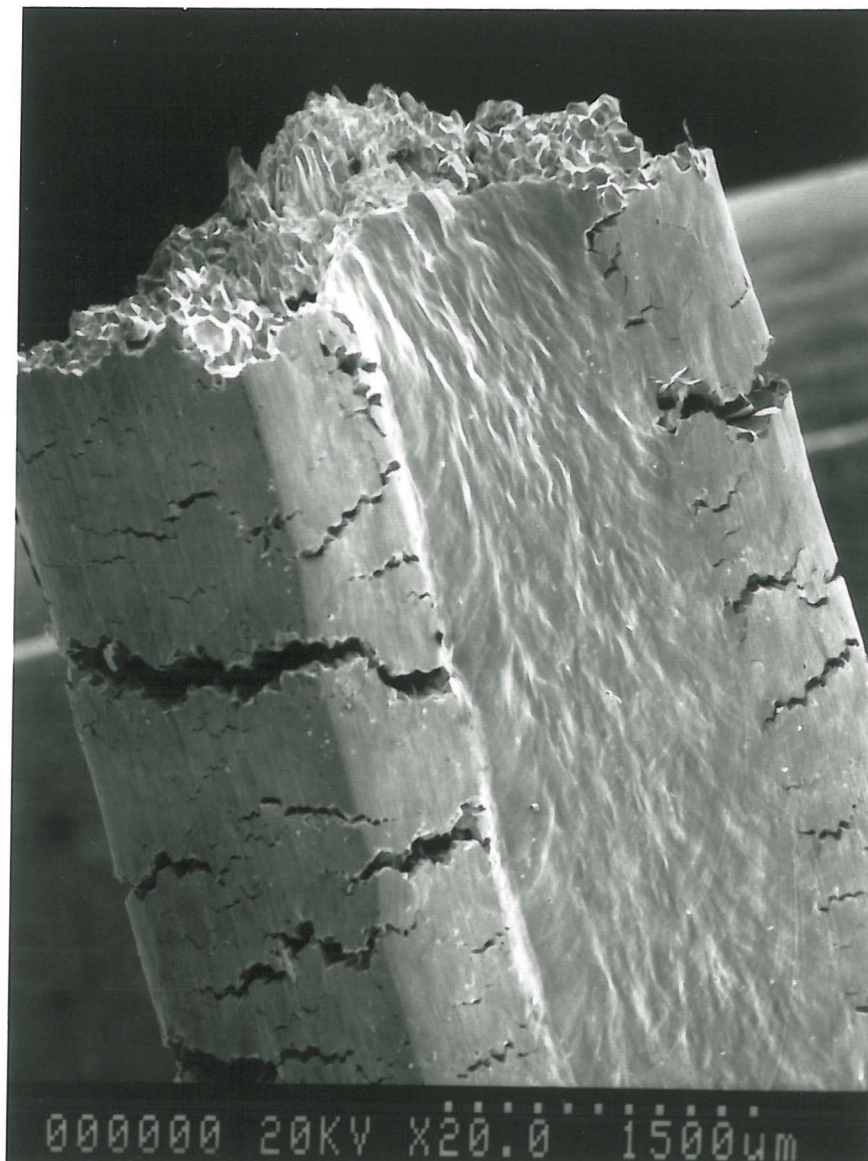


Figure 6.22 Scanning electron micrograph showing that while intergranular cracking was extensive on untreated regions, no cracking occurred in the laser-melted zone

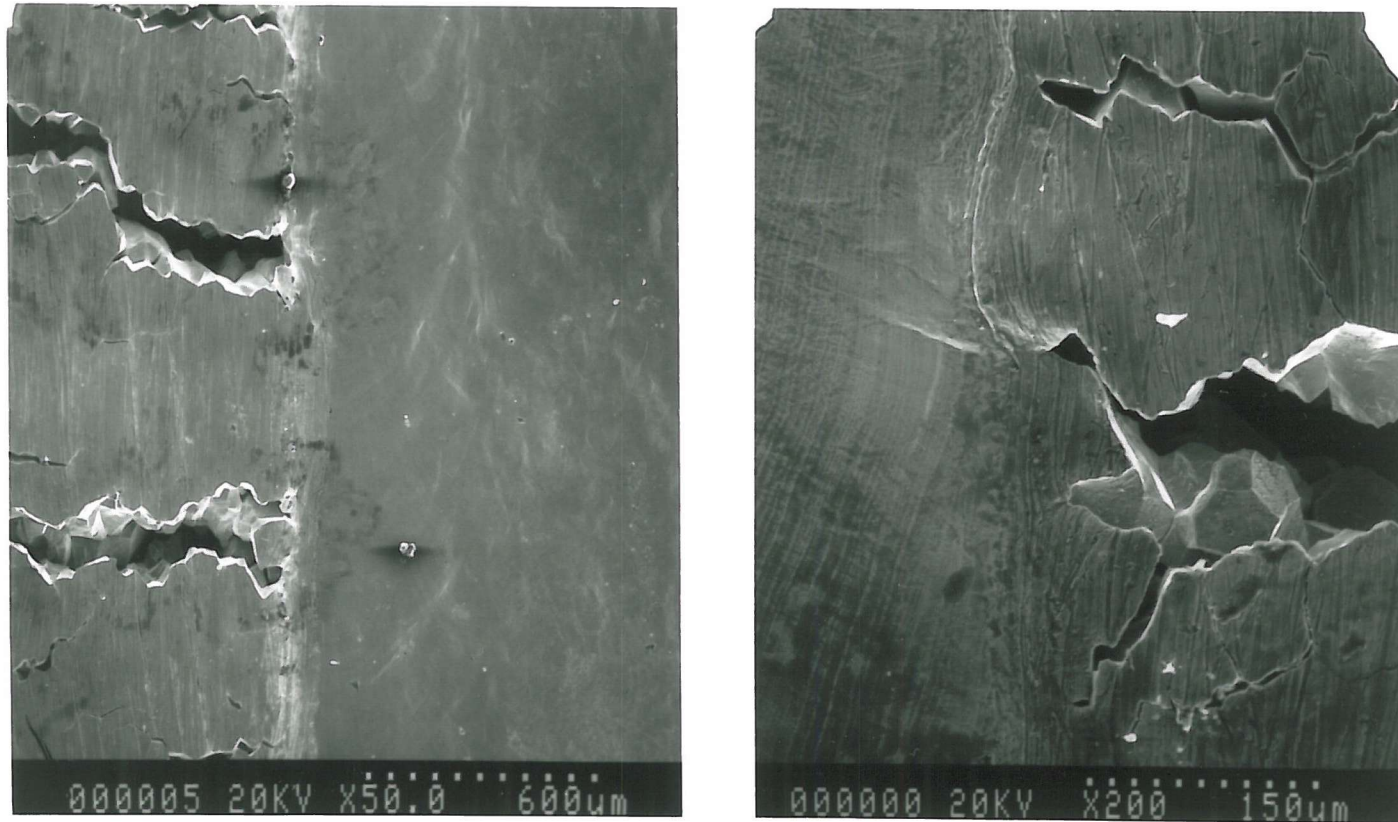


Figure 6.23 Scanning electron micrographs showing crack-arrest at the interface between the laser melt zone and the untreated steel. Note the clean intergranular facets in the parent metal cracks.

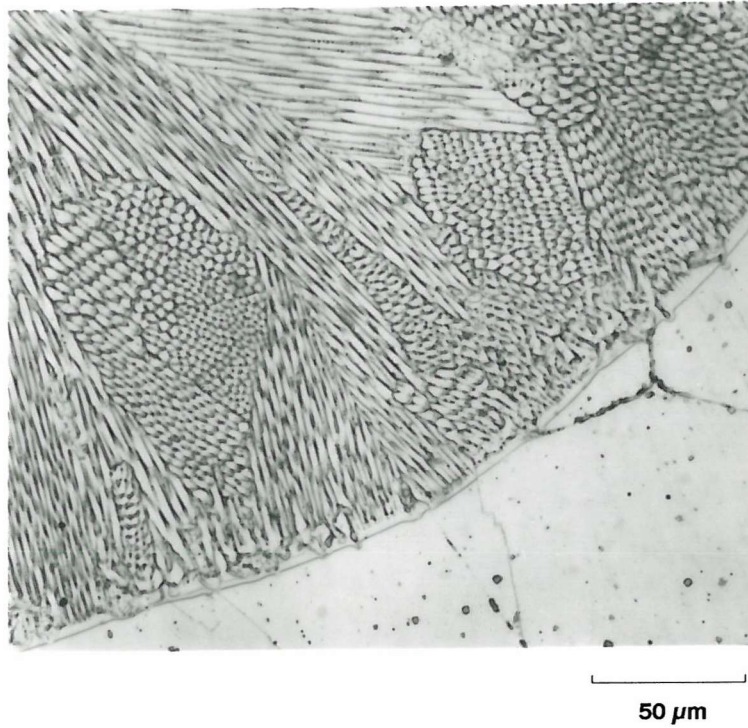


Figure 6.24 Optical micrograph of a transverse section through the gauge length showing detail of the microstructure in the laser melt zone (electrolytic etch)

In an extension to this work, laser treatment was found to be equally as effective in preventing stress corrosion cracking in simulated BWR water (288 °C, high purity water with 1ppm dissolved oxygen)(14).

These results indicate that laser melting a thin surface layer of a sensitised component can prevent IGSCC. The fine cellular-dendritic and unsensitised microstructure which results from this treatment provides an effective barrier between the corrosive environment and the underlying sensitised boundaries, even at high levels of strain.

In view of the effectiveness of this method, it is perhaps surprising that the technique has not been developed for practical applications. The pioneering work in this area, of Anthony and Cline(15), appears to have been largely ignored. This may be because, in their work, the laser melted region cracked, which the authors attributed to mechanical cracking associated with strain induced martensite formation during slow strain rate tests. This was also probably due in part to the residual stresses and strains from the laser treatment: they estimated the yield strength of the laser melted layer to be 10 times that of the remainder of the sample. The work reported in this chapter demonstrates that these problems can be overcome by using laser processing variables which produce a tough, ductile melt zone.

6.4 SUMMARY

Laser surface melting has been shown to be a very effective method for improving the pitting resistance of stainless steels, and for preventing IGSCC in sensitised stainless steels.

Improved pitting resistance is associated with the removal of some of the large deleterious inclusions, most of which subsequently re-precipitate as a fine dispersion of sulphides which are more resistant to pit initiation. Based on these results it has been suggested that, below a certain size, sulphide inclusions are too small to nucleate a detectable pit. These findings indicate that a route to improved pitting resistance is through microstructural engineering, for which possible strategies have been outlined.

The proximity of the cumulative breakdown distribution curves for the laser treated commercial 304L and the high purity model alloy (from the previous chapter) to that for commercial 316L has led to a suggestion that the addition of molybdenum (added

at 2-4% to 316L) may be unnecessary if the sulphur content of the alloy is sufficiently low, or if sulphide particles are present in the form of a dispersion of fine particles. In a follow up to this suggestion, a study of pit nucleation on 316L is reported in the next chapter.

In preventing IGSCC in sensitised stainless steels, the method works by introducing a barrier of laser melted, and unsensitised, material between the underlying (sensitised) microstructure and the environment.

CHAPTER 7

PIT NUCLEATION ON 316L

CHAPTER 7 - PIT NUCLEATION ON 316L

7.1 INTRODUCTION

The beneficial effects of molybdenum on the pitting resistance of stainless steels in chloride solutions are well known, although the mechanisms involved are not clear and remain controversial. Molybdenum is beneficial in conjunction with chromium: the pitting breakdown potential is increased, and the critical current density for passivation is decreased with increasing Mo content, whilst the passivation potential appears to be little affected⁽¹⁾. It has been demonstrated that, in the absence of chromium, molybdenum additions are not beneficial⁽²⁾, and indeed have been reported to be detrimental⁽³⁾. Various empirical correlations have been published which indicate the extent of the improvement of pitting resistance afforded by molybdenum. Here, only literature relevant to this study will be considered. The reviews by Wanklyn⁽⁴⁾ and Smialowska⁽¹⁾ provide a more comprehensive survey of the literature concerning the effects of molybdenum on the corrosion resistance of stainless steels.

Molybdate additions to an electrolyte have been shown to exert a similar influence to molybdenum in the alloy, leading some authors^(5,6) to conclude that molybdate ions adsorb on the dissolving metal surface, inhibiting the anodic dissolution, and promoting passivation. This hypothesis, which requires that Mo dissolved from the alloy produces molybdate ions, is questioned by Newman^(7,8) and Smialowska⁽¹⁾ who point out that molybdates would not be expected to be produced at the potentials where pitting occurs in less highly alloyed stainless steels, such as 316L. Nevertheless, pitting resistance is improved by molybdenum additions to these alloys.

A number of studies suggest that Mo improves the stability of passivating oxide films⁽⁹⁻¹²⁾. Other results appear to contradict this, indicating minor or no influence of Mo on the passive current^(3,7,13). Molybdenum facilitates the attainment of the passive state without changing the composition of the passive film, according to Hashimoto and co-workers⁽¹⁴⁻¹⁷⁾, who also asserted that the passive film is unstable at relatively high potentials, due to transpassive dissolution of Mo (as Mo(VI)). The beneficial effect of Mo is attributed to the elimination of active spots on the metal surface, associated with the formation of oxyhydroxide or molybdate⁽¹⁵⁾. Sugimoto and Sawada⁽¹⁰⁾ argue differently: the presence of Mo(VI) oxide *promotes* the stability of Cr(III) oxyhydroxide, due to the high stability of Mo(VI) in acid solutions

containing chloride ions. These authors also found (using XPS) that the Mo content of the film increased almost linearly with the Mo content of the alloy, and that the thickness of the passive film increased with Mo content. In contrast, the more recent results of a European "round robin" on the characterisation of passive films on Fe-Cr and Fe-Cr-4%Mo alloys using AES/ESCA, involving 10 laboratories and reported by Marcus and Olefjord⁽¹³⁾, found no marked change in the composition of the passive film in the presence of Mo. Also, the passive film thickness was little changed in thickness (ESCA) or made slightly thinner (AES) by the addition of 4% Mo.

Some investigators claim that the action of Mo is restricted to the pit nucleation stage and that it does not affect the growth rate of pits already initiated^(18,19). However, there is considerable evidence that Mo inhibits anodic dissolution.

Yang and Pourbaix⁽²⁰⁾ and Wanklyn⁽⁴⁾ recognised that the main effect of Mo was on the active dissolution in acid solutions. Under these conditions, MoO_2 can form and is highly protective. Wanklyn applied his reasoning to crevice corrosion rather than to pitting on the grounds that pitting occurred at "higher" potentials where more complicated reactions such as molybdate formation is possible. In contrast, Newman^(7,8) observed that steady state dissolution was rapidly attained on a Fe-18.6Cr-2.5Mo alloy, scratched in 4M HCl, suggesting that Mo inhibits active dissolution in its elemental or partially oxidised form, rather than by forming a 3-dimensional oxide such as MoO_2 (which is only stable at more oxidising potentials, or in less acidic solutions). He further pointed out that the $\text{Mo} \rightarrow \text{Mo(VI)}$ reaction must always be orders of magnitude slower in a pit or pit nucleus than simple metal dissolution reactions, and anticipated that the inhibiting effect of elemental Mo would persist in very rapidly dissolving pit nuclei because the important parameter is the ratio in which the alloying elements can dissolve. In an extension of this work, Newman considered the dissolution and passivation kinetics of stainless steels containing Mo, using an artificial pit method. High purity Fe-Cr-Ni electrodes, with and without 1.6 at% Mo additions, were anodically polarised in neutral 1M KCl: Mo was found to depress the dissolution rate in the active region by a factor of 5-10, depending on the potential.

Molybdenum and sulphur have a strong affinity for one another, and therefore might be expected to form the sulphide MoS_2 ⁽²¹⁾ (free energy of formation -112 kJ/mole). However, Mo-containing sulphide inclusions are not found in stainless steels: the

formation of molybdenum sulphide is unfavourable because the vapour pressure of MoS_3 at molten steel temperatures is higher than that of iron sulphide. Assuming that sulphide impurities on a metal surface play a decisive role on the process of pit nucleation, Kesten⁽²²⁾ explained that the specific influence of Mo was to precipitate, at the metal solution interface, a stable molybdenum sulphide (MoS_3) which is insoluble even in concentrated acids. In an extension of his artificial pit studies, described above, Newman⁽⁸⁾ found that when 0.0065M sodium thiosulphate was added to the artificial pit, the acceleration of anodic dissolution was much less marked on the alloy with Mo than on the alloy without Mo, suggesting that perhaps sulphur was being adsorbed onto the actively dissolving surface. Supposedly, the Mo-containing alloy is not as sensitive to S because dissolution is controlled by Mo enrichment at critical sites, such as kink sites, on the dissolving surface (Mo is not as sensitive as Ni to S adsorption).

It was shown, by Lott and Alkire⁽²³⁾ (and discussed in Chapter 5) that elemental sulphur may be produced from thiosulphate, arising from the dissolution of sulphide inclusions in neutral chloride solutions.

The recent work of Marcus and Moscatelli⁽²⁴⁾ provides a further mechanistic insight into the interaction between Mo and S. Their studies, on single crystals of nickel and nickel doped with 2 at% molybdenum, show that sulphur, pre-adsorbed on the surface by vapour deposition, becomes progressively de-sorbed during active dissolution (in 0.05M sulphuric acid solution) of the Ni + Mo alloy but is unaffected during the active dissolution of pure Ni. The suggested mechanism is that Mo cleans the dissolving surface of adsorbed sulphur, and they estimate that two Mo atoms are required to remove each sulphur atom. The resulting surface cluster then dissolves. Therefore, as active dissolution continues, a situation will arise where the sulphur coverage becomes insufficient to poison repassivation (suggested to be 70-80% of a monolayer by Marcus and Oudar⁽²⁵⁾) and active dissolution will stop. The neutralisation of the effect of sulphur increases with Mo content, but the effect of Mo is only observed in the presence of sulphur. The intrinsic effect of Mo on the passivation of Ni is not beneficial: increasing the Mo content in a Ni-Mo alloy increases the current at the passivation peak, and gives an increased current in the passive state, attributed to the presence of Mo(VI) in the passive film. This suggests that the role of Mo is not to prevent pit initiation, but is to assist the process of repassivation by removing sulphur from the active surface. Since sulphide inclusions dissolve in the active part of the

polarisation curve, this process could account for the observation that the critical current density for passivation is decreased with increasing Mo content, as the sulphur is removed more quickly.

Kolotyrkin and Freiman⁽²⁶⁾ found that the introduction of Mo to austenitic stainless steels containing Mn and S resulted in the formation of pits smaller by one order of magnitude (both in diameter and depth) relative to those observed in a Mo-free steel. However, when Mo was added to a steel in which Mn and S were absent, the sizes of the pits were the same as those on the Mo-free steel. Thus they suggested that one of the beneficial effects of molybdenum is to reduce the detrimental effect of sulphide inclusions.

In summary, molybdenum additions are undoubtedly beneficial to the pitting resistance of commercial stainless steels. However, there is no general consensus on the mechanism by which this improvement occurs. Surface analytical techniques may provide some useful information, but the specific mechanism of Mo is probably electrochemical. The effect of Mo on pit initiation is unclear, but electrochemical studies have shown that Mo reduces the rate of the anodic dissolution reaction in a growing pit. The interpretations of this effect differ. Of the two proposed mechanisms which appear particularly relevant to this study (i.e. relatively low electrode potentials), Newman^(7,8) has suggested that Mo controls dissolution by enriching at critical sites on the surface, and therefore is effective even when sulphur is absent whilst Marcus and Moscatelli⁽²⁴⁾, using model alloys, conclude that Mo is only beneficial when detrimental sulphur species are present, since the specific mechanism involves a removal of sulphur atoms from the dissolving surface.

The study reported here is a preliminary investigation of pit initiation on 316L, and was undertaken to follow up suggestions from the work reported in the previous chapters. There it was shown that pits nucleate at sulphur-rich inclusions and that by removing these inclusions, or reducing their size, the resistance to pitting of 304L was improved to a level approaching that of 316L (which contains 2.5% Mo). Here the features of pit initiation on 316L are described. Combined microstructural characterisation and corrosion testing show that there is little difference between 304L and 316L, apart from the consistently lower dissolution rates (in a given potential range) on 316L. It is clearly shown that Mo, at the levels present in 316L

(about 2.5%) does not inhibit pit initiation. The results are supportive of a mechanism in which Mo acts by providing an "antidote" to the "poisoning" effect (i.e. on repassivation) of sulphur.

7.2 EXPERIMENTAL

The composition of the type 316L stainless steel used in this study is given in Table 7.1. The experimental procedure was unchanged from that described in previous chapters for the type 304L steels, and utilised the same data acquisition and analysis routines (see Chapter 2).

One specimen was prepared to a $1\text{ }\mu\text{m}$ polish, and the inclusion volume fraction and distribution determined by image analysis, again as described previously for the 304L specimens. One addition was made to the image analysis routine (Figure 5.7) to enable the distribution of particle shapes to be measured. This was done by measuring the longest length (D) and dividing it by the width (d), and facilitates a comparison between the shape factor determined in previous chapters, in which the mean particle lengths and areas (from which d was determined) were used, and the measured values. Qualitative EDAX analysis of inclusions was performed in the SEM.

7.3 RESULTS AND DISCUSSION

The results described here are based on 7 experiments. Figure 7.1 shows the nucleation frequency of unstable pits as a function of potential for the 316L specimens, and re-plots the 304L results (from Figure 3.7). The nucleation frequencies of unstable pits were similar for the two alloys, although at increasingly anodic potentials, the 316L exhibited a *higher* frequency. It is concluded therefore, that Mo does not inhibit the nucleation of pits.

Attention is now turned to the characteristics of the individual transients.

Initial comparisons between the current-time series obtained for the 316L steel and the 304L steel indicate little difference between the two. However, when the transients from each experiment were digitised, and then analysed using the routines described in Chapter 2, some small but consistent differences between the two alloys did become apparent. The lifetime distributions for the two alloys, shown in Figure

Table 7.1 Composition of Steel¹

STEEL TYPE	Weight % (Fe Balance)									
	Cr	Ni	Mn	Si	C	P	S	Mo	Cu	Ti
AISI 316L - Spec. ²	16-18	10-14	2.00	1.0	0.03	0.045	0.030	2-4		
316L - CP	17.3	12.5	1.65	0.40	0.023	0.033	0.016	2.47	0.35	<0.02

NOTES

- ¹ - Analysis determined by X-ray fluorescence, except S and C (LECO)
² - Single figures are maximum values
 CP = Commercial Purity

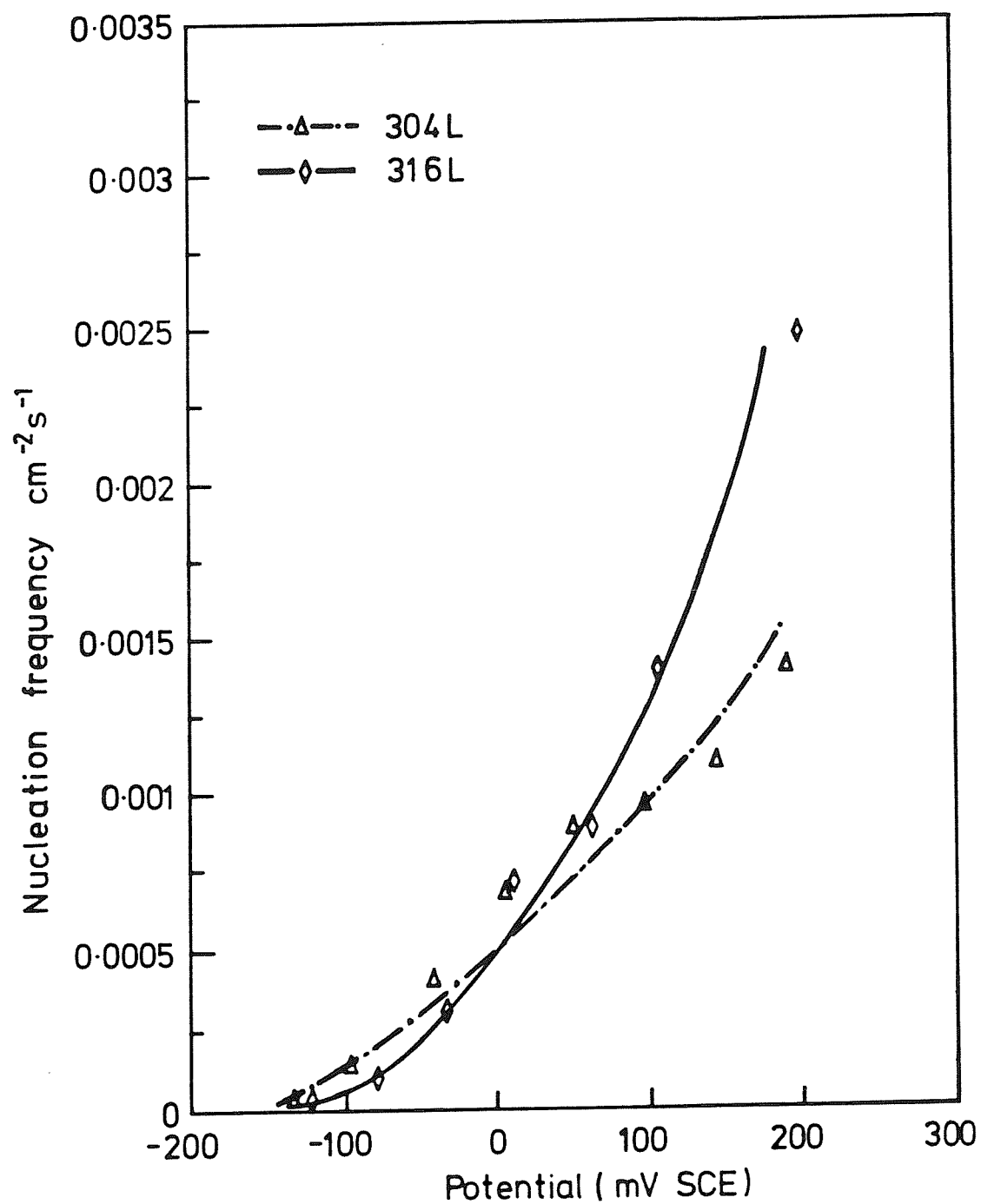


Figure 7.1 Nucleation frequency of unstable pits for commercial purity 304L and 316L (1000 ppm chloride, 0.005 mV/s)

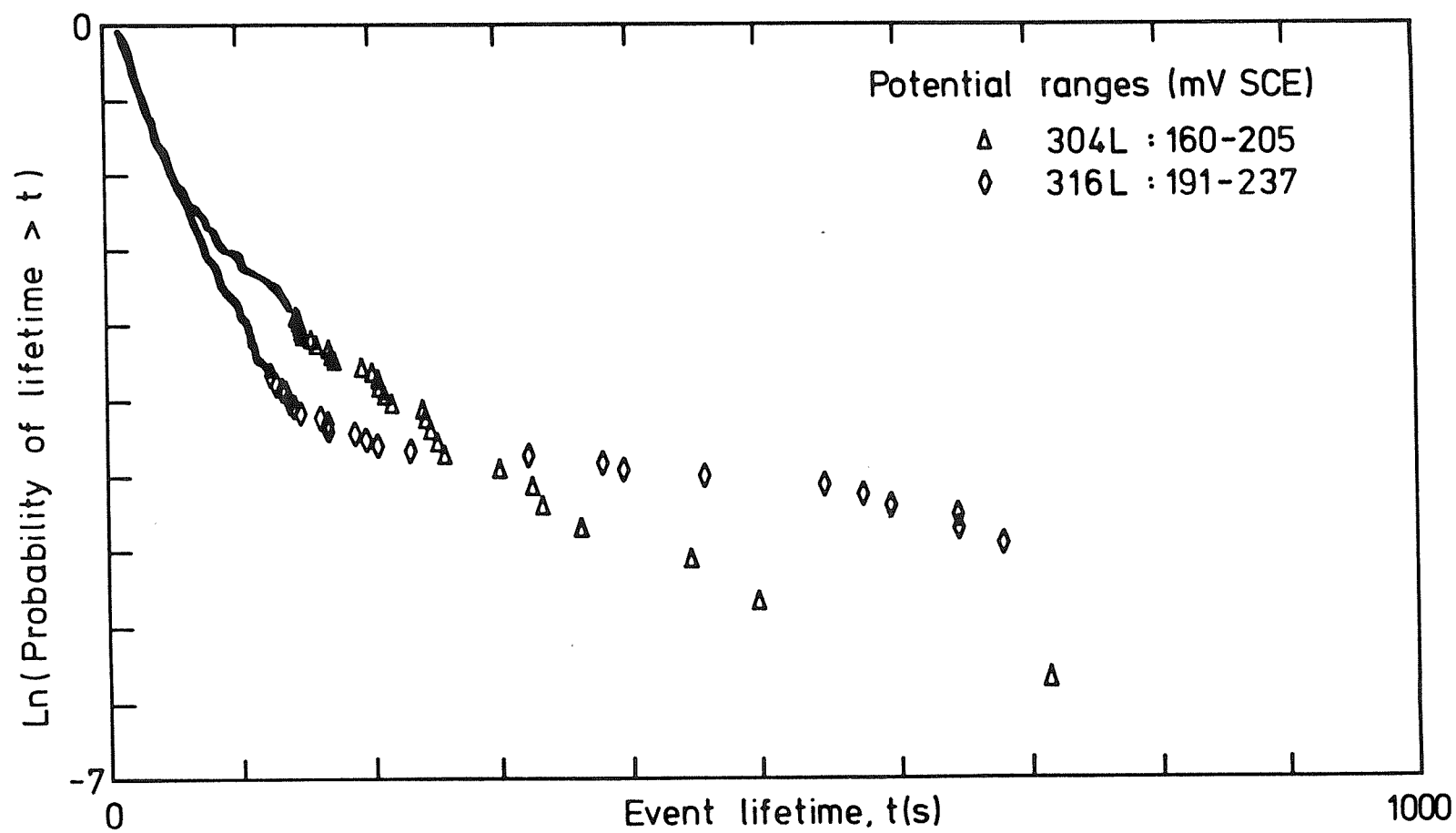


Figure 7.2 Distribution of lifetimes of current transients commercial purity 304L and 316L

7.2, are similar. However, the scatter diagrams of peak current vs. lifetime for 316L, shown in Figure 7.3, illustrate that the peak currents were generally lower at a comparable potential than those on the 304L specimens (see Figure 3.12). Average pit radii, calculated from the transients, indicate that unstable pits formed on 316L were smaller than those on the 304L at a given potential, and were in fact similar in size to those formed on the model alloys, Figure 7.4. The passive current densities were similar for the two alloys across the range of applied electrode potentials, Figure 7.5.

The results of the image analysis revealed that the particle sizes were similarly distributed to the 304L steel, Figures 7.6 and 7.7. Table 7.2, which summarises the results of the image analysis and includes the data presented previously (Figure 5.2) for 304L, further illustrates this point. The distribution of particle shapes, given in Figure 7.8, indicates that few particles were significantly elongated. The measured mean particle shape factor was 2.38. The shape factor was also calculated from the average particle area and length, as in previous chapters. The resulting value, 2.64, compares well with the measured value, indicating that the shape factors similarly calculated for the other steels (summarised in Appendix F) are in fact reasonable estimates. Qualitative EDAX analysis of 120 particles in the SEM revealed that 43% were sulphur-rich. This compares to 25% for the 304L steel. The higher pit nucleation frequency observed on 316L (Figure 7.1) may well be associated with this.

Taken together, these results show that although the dissolution rates in the pits growing on 316L were not *greatly* different from that of pits on 304L, the nucleated pits were indeed consistently growing more slowly. It would seem that this small difference is sufficient account for the anodic shift in the breakdown distribution (about 120 mV - see figure 6.8) for 316L compared to 304L. These findings are consistent with a mechanism in which Mo, present in 316L, does not inhibit pit nucleation, but does inhibit dissolution in the growing pit. Strong evidence has been presented in the preceding chapters that pits nucleate at sulphur-rich inclusions. It is reasonable to suppose, and has recently been shown⁽²⁷⁾, that pits nucleate at sulphides in the 316L steel also: in addition to the similarity in nucleation frequency between the commercial 304L and 316L steels (Figure 7.1), the sulphide inclusion volume fraction and size distributions, Figures 7.6 and 7.7, and the passive current densities, Figure 7.5, were also similar on the two alloys. These observations strengthen support for the idea, discussed in previous chapters, that the passive current provides the driving force

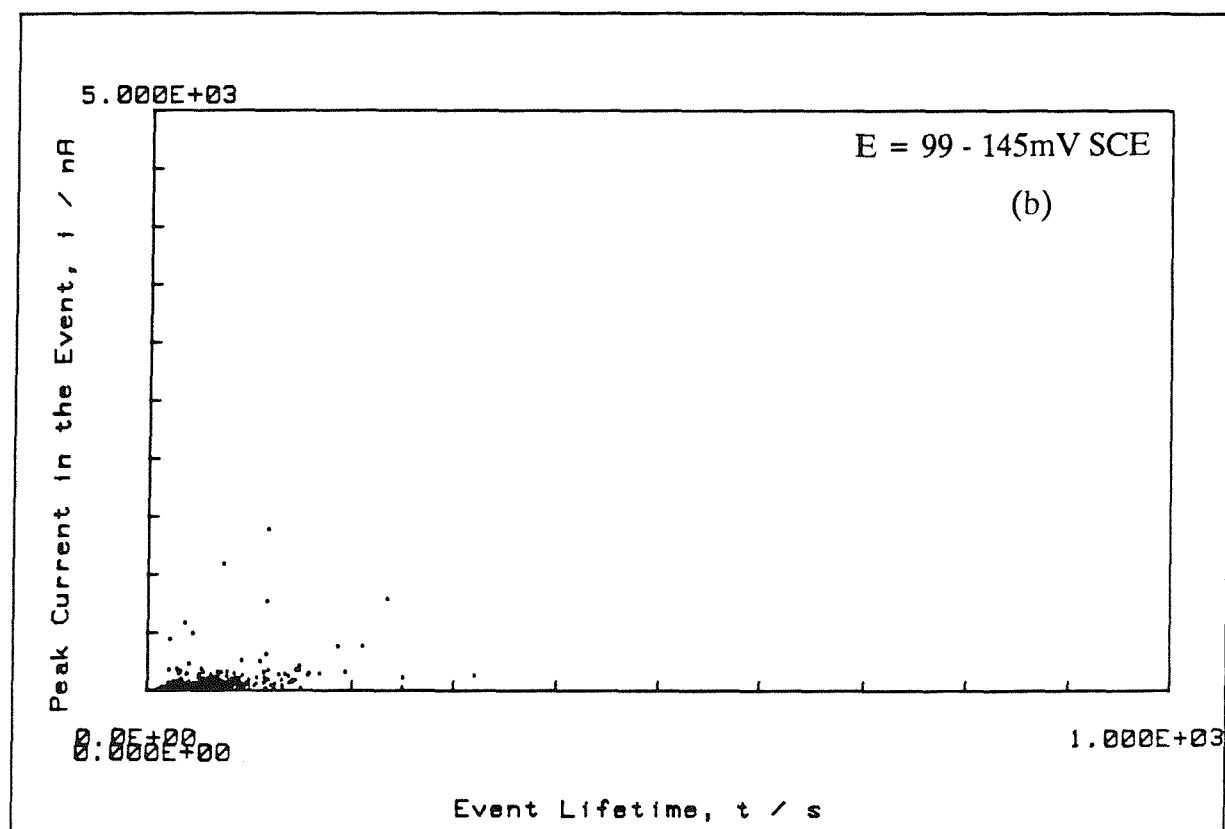
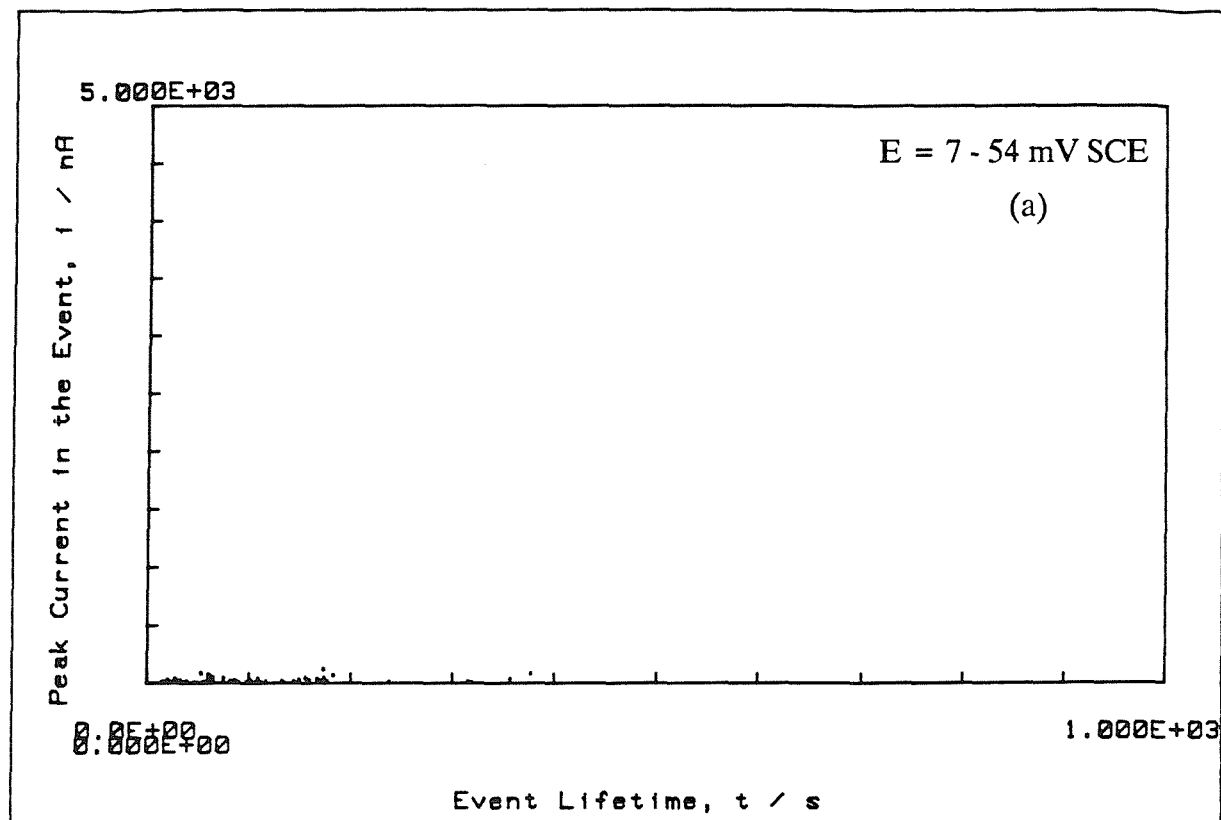


Figure 7.3 Scatter diagrams of transient peak height vs. lifetime for commercial purity 316L

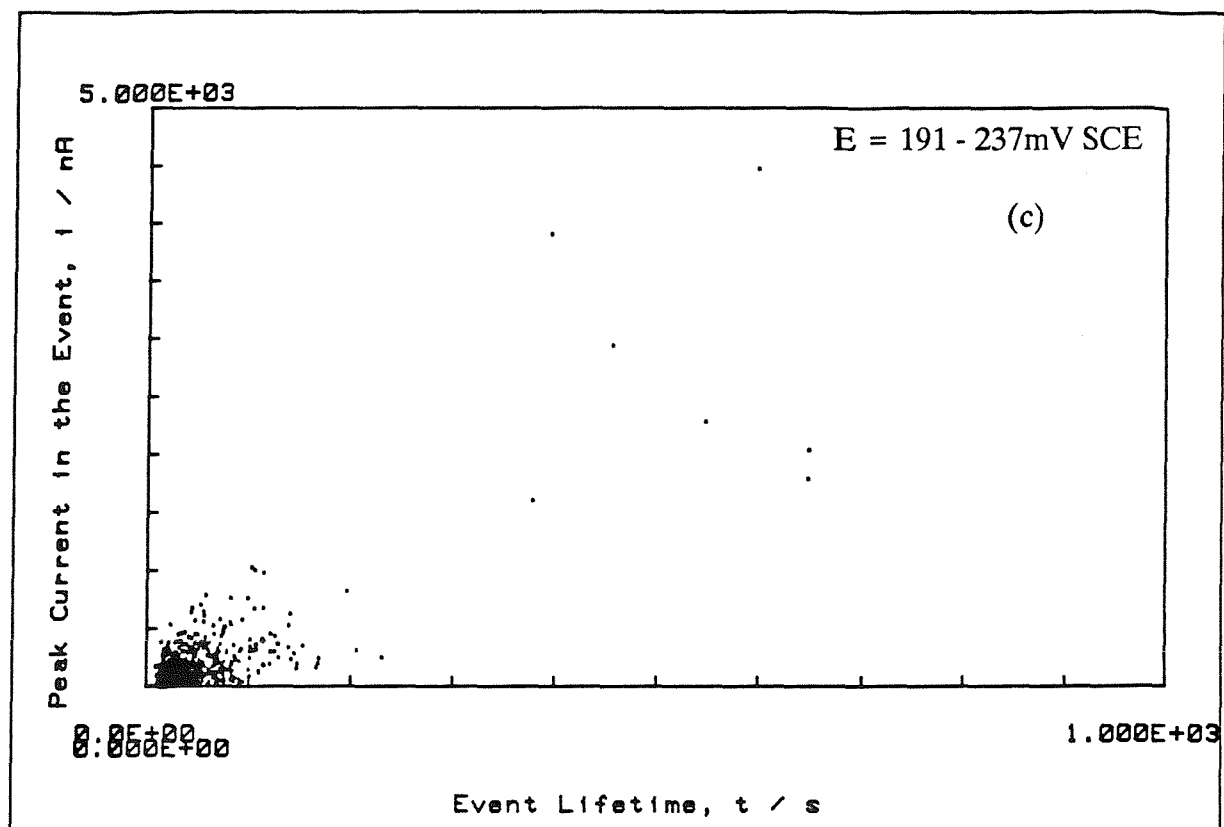


Figure 7.3 (continued)

Figure 7.4 Average Calculated Pit Radius

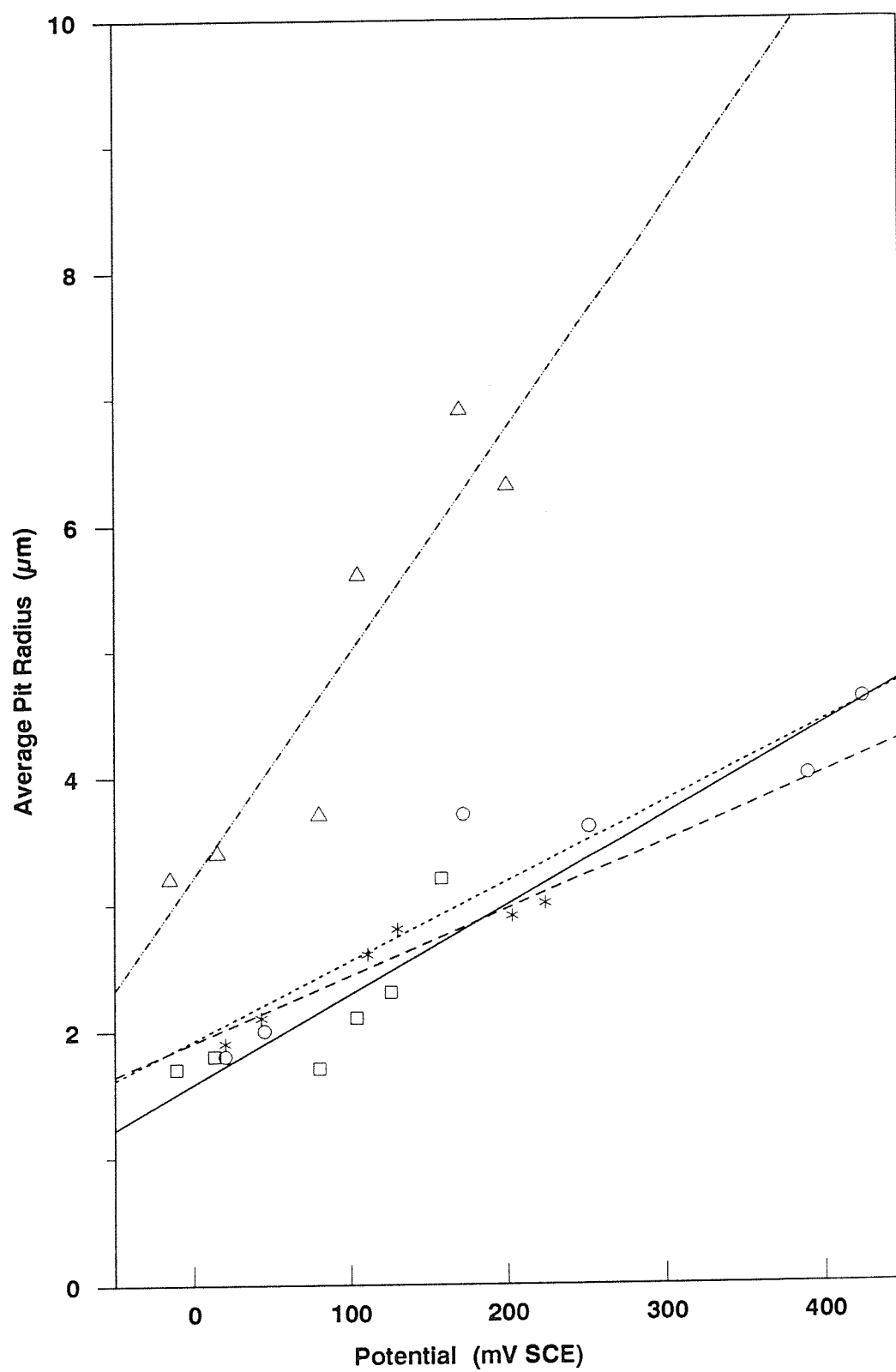


Figure 7.5 Passive Current Densities

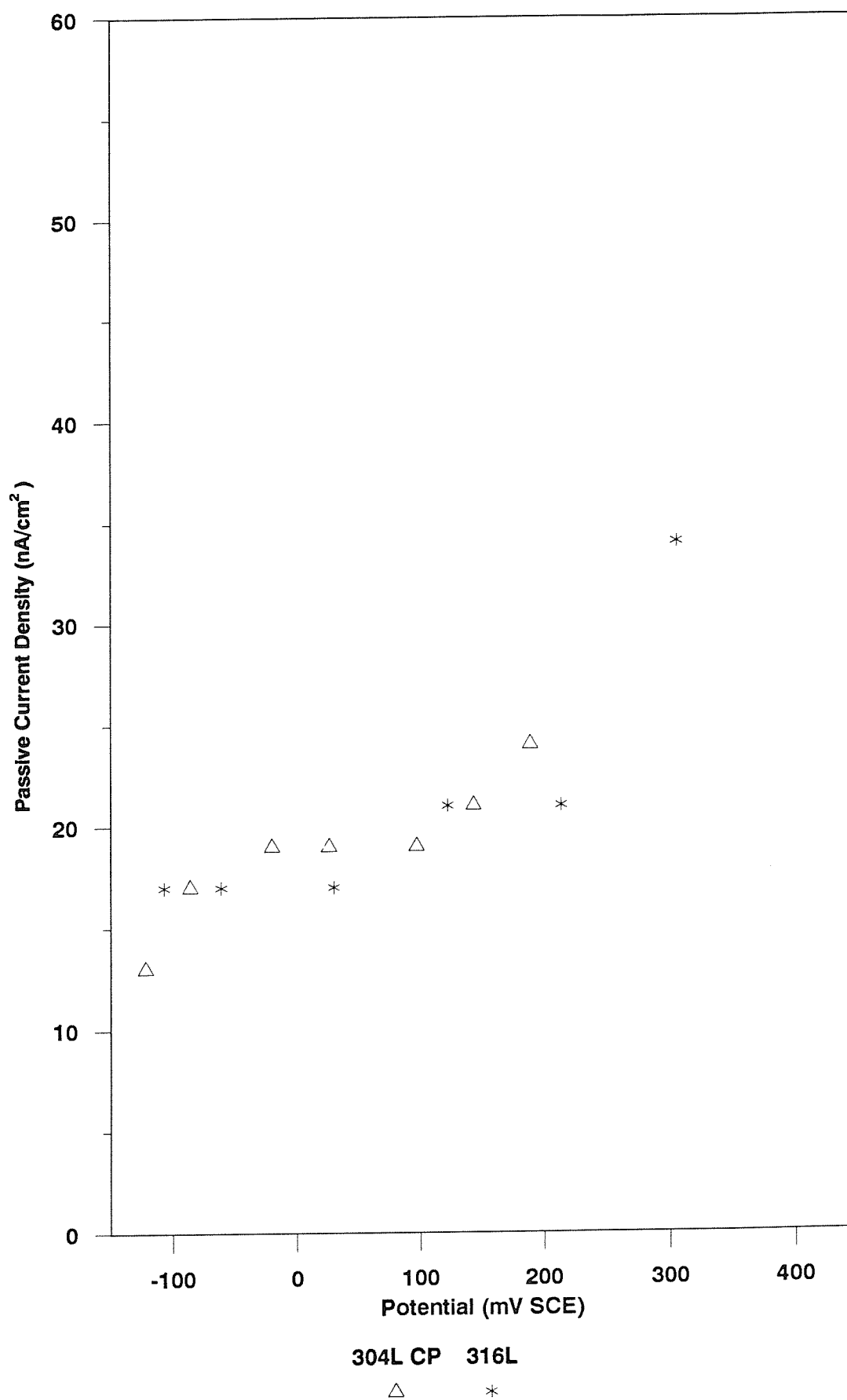
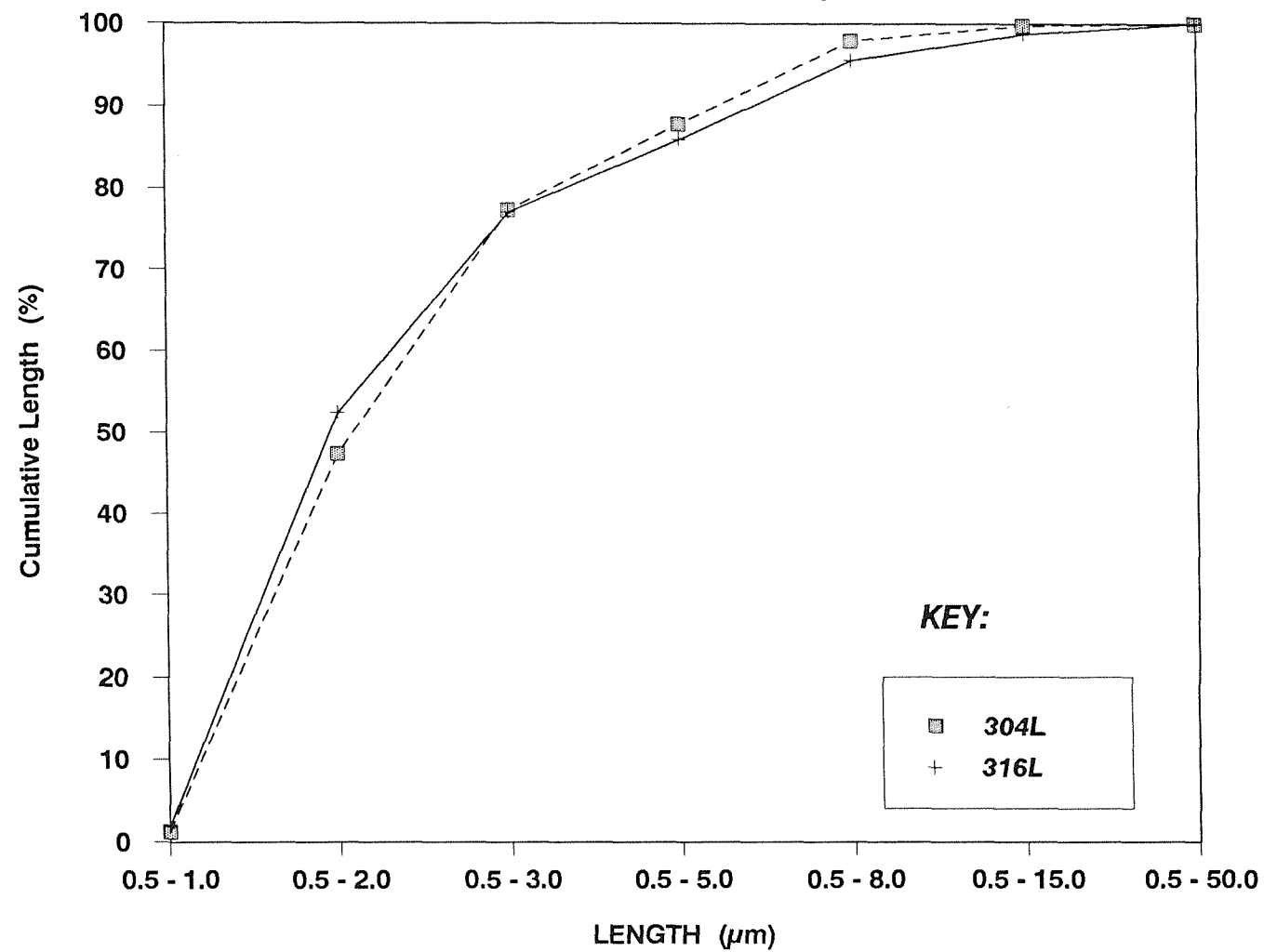


Figure 7.6 Cumulative Length Distribution of Inclusions
Measured by Image Analysis



**Figure 7.7 Cumulative Area Distribution of Inclusions
Measured by Image Analysis**

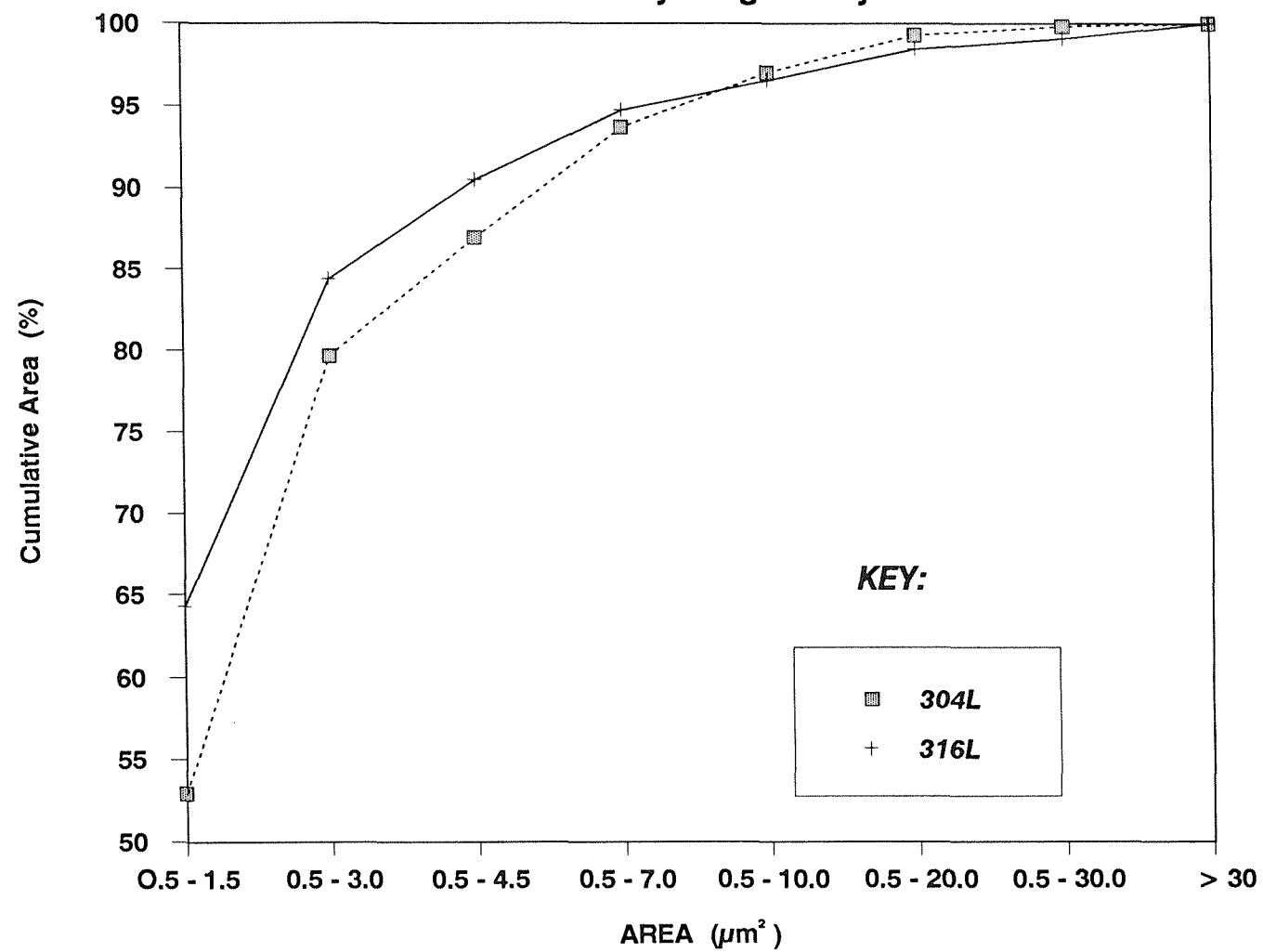
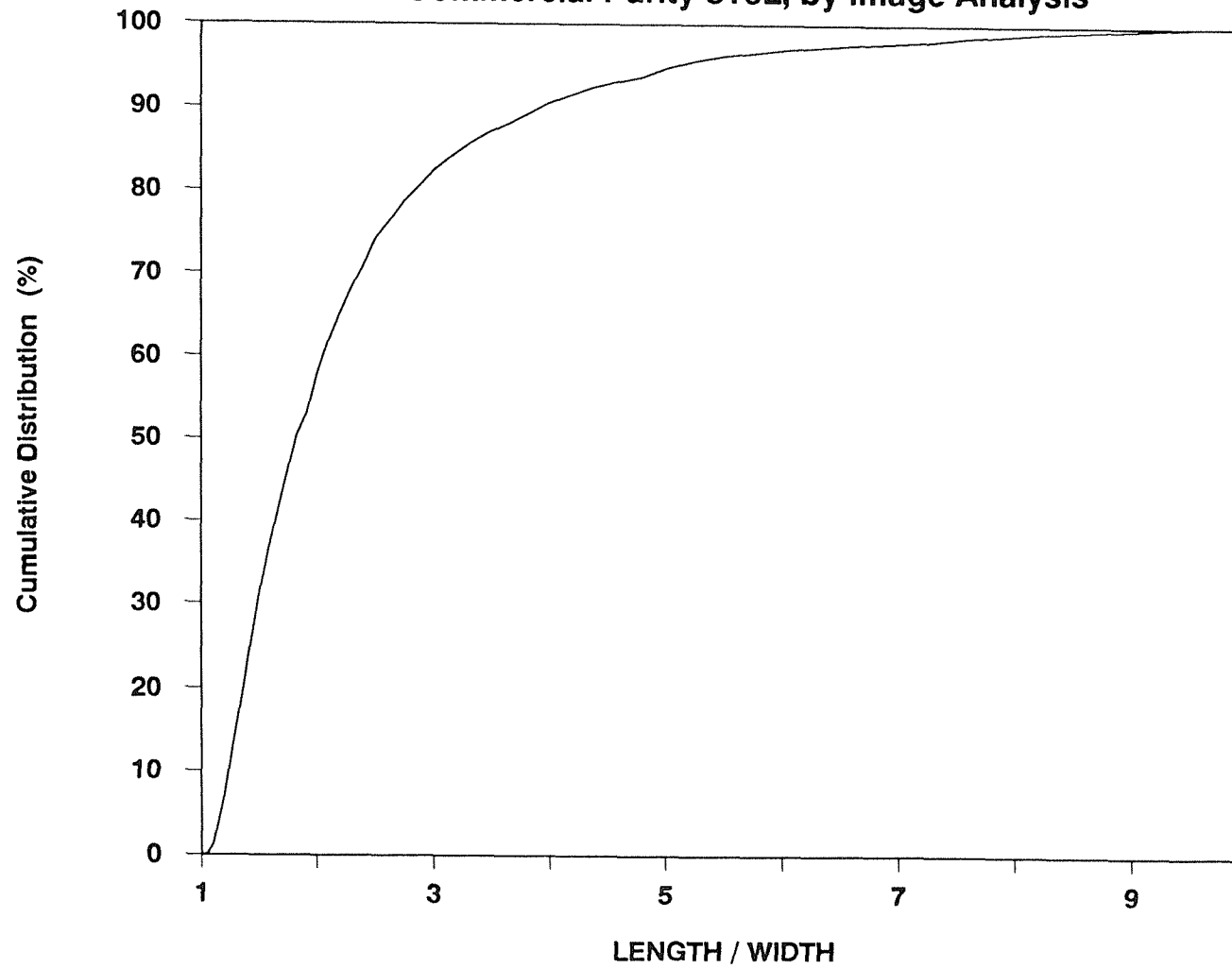


Table 7.2 Summary of Image Analysis Results

	304L	316L
Total Number of Fields	225	500
Field Size (mm²)	0.0146	0.0150
Total Number of Particles	2,456	3,634
Area % of Particles	0.178	0.115
Standard Deviation	0.116	0.15
Mean Length (μ m)	2.63	2.88
Standard Deviation	1.96	3.41
Mean Area (μ m²)	2.46	2.47
Standard Deviation	3.60	6.60

Figure 7.8 Shape Factor Distribution for Particles Measured on Commercial Purity 316L, by Image Analysis



for pit nucleation, and that the sulphides on the surface of the steel make a significant contribution to the current flowing in the passive state. It would therefore be surprising if Mo and sulphur-species *did not* react in some way during dissolution in the pit. It can be suggested on the basis of these results that Mo acts by inhibiting the accelerating effect of sulphur species on anodic dissolution kinetics, which was inferred by Kolotyrkin and Freiman⁽²⁶⁾, and demonstrated for a model system by Marcus and Moscatelli⁽²⁴⁾. It remains to be demonstrated whether Newman's suggestion^(7,8) that Mo inhibits anodic dissolution *per se* is valid. For real alloys, in which sulphur may be derived from inclusions, it is difficult to separate a beneficial effect of Mo on S from a beneficial effect of Mo alone, given that sulphides are always likely to be present. One possible way to address this problem might be to use a Mo containing ferritic stainless steel, since these alloys are less sensitive to pitting at sulphides⁽²⁸⁾.

Confirmation of the importance of sulphide inclusions in the nucleation of pitting on 316L could be demonstrated by performing controlled heat treatments on laser surface melted specimens, to allow the fine sulphide particles to coalesce and grow (by Ostwald ripening). It would be expected that, as the sulphides are allowed to coarsen, the unstable pit nucleation frequency will increase, and the distribution of breakdown potentials will be shifted to lower (more active) potentials.

It was shown in the previous chapter, Figure 6.8, that the breakdown distribution for 316L was about 120mV more noble than the distribution for 304L. It is suggested that this improvement arises directly from lower anodic dissolution rates in the growing pit. Specifically, by removing or reducing the deleterious sulphur species, the dissolution rate is reduced. Presumably, higher Mo-additions improve pitting resistance by removing a given amount of sulphur more rapidly, decreasing the probability of a pit reaching a given size. These predicted effects are amenable to future study, for example using the techniques described in this work.

CHAPTER 8

CONCLUSIONS

CHAPTER 8 - CONCLUSIONS

The main conclusions arising from this study are now summarised, along with some suggested future directions.

It has been established that a high sensitivity to micropitting events can be achieved by, (a) using high resolution equipment, (b) taking suitable precautions against electrical interference, and (c) using a slow potential scan rate. It has been found that the exchange current density for film growth during the slow potential ramp experiment is exceedingly small, indicating that a simple model of uniform dissolution is unlikely to apply, and that steady state is never reached, even under conditions of natural immersion. A direct correspondence has been established between the occurrence of anodic current transients and the nucleation, temporary growth and repassivation of micropits. Prior to repassivation of unstable micropits, there was no difference in their current-time evolution to distinguish them from pits which continued to propagate to form macropits. Current transients were first observed at electrode potentials considerably lower (down to -190mV SCE) than the reported "repassivation potentials" obtained from conventional cyclic polarisation experiments, an observation which questions the reliability and meaning of the "repassivation" potential.

It has been shown theoretically that there are two limiting forms of current evolution with time during the growth of a pit: $i \propto t^2$, where the current is limited by the surface area of the growing pit, and $i \propto t^{1/2}$, where the current is solution resistance limited. The relationship between current and time for the more commonly observed $i \propto t$ has also been described by this model. The experimentally observed current transients evolved in a manner fully consistent with the model predictions. Microscopy revealed that many pits were covered with remnants of the surface metal. It has been suggested that the integrity of this film is a vital element in providing resistance to current flow, helping to maintain the potential drop between the passive surface and the dissolving pit surface.

A preliminary study has indicated that the initiation frequency of pits is not strongly dependent on solution flow. However, a specific effect of turbulent flow was to stop or inhibit the growth of a developing pit. This result, which is consistent with practical experience (where, for example a minimum flow velocity of 5ft/s is recommended for stainless steels in seawater), has been interpreted in terms of a reduction in the

concentration boundary layer outside the growing pit. This has two effects: an increased solution resistance outside the pit as the concentration gradient is swept away causes a reduction in current at a given potential and hence reduces electromigration (e.g. of chloride) into the pit; the increase in the material out of the pit (by convection) is such that the concentrated pit solution, which is required for continued propagation, cannot be maintained. A more speculative interpretation has been given in which the morphology of the pit and the strength of the pit cover may contribute to the effects of flow. The effects of turbulent flow noted in the present study suggest that the pitting breakdown potential of steels tested under conditions of turbulent flow should be shifted to more anodic values. Interestingly, this is at odds with most other studies involving flow, where no effect on the "pitting potential" was found. Future work aimed at establishing the pitting breakdown distributions in the various flow regimes would resolve this issue.

Many small pits were observed to be associated with sulphur-rich inclusions, prompting a detailed study of the role of inclusions on pit initiation. By combining rigorous microstructural characterisation and multiple slow potentiodynamic sweep experiments on commercial 304L and two high purity 304L model alloys, one of which was doped with sulphur, it has been shown conclusively that pits nucleate predominantly at sulphur-rich inclusions. The nucleation frequency of unstable pits reflected the sulphur content of the alloy. It is proposed that in order to nucleate a pit which will continue to propagate, initiation must occur at a sufficiently large supply of sulphur - either a single inclusion or a cluster of smaller inclusions. Otherwise the pit may repassivate when the supply of sulphur is exhausted. In support of this, for each of the three steels, the distribution of particle sizes showed a good correspondence with the distribution of the lifetimes of the current transients. It is further suggested that the size and distribution of the inclusions influences the size of pits, and their shape dictates the shape of the current transients. In order to test more quantitatively the proposed relationship between inclusion distribution and pit size, i.e. that clusters of small inclusions can nucleate and help sustain a large pit, information on the *spatial* distribution of inclusions is required. Testing this hypothesis, by applying the methods of spatial statistics, would be a useful direction for future study. In addition to a clear effect on the unstable pit nucleation frequency of changing the sulphur content and inclusion volume fraction, the distribution of pitting breakdown potentials was also affected. These shifted to more anodic values as the sulphur content of the alloy was decreased. The different sulphide inclusion volume fraction of the alloys was

reflected in the passive current densities, being lowest in the high purity alloy and highest in the high sulphur alloy at a given electrode potential. This indicates that electrochemical dissolution at sulphide inclusions contributes to the current in the passive state.

Laser surface melting has been shown to be a very effective method for improving the pitting resistance of stainless steels. For example, the distribution of breakdown potentials measured for laser treated commercial purity 304L was very similar to that for untreated 316L. This improvement was due to the removal and re-distribution of sulphur-rich inclusions. Some inclusions were evaporated during the laser processing, evidence for which has been provided by examination of specimens in the scanning electron microscope. However, chemical analysis of the melt-zone revealed that only about 10% or so of the sulphur was removed in this way. Transmission electron microscopy showed that the remaining sulphur was distributed in the melt-zone as small sulphur-rich inclusions (typically 100nm in diameter). This work indicates that below a certain size, inclusions are too small to nucleate a damaging pit. Further work, with the aim of specifying and achieving microstructures in which the sulphides are small and evenly distributed, could lay the foundations for the design of alloys with improved pitting resistance. Three routes could be considered to achieve this microstructure. Based on the results of this study, high purity alloys certainly exhibit enhanced pitting resistance, although this route is probably impractical on the basis of cost, and also because some sulphur is desirable for machinability. A second suggestion is to laser-melt the surface of the steel. This would have advantages where fabricated, critical components could be laser treated prior to installation in plant. It would have particular advantages for free-machining grades (which are high in sulphur), which rely on sulphide stringers for their improved machinability, and as a result have a rather poor corrosion resistance compared to low sulphur grades. The main disadvantage of this route is likely to be the processing times: coverage rates would be much too slow for bulk steel products such as plate and strip (where, for example, passivation treatments are likely to be cheaper). A third alternative would be to inoculate the molten steel with an addition which nucleates a large number of small inclusions, rather than a smaller number of large (and damaging) inclusions. According to the results presented in a recent publication⁽¹⁾, cerium would appear to be a candidate as a suitable addition, as it improves both the pitting resistance and hot

workability of highly alloyed stainless steels. Laser melting followed by controlled heat treatment, to allow the small sulphide inclusions to coalesce and grow, provides a route to determine the particle size regime for optimum pitting resistance.

In another study of the effects of laser treatment on the corrosion resistance of stainless steels, it was shown that intergranular stress corrosion cracking of sensitised type 304 stainless steel can be prevented by using the laser to melt a thin surface layer. This creates a barrier of unsensitised material between the corrosive environment and the underlying susceptible microstructure. Provided that the necessary attention is given to developing the optimum laser processing parameters for a particular task (for example to prevent the initiation of IGSCC, a tough and ductile melt zone is essential) laser processing has the potential to improve the corrosion resistance of a wide range of components.

In a follow-up to the observation that laser treated 304L (i.e. small, well dispersed sulphide inclusions) exhibited a similar distribution of breakdown potentials to untreated 316L, it has been shown that Mo (at the levels present in 316L) does not inhibit pit initiation. The results are supportive of a mechanism in which Mo acts by providing an "antidote" to the "poisoning" effect (i.e. on repassivation) of sulphur in the active pit. Whether Mo has an effect in the absence of sulphur on commercial alloys remains to be demonstrated. A possible approach would be to use a Mo-containing ferritic stainless steel, as these alloys are apparently less sensitive to pitting at sulphides⁽²⁾. Confirmation of the importance of sulphide inclusions in pit nucleation on 316L could be demonstrated by laser treatment followed by controlled heat treatment to enable the sulphides to coalesce and grow (i.e. Ostwald ripening). The prediction would be that, as the sulphides are allowed to coarsen, the pit nucleation frequency will increase and the distribution of breakdown potentials will shift to lower (more active) potentials.

A consistent observation throughout this study has been the scaling between the passive current density and the level of pitting activity for the various alloys studied. This observation, which has been confirmed in subsequent studies⁽³⁾, is consistent with a general class of "feedback" models in which any local transient in the passive current would feed back on the local potential, pH and chloride concentration, which might then amplify the current to a level where it becomes unstable, leading to a large increase in the local current density *viz* pitting. The implication of such theories is that

the driving force for pit nucleation is the current in the passive state. In the present study it has been shown that the passive current and pitting activity are dependent on the volume fraction of sulphides in the steel, implying that the local instabilities in the passive current are associated with sulphide inclusions. The observation that many small pits were associated with sulphide inclusions is consistent with this general interpretation.

APPENDICES

APPENDIX A

METALLURGICAL ASPECTS OF STAINLESS STEEL

Some of the earliest work on stainless alloys was carried out in the first part of the nineteenth century. Stodart and Faraday⁽¹⁾ and Berthier (in 1821)⁽²⁾ both noticed that chromium increased staining resistance. Indeed Berthier is reported to have suggested the use of chromium steels for cutlery⁽²⁾. These observations did not receive the attention they deserved largely because the detrimental effect of carbon (the content of which was very high in the early alloys, > 0.4%) was not appreciated, and also because an extensive programme of research by Hadfield⁽³⁾ in 1892 had shown that chromium *decreased* the corrosion resistance of steel in sulphuric acid. This was an unfortunate observation, since we now know that stainless steel is corrosion resistant in sulphuric acid only under certain conditions. By the end of the nineteenth century the detrimental effect of carbon had been recognised⁽⁴⁾ and Monnartz⁽⁵⁾ demonstrated the corrosion resistance of chromium steels. Brearley is accredited as the founder of the stainless steel industry. He recognised the commercial usefulness of 12% Cr 0.3% C alloys prior to world war one^(2,7). It seems his initial work was carried out independently from that of Haynes in America, who worked on very similar material at about the same time⁽⁶⁾, and that of Monnartz⁽⁵⁾. The 13% Cr 0.25% C steel commercially launched by Brearley in 1915 is still almost identical to the current steel used for stainless knives. During the first world war Maurer and Strauss⁽⁷⁾ developed higher chromium alloys (about 20%) with nickel additions of about 8%.

These early steels became the forerunners of the major categories of present day stainless materials - the austenitic grades based on Fe-Cr-Ni alloys and the martensitic and ferritic grades, both developed from the Fe-Cr alloys. Much more recently widespread interest has been generated by the useful combination of mechanical properties and corrosion resistance exhibited by the duplex austenite-ferrite grades. This chapter is concerned with the evolution, properties and uses of austenitic, and particularly type 304, stainless steel. However, most of it is relevant to the other classifications.

A.1 STEEL MAKING

The first stainless steels were made in gas fired crucibles and in later years in electric induction furnaces. However, these were incapable of reducing the carbon content of the charge, which was usually high because most of the ferrochrome used had a high carbon content. This was improved in the 1930s and 1940s when electric arc furnace temperatures exceeded $2,000^{\circ}\text{C}$ and cheap tonnage oxygen also became available. These were the major steps that led to the manufacture of lower carbon steels with better corrosion resistance.

In the 1940s many pneumatic steel making processes were developed and it was found that the blowing of large quantities of oxygen into stainless steel melts in electric arc furnaces enabled the carbon content to be reduced to $<1\%$. Further blowing could achieve $0.03\% \text{ C}$ but the thermodynamics of the process led to large chromium losses such that the final chromium level would be only $7-8\%$. Enhancement of the chromium by further additions of ferrochrome had the disadvantage of again raising the carbon content. Figure A.1⁽⁸⁾ shows the effect of temperature on the equilibrium between carbon and chromium in iron melts. It can be seen that as the bath temperature is increased, the amount of chromium which can be retained at a given carbon content increases rapidly⁽⁹⁾. The high temperatures necessary to retain $18\% \text{ Cr}$ in the melt, and thus facilitate the economic use of large amounts of stainless steel scrap in the furnace charge - about $2,000^{\circ}\text{C}$ for carbon contents below 0.03% - led to major furnace lining wear problems. Consequently, lower temperatures had to be used, necessitating ferrochrome additions to achieve the requisite $17 - 19\% \text{ Cr}$. In order to maintain a very low carbon content, very low carbon ferrochrome had to be used, which was expensive. The minimum economic carbon content was about 0.06% - which is just about the carbon content of the type 304 stainless steel used in the section describing a stress corrosion cracking countermeasure in Chapter 7 of this thesis. Such carbon levels were typical in the stainless steels produced in the late 1960s and early 1970s.

An alternative way of influencing the thermodynamics in favour of carbon (as opposed to chromium) removal from Fe-Cr melts came from the appreciation that a given retained chromium content in the melt was inversely proportional to the partial pressure of carbon monoxide in the system. This led to the development of several processes which used low partial pressures of CO to enable low carbon and high

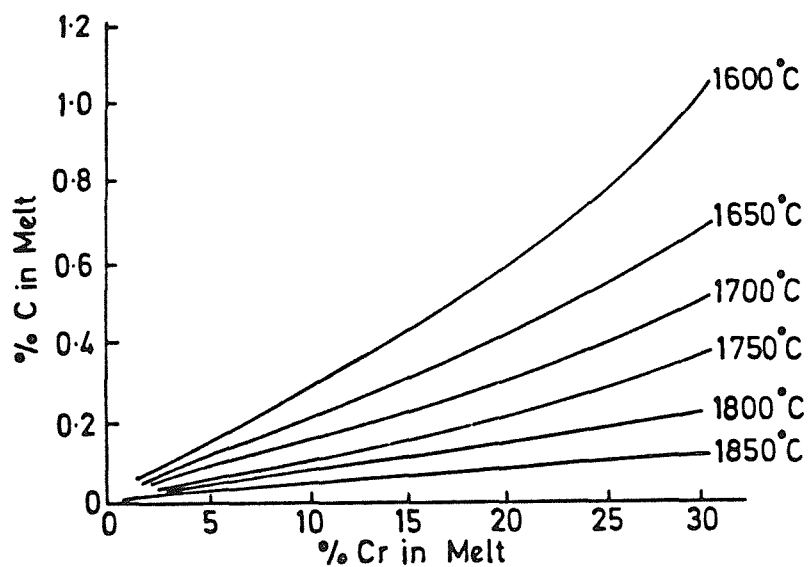


Figure A.1 Effect of temperature on the equilibrium Between C and Cr in iron melts⁽⁸⁾

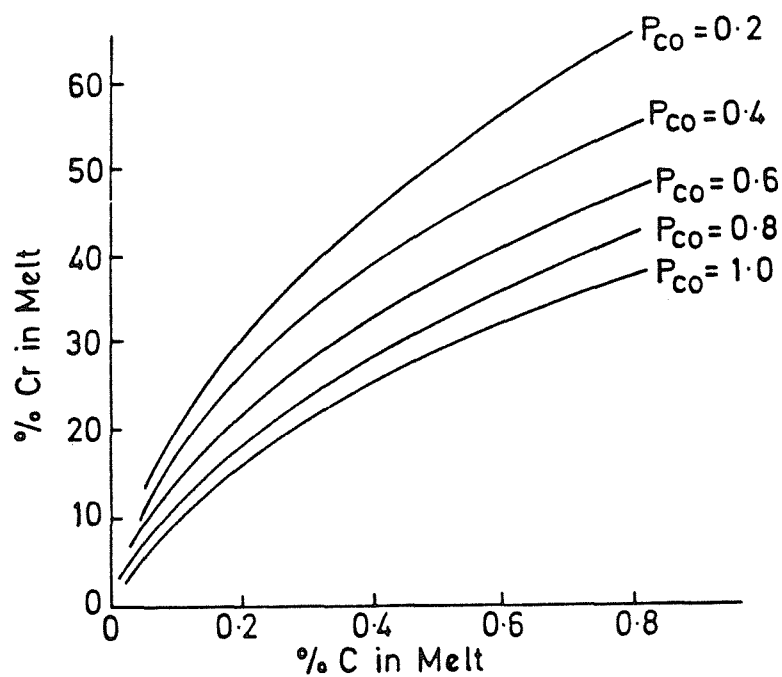


Figure A.2 Effect of P_{CO} on Cr-C equilibrium in iron melts at 1700° C⁽⁸⁾

chromium contents to be obtained in the steel bath, without the need for very high temperatures⁽¹⁰⁾, Figure A.2(8). Initially this was done by vacuum oxygen decarburisation (VOD), a process in which the furnace was partially evacuated whilst oxygen was bled into the melt. An alternative method was the steam oxygen decarburisation (SOD, or Creusot-Loire-Uddeholm) process in which steam was the diluent gas. The steam dissociated to give hydrogen and oxygen at reduced partial pressure. Although both of these systems survive, the vast majority of stainless steel is now made by the argon oxygen decarburisation (AOD) process, which was established in about 1970.

In the AOD process the electric arc furnace is essentially used as a melting unit, the charge comprising stainless steel scrap and ferrochromium to achieve more or less the correct chromium (and nickel etc.) content but with up to 2% C. The melt is then transferred to the AOD converter, where it is blown with argon/oxygen gas mixtures through tuyeres located at the bottom of the vessel (cheaper nitrogen may replace argon in the early part of the blow). The ratio of the two gases varies with the carbon content of the melt, finally achieving a partial pressure of CO of about 0.1 atmospheres, which results in a carbon content of below 0.02%. The vigorous stirring from the bottom blowing gives good slag/metal mixing which results in efficient desulphurisation - sulphur contents as low as 0.002% can be achieved, but in practice the level is maintained around 0.01% for improved welding and machining properties⁽¹¹⁾. The AOD process therefore produces cleaner steels (with respect to non-metallic inclusions) than the electric arc furnace because of this efficient desulphurisation, and because the oxygen content is lower (0.005-0.01% after the final reducing blow with pure oxygen). The type 304L stainless steel used in most of the experiments described in this thesis was a product of the AOD process.

The general alloy classification of "Stainless Steel" spans a broad range of compositions and constitutions, which is continually expanding as new alloys are designed and developed to meet specific requirements. Consequently, a number of systematic naming conventions have evolved. Of these, that of the AISI (American Iron and Steel Institute) has found widest acceptance, often used in the U.K. in conjunction with the appropriate British Standard. The convention classifies alloys according to their major microstructural constituent. Thus alloys are designated austenitic, ferritic, martensitic etc.. Alloying elements play a dominant role in determining the microstructure of a stainless steel.

A.2 THE CONSTITUTION OF STAINLESS STEELS

By determining the proportions of the microstructural phases present, the constitution of all the stainless steels plays an important role in controlling their metallurgical characteristics, mechanical properties and corrosion resistance. The two main alloying elements associated with stainless steels are chromium and nickel. They have opposing effects on the constitution: chromium favours the stabilisation of ferrite, whilst nickel is an austenite stabiliser. Hence Fe-Ni alloys show an expanded temperature/composition range for austenite stability whilst Fe-Cr alloys show the reverse effect and a closed austenite (γ) loop. Other alloying elements can be conveniently classified as austenite stabilisers (C, N, Cu, Co, Mn) or ferrite stabilisers (Mo, W, Nb, Ti, V, Si, Al) which respectively increase or decrease the extent of the austenite phase field. Empirical data is available on the relative tendency of an alloying element to stabilise austenite or ferrite, and the values can be incorporated into chromium or nickel equivalents. Many different nickel and chromium equivalent equations have been proposed, one such applicable to the higher chromium austenitic steels being⁽⁸⁾:

$$\%Cr \text{ equivalent} = \%Cr + 3(\%Si) + \%Mo + 10(\%Ti) + 4(\%Nb)$$

$$\%Ni \text{ equivalent} = \%Ni + 0.5(\%Mn) + 21(\%C) + 11.5(\%N)$$

(all concentrations expressed as weight percent)

A convenient way of predicting the likely structure of a given stainless steel is the modified Schaeffler diagram⁽¹²⁾ (Figure A.3). It plots the compositional limits at room temperature of austenite, ferrite and martensite, in terms of nickel and chromium equivalents. It is very useful in determining whether a particular steel will be fully austenitic at room temperature. The diagram shows that fully austenitic structures can be obtained for alloys containing less than 30% chromium equivalent provided that the nickel equivalent is greater than 25%. As the nickel equivalent is reduced, so the range is reduced over which a fully austenitic structure can be achieved. Thus it can be seen that the minimum chromium and nickel equivalents consistent with a fully austenitic room temperature structure are about 18% and 10% respectively, leading to the familiar group of austenitic steels based on 18% Cr, 8% Ni, of which the AISI type 304 used in this study is the best known example.

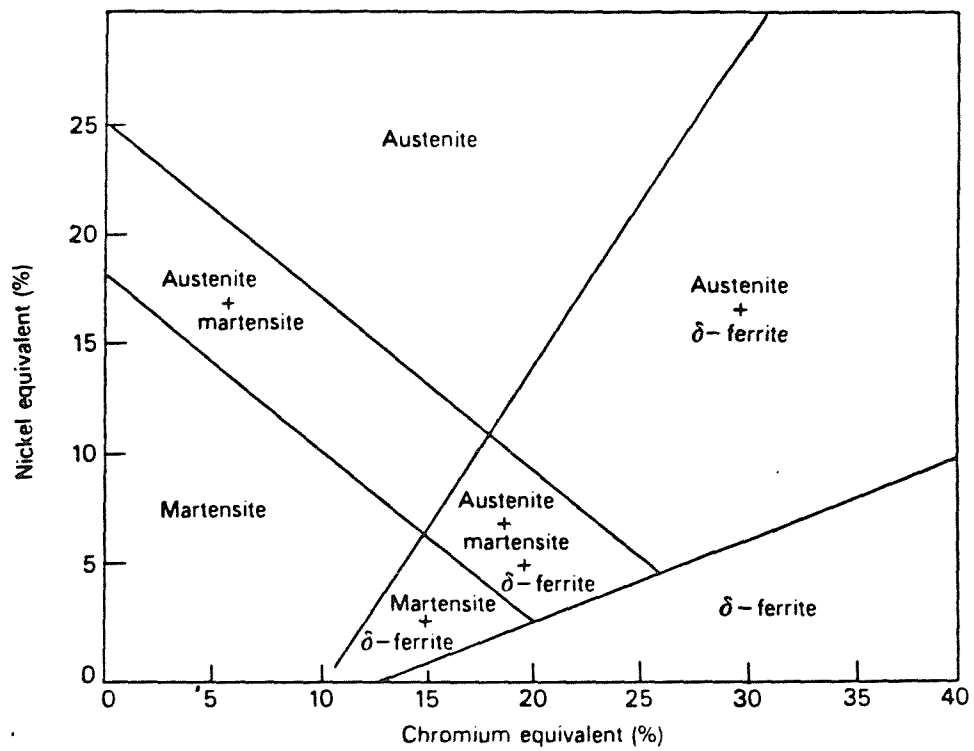


Figure A.3 The Schaeffler diagram, modified by Schneider⁽¹²⁾

A.3 AUSTENITIC STAINLESS STEELS

Austenitic stainless steels are so-called because they share the face-centred cubic crystallography of the austenite phase found in low-carbon steels. They are by far the most widely used of stainless steels, comprising 70-80% of all stainless production. In turn, about 70% of all austenitic stainless steel produced is based on 18Cr-8Ni. Indeed this basic composition forms a starting point for compositional modifications to enhance specific properties, Figure A.4⁽¹³⁾. The austenitic steels have lower proof stresses but higher work hardening rates than the ferritic steels, and are more easily welded and cold formed. Their toughness is high, and they exhibit no ductile-brittle fracture transition. Their exceptional corrosion resistance is mainly marred by a susceptibility to localised corrosion in certain environments.

In some so-called "leaner" grades of austenitic stainless steels such as the basic 18Cr-8Ni, the austenite is only just stable at room temperature. On cooling (for example in liquid nitrogen), or plastically deforming (for example in stretch forming) the microstructure will partially transform to martensite.

The applications of these steels are widespread in the chemical processing, food, construction, power plant and other industries where, depending on the alloy type, their corrosion resistance, high level of fabricability, cryogenic properties, creep and oxidation resistance, and lack of ferromagnetism are of predominant importance.

REFERENCES

1. J. Stodart and M. Faraday, *Phil. Trans. Royal Society*, **112**, p.253, (1822).
2. J.E. Truman, *The Metallurgist and Materials Technologist*, **1**, p.15, and **2**, p.75, (1908).
3. R.A. Hadfield, *JISI*, **2**, p.49, (1892).
4. A. Carnot and E. Gautal, *Comptes Rendues*, **126**, p.1240, (1898).
5. P. Monnartz, *Metallurgie*, **8**, p.16, (1911).

APPENDIX A - STAINLESS STEELS

6. Anon, Steel and Coal, p.305, (1963).
7. R.A.E. Hooper, Metals and Materials, p.10, (1986).
8. F.B. Pickering, in "Stainless Steels '84", p.2, Institute of Metals, (1985).
9. D.C. Hilty and T.F. Kaveney, in "Handbook of Stainless Steels", eds. D. Peckner and I.M. Bernstein, p.3.1, McGraw Hill, (1977).
10. J.C.C. Leach, A. Rodgers, and G. Sheehan, in "Secondary Steelmaking", p.73, The Metals Society, London, (1978).
11. A.J. Sedriks, Int. Met. Rev., 28, p.295, (1983).
12. H. Schneider, Foundry Trade J., 108, p.562, (1960).
13. A.J. Sedriks, "The Corrosion of Stainless Steels", p.12, Wiley, (1979).

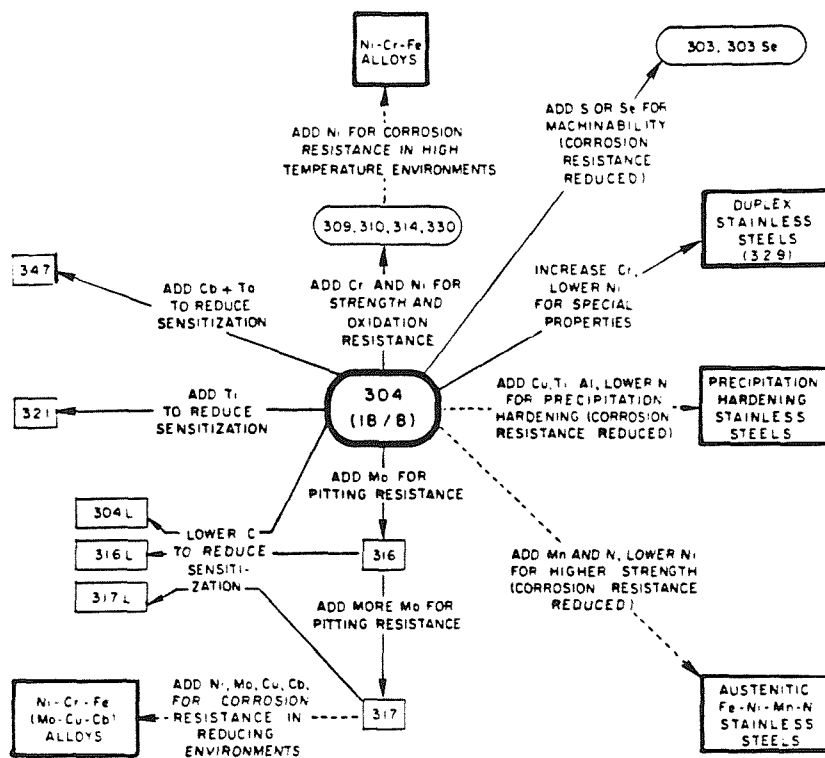


Figure A.4 Some compositional modifications of 18-8 austenitic stainless steels to enhance specific properties⁽¹³⁾

APPENDIX B

COMPOSITION OF STAINLESS STEELS USED IN THIS STUDY¹

STEEL TYPE	Weight % (Fe Balance)									
	Cr	Ni	Mn	Si	C	P	S	Mo	Cu	Ti
AISI 304L Spec. ²	18-20	8-12	1.50	1.00	0.030	0.045	0.030			
304L - CP	18.2	9.3	1.13	0.42	0.020	0.026	0.011	0.38	0.21	<0.02
304L - HiP	18.4	10.4	0.55	0.30	0.003	<0.01	0.003	<0.02	<0.02	<0.02
304L - HiS	18.4	10.4	0.82	0.28	0.004	<0.01	0.080	<0.02	<0.02	<0.02
304L - HiS, Laser Treated							0.071			
AISI 304 Spec. ²	18-20	8-10.5	2.00	1.00	0.080	0.045	0.030			
304 - CP, SCC Expts	17.8	9.07	1.5	0.5	0.059	0.03	0.025	0.38	0.4	<0.02
AISI 316L Spec. ²	16-18	10-14	2.00	1.00	0.03	0.045	0.030	2-4		
316L - CP	17.3	12.5	1.65	0.40	0.023	0.033	0.016	2.47	0.35	<0.02

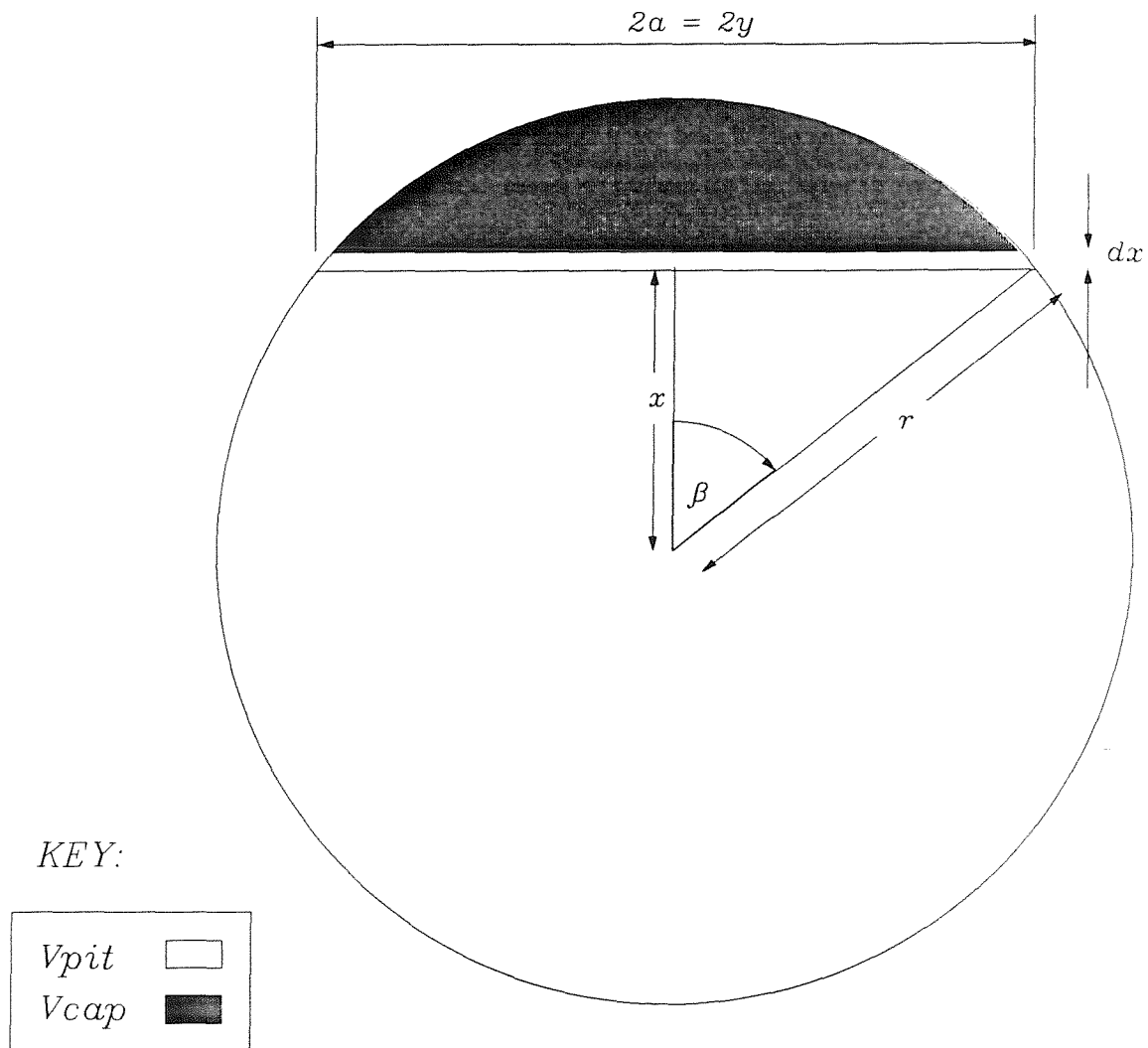
NOTES

- ¹ - Analysis determined by X-ray fluorescence, except S and C (LECO)
- ² - Single figures are maximum values
- CP = Commercial Purity
- HiP = High Purity
- HiS = High Sulphur

APPENDIX C - RELATIONSHIP BETWEEN CONSTANTS (K_a and K_v)

Consider a simple model for a pit, viz a sphere, of which the pit mouth is a chord. The assumption is that the pit mouth increases in radius as the sphere increases in radius.

Figure C.1 - Relationship between k_a and k_v



Now from Chapter 3 the following relationships have been assumed:

$$a = k_a r \quad (3.10)$$

APPENDIX C - RELATIONSHIP OF CONSTANTS

$$V = k_v r^3 \quad \left(\frac{4}{3} \pi > k_v > \frac{2}{3} \pi \right) \quad (3.11)$$

where:

a = pit mouth radius

r = pit radius

V = pit volume

The relationship between k_a and k_v can be derived by considering their geometric relationship as illustrated in Figure C.1. Now:

$$a = r \sin \beta \quad (C.1)$$

It therefore follows, from Equation 3.10 and C.1, that:

$k_a = \sin \beta$	(C.2)
--------------------	-------

Find the volume of the cap, V_{cap} :

$$dV_{cap} = \text{Area of disc} \cdot dx$$

where:

$$\text{Area of disc} = \pi \times \text{disc radius}^2$$

$$dV_{cap} = \pi y^2 \cdot dx \quad (C.3)$$

From Pythagoras Theorem:

$$y^2 = r^2 - x^2$$

Substituting for y in Equation C.3:

$$dV_{cap} = \pi (r^2 - x^2) \cdot dx$$

$$V_{cap} = \int_{r \cos \beta}^r \pi (r^2 - x^2) \cdot dx$$

$$V_{cap} = \pi \left[r^2 x - \frac{x^3}{3} \right]_{r \cos \beta}^r$$

$$V_{cap} = \pi r^3 - \frac{\pi r^3}{3} - \pi r^3 \cos \beta + \frac{\pi r^3 \cos^3 \beta}{3}$$

$$V_{cap} = \frac{2}{3} \pi r^3 - \pi r^3 \cos \beta \left(1 - \frac{\cos^2 \beta}{3} \right) \quad (C.4)$$

Now, the volume of the pit is the volume of the sphere with the cap removed, therefore, since:

$$V_{\text{sphere}} = \frac{4}{3} \pi r^3 \quad (\text{C.5})$$

$$V_{\text{pit}} = V_{\text{sphere}} - V_{\text{cap}}$$

it follows that:

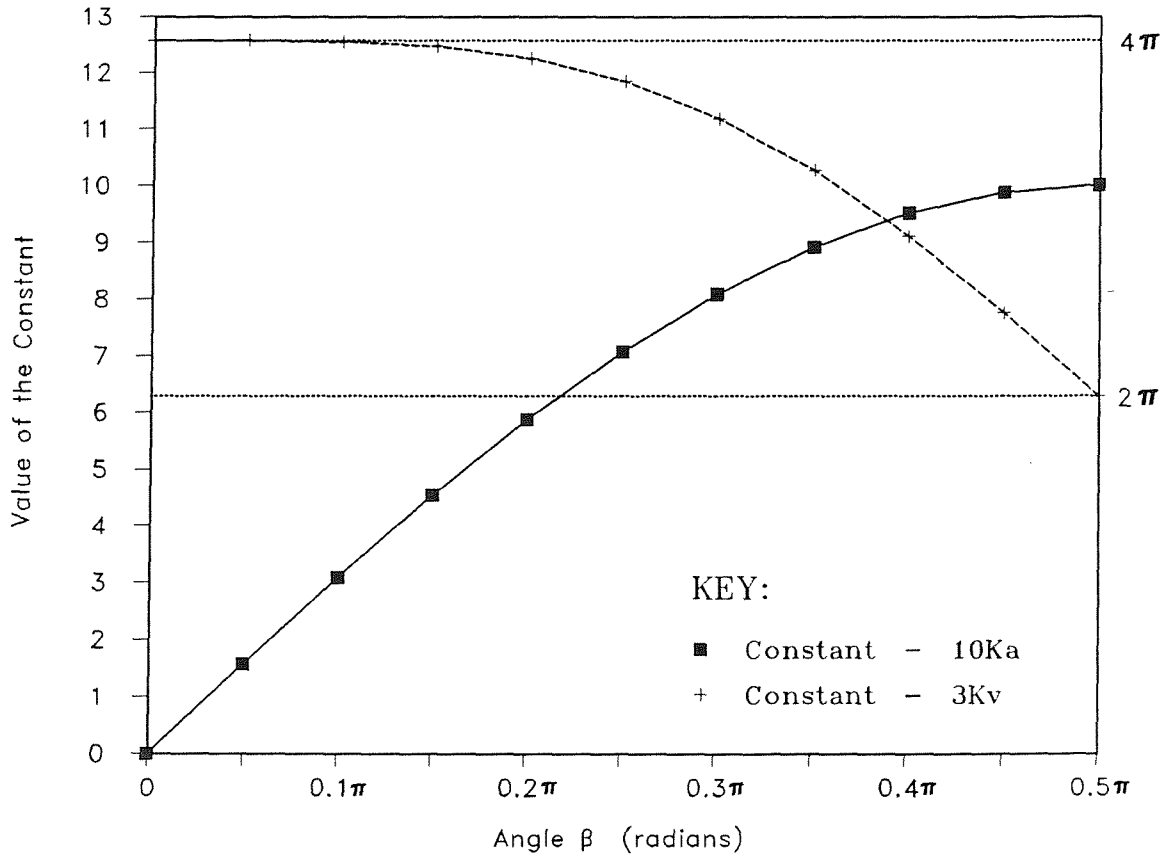
$$V_{\text{pit}} = \pi r^3 \left(\frac{2}{3} + \cos \beta \left(1 - \frac{\cos^2 \beta}{3} \right) \right) \quad (\text{C.6})$$

Using Equation 3.12 and C.6:

$$k_v = \pi \left(\frac{2}{3} + \cos \beta \left(1 - \frac{\cos^2 \beta}{3} \right) \right) \quad (\text{C.7})$$

Figure C.2 shows how k_a and k_v vary as the angle β , where the pit varies from a hemisphere to a full sphere (i.e. $\frac{\pi}{2} > \beta > 0$).

Figure C.2 - Relationship Between Constants k_a and k_v



APPENDIX D

COMPUTER PROGRAM FOR THE SOLUTION OF EQUATION 3.41

```

10 REM !!!!!!!!!!!!!!!!!!!!!!!!!!!!!!!!!!!!!!!!!!!!!!!!!!!!!!!
20 REM ! PROGRAM CALCULATES RADIUS AND CURRENT VS TIME
30 REM !
40 REM ! VERSION PIT5 NOVEMBER7 1989
50 REM !
60 REM ! SOLUTION FOR DUMMY PARAMETER Y BY NEWTON-RAPHSON METHOD
70 REM ! Y GIVES dR/dT. SIMPLE NUMERICAL INTEGRATION GIVES R AND I
80 REM !
81 REM ! PARAMETER DE IS THE DIMENSIONLESS POTENTIAL DIFFERENCE
82 REM ! BETWEEN PIT BASE AND EXTERNAL SOLN
90 REM !!!!!!!!!!!!!!!!!!!!!!!!!!!!!!!!!!!!!!!!!!!!!!!!!!!!!!!
100 INPUT "DELTA E ",DE
110
120 A=DE/2+0.25:B=2*A :REM ! AUXILIARY VARIABLES
130 R=0:T=0:I=0 :REM ! INITIAL VALUES
140 OUTFILE%=OPENOUT("DATA") :REM ! FILE RESULTS FOR PLOTTER
150 PRINT%OUTFILE%,DE
160 PRINT%OUTFILE%,R,T,I
161 REM calculation carried out over three time ranges
162 REM with different step size,DT
170 T1=1E-5:DT=1E-8:TO=DT :REM ! 0 - 1E-5, STEP 1E-8
180 PROCYDET(TO,T1,DT) :REM PROCEDURE DOES CALCN
190 T1=1E-4:DT=1E-7:TO=TF+DT :REM ! 1E-5 - 1E-4, STEP 1E-7
200 PROCYDET(TO,T1,DT)
210 T1=1E-3:DT=1E-6:TO=TF+DT :REM ! 1E-4 - 1E-3, STEP 1E-6
220 PROCYDET(TO,T1,DT)
230 T1=1E-2:DT=1E-5:TO=TF+DT :REM ! 1E-3 - 1E-2, STEP 1E-5
240 PROCYDET(TO,T1,DT)
250 CLOSE%OUTFILE%
260 CHAIN"READPLOT2" :REM PLOTTER PROGRAM
270 END
271 REM*****
280 DEF PROCYDET(TO,T1,DT) :REM ! CALCN DONE HERE
290 FOR T=TO TO T1 STEP DT
300 C=LN(T+EXP(-2*DE))/4)
310 PROCNR :REM ! CALL NEWTON-RAPHSON
320 DRDT=EXP(Y1) :REM ! dR/dT = exp(y) - defn
330 R=R+DRDT*DT :REM ! SIMPLE INTEGRATION
340 I=R*R*DRDT
350 PRINT T "Y1" "R" "I
360 PRINT%OUTFILE%,T,R,I
370 TF=T
380 NEXT T
390 ENDPROC
400
410 REM*****
420 DEF PROCNR :REM ! SOLVE FOR y BY ITERATION
430 YO=DE :REM ! NEWTON-RAPHSON METHOD
440 REPEAT
450 Y1=YO-FNF(YO)/FNF1(YO)
460 DELTA = ABS(Y1-YO):YO=Y1
470
480 UNTIL DELTA<1E-6
490
500 ENDPROC
510 REM*****
520 DEF FNF(Y)=-2*Y+LN(A-Y/2)-C :REM ! eqn to solve for y
530 DEF FNF1(Y)= -2-1/(B-Y) :REM ! derivative
540 REM*****

```

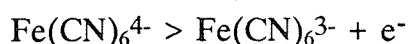

APPENDIX E

CALIBRATION OF THE FLOW RIG

Calibration was carried out using the diffusion limited current in the potassium ferricyanide-ferrocyanide redox system⁽¹⁾.

The solution contained equimolar (10⁻³M) potassium ferrocyanide and potassium ferricyanide with a large excess (0.1M) of sodium hydroxide as a supporting electrolyte.

With the electrolyte flowing at 500ml/min the polarisation curve was obtained for each of the 10 cells (specimens) for the oxidation of ferrocyanide to ferricyanide:



Here, the limiting current is caused by the depletion of the reactant species at the anode⁽²⁾. Figure E.1 schematically shows a polarisation curve. The potential range of the limiting current tended to be narrow. This was probably because the potential for oxygen liberation in alkaline solution is close to the potential of the ferrocyanide couple⁽²⁾.

A potential common to the plateaux of each of the 10 electrodes was chosen, and by maintaining this potential whilst varying the indicated flowrate, the variation of the mass transport coefficient and diffusion boundary layer thickness was obtained:

$$i_{lim} = z F c_b k_m$$

where:

c_b = bulk concentration of electro-active species

$$k_m = \frac{D}{\delta_d}$$

F = 96,500 coulombs

z = no. of electrons transferred in the reaction (=1)

Measurements were made on each electrode, one at a time. As anticipated, the diffusion limited current, i_{lim} , was the same for each of the 10 electrodes at a given

flowrate in the laminar flow regime, Figure E.2 for example. The results of the calibration in the laminar flow regime are given in Table E.1, and showed good agreement with literature correlations^(1,3), Figure E.3a.

On increasing the flowrate above about 4 litres/minute ($Re \approx 2,150$) the mass transfer coefficient showed quite a wide variation from specimen to specimen, which was indicative of transitional flow. This effect persisted at flowrates in excess of 20 litres/minute ($Re \approx 10,000$) and fully turbulent flow was not developed.

For calibration in the turbulent flow regime, the plastic mesh was installed. This time, the reduction of ferricyanide to ferrocyanide was used since the limiting plateaux were better defined. The results are presented in Table E.2. The literature on mass transfer in a channel with turbulence promoters over the flowrates of interest is limited. A best approximation is the work of Leitz and Marincic⁽⁴⁾ who looked at the shape and position of turbulence promoters on mass transfer in a rectangular channel, Figure E.3b.

The enhanced mass transfer accorded by the turbulence promoters is clearly evident in Figure E.4.

REFERENCES

1. J.R. Selman and C.W. Tobias, in "Advances in Electrochemical Engineering", volume 10, p.212, Academic Press, (1978).
2. Eisenberg, C.W. Tobias and Wilkie, J. Electrochem. Soc., **101**, p.306, (1954).
3. C.W. Tobias, R.G. Hickman, Z. Phys. Chem., Leipzig, **220**, p.145, (1954).
4. F.B. Leitz and L. Marincic, J. Appl. Electrochem, **7**, p.474, (1977).
5. N. Ibl and D. Landolt, J. Electrochem. Soc., **115**, p.713, (1968).
6. R.A. Robinson and R.H. Stokes, "Electrolyte Solutions", 2nd Edition, p.513, Butterworths, London, (1959).

Table E.1 Variation with Reynold's Number of Experimental Values of Limiting Current and Derived Values of Mass Transport Coefficient, Diffusion Boundary Layer Thickness and Sherwood Number

FLOWRATE (Litres/min)	VELOCITY (cm/s)	REYNOLD'S NUMBER ⁽¹⁾ (Re)	i_{LIM} (A/cm ²)	$k_m^{(2)}$ (cm/s)	δ_d (μm)	SHERWOOD NUMBER ⁽³⁾ (Sh)
0.4	3.2	214	1.14×10^{-4}	1.18×10^{-3}	110	54.3
0.5	4.0	269	1.18×10^{-4}	1.22×10^{-3}	100	56.1
1.0	7.9	537	1.46×10^{-4}	1.51×10^{-3}	83	69.5
1.5	11.9	805	1.62×10^{-4}	1.68×10^{-3}	74	77.3
2.0	15.9	1074	1.80×10^{-4}	1.87×10^{-3}	67	86
2.5	19.8	1342	1.92×10^{-4}	1.99×10^{-3}	63	91.5
3.0	23.8	1611	2.04×10^{-4}	2.11×10^{-3}	59	97.1
3.5	27.8	1879	2.16×10^{-4}	2.24×10^{-3}	56	103.0
4.0	31.8	2148	2.22×10^{-4}	2.40×10^{-3}	52	110.4

NOTES: (1) $Re = \frac{ud}{\nu}$

d = hydraulic diameter

= 0.575 cm

ν = 0.85×10^{-2} (cm²/s)⁽⁵⁾

u = velocity (cm/s)

(2) $\delta_d = \frac{D}{k_m}$

D = 1.25×10^{-5} (cm²/s)⁽⁶⁾

(3) $Sh = \frac{k_m d}{D}$

**Table E.2 Variation with Reynold's Number of Experimental Values of Limiting Current and
Derived Values of k_m and Sh with Turbulence Promotion (for notes - see Table E.1)**

FLOWRATE (Litres/min)	VELOCITY (cm/s)	REYNOLD'S NUMBER⁽¹⁾ (Re)	i_{LIM} (A/cm²)	$k_m^{(2)}$ (cm/s)	SHERWOOD NUMBER⁽³⁾ (Sh)
0.5	4.0	269	1.41×10^{-4}	1.46×10^{-3}	67.2
1.0	7.9	537	1.79×10^{-4}	1.85×10^{-3}	85.3
1.5	11.9	805	2.30×10^{-4}	2.38×10^{-3}	109.6
2.0	15.9	1074	2.55×10^{-4}	2.64×10^{-3}	121.6
2.5	19.8	1342	2.79×10^{-4}	2.89×10^{-3}	133.0
3.0	23.8	1611	3.09×10^{-4}	3.20×10^{-3}	147.3
3.5	27.8	1879	3.32×10^{-4}	3.44×10^{-3}	158.3
4.0	31.8	2148	3.51×10^{-4}	3.64×10^{-3}	167.3
4.5	35.7	2416	3.69×10^{-4}	3.82×10^{-3}	175.9
7.0	55.6	3758	4.33×10^{-4}	4.49×10^{-3}	206.4
10.0	79.4	5639	5.39×10^{-4}	5.59×10^{-3}	256.9
12.0	95.2	6443	5.95×10^{-4}	6.16×10^{-3}	283.2
14.8	117.8	7946	6.61×10^{-4}	6.85×10^{-3}	315.1

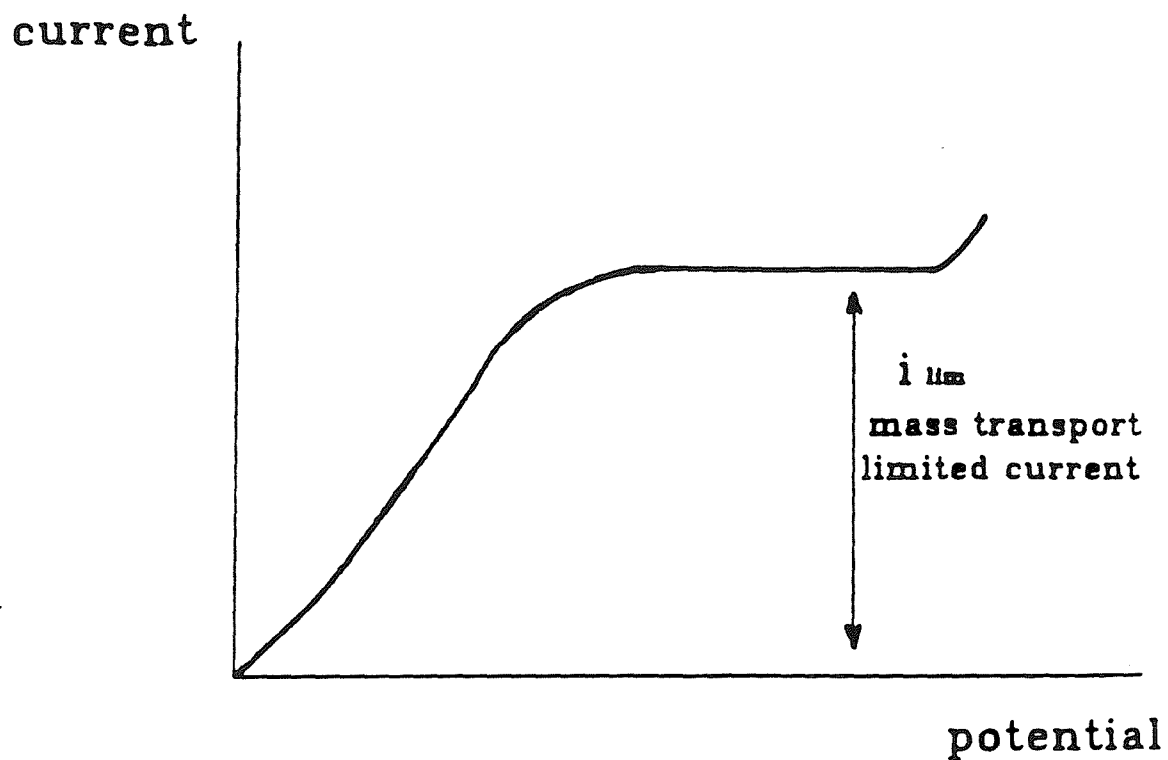


Figure E.1 Typical polarisation curve for the ferrocyanide/ferricyanide system (schematic)

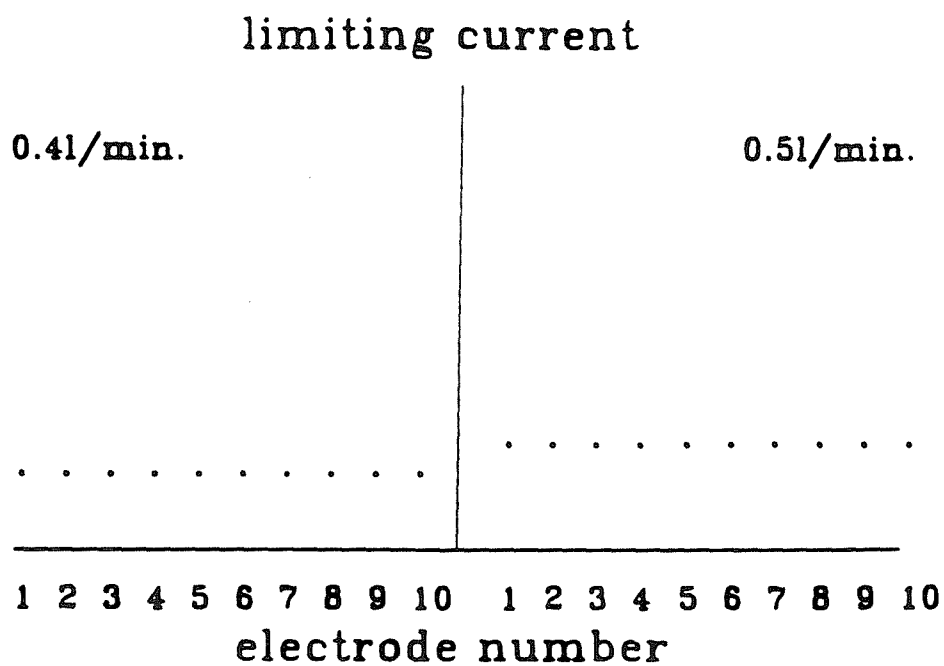
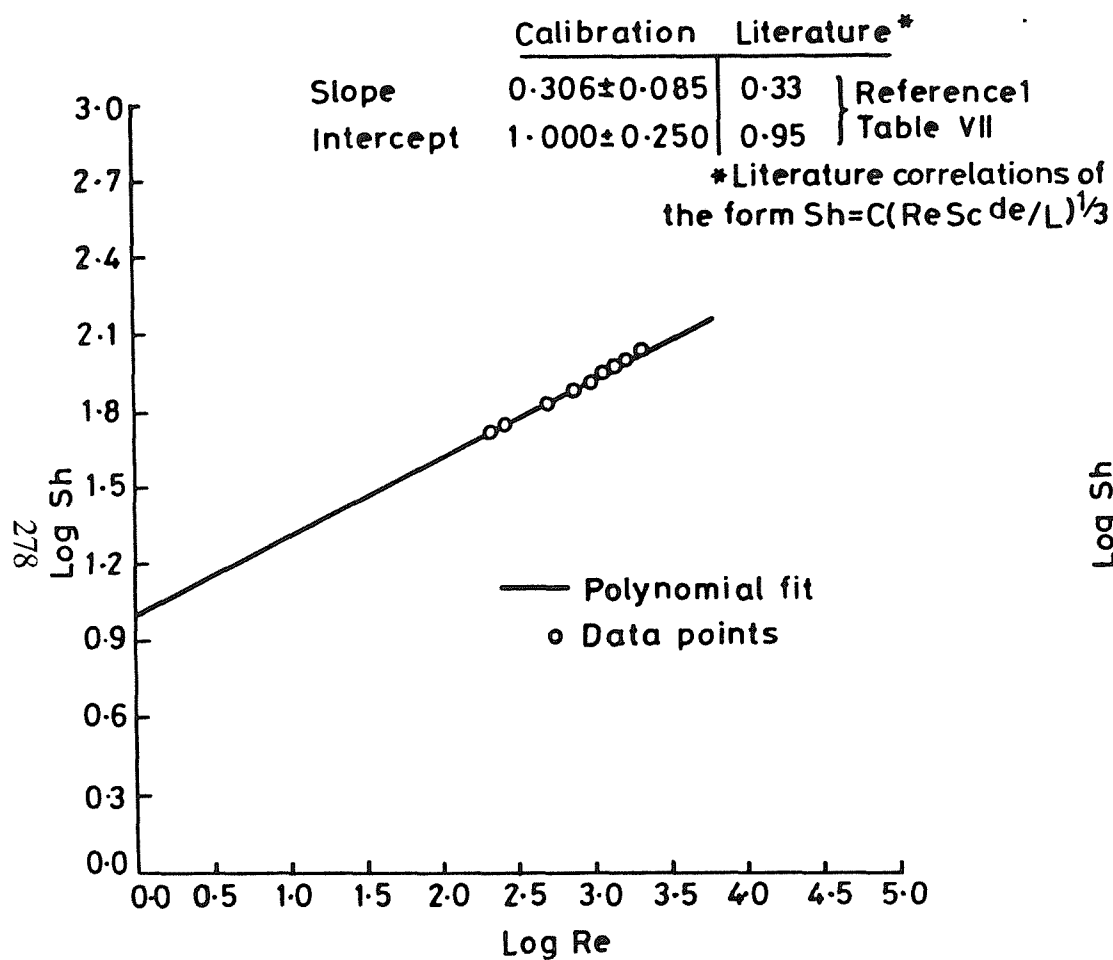


Figure E.2 Diffusion-limited current for ten electrodes in the laminar flow regime (schematic)

(a) Laminar Flow



(b) Turbulence Promoters

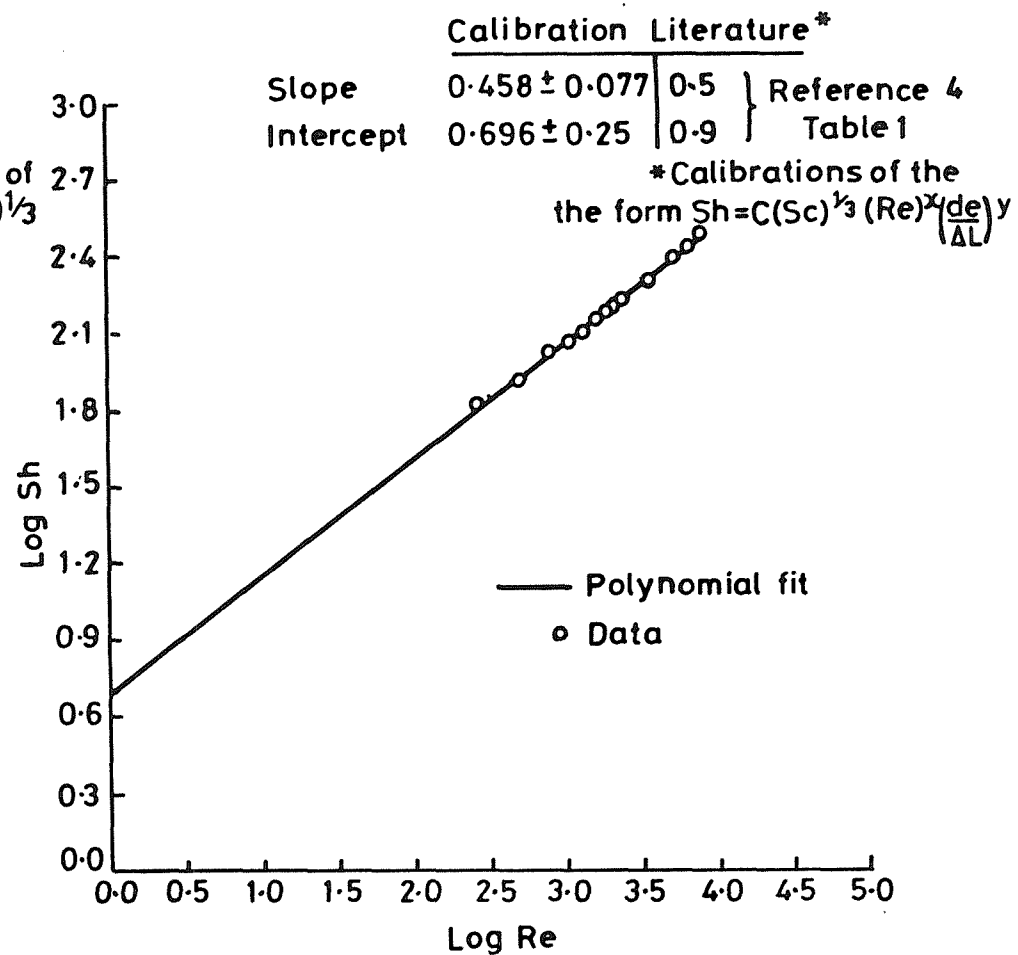


Figure E.3 Results of flow channel calibration

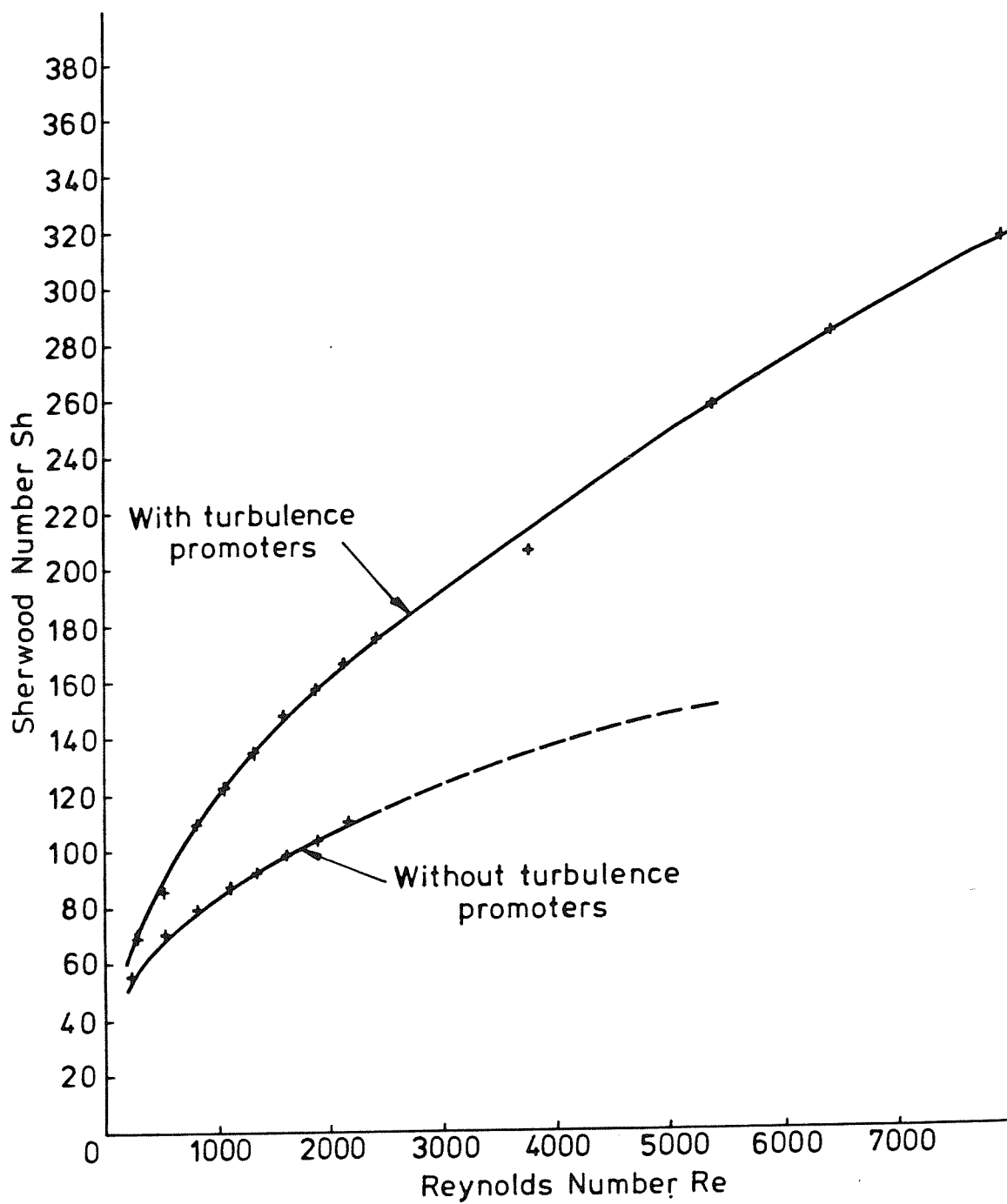


Figure E.4 Enhanced mass transfer due to turbulence promotion

APPENDIX F

INFORMATION ON INCLUSION SIZE AND SHAPE DERIVED FROM IMAGE ANALYSIS

	Mean Area (μm^2)	D (μm)	d (μm)	$\frac{d}{D}$	V_{s1} (μm^3)	V_{s2} (μm^3)	V_{s3} (μm^3)
304L Commercial Purity	2.46	2.63	1.19	2.21	1.95	4.31	2.9
304L Commercial Purity (Laser Treated)	1.64	2.32	0.90	2.58	0.98	2.54	1.6
304L High Sulphur	2.34	2.15	1.39	1.55	2.18	3.36	2.7
304L High Sulphur (Laser Treated)	2.37	2.16	1.40	1.54	2.22	3.42	2.7
304L High Purity	1.77	1.83	1.27	1.09	1.55	2.23	1.9
316L Commercial Purity	2.47	2.88	1.09	$\frac{2.64}{\{2.38\}}$	1.80	4.73	1.5

NOTES

1. Mean Area = mean particle area of inclusion measured by image analysis
2. D = major axis of particles (measured by image analysis)
3. d = calculated minor axis of particle (from: $\text{Area} = \frac{\pi}{4} \cdot Dd$)
4. $\frac{d}{D}$ = calculated degree of "roundness" ($\{ _ \}$ value measured by image analysis)
5. V_{s1} = volume of *prolate spheroid* where: $V_{s1} = \frac{\pi}{6} \cdot Dd^2$
6. V_{s2} = volume of *oblate spheroid* where: $V_{s2} = \frac{\pi}{6} \cdot D^2 d$
7. V_{s3} = volume of *spheroid* where: $V_{s3} = \frac{4\pi}{3} \cdot r^3$ (radius of spheroid (r) calculated from the Area)

REFERENCES

REFERENCES

CHAPTER 1

1. J. Stewart, D.B. Wells, P.M. Scott, "The Initiation of Intergranular Stress Corrosion Cracking on Sensitised Stainless Steel in Dilute Thiosulphate Solutions" in "Environment Induced Cracking of Metals" ed. M.B. Ives, Kohler, Wisconsin, October 2-6 1988, NACE, Houston, Texas (in press).
2. D.B. Wells, D.Phil. University of Oxford, 1989.
3. U.R. Evans and J. Stockwell, J. Chem. Soc. London, **2**, p.2651 (1927).
4. P. Marcus and I. Olefjord, Corrosion Science, **28**, p.589 (1988).
5. A.G. Revesz and J. Kruger in "Passivity of Metals", eds. R. Frankenthal and J. Kruger, p.137, The Electrochemical Society, Princeton N.J, (1978).
6. J.B. Lumsden and R.W. Staehle, "Surface Analysis Techniques for Metallurgical Applications", ASTM STP 596, (1976).
7. K. Hashimoto and K. Asami, Corrosion Science, **19**, p.251, (1979).
8. J.R. Cahoon and R. Bandy, Corrosion, **38**, p.299, (1982).
9. J. Yahole, J.K. Ives, in "Passivity and its Breakdown on Iron and Iron-base Alloys" eds. R.W. Staehle and H. Okada, p.69, NACE, Houston Texas, (1976).
10. A.T. Fromhold, *ibid.*, p.85.
11. Z. Szklarska-Smialowska, "Pitting Corrosion of Metals", p.20, NACE, Houston, Texas, (1986).
12. S. Matsuda, K. Sugimoto, Y. Sawada, in "Proc. 4th Int. Symp. on Passivity", p.699, Airlie, West Virginia (1977).
13. M.J. Graham, "The Formation and Breakdown of Passive Oxide Films", at 26th Corrosion Science Symposium, UMIST, U.K., (1985).
14. J. Stewart and D.E. Williams, in "Localised Corrosion" eds. H.S. Isaacs and U. Bertocci, Orlando, Florida, June 1-5 1987, NACE, Houston, Texas, (in press).
15. Y.M. Kolotyrkin, Corrosion, **19**, p.261, (1963).
16. Z. Szklarska-Smialowska, Corrosion, **27**, p.223, (1971).
17. J. Kruger, in "Passivity and its Breakdown in Iron and Iron-base Alloys" eds. R.W. Staehle and H. Okada, p.61, NACE, Houston Texas, (1976).
18. Y. Hisamatsu, *ibid.*, p.99.
19. J.R. Galvele in "Passivity of Metals", p.285, The Electrochemical Society, Princeton NJ, (1978).

REFERENCES

20. J.R. Galvele, in "Treatise on Materials Science and Technology" vol. 23, ed. J.C. Scully, p.1, Academic Press, London (1983).
21. C. Westcott, in "Electrochemistry - A Specialist Periodical Report", vol. 10, p.85, The Royal Society of Chemistry, London, (1985).
22. H.-H. Strehblow, in "9th International Congress on Metallic Corrosion", vol.2, p.99, Toronto, 3-7 June, (1984).
23. Z. Szklarska-Smialowska, "Pitting Corrosion of Metals", NACE, Houston, Texas, (1986).
24. R.C. Newman, Corrosion Science, **25**, p.331, (1985).
25. R.C. Newman and H.S. Isaacs, in "Passivity of Metals and Semiconductors", ed. M. Froment, p.269, Elsevier Science Publishers B.V., Amsterdam, (1983).
26. Z. Szklarska-Smialowska, "Pitting Corrosion of Metals", p.312, NACE, Houston, Texas, (1986).
27. J. Mankowski and Z. Szklarska-Smialowska, Corrosion Science, **15**, p.493, (1975).
28. T. Hakkarainen in "Metallic Corrosion: Proceedings of the 8th International Congress", p.157, Mainz, DECHEMA, (1981)
29. T. Hakkarainen in "Corrosion Chemistry within Pits, Crevices and Cracks", ed. A. Turnbull, p.17, HMSO, (1987).
30. T. Hakkarainen, in "Electrochemical Methods in Corrosion Research", ed. M. Duprat, p.81, vol. 8, Materials Science Forum, (1986).
31. R.C. Newman and H.S. Isaacs, J. Electrochem. Soc, **103**, p.1621, (1983)
32. R.C. Newman, Corrosion Science, **25**, p.341, (1985).
33. G.T. Gaudet, W.T. Mo, T.A. Hatton, J.W. Tester, H.S. Isaacs, and R.C. Newman, A.I.Ch.E. Journal, **32**, p.949, (1986).
34. C. Westcott, Ph.D Thesis, University of Southampton, (1987).
35. D.E. Williams, C. Westcott, M.Fleischmann, J. Electrochem. Soc., **132**, p.1804, (1985).
36. M. Keddam, M. Krarti, C. Pallotta, Corrosion, **43**, p.454, (1987).
37. H. Ezuber, A.J. Betts, R.C. Newman, Materials Science Forum, vols. 44 and 45, p.247-258, (1989).
38. U.R. Evans J. Chem. Soc. London, p.1020, (1927).
39. T.P. Hoar, D.C. Mears, G.P. Rothwell, Corrosion Science, **5**, P.279, (1965)
40. T.P. Hoar, Disc. Faraday Soc., **1**, p.299, (1947).
41. T.P. Hoar, Trans. Faraday Soc., **45**, p.683, (1949).

REFERENCES

42. N. Sato, *Electrochimica Acta*, **16**, 1683, (1971).
43. N. Sato, K. Kudo, T. Noda, *ibid.*, p.1909.
44. H.H. Uhlig, *J. Electrochem. Soc.*, **97**, p.215c, (1950)
45. H.P. Leckie and H.H. Uhlig, *J. Electrochem. Soc.*, **113**, p.1261, (1966).
46. H. Boehni and H.H. Uhlig, *J. Electrochem. Soc.*, **116**, p.906, (1969).
47. Y. M. Kolotyrkin, *J. Electrochem. Soc.*, **108**, p.209, (1961).
48. B. MacDougall, *J. Electrochem. Soc.*, **126**, p.919 (1979)
49. Z. Szklarska-Smialowska and M. Janik-Czachor, *Corrosion Science*, **11**, P.901, (1971).
50. P. Leckie, *J. Electrochem. Soc.*, **117**, p.1152, (1970)
51. W. Schwenk, *Corrosion*, **20**, 4, p.129t, (1964).
52. W. Schwenk, *Corrosion Science*, **5**, p.245, (1965).
53. E. A. Lizlovs and A.P. Bond, *J. Electrochem. Soc.*, **115**, p.1130, (1968).
54. P.H. Balkwill, C. Westcott, D.E. Williams, *Materials Science Forum*, Vols. 44 & 45, p.299 (1989).
55. R.C. Newman, *Corrosion Science*, **23**, p.1045, (1983).
56. N. Azzeri, F. Mancia, A. Tamba, *Corrosion Science*, **22**, p.675, (1982).
57. C. Westcott and I.W. Cavell, unpublished work, (1987).
58. G.S. Frankel, L. Stockert, F. Hunkeler, H. Boehni, *Corrosion*, **43**, p.429, (1987).
59. U.R. Evans, "Corrosion and Oxidation of Metals", Edward Arnold, London, (1960).
60. D.E. Williams, C. Westcott, M.Fleischmann, *J. Electrochem. Soc.*, **132**, p.1796, (1985).
61. T. Shibata and T. Takeyama, *Corrosion*, **33**, p.243, (1977).
62. N. Sato, *J. Electrochem. Soc.*, **123**, p.1197, (1976).
63. P. Forchhammer and H.J. Engell, *Werks. und Korros.*, **20**, p.1, (1969).
64. Y. Hisamatsu, T. Yoshii, Y. Matsumura, "Localised Corrosion", NACE 3, eds. R. Staehle, B. Brown, J. Kruger, A. Agrawal, p.547, NACE, Houston Texas, (1974)
65. N. Sato, *J. Electrochem. Soc.*, **129**, p.255, (1982).

REFERENCES

66. D.E. Williams, M. Fleischmann, J. Stewart, T.P. Brooks, in "Electrochemical Methods in Corrosion Research", ed. M. Duprat, p.151, vol. 8, Materials Science Forum, (1986).
67. G. Daufin, J. Pagetti, J.P. Labbe, F. Michel, Corrosion, **41**, p.533, (1985).
68. G.S. Eklund, J. Electrochem. Soc., **121**, p.467, (1974).
69. U.Bertocci, M. Koike, S. Leigh, F. Qiu, G. Yang, J. Electrochem. Soc., **133**, p.1782, (1986).
70. B. Baroux, Corrosion Science, **28**, p.969, (1988).
71. P. Bindra, M. Fleischmann, J.W. Oldfield, D. Singleton, Disc. Chem. Soc., **56**, p.180, (1973).
72. S.M. Sharland, C.M Bishop, P.H. Balkwill, J. Stewart, in "Localised Corrosion" eds. H.S. Isaacs and U. Bertocci, Orlando, Florida, June 1-5 1987, NACE, Houston, Texas, (in press).
73. S.M Sharland, Ph.D Thesis, Imperial College, London, (1988).

CHAPTER 2

1. H.B. Thompson, personal communication.
2. J. Stewart and T.P. Brooks, unpublished work (1984)

CHAPTER 3

1. M. Keddam, M. Krarti, C. Pallotta, Corrosion, **43**, p.454, (1987).
2. P.H. Balkwill, C. Westcott, D.E. Williams, Materials Science Forum, Vols. 44 & 45, p.299 (1989).
3. E. Brauns and W. Schwenk, Arch. Eisenhuettenw., **32**, p.387, (1961).
4. D.E. Williams, C. Westcott, M.Fleischmann, J. Electrochem. Soc., **132**, p.1796, (1985).
5. D.E. Williams, C. Westcott, M.Fleischmann, J. Electrochem. Soc., **132**, p.1804, (1985).
6. R.C. Newman, Corrosion Science, **23**, p.1045, (1983).
7. N. Azzeri, F. Mancia, A. Tamba, Corrosion Science, **22**, p.675, (1982).
8. B. Baroux, Corrosion Science, **28**, p.969, (1988).
9. D.E. Williams, D.B. Wells, A.M. Riley, J. Stewart, "Trigger Events for Pitting Corrosion" Electrochemical Society, Extended Abstracts, vol.87II, (1987)

REFERENCES

- 10 Z. Szklarska-Smialowska, "Pitting Corrosion of Metals", NACE, Houston, Texas, (1986).
- 11 K.E. Heusler and L. Fischer, *Werkst. und Korros.*, **27**, p.551, (1976).
- 12 T.P. Hoar, *Corrosion Science*, **7**, p.341, (1967).
- 13 M. Janik-Czachor, G.C. Wood, G.E. Thompson, *Brit. Corros. J.*, **15**, p.154, (1980).
- 14 M. Janik-Czachor, *J. Electrochem. Soc.*, **128**, p.513c, (1981).
- 15 L.F. Lin, C.Y. Chao, D.D. MacDonald, *J. Electrochem. Soc.*, **128**, p.1194, (1981).
- 16 A.J. Sedriks, *Int. Met. Rev.*, **28**, p.295, (1983).
- 17 K-J. Blom, *Corrosion '82*, Paper #87, NACE, Houston, Texas, (1982).
- 18 K.J. Vetter and H.H. Strehblow, *NACE 3*, eds. R. Staehle, B. Brown, J. Kruger, A. Agrawal, p.240, NACE, Houston Texas, (1974)
- 19 T.R. Beck and R.C. Alkire, *J. Electrochem. Soc.*, **126**, p.1662, (1979).
- 20 G.S. Frankel, L. Stockert, F. Hunkeler, H. Boehni, *Corrosion*, **43**, p.429, (1987).
- 21 H.W. Pickering and R.P. Frankenthal, *J. Electrochem. Soc.*, **119**, p.1297, (1972).
- 22 D.A. Vermilyea, *J. Electrochem. Soc.*, **118**, p.529, (1971).
- 23 I.L. Rosenfeld and I.S. Danilov, in *Proceedings of 3rd International Congress on Metallic Corrosion*, vol. 1, p.139, (1966).
- 24 H.S. Isaacs and G. Kissel, *J. Electrochem. Soc.*, **119**, p.1628, (1972).
- 25 J. Newman, *J. Electrochem. Soc.*, **113**, p.501, (1966).
- 26 R.C. Newman, M.A.A. Ajjawi, H. Ezuber, and S. Turgoose, *Corrosion Science*, **28**, p.471, (1988).

CHAPTER 4

1. M.G. Fontana and N.D. Greene, "Corrosion Engineering", p.271, McGraw Hill, New York, (1978).
2. G.E. Moller, *Corrosion '75*, Paper #120, NACE, Houston, Texas, (1975).
3. G.J. Danek, *Naval Engrs. J.*, **78**, p.763, (1966).
4. F.L. LaQue, *Corrosion Handbook*, ed. H.H. Uhlig, p.414, Wiley, New York, (1984).

REFERENCES

5. F.L. LaQue, "Marine Corrosion", p.141, Wiley, New York, (1975).
6. F. Mansfeld and J.V. Kenkel, Corrosion, **35**, p.43, (1979).
7. N. Sato, T. Nakagawa, K. Kudo, M. Sakashita, in "Localised Corrosion", NACE-3, eds. R. Staehle, B. Brown, J. Kruger, A. Agrawal, p.447, NACE, Houston Texas, (1974).
8. M.A.C. Castro, B.E. Wilde, Corrosion, **35**, p.560, (1979).
9. J. Postlethwaite, B. Huber, D. Makepeace, Corrosion, **42**, p.646, (1986).
- 10 M. Karamineshaad-Ranjbar, J. Mankowski, D.D. MacDonald, Corrosion, **41**, p.197, (1985).
- 11 F. Franz and P. Novak, in "Localised Corrosion", NACE-3, eds. R. Staehle, B. Brown, J. Kruger, A. Agrawal, p.576, NACE, Houston Texas, (1974).
- 12 B. Nakeyama and K. Sasa, Corrosion, **32**, p.283, (1976).
- 13 T.R. Beck and S.G. Chan, Corrosion, **37**, p.665, (1981).
- 14 C. Westcott, Ph.D Thesis, University of Southampton, (1987).
- 15 B. Poulson, Corrosion Science, **23**, p.391, (1983).
- 16 J. Stewart, AERE Report M3455, (1985).
- 17 P.H. Balkwill, C. Westcott, D.E. Williams, Materials Science Forum, Vols. 44 & 45, p.299 (1989).
- 18 P.H. Balkwill, J. Stewart, D.B. Wells, C. Westcott, D.E. Williams, "Current Fluctuations associated with Localised Corrosion: Mechanistic Studies of the early stages of pitting and stress corrosion on stainless steel", International Symposium on Corrosion Science and Engineering, Brussels, March 12-15 (1989), in press.
- 19 R. Marshall, personal communication (1984).
- 20 D.E. Williams, M. Fleischmann, J. Stewart, T.P. Brooks, in "Electrochemical Methods in Corrosion Research", ed. M. Duprat, p.151, vol. 8, Materials Science Forum, (1986).
- 21 J. Stewart and D.E. Williams, in "Localised Corrosion" eds. H.S. Isaacs and U. Bertocci, Orlando, Florida, June 1-5 1987, NACE, Houston, Texas, (in press).

CHAPTER 5

1. A.J. Sedriks, in "Stainless Steels '87", p.127, Institute of Metals, (1987).
2. Z. Szklarska-Smialowska and E. Lunarska, Werkst. und Korros., **32**, p.478, (1981).
3. G. Wranglen, Corrosion Science, **9**, p.585, (1969).

REFERENCES

4. G. Wranglen, in "Sulphide Inclusions in Steel", eds. J.J. deBarbadillo and E. Snape, p.361, ASM, Metals Park, Ohio, (1975).
5. A.J. Sedriks, *Int. Met. Rev.*, **28**, p.295, (1983).
6. Z. Szklarska-Smialowska, "Pitting Corrosion of Metals", NACE, Houston, Texas, (1986).
7. R. Kiessling, in "Sulphide Inclusions in Steel", eds. J.J. deBarbadillo and E. Snape, p.104, ASM, Metals Park, Ohio, (1975).
8. K. Sano and M. Inoye, *J. Iron Steel Inst. (Japan)*, **45**, p.9, (1959).
9. I.S. Brammar and R.W.K. Honeycombe, *JISI*, **202**, p.335, (1964).
10. C.W. Kovach, R.G. Wells, A.M. Moskwitz, *Trans. ASM*, **61**, p.575, (1968).
11. I. Takahashi, T. Sakai, M. Aoki, T. Kotaki, *Nippon Sutenresn Giho*, **16**, p.47, (1981).
12. M. Henthorne, in "Sulphide Inclusions in Steel", eds. J.J. deBarbadillo and E. Snape, p.445, ASM, Metals Park, Ohio, (1975).
13. T. Sydberger, *Jernkontorets, Forskning, Report D305*, (1979).
14. M. Smialowska, Z. Szklarska-Smialowska, M. Rychink, A. Szummer, *Corrosion Science*, **9**, p.123, (1969).
15. P. Poyet and A. Desestret, *Mem. Sci. Rev. Met*, **72**, p.133, (1975).
16. R. Kiessling and N. Lange, *JISI*, **201**, p.761, (1963).
17. Li Pei Zhong, R. Jargelius, R. Otterberg, in "Stainless Steels '84", p.158, The Institute of Metals, (1985).
18. J.W. Cobb, *JISI*, **83**, p.170, (1911).
19. J.E. Stead, *JISI*, **88**, p.74, (1916).
20. U.R. Evans, "Corrosion and Oxidation of Metals", First Supplementary Volume, p.193, Edward Arnold, London, (1968).
21. L. Tronstad and J. Sejersted, *JISI*, **127**, p.425, (1933).
22. C.E. Homer, Iron and Steel Institute, 2nd Rep. Corr. Comm., p.225, London (1934).
23. H.H. Uhlig, *Trans. AIMME*, **140**, p.411, (1940).
24. M.A. Streicher, *J. Electrochem. Soc.*, **103**, p.375, (1956).
25. N.D. Greene and M.G. Fontana, *Corrosion*, **15**, p.25, (1959).
26. W. Schwenk, *Korrosion*, **13**, p.22, (1959).
27. B.E. Wilde and J.S. Armijo, *Corrosion*, **23**, p.208, (1967).

28. S. Steinmann, *Mem. Sci. Rev. Met.*, **65**, p.615, (1969).
29. G.S. Eklund, *Jernkont. Ann*, **155**, p.637, (1971).
30. Z. Szklarska-Smialowska, A. Szummer, M. Janik-Czachor, *Brit. Corros. J.*, **5**, p.159, (1970).
31. M.B. Ives, G. Ruijin, S.C. Srivastava, in "10th International Congress on Metallic Corrosion", volume IV, p.3225, Trans. Tech. Publications, (1987).
32. D. Brooksbank and K.W. Andrews, *JISI*, **210**, p.246, (1971).
33. D. Brooksbank and K.W. Andrews, *JISI*, **206**, p.595, (1968).
34. B. Richter and W. Prause, *Werkst. und Korros.*, **27**, p.856, (1976).
35. V. Scotto, G. Ventura, E. Traverso, *Corrosion Science*, **19**, p.237, (1979).
36. P.E. Manning, D.J. Duquette, W.F. Savage, *Corrosion*, **35**, p.151, (1979).
37. B. Forchhammer and H.J. Engell, *Werkst. und Korros.*, **20**, p.1, (1969).
38. P.C. Searson and R.M. Latanision, *Corrosion*, **42**, p.161, (1986).
39. P.E. Manning, C.E. Lyman, D.J. Duquette, *Corrosion*, **36**, p.246, (1980).
40. J.L. Crolet, L.Seraphin, R. Tricot, *Metaux Corrosion Industrie* No. 616, (1976).
41. S. Brennert, in "6th European Congress on Metallic Corrosion", p.255, London, (1977).
42. G. Riedel, C. Voigt, H. Werner, K-P. Erkel, M. Gunzel, *Corrosion Science*, **27**, p.533, (1987).
43. M. Janik-Czachor, A. Szummer, Z. Szklarska-Smialowska, *Corrosion Science*, **15**, p.775, (1975).
44. R. Kiessling, *Jernkont. Ann.*, **153**, p.295, (1965).
45. G. Wranglen, *Corrosion Science*, **14**, p.331, (1974).
46. G.S. Eklund, *J. Electrochem. Soc.*, **121**, p.467, (1974).
47. S.E. Lott and R.C. Alkire, *J. Electrochem. Soc.*, **136**, p.973, (1989).
48. G. Valensi, "Contibution au Diagramme Potential-pH du Soufre", International Committee of Electrochemical Thermodynamics and Kinetics, p.51, (1950).
49. G. Valensi, CEBELCOR Report 121, R207, (1973).
50. R.C. Newman, H.S. Isaacs, B. Alman, *Corrosion*, **38**, p.261, (1982).
51. R.C. Newman, *Corrosion*, **41**, p.450, (1985).

REFERENCES

52. R.C. Newman and E.M. Franz, *Corrosion*, **40**, p.325, (1984).
53. A. Garner, *Corrosion '85*, Paper #170, NACE, Houston, Texas, (1985).
54. R.C. Newman and K. Sieradzki, *Corrosion Science*, **23**, p.363, (1983).
55. R.C. Newman, K. Sieradzki, H.S. Isaacs, *Met. Trans*, **13A**, p.2015, (1982).
56. J.Stewart, D.B. Wells, P.M.Scott, D.E. Williams, *Corrosion '88*, Paper #285, NACE, Houston, Texas, (1988).
57. P. Marcus and J. Oudar, in "Fundamental Aspects of Corrosion Protection by Surface Modification", eds. E. McCafferty, C.R. Clayton, J.Oudar, p.173, The Electrochemical Society, Pennington NJ, (1984).
58. J. Oudar and P. Marcus, in "Applications of Surface Science 3", p.48, North Holland Pub. (1979).
59. P. Marcus, A.Tessier, J. Oudar, *Corrosion Science*, **24**, p.259, (1984).
60. P. Marcus, I. Olefjord, J.Oudar, *Corrosion Science*, **24**, p.269, (1984).
61. R.C. Newman, "The Influence of Thiosulphate ions on the Localised Corrosion of Stainless Steel", AERE Report R12664, (1987).
62. R.C. Newman, *Corrosion Science*, **25**, p.341, (1985).
63. M. Henthorne, *Corrosion*, **26**, p.511, (1970).
64. M. Henthorne and R.J. Yinger, in "Cleaning Stainless Steels", STP 538, p.90, ASTM, Philadelphia PA, (1973).
65. M.A. Barbosa, *Corrosion Science*, **23**, p.1296, (1983).
66. K-J. Blom, *Corrosion '82*, Paper #87, NACE, Houston, Texas, (1982).
67. E. McCafferty, P.G.Moore, J.D. Ayers, G.K. Hubler, in "Corrosion of Metals Processed by Directed Energy Beams", eds. C.R. Clayton and C.M. Preece, Warrendale PA, AIME, (1982).
68. E. McCafferty and P.G.Moore, *J. Electrochem. Soc.*, **133**, p.1090, (1986).
69. E. McCafferty and P.G.Moore, in "Fundamental Aspects of Corrosion Protection by Surface Modification", eds. E. McCafferty, C.R. Clayton, J.Oudar, p.112, The Electrochemical Society, Pennington NJ, (1984).
70. J.B. Lumsden, D.S. Gnanamuthu, R.J. Moores, *ibid*, p.122.
71. F.B. Pickering, "The Basis of Quantitative Metallography" Institute of Metallurgical Technicians Monograph No.1, (1976).
72. K. Ruoru, Ph.D Thesis, University of Surrey, (1988).
73. A. Moskowitz, "Effects of Residual Elements on the Properties of Stainless Steels", ASTM-STP 418, p.3, Philadelphia PA (1967).

74. H.J. Dundas and A.P. Bond, Corrosion '75, Paper #159, NACE, Houston, Texas, (1975).
75. H. Pickering and D. Frankenthal, J. Electrochem. Soc., **119**, p.1305, (1972).
76. G.H. Wagner, A. Desestret, H. Coriou, L. Grall, C.R. Hebd. Seances Acad. Sci. ser.c, Sci. Chem, **270**, p.1093, (1970).

CHAPTER 6

1. P.G. Moore and E. McCafferty, J.Electrochem. Soc., **128**, p.1391, (1981).
2. J.B. Lumsden, D.S. Gnanamuthu, R.J. Moores, in "Corrosion of Metals Processed by Directed Energy Beams", eds. C.R. Clayton and C.M. Preece, p.129, Warrendale PA, AIME, (1982).
3. E. McCafferty and P.G.Moore, J. Electrochem. Soc., **133**, p.1090, (1986).
4. E. McCafferty and P.G.Moore, in "Fundamental Aspects of Corrosion Protection by Surface Modification", eds. E. McCafferty, C.R. Clayton, J.Oudar, p.112, The Electrochemical Society, Pennington NJ, (1984).
5. J.B. Lumsden, D.S. Gnanamuthu, R.J. Moores, in "Fundamental Aspects of Corrosion Protection by Surface Modification", eds. E. McCafferty, C.R. Clayton, J.Oudar, p.122, The Electrochemical Society, Pennington NJ, (1984).
6. J. Stewart, unpublished work, (1989).
7. A.S. Bransden, personal Communication
8. P.C. Searson and R.M. Latanision, Corrosion, **42**, p.161, (1986).
9. A.J. Sedriks, Int. Met. Rev., **28**, p.295, (1983).
10. Li Pei Zhong, R. Jargelius, R. Otterberg, in "Stainless Steels '84", p.158, The Institute of Metals, (1985).
11. D.B. Wells, J. Stewart, A.W. Herbert, P.M. Scott, D.E. Williams, Corrosion, **45**, p.649, (1989).
12. R.C. Newman, K. Sieradzki, H.S. Isaacs, Met. Trans, **13A**, p.2015, (1982).
13. P.G. Moore, in "Fundamental Aspects of Corrosion Protection by Surface Modification", eds. E. McCafferty, C.R. Clayton, J.Oudar, p.102, The Electrochemical Society, Pennington NJ, (1984).
14. J. Stewart, D.B. Wells, A.S. Bransden, P.M. Scott, Submitted to Corrosion Journal, (November 1989).
15. T.R. Anthony and H.E. Cline, J. Appl. Phys., **49**, p.1248, (1978).

CHAPTER 7

1. Z. Szklarska-Smialowska, "Pitting Corrosion of Metals", Chapter 8, NACE, Houston, Texas, (1986).
2. P. Marcus, M. Moscatelli, J. Oudar, "Surfaces, Inhibition and Passivation", eds. E. McCafferty and R.J. Brodd, The Electrochemical Society, Pennington NJ, P.281, (1986).
3. I. Olefjord and P. Marcus, in Proceedings of Eurocorr. '87, p.361, DEHEMA, (1987)
4. J.N. Wanklyn, Corrosion Science, **21**, p.211, (1981).
5. H. Ogawa, H. Omata, I. Itoh, H. Okada, Corrosion, **34**, p.53, (1978).
6. K. Sugimoto and Y. Sawada, Corrosion, **32**, p.347, (1976).
7. R.C. Newman, Corrosion Science, **25**, p.331, (1985).
8. R.C. Newman, Corrosion Science, **25**, p.341, (1985).
9. Y.M. Kolotyrkin, W.M. Knyazheva, in "passivity of Metals", eds. R.P. Frankenthal, J.Kruger, p.678. The Electrochemical Society, Princeton NJ, (1978).
10. K. Sugimoto and Y. Sawada, Corrosion Science, **17**, p.425, (1977).
11. T.P. Hoar, J. Electrochem. Soc, **117**, p.17c, (1970).
12. M. da Cunha Belo, B. Rondot, F. Pons, J. Le Hericy, J.P. Langerons, J. Electrochem. Soc, **124**, p.1317, (1977).
13. P. Marcus and I. Olefjord, Corrosion Science, **26**, p.589, (1988).
14. K. Hashimoto, in "Passivity of Metals and Semiconductors", ed. M. Froment, p.235, Elsevier Science Publishers BV, Amsterdam (1983).
15. K. Hashimoto, K. Asami, K. Teramoto, Corrosion Science, **19**, p.3, (1979).
16. K. Hashimoto, K. Asami, M. Naka, T. Masumoto, Corrosion Science, **19**, p.165, (1979).
17. K.Asami, M. Naka, K. Hashimoto, T. Masumoto, J. Electrochem. Soc., **127**, p.2130, (1980).
18. B. Forchhammer and H.J. Engell, Werkst. und Korros., **20**, p.1, (1969).
19. G. Herbsleb and W. Schwenk, Corrosion Science, **13**, p.739, (1973).
20. W. Yang and A. Pourbaix, in Proceedings of 8th International Congress on Metallic Corrosion, Vol.1, p.172, Mainz, DEHEMA, (1981).
21. W.M. Latimer, "Oxidation Potentials", 2nd edition, Prentice Hall, New York, (1952).

22. M. Kesten, *Corrosion*, **32**, p.94, (1976).
23. S.E. Lott and R.C. Alkire, *J. Electrochem. Soc.*, **136**, p.973, (1989).
24. P. Marcus and M. Moscatelli, *J. Electrochem. Soc.*, **136**, p.1634, (1989).
25. P. Marcus and J. Oudar, in "Fundamental Aspects of Corrosion Protection by Surface Modification", eds. E. McCafferty, C.R. Clayton, J.Oudar, p.173, The Electrochemical Society, Pennington NJ, (1984).
26. Y.M. Kolotyrkin and L.I. Freiman, "Korroziya i Zashita ot Korrozii", Izd. WINITI, Moscow, **5**, p.5, (1978).
27. K. Ruoru, Ph.D Thesis, University of Surrey, (1988).
28. R.C. Newman, personal Communication

CHAPTER 8

1. Li Pei Zhong, R. Jargelius, R. Otterberg, in "Stainless Steels '84", p.158, The Institute of Metals, (1985).
2. R.C. Newman, personal Communication
3. P.H. Balkwill, J. Stewart, D.B. Wells, C. Westcott, D.E. Williams, "Current Fluctuations associated with Localised Corrosion: Mechanistic Studies of the early stages of pitting and stress corrosion on stainless steel", International Symposium on Corrosion Science and Engineering, Brussels, March 12-15 (1989), in press.